# DOTTORATO DI RICERCA IN SCIENZE DELLA TERRA

*Università degli Studi di Firenze*

## ANDREA AGOSTINI

## Structural evolution of the Main Ethiopian Rift: integration between modelling and field data

**settore scientifico disciplinare: GEO-03**

**Tutore**:     Prof. Federico Sani

**Co-Tutori**:  Dott. Marco Bonini

           Dott. Giacomo Corti

Coordinatore: Prof. Federico Sani

XXII CICLO

Firenze, 31 Dicembre 2009

# Structural evolution of the Main Ethiopian Rift: integration between modelling and field data

**INDEX**

# Riassunto

Questa tesi si focalizza sull'evoluzione del *Main Ethiopian Rift* (MER), un *rift* continentale che separa la placca nubiana dalla Somalia. Il MER offre una documentazione completa dell'evoluzione spazio temporale di un *rift* continentale, dai suoi stadi precoci fino a quelli più evoluti. Può quindi essere considerato come un archetipo per il processo di rottura continentale e per lo studio dell'evoluzione dei *rift* continentali.

Questo lavoro si propone di studiare e migliorare la comprensione di alcuni aspetti dell'evoluzione del MER attraverso un approccio multidisciplinare, che integra modelli analogici deformati in centrifuga applicati alle problematiche relative al MER, analisi di foto satellitari e lavoro di campagna, effettuato durante tre missioni nel 2007-2009.

I modelli analogici in centrifuga hanno migliorato gli esistenti studi di modellizzazione analogica sperimentale sui *rift* obliqui, utilizzando un complesso set-up che ricrea la litosfera tramite la sovrapposizione di differenti livelli fragili e duttili, e condizioni al contorno più realistiche in termini di applicazioni degli stress estensionali. I risultati suggeriscono come l'obliquità di un *rift* possa essere uno dei più importanti parametri che controllano le caratteristiche di un *rift* obliquo in natura non solo in termini di *pattern* di fagliazione, come sottolineato anche da precedenti lavori, ma anche in termini di evoluzione, architettura e partizione cinematica della deformazione. In particolare, grosse differenze in questi parametri sono state osservate tra modelli che riproducono *rift* a bassa e ad alta obliquità (angolo tra la perpendicolare all'orientazione del *rift* e la direzione di estensione). I più grandi cambiamenti nello stile deformativo si verificano per obliquità di circa 30°/45°, valore che segna il passaggio tra modelli caratterizati da una deformazione prevalentemente estensionale a modelli con deformazione prevalentemente trascorrente. In dettaglio, per modelli a bassa obliquità (compresa tra 0° e 30°-45°) si osservano due distinte fasi evolutive, caratterizzate dalla diacronia attivazione di due principali sistemi di faglie e una partizione della deformazione tra i bordi e la *rift valley* che varia da elevata (obliquità da 0° a 30°) a moderata (obliquità 45°). I modelli ad alta obliquità (60°-75°) sono invece caratterizzati da una singola fase evolutiva (con l'attivazione di un solo sistema di faglie) e partizione della deformazione assente.

L'analisi delle immagini satellitari ha permesso una migliore caratterizzazione dei due principali sistemi di faglie che interessano il MER (faglie bordiere e fagli associate alla *Wonji Fault Belt,* WFB), in termini di lunghezza e orientazione media. In particolare, i risultati sottolineano una variazione del peso statistico dei due differenti sistemi di faglie lungo l'asse

del *rift*, mostrando una diminuzione dell'importanza relativa delle faglie della WFB andando dal segmento più settentrionale del MER verso sud.

Il lavoro di campagna ha permesso di documentare evidenze di attività tettonica quaternaria, e in alcuni casi olocenica, di faglie sia su entrambi i bordi che nella *rift valley*, lungo le faglie della WFB. In particolare, evidenze di recente attività tettonica sono state trovate anche su faglie bordiere alla transizione tra i segmenti settentrionale e centrale del MER. Questo in parte può essere in contrasto con precedenti studi che indicano come totalmente disattivate le faglie bordiere a queste latitudini. Le direzioni di estensione ottenute dell'analisi degli indicatori cinematici variano da circa N110°-130°E sui margini del MER, a N90°-100°E sulle faglie interne (WFB).

Le somiglianze riscontrabili tra i modelli analogici e i differenti segmenti del MER in termini di *pattern* di fagliazione, architettura del *rift* e diacrona attivazione di differenti sistemi di faglie, hanno permesso di confrontare i risultati ottenuti con le differenti metodologie di studio utilizzate in questa tesi.

Il *best-fit* delle orientazioni medie dei due principali sistemi di faglie dei modelli con i risultati dell'analisi delle immagini satellitari implica una direzione di estensione ~N100°E. Questa è in buon accordo con precenti risultati di misure geodetiche, analisi del movimento delle placche e dati geofisici. Inoltre, l'analisi cumulativa degli indicatori cinematici delle faglie interne (WFB) rivela una consistente direzione di estensione N100°E che quindi, sulla base dei risultati dei modelli, si ritiene rappresenti la direzione regionale di estensione che agisce nel sistema. La direzione di estensione N110°-130°E determinata per le faglie bordiere del MER evidenzia invece una locale riorientazione del campo dello stress intorno alla discontinuità reologica a scale litosferica che caratterizza i margini del *rift*. Poiché inoltre, l'intera evoluzione dei modelli analogici è determinata da una cinematica costante, si ipotizza che il movimento tra Nubia e Somalia sia stato costante lungo una direzione ~N100°E dall'inizio del processo di *rifting* nel tardo Miocene.

La comparazione tra le caratteristiche di differenti segmenti che compongono il MER e l'evoluzione dei modelli ha permesso inoltre di discriminare una variazione dell'evoluzione del *rift* lungo l'asse. Più precisamente si osserva una diminuzione della maturità del sistema andando da nord a sud: a nord il MER si trova in uno stadio di incipiente rottura continentale, al centro in uno stadio transizionale e a sud in uno stadio di precoce *rifting* continentale. In questo scenario, i differenti segmenti del MER esemplificano la tipica evoluzione di un *narrow rift* continentale.

# Chapter 1

# Introduction

Continental rifting represents one the most important geodynamical processes affecting the lithosphere-asthenosphere system. This process proceeds from the application of extensional stresses to the continental lithosphere to the accumulation and localization of strain until the lithosphere ruptures, whereupon seafloor spreading and production of oceanic lithosphere accommodate most of the extension. Thus -if successful- the process ends with the formation of a new ocean bordered by a pair of passive continental margins; therefore, rifting is fundamental in the growth and evolution of continents.

The East African System, and in particular the Main Ethiopian Rift (MER), is one of the areas on the Earth offering a complete record of the time-space evolution of a continental rift, from its early stages to the more evolved stages. The MER thus represents a key area to analyse the evolution of continental rifting and it is taken as archetype for the continental break-up evolutionary process.

As a consequence, many scientists have focused their studies in this area, and a large amount of geological, geophysical and petrological data have been collected in last decades to better constrain the mechanism and the processes that act and acted in the MER.

However, many aspects of the rifting process still remain unclear and the influence on the process of boundary conditions such as rift kinematics, magmatism, lithosphere rheology and the role of inherited structures are still poorly understood.

This thesis aims to address some of these main aspects of rift evolution through a multidisciplinary approach that integrates experimental modelling applied to the MER, satellite images analysis and structural analyses in the field.

After a brief review of the state of art of knowledge of the geological evolution of the MER (Chapter 2), the application of the analogue modelling to the studied problems has been analysed. Analogue modelling (Chapter 3), through the extension of a multilayered brittle-ductile analogue lithosphere, provided a powerful tool in constraining the evolution of an oblique continental rift. In particular, we have investigated the role of a pre-existing lithospheric weakness. During extension, this weakness localizes deformation, and different rift obliquity is obtained by varying its trend with respect to the stretching direction.

Structural analysis from satellite images provided a new faults database and a better definition of the characteristics (in term of number, length and trend) of the different fault systems affecting the MER.

The field work (Chapter 5) was planned in order to better characterize the kinematics of the rift-related fault systems and find evidences of Quaternary activity along the MER structures as well as to verify the remote sensing analysis results.

Finally (Chapter 6), we integrated the results yielded with the different utilized method. This comparison allowed us to propose new constraints on the MER evolution.

# Chapter 2

## The Main Ethiopian Rift

the East African Rift System is One of the best examples of continental rifting is (Fig. 2.1a): along its length (~ 3000 km), all the different stages of the rifting process -from rift initiation to continental break-up- can be identified. The Main Ethiopian Rift (MER), object of this thesis, is a key sector of the East African Rift System and it represents the link region between the Afar triple junction to the North and the Kenya rift to the South (Fig. 2.1b), marking the incipient plate boundary separating Nubia and Somalia plates (e.g., Ebinger, 2005).
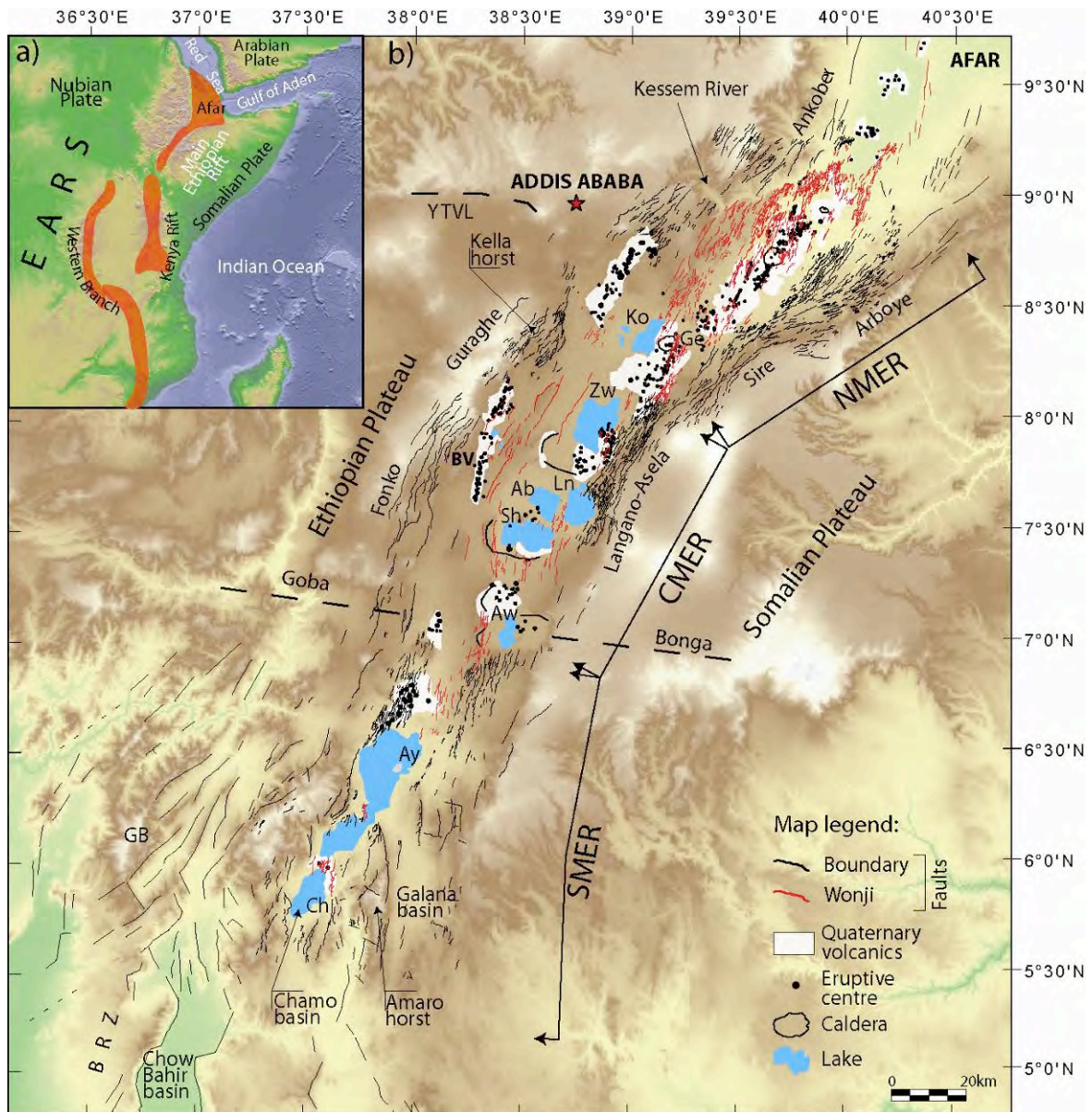


Fig. 2.1: a) location of the MER inside the East African Rift System (after Corti, 2009). b)Tectonic sketch map of the Main Ethiopian Rift superimposed onto a digital elevation model from SRTM data. Ko: Lake Koka; Ge: Gedemsa Caldera; Zw: Lake Ziway; Ln: Lake Langano; Ab: Lake Abyata; Sh: Lake Shala; Aw: Lake Awasa; Ay: Lake Abaya; Ch: Lake Chamo; BV: Butajira volcanic chain; GB: Gofa Basin and Range; BRZ: broadly rifted zone; YTVL: Yerer-Tullu Wellel volcano-tectonic lineament.

The MER extends for about 500 km in a NE-SW to N-S direction. Along its axis, the MER shows a great variability in term of fault architecture, volcanism, timing of deformation, crustal and lithospheric structures. This leads to traditionally differentiate the MER into three main segments from North to South that reflect the observed differences: the Northern, the Central and the Southern (e.g. Mohr, 1983; WoldeGabriel et al., 1990; Hayward and Ebinger, 1986; Bonini et al., 2005; Corti, 2009) (Fig. 2.1).

The Northern MER (NMER) extends from the Afar depression to the region of Lake Koka and Gedemsa caldera (Fig. 2.1), showing a roughly NE-SW trend. The Central MER (CMER), extends southward in a rough N25°-30°E direction from the Lake Koka up to Lake Awasa and the E-W Goba-Bonga tectonic lineament (Boccaletti et al., 1998) (Fig. 2.1). The Southern MER (SMER) extends southward of Lake Awasa up to the overlapping region between the MER and the Kenya Rift, characterised by a ~300 km-wide broadly rifted zone of basins and ranges (Moore and Davison, 1978; Davison and Rex, 1980; Ebinger et al., 2000)(Fig. 2.1).

## 2.1. Nubia-Somalia kinematics

Many plate kinematics models and a large amount of geological data have been proposed to constrain the Nubia-Somalia kinematics. The majority of these studies point to an average roughly N100°E direction of extension. For instance, GPS data and geodetic measurement (Billahm et al, 1999; Fernandes et al., 2004; Calais et al., 2006; Pizzi et al., 2006) indicate a direction of extension trending between N105° and N108°. These results are consistent with the Late Pleistocene-Holocene kinematics resulting from geological and geophysical data. In particular a roughly N100°E ± 10° direction of extension is derived from elongation caldera complexes (e.g. Boccaletti et al., 1998; Ebinger and Casey, 2001; Casey et al., 2006) and analysis of fault slip data (e.g. Boccaletti et al., 1998; Bonini et al., 2005; Pizzi et al., 2006). Kurz et al.(2007) proposed a Quaternary N96°±5° direction of extension from faults and satellite images analyses. Geological data from the NMER indicate a similar (N105°E) direction of extension in the last 3 Ma (Wolfenden et al., 2004). Recent GPS and earthquake slip vectors indicate a ~N100°E direction of extension (Stamps et al., 2008) over the past 3.2 Ma (Horner-Johnson et al., 2007). Other models propose the MER to have been undergoing a Late Pleistocene-Quaternary NW to NNW extension (Chorowicz et al., 1994; Acocella and Korme, 2002).

An average N100°E ± 5° direction of extension results from the existing data. This direction is thus not perpendicular to the rift axis, especially in the NMER and CMER. Consequently, the MER is essentially controlled by oblique rifting conditions.

The consistency between geological and geodetic data illustrated above, suggests that Nubia-Somalia relative motion may have remained steady over the past 3 Ma, even if local kinematics changes cannot be excluded as the rift structures evolved (Stamps et al., 2008).

Conversely, the pre-3 Ma Nubia-Somalia kinematics is less constrained. Plate kinematics models are highly variable in constraining movements between the two plates. Lemaux et al. (2002) predict a shift in the pole of rotation between Nubia and Somalia (i.e., a change in kinematic in the EARS) in the Pliocene. Recent models (Royer et al., 2006) predict instead a constant motion since 11Ma with a roughly ESE-WNW direction of extension, consistent with the results of the analogue modelling presented in Corti (2008). Moreover existing field geological data point to a polyphase history of the MER related to a change in the displacement vector in the interval 6.6 to 3 Ma (Wolfenden et al., 2004) or at the Pliocene-Quaternary boundary (Boccaletti et al., 1998; Bonini et al., 2005).

2.1.1 Estimates of the separation of the Nubia and Somalia plates

Existing data show an extreme variability in the definition of the extension amount experienced by the separating Nubia and Somalia plates at the MER latitude. Plate kinematic model of Lemaux et al. (2002) predicted ~23 km of extension since 11 Ma (corresponding to rates of ~2 mm/yr). On the opposite side, Royer et al. (2006) pointed to ~130 km of extension over the same span of time (corresponding to rates of ~12 mm/yr). Between these two extreme values, most models suggest an average value of 30-40 km of Nubia-Somalia relative motion in the MER (e.g. Garfunkel and Beyth, 2006; Maguire et al., 2006), roughly corresponding to stretching values ($\beta$, i.e. the ratio between the current and the pre-rift width) varying between 1.5 and 1.7. Moreover, it must be noted an increasing trend in stretching from the SMER northward. In the SMER, Ebinger et al. (1993) suggest a $\beta \approx 1.12$; gravity data by Tiberi et al. (2005) point to $\beta \approx 1.2$ in the CMER, while, geological data predict a stretching value of $\beta \approx 1.5$ in the NMER (Wolfenden et al., 2004).

**2.2. Fault pattern**

The MER is characterized by two different normal fault systems (e.g. Mohr, 1962; Mohr and Wood, 1967; Gibson, 1969; Boccaletti et al., 1998) that differ in term of orientation, structural characteristics (e.g. length, vertical throw), timing of activation and relation with magmatism: the border faults system and a system of faults affecting the rift floor, usually referred to as Wonji Fault Belt (e.g. Mohr, 1962, 1967).

2.2.1. Border fault system

The border faults have the most important morphological expression and give rise to the major fault-escarpment defining the rift valley between the Ethiopian and the Somalian plateaus (Figs. 2.1, 2.2).

The border faults are normally long (>10km), widely spaced and characterized by large vertical offset (normally >1km; e.g. Boccaletti et al., 1998). They are usually en-echelon arranged and locally characterized by complex geometries like curvilinear segments and pull-apart-like strutures, interpreted as a consequence of an oblique component of motion (Boccaletti et al., 1992, 1998); locally curvilinear are linked by complex transfer zones. Along the Eastern margin at the CMER, the Langano Rhomboidal Fault System, result from the interaction between NE-SW border faults and pre-existing NW-SE structures (e.g. Boccaletti et al., 1998; Le Turdu et al., 1999; Korme et al., 2004). Border fault orientation varies in the different MER segments: they trends ~N45°E in the NMER, ~N30°E in the CMER, and from ~N15°E to ~N-S in the SMERn and in the SMERs respectively. The activation of the border faults results diachronous along the rift axis (see also section 2.4.2.); it is commonly referred to the late Miocene, ~11Ma in the NMER (Wolfenden, 2004); to the late Miocene-Early Pliocene (post ~6Ma) in the CMER (Bonini et al. 2005) although WoldeGabriel et al. (1990) suggest a Late Miocene (pre ~8Ma) activation, and to the Late Miocene (~10Ma) in the SMER (WoldeGabriel et al., 1990). For the SMER, Bonini et al. (2005) suggest an earlier Miocene (~20Ma) activation, related to the Kenya Rift, and a later (Plio-Pleistocene) reactivation of the structures after a period of quiescence.

Geological data and historic and local seismicity (Gouin, 1979; Wolfenden et al., 2004; Keir et al., 2006) indicate that the NMER border faults are largely inactive and consequently they results on the whole eroded (Wolfenden et al., 2004). CMER and SMER border faults are instead still active (Keir et al., 2006) and present a more clear morphology.

Fault slip data on border faults indicate a stress field characterized by an extension direction oriented roughly ESE-WNW with local variation between E-W and NW-SE (e.g. Boccaletti et al, 1992, 1998, Acocella and Korme, 2002; Bonini et al., 2005; Pizzi et al., 2006).

2.2.2. Wonji Fault Belt system

The Wonji Fault Belt (WFB) (Mohr 1962, 1967) is a tectono-volcanic system characterized by short, closely spaced, active faults that exhibit minor vertical throw (<1km; e.g. Boccaletti et al., 1998). The WFB faulting developed essentially in the last 2 my (e.g. Mohr 1962, 1967; Meyer et al., 1975; Boccaletti et al., 1998; Ebinger and Casey, 2001) and was closely associated with the intense Quaternary magmatism in the rift floor. The characteristics of the WFB faults vary along the rift axis. The WFB faults are well developed, widely affecting the centre of the depression in the NMER, and are arranged in ~N20°E-trending right-stepping en-echelon segments. In the CMER, the WFB faults are oriented ~N10°E and their number markedly decreases with respect to NMER; they are mainly concentrated not far from the borders of the rift depression, and only few faults affect the centre of the rift floor (Fig. 2.1). In the SMER the WFB faults are again oriented ~N10°E but they are comparatively fewer in number and less developed than in the other rift segments.

Results of structural analysis suggest that the WFB fault system is compatible with a roughly E–W oriented extension (e.g., Bonini et al., 1997; Boccaletti et al., 1998; Pizzi et al., 2006; Kurz et al., 2007), although a roughly NW–SE extension has been deduced from the analysis of open fractures within different Wonji segments (Acocella and Korme, 2002)


## 2.3. Crustal and mantle structures

In the last year, the Ethiopian Broadband Experiment (Nyblade and Langston, 2002; Dugda et al., 2005; Benoit et al., 2006a, b) and the EAGLE (Ethiopia-Afar Geoscientific Lithospheric Experiment; Maguire et al., 2003) collected a large amount of new data that have increased the knowledge of the crustal and lithospheric features in the MER.

These results show that the three MER segments are characterized by a high variability in the crustal and mantle structures and, in particular, by an overall southward decreasing of magmatic modification of the lithosphere (Corti, 2009).

The NMER is characterized by a progressive decrease in the lithospheric and crustal thickness in a N-NE direction associated with an increase in the basaltic magmatism related to the tectono-magmatic segments (Ebinger and Casey, 2001). Crustal thickness thins from ~33-35 km at the NMER-CMER transition, to ~24-26 km in southern Afar (e.g. Dugda et al., 2005; Maguire et al., 2006; Mickus et al., 2007; Cornwell et al., 2010; Fig. 2.2). Geophysical data reveals 20 km wide, 50 km long cooled mafic intrusions in the mid and lower crust (Keranen et al., 2004; Daly et al., 2008), arranged in a right stepping en-echelon pattern that approximately trace out the superficial expression of the Quaternary tectono-magmatic

segments. The crust and the upper mantle underneath the WFB segments are also characterized by the presence of melt (Corti, 2009 and references therein). Some authors (Kendall et al., 2005; Keir et al., 2005; Kendall et al., 2006) suggest that melt-filled dykes extend through the entire crust reaching the upper mantle up to a depth of ~75 km. Moreover, the NMER upper mantle beneath the rift depression is characterized by a low-velocity (Mackenzie et al., 2005, Keranen et al., 2009) and low-density (Cornwell et al., 2006) anomaly probably due to hot rocks with 3-5% of melt. All these features lead to consider the WFB segments as tectono-magmatic segments within the rift depression (Ebinger and Casey, 2001), with a well developed magmatic system beneath them (Rooney et al., 2007) that allows a fast magma rising and an extensive modification of the lithospheric features.
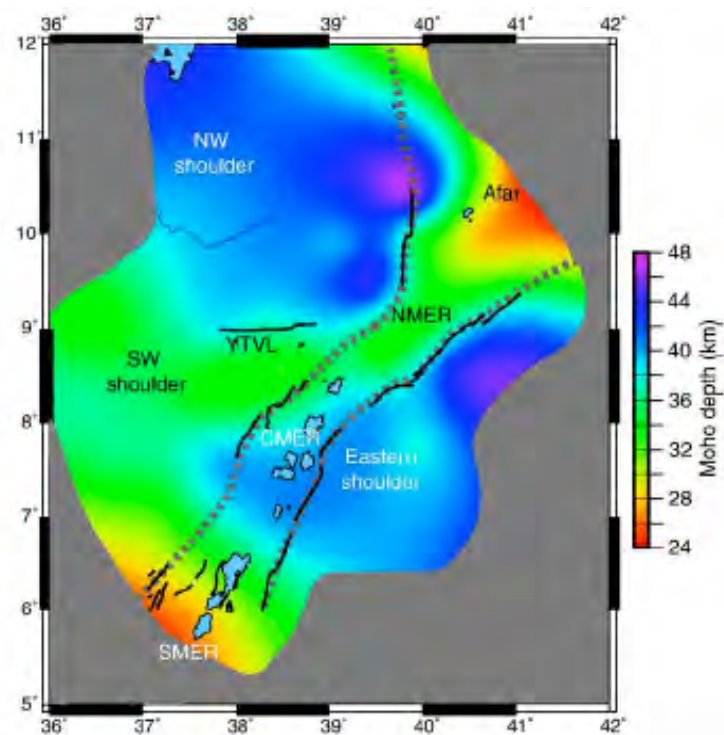


Fig. 2.2: Contour map of Moho depth after Keranen et al. (2009). The dashed gray lines show the rift outlines. Solid black lines are the rift border faults.

The CMER and SMER are instead characterized by a thicker crust. Moho depth increases from ~33-35 km at the NMER-CMER boundary to reach ~38-40 km depth in the Central MER (e.g. Dugda et al., 2005; Maguire et al., 2006; Mickus et al., 2007, Cornewell et al., 2010; Fig. 2.2), rising up again at ~30 km in the SMER (Dugda et al., 2005). Moreover, these segments are characterized by higher density of the uppermost mantle (Mickus et al., 2007), lower magnitude of upper-crustal velocities, southward increase of lithospheric elastic thickness (Ebinger and Casey, 2001). At the surface we observe a minor amount of Quaternary volcanic products in respect with the NMER (Fig 2.1). Moreover rare evidence of cooled intrusions and crustal melt underneath the rift depression were found in the CMER and

10

SMER (i.e. beneath the Debre Zeyt volcanic field (Keranen et al., 2004; Whaler and Hautot, 2006). These features concur to highlight a lower rate of magmatic modification in the lithosphere of Central and Southern MER segments.

## 2.4. Rift evolution

2.4.1. Pre-rift episodes and onset of the rifting process

Many authors have hypothesized a correlation between the MER localisation and a NE-SW-trending lithospheric-scale pre-existing weakness zone (Bastow et al., 2005, 2008; Corti, 2008; Keranen and Klemperer, 2008; Keranen et al., 2009) represented by a suture zone separating two distinct Proterozoic basement terranes underlying the Ethiopian and Somalian plateaus (Keranen and Klemperer, 2008). Differences in crustal thickness (Corti, 2009 and references therein), Vp/Vs ratio (Stuart et al., 2006) and upper-mantle velocities (e.g. Bastow et al., 2005) concur to highlight two distinct basement terranes. In the MER, pre-Cambrian deformation episodes are recorded on the extremely folded and foliated basement rocks that are exposed only in the SMER and in a small outcrop on the western margin of CMER (Kella horst; e.g. Di Paola, 1972). The pre-Cambrian and the following pre-Tertiary tectonic phases (see Corti, 2009 for details), and their correlated structures, may have influenced the MER evolution.

The first tectono-magmatic episode related to the onset of MER rifting process was the eruption of a huge amount (estimated volume 300 000 km$^3$, e.g. Mohr, 1983) of flood basalts, mainly of fissural origin, during the Eocene-Late Oligocene. The greatest eruption rate occurred from 31 to 28 Ma (Corti, 2009 and references therein), concomitant with the onset of the rifting process in the Red Sea – Gulf of Aden (Wolfenden et al., 2005). The peak of the flood basalt magmatic activity was followed by the eruption of numerous large shield volcanoes on the surface of the volcanic plateau, from 30 Ma to about 10 Ma (e.g. Kieffer et al., 2004).

These terrains were, contemporaneously or shortly after their eruption, uplifted and form the current Ethiopian and Somalian plateaus. The uplift was associated with the activity of mantle plumes (one or two plumes, or multiple plume stems rising from a lower mantle giant plume, the African superplume; see Corti, 2009 for a review). The plume effects (i.e. thermal alteration of the lithosphere, e.g. Dugda et al., 2007) were not only connected to the plateaus uplift but also to the eruption of the flood basalts itself (e.g. Ebinger and Sleep, 1998; George et al., 1999).

Moreover, mantle plumes likely concurred to trigger the extensional deformation correlated to the rifting process, by weakening the lithosphere and favouring the reactivation of the pre-existing weakness, together with the action of external plate-boundary forces (e.g. Courtillot et al., 1999, Couliè et al., 2003).

2.4.2. MER evolution

*2.4.2.1. Border faults stage*

Extensional deformation started diachronously along the MER axis in the Mio-Pliocene. An early deformation stage, probably related to a northward propagation of the Kenya Rift, affected the SMER in the Early Miocene (20-21 Ma) and lasted until 11 Ma, followed by a period of quiescence (Bonini et al., 2005; Fig. 2.3); only during the Plio-Pleistocene the structures related to the previous deformation stage were reactivated. Successively, extensional deformation began in the NMER at ~11 Ma (Wolfenden et al., 2004). In the CMER extensional deformation started only at about 5-6 Ma (Bonini et al., 2005) even if some authors suggest an older activation time at about 8-10 Ma (WoldeGabriel et al., 1990).

This early deformation phase was correlated to the evolution of the border faults defining the major rift escarpment and the subsidence of the rift floor, and was associated to a diffuse bimodal volcanic activity, which encompassed the whole rift depression.

The diachronous activation of the different MER segments has been interpreted with different models. Bonini et al. (2005) propose a Miocene-recent southward rift migration from the Afar: rifting interested the NMER in the Late Miocene, successively (Pliocene) was transferred in the CMER at the Boru Toru structural high, and only during the Late Pliocene-Pleistocene started to affect the SMER (Fig. 2.3).

Similarly, Keranen and Kemplerer (2008) proposed a southward propagation that started in the NMER at ~11 Ma, then stalled at the NMER-CMER boundary where it was deflected along the Yerer Tullu-Wellel volcanotectonic lineament (YTWL, see Fig. 2.1); according to this models extensional deformation affected the CMER and the SMER only after a stress field rotation that made the rifting in the YTWL direction less favourable.

In contrast to the propagation models showed above, Wolfenden et al. (2004) suggest a northward propagation of the deformation from the SMER, where it started at ~18 Ma, to the CMER and the NMER.

Rooney et al. (2007) suggest instead a model that indicates the MER as the result of the unification of two different rifts: the Red Sea Rift, propagating southward, and the East African Rift Systems, propagating northward. The Boru Toru Structural High represented, in

this setting, the threshold separating the two rifts, that was breached in the Pleistocene joining the two different rifts.

Moreover, according to Chorowitz et al. (1994), the WFB faults development is related to the reactivation of pre-existing Pan-African fabrics.
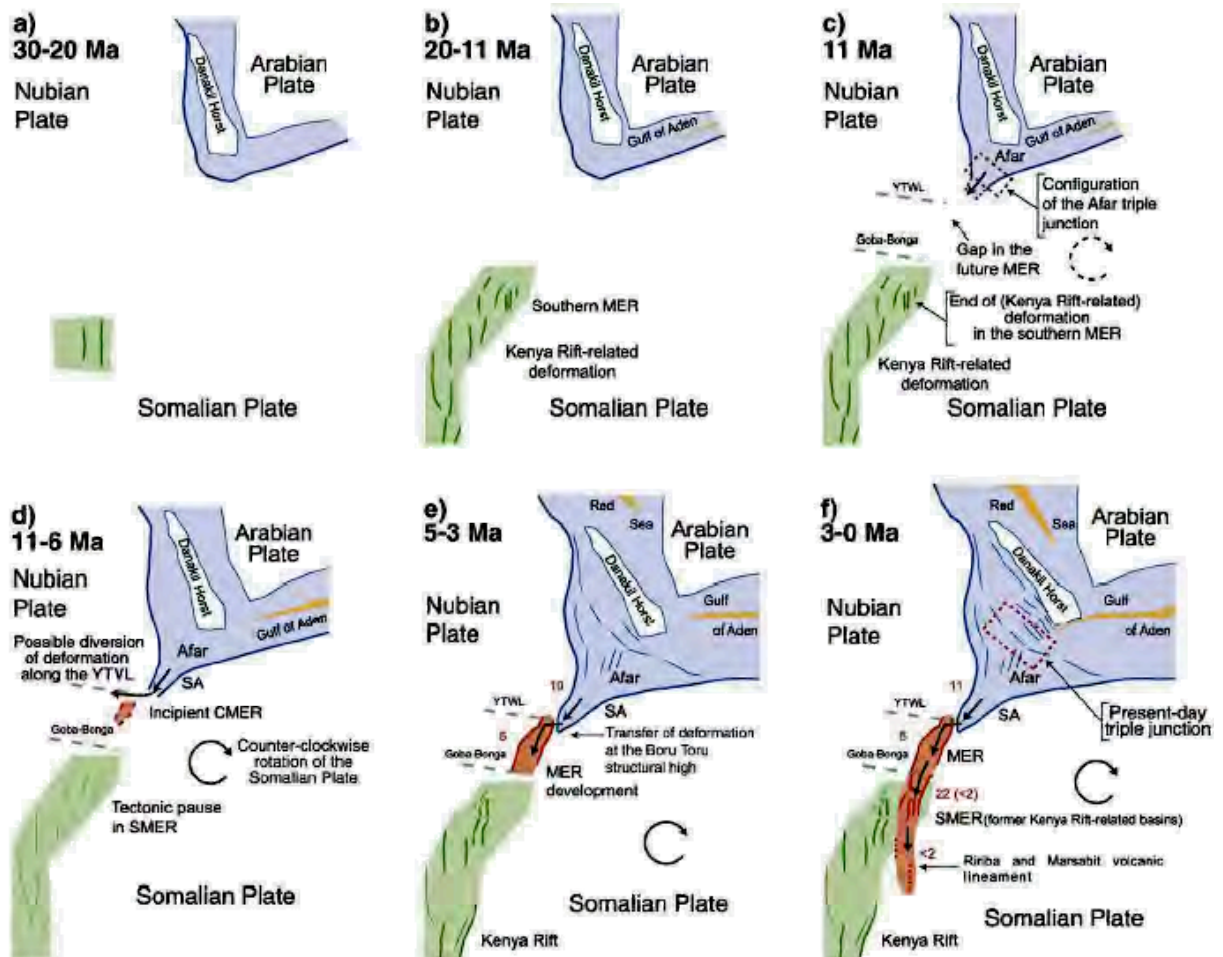


Fig. 2.3: Schematic Miocene to Present evolution of the MER (modified after Bonini et al., 2005). Black arrows indicate the direction of propagation of the extensional deformation. Red numbers indicate the timing of onset of extensional activation, or reactivation. Abbreviation as follows: MER, Main Ethiopian Rift; SA, Southern Afar; SMER, Southern MER; YTWL. Yerer Tullu-Wellel Volcanotectonic lineament.

### 2.4.2.2. WFB faults stage

Extensional deformation in the MER was exclusively accommodated by slip on the border faults up to about 2 Ma, with consequent deepening of the rift depression. At about 2 Ma an important change in deformation style occurred: the border faults were progressively abandoned and the deformation shifted and focused within the rift floor where it was accommodated by the formation of the Wonji faults. The WFB faults were associated with the Quaternary volcanism, and together gave rise to tectono-magmatic segments that focused most of the extensional deformation (see section 2.2, e.g. Ebinger and Casey, 2001). Nevertheless, this riftward migration of deformation is clear in the NMER (where we can

observe well developed en-echelon arranged WFB segments), whereas it is less obvious in the CMER and SMER, probably because they are in a less evolved stage (Corti, 2008). Consequently, in these sectors also the evidence of the Quaternary volcanism is expressed only in a few locations as at the Butajira volcanic chain (Fig. 2.1; e.g. Mohr, 1968; Mazzarini et al., 2004; Abebe et al., 2005), which however is characterized by a lower degree of seismic activity with respect to the northernmost WFB segments (Keir et al., 2006). A two phases MER evolution is thus outlined: (1) a Mio-Pliocene phase characterized by the development of the border faults and the deepening of the rift depression, and (2) a Quaternary phase characterized by the abandonment of boundary faults and localisation of deformation and volcanism along the WFB segments (Figs. 2.4, 2.5).
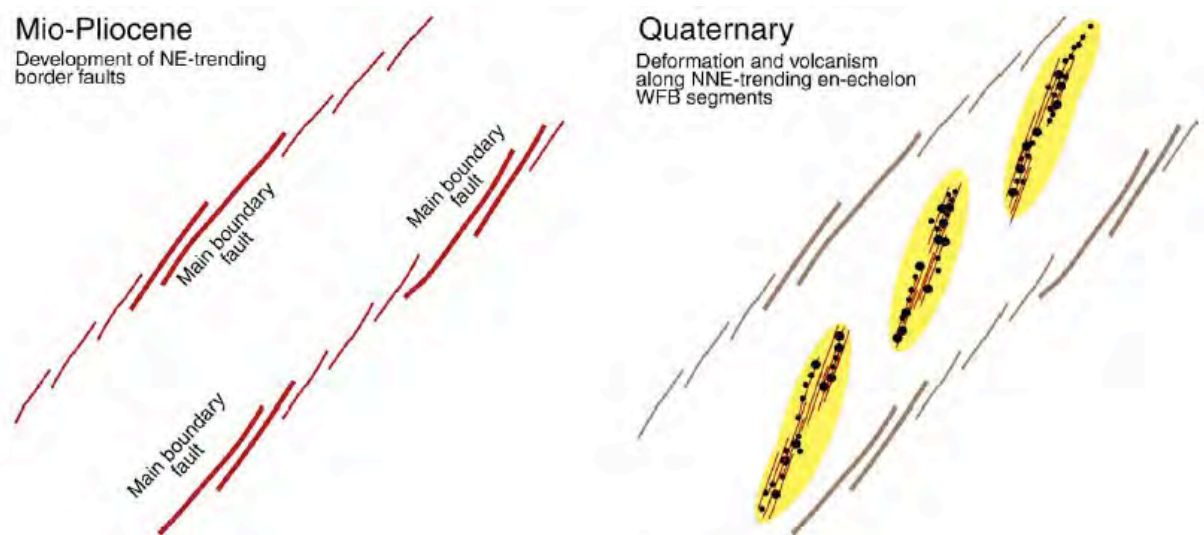


Fig. 2.4: Two-phase volcano-tectonic evolution of the Main Ethiopian Rift (redran after Corti, 2008).

Several models have been proposed to explain the transition from the boundary faults stage to the WFB faults stage. Among others, Bonini et al. (2005, and references therein) suggest that the different orientation of the border faults and WFB faults (see section 2.2) is a consequence of two distinct directions of extension. From this point of view, the change of the direction of extension (from a Mio-Pliocene NW-SE to a Quaternary roughly E-W direction of extension) would be the cause of the observed riftward migration of the deformation. In this model the focusing of the magmatic activity along the WFB segments is interpreted as a passive feature (e.g. Corti et al., 2003). An active role of magmatism is instead invoked in the magma assisted model (e.g. Keranen et al., 2005). In this model, the change in deformation style is controlled by the magma supply which accommodates most of the deformation, preventing the increasing of the stress to a level able to activate the border faults, that consequently reduce or cease their activity (Buck, 2004). Recently, Corti (2008) proposed a model where

the two-phase MER evolution is explained as the result of a constant ~N100°E trending extension direction, without invoking a change in plate kinematics or magma weakening. In this model all the evolution is driven by the reactivation, under an oblique kinematics, of a NE-SW trending pre-existing lithospheric weakness, inherited from previous tectonic phase. Regardless of the different models, it must be stressed that this change in deformation style led to a strong feedback between magmatism and tectonics. About 80% of the current extensional deformation is accommodated along the WFB segments (Billham et al., 1999), in correspondence to the narrow, 10 km wide, seismically active area (Keir et al., 2006). Here, most of the strain is probably accommodated by magmatic intrusion and diking (Ebinger and Casey, 2001; Keranen et al., 2004; Keir et al., 2006), and only less than 50% of extension is accommodated by slip along the faults (Hofstetter and Beyth, 2003). Moreover, underneath the tectono-magmatic WFB segments, wide magma intrusion and the presence of a molten fraction of rock are individuated (see section 2.3). All these WFB features point to a similarity with the characteristic segmentation of a slow spreading mid-oceanic ridge (e.g. Ebinger and Casey, 2001; Keranen et al., 2004; Daly et al., 2008). From this point of view, WFB segments could act as incipient slow-spreading centres dividing two continental plates (e.g. Ebinger, 2005). The combination of the magmatic processes weakening the lithosphere and a further extension would lead to the creation of new oceanic lithosphere and a pair of passive continental margins (Fig. 2.5). These WFB segments characteristics are mainly typical of the NMER, while they are almost absent, as in an incipient stage, in the CMER and SMER. Following geophysical indications, Rooney et al. (2007) suggest that these MER segments are characterized by a lower degree of extension and magmatic modification. The differences observed among the main MER segments may thus represent the expression of a different evolutionary stage (e.g. Hayward and Ebinger, 1996).
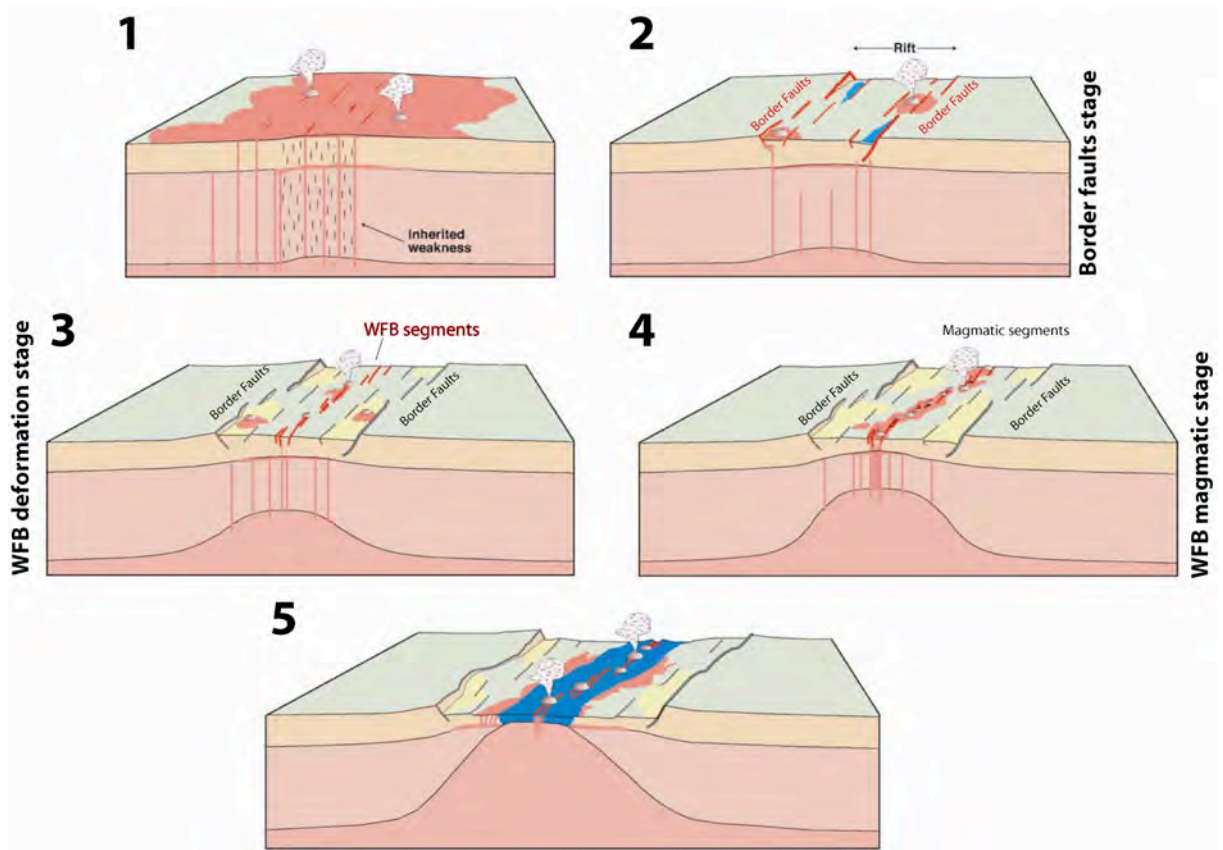
Fig. 2.5: Schematic model of rift evolution in the Main Ethiopian Rift (modified after Ebinger, 2005 and Corti, 2009). 1) Flood-basalt event affecting Ethiopia before the main extensional events. Note the presence of an inherited weakness zone that localises rifting in the subsequent deformation phases. 2) Activation of large boundary faults (11–2 Ma), giving rise to major fault-escarpments and rift-floor subsidence. This first (Mio-Pliocene) rift phase was associated with diffuse volcanism, which encompassed the whole rift depression. 3) Abandonment of large boundary faults and shift of deformation within the rift valley, with activation of the oblique Wonji Fault Belt (~2 Ma) and focusing of magmatic activity that became then localised along the Wonji segments (4). As soon as the volcano-tectonic activity localised within the Wonji segments, a strong feedback between deformation and magmatism developed: the thinned lithosphere is strongly modified by the extensive magma intrusion and extension is facilitated and accommodated by a combination of magmatic intrusion, dyking and faulting. 5) With further thinning, heating and magma intrusion, the tectonically and magmatically thinned lithosphere may rupture in the heavily intruded zones, and new oceanic lithosphere is created.

# Chapter 3
# Oblique rifting: results from analogue models

As observed in Chapter 2, the Main Ethiopian Rift is not fully defined in many details. In particular the rift evolution and architecture in relation to the kinematics acting between the diverging plates need a better definition.

In this chapter we presents a complete experimental series of centrifuge analogue models (see below) that were designed to investigate how a continental rift evolves in response to different angles between the direction of extension and the rift trend. As continental rifts tend to localise preferentially along pre-existing lithospheric rheological variations (such as ancient orogenic belts or suture zones) (e.g. Dunbar and Sawyer, 1989; Ziegler and Cloetingh, 2004, Keranen and Kempeler, 2008; Corti, 2009, Keranen et al., 2009), our model set-up is characterized by a weakness zone (on the basis of previous analogue (Corti, 2008) and numerical (Van Wijk, 2005) models), that focus and localize deformation during extension. We focus our investigation on the different deformation style, rift segmentation and evolution that arise from a simple constant extensional kinematics affecting a weak zone with variable orientation. After briefly introducing the analogue modelling techniques, we present the modelling results. Then, in Chapter 6, we present the results of the comparison between these models and the results of the structural analysis of the MER faulting (Chapters 4,5).

## 3.1. Introduction and brief history of analogue modelling

The analogue modelling is a laboratory technique that allows reproducing and verifies the mechanisms responsible for natural phenomena and geological processes through scaled models. Building and deforming a model is thus an attempt at obtaining a (simplified) representation of nature. The peculiarity of this technique is to weigh up the goodness of proposed driving mechanisms for tectonic processes and reject the models that result instead unrealistic. Analogue modelling makes use of data collected with other methodologies in the definition of the set-up. Summarizing all the information in the building and deformation of the models themselves, analogue modelling alloes countering problems connected to spatial (e.g. geophysics, geochemistry and petrology provide punctiform data) and temporal (most of the information furnished by field data cover a limited span of time) limitations. This results in a powerful tool in investigating geological processes as it allows studying how each

different parameter influence the investigated process evolution and provides a complete 4D (space plus time) overview on the studied problem.

Analogue modelling is not in opposition with numerical modelling, but, instead link these two techniques would help to obtain a more complete approach to the analysed problem; for example analogue modelling could compensate for the difficulty in simulating faulting in the upper brittle layers and for the extreme simplification of the nature required by the numerical modelling; this latter, instead, could yield a quantitative approach and provide for rheological modifications due to temperature variations during crustal or lithospheric scale deformation (Brun, 1999), that can not be taken in account with analogue modelling.

Usually, the birth of this technique is referred to the beginning of the XIX century with the first experiments performed by Sir James Hall (Hall, 1815). Sir Hall used the experimental results from models consisting in a stack of different materials (firstly clothes and clay layers successively, compressed by two mobile walls) to verify his hypothesis concerning the formation of folded strata on the Scottish Uplands (Fig. 3.1). His modus operandi laid the foundations of the analogue modelling as it resume the three principal step that are the hinges of this technique:

1) analysis of the natural processes and formulation of hypotheses on the mechanisms responsible for the observed structures.

2) building and deformation of model, built on the basis of the previously formulated hypothesis

3) analysis and interpretation of the models results; comparison between experimental results and natural observations and test of the reliability of the formulated hypothesis.
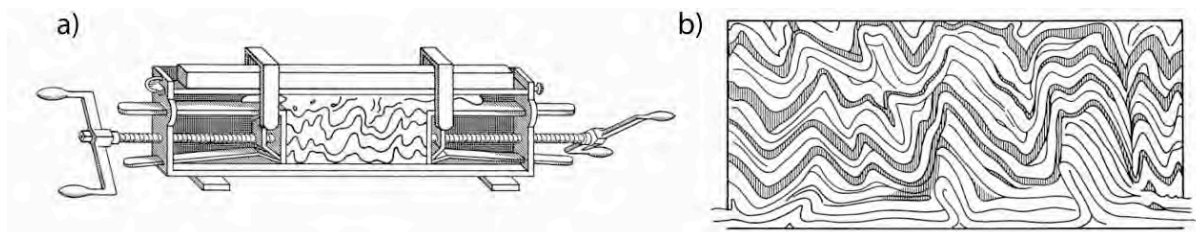


Figure 3.1: a) Machine for scale model, presented by Hall to the Royal Society of Edinburgh in 1812, and b) results from Hall's experiments (figure from Ranalli, 2001).

After the Hall's first experiments, this technique was sparsely employed during the XIX century, and only in the XX century the analogue modelling became a widely used technique in the study of geological processes (see Koyi, 1997 and Ranalli, 2001 for a complete treatment of the analogue modelling techniques and its evolution during time). A major step forward in analogue modelling came from Hubbert (1937). In this work, the scale model

theory was introduced for the first time. Thanks to the scaling theory, models became a realistic replica of the natural prototype. Correct scaling requires three aspects of similarity: geometric, kinematic and dynamic (see section 3.1.1). The scaling theory changed modelling from a descriptive tool to a quantitative technique, thus making it an efficient and reliable tool to study geological processes at various scales (e.g. from microstructure analysis to large scale tectonic processes) (Koyi, 1997).

Ramberg (1963, 1967) gave an important contribution to the development of the analogue modelling, underlining how this technique could be useful in the study of geodynamics problems. Moreover, Ramberg fully developed the centrifuge technique (introduced for the first time by Bucky (1931)) that allows analysing the role gravity-driven processes.

The last decades have witnessed an improvement of the laboratory techniques and a widening of the application fields, with experiments investigating processes that cover a very large range of scale, from few millimetres (e.g. shear indicator) to thousands of kilometres (lithospheric scale processes). New tools have been used in the model result analysis, as X-ray tomography, that allows to monitor the three-dimensional evolution of the structures inside a model (e.g. Colletta et al., 1991; Schreurs et al., 2001), and the 3D laser scanner that provides detailed information of the models surface topography and allows to reconstruct a digital elevation model (e.g. Benes and Davy, 1996; Agostini et al., 2009; this thesis work).

Furthermore, parameters that can affect the final deformation patterns are introduced during the experimental development, such as the influence of erosion and sedimentation (e.g. Davy and Cobbold, 1991; Storti et al., 2000; Person and Sokoutis, 2002 among the others) and the use of materials with a temperature-dependent rheology (see Ranalli, 2001 for review; Rossetti et al. 2002). In particular, these latter allows to run against one of the principal limitation of analogue modelling, that is the impossibility in taking in account for the rheological modifications due to temperature (and depth-dependent) variations during crustal or lithospheric scale deformation.

### 3.1.1. Scaling

Anologue models aim to be representative of the studied natural processes. The building of a model follows thus a careful analysis of nature, but it will never lead to an exact replica of the natural setting. Necessarily, the geometry, properties of materials and kinematics of the examined process will be simplified. In order for a model to be representative of a natural process, it has to be scaled to nature and its construction must follow scaling criteria. According to Hubbert (1937), a model is properly scaled to its natural counterpart if it is geometrically, dynamically, kinematically and rheologically similar.

The geometrical similarity requires all the model lengths and angles to be equal to the correspondent ones found in natural settings. This implies that all the length ratios in the model must be equal and proportional to natural prototype.

To ensure the dynamic similarity, the two bodies must have similar ratios and distributions of different kinds of driving and resistive forces (gravitational, frictional and viscous). Ramberg (1981) shows that the dynamic similarity can be tested using the dimensionless ratios of forces (see Ramberg, 1981 and Weijermars and Schmeling, 1986 for details).

When a model is proper built to be geometrically and dynamically scaled, the kinematical similarity is ensured, and thus a proper ratio between the deformation times.

The rheological similarity requires that the analogue materials used in the building of a models must have a similar rheological behaviour with respect to the rheological characteristics of the prototype (Weijermars and Schmeling, 1986).

### 3.1.2. Analogue materials

One of the most difficult problems to solve during the building of an analogue model is to find the right materials. These must allow to reconstruct a stacking of various layers composed by different materials that mimics the rheological layering of the natural case under study and reacts to the imposed forces in a similar manner (e.g. Weijermars and Schmeling, 1986) (Fig. 3.2). In literature, a wide variety of analogue materials has been employed to reproduce different natural materials: among others silicone, plasticine, different kind of sand, clay, honey, foam, liquids with various density and viscosity, sugar, ecc.. The different analogue materials can be subdivided in two major categories: materials that simulate a brittle behaviour and materials that simulate a ductile behaviour.
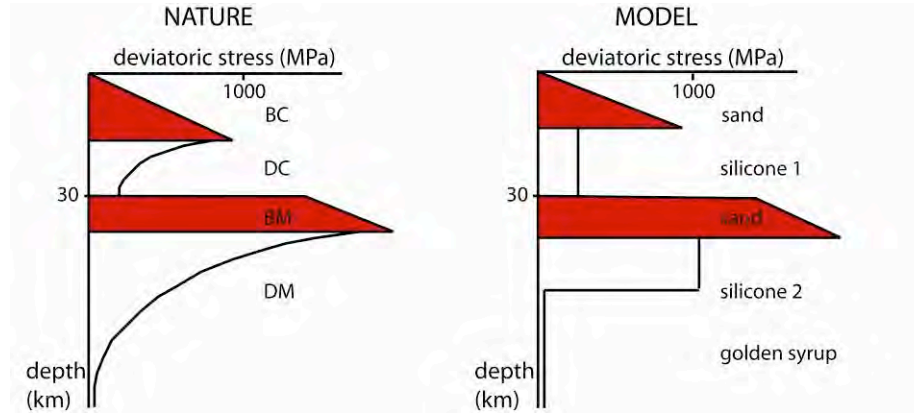
Figure 3.2: Comparison between a four-layer strength profile in nature and in models, reconstructed by stacking of different material layers (Modified after Davy and Cobbold, 1991). BC: brittle crust; DC: ductile crust; BM: brittle mantle; DM: ductile mantle.

### 3.1.2.1. Brittle behaviour analogue materials

Sand, and in particular quartz sand, is the most common analogue material employed to model a brittle behaviour, like, for example, the behaviour of upper crust and sedimentary cover (this thesis work, and among others, Davy and Cobbold, 1991; Tron and Brun, 1991; Brun and Tron, 1993; McClay at al., 1995, 2002; Mart and Dauteil, 1999; Corti, 2001, 2004, 2008, Agostini et al., 2009).

Brittle rheological behaviour is typical of low temperature and high strain rates is expressed by the Coulomb-Navier frictional shear failure criterion, commonly knows in term of shear and normal stress (Fig. 3.3):

$$\tau = C + \mu_f \left( \sigma - p_f \right) \tag{3.1}$$

(where $\tau$ and $\sigma$ are the share and normal stress acting on the failure plane, C is the cohesion, $\mu$ the frictional coefficient and, if present, $p_f$ is the fluid pressure) and in term of critical stress difference:

$$\frac{1}{2}(\sigma_1 - \sigma_3)\sin 2\theta = C + \mu_f \left[ \frac{1}{2}(\sigma_1 + \sigma_3) - \frac{1}{2}(\sigma_1 - \sigma_3)\cos 2\theta \right] \tag{3.2}$$

(where $\sigma_1$-$\sigma_3$ is the critical stress difference, $\theta$ is the angle between the failure plane and the $\sigma_1$ direction and C is the cohesion).

If one of the principal stress directions is vertical (no shear stress is present on a free surface), the stress system is Andersonian (Anderson, 1951) and the failure criterion can be written as follow (Ranalli, 1995):

$$(\sigma_1 - \sigma_3) = \alpha \rho g l (1 - \lambda) \tag{3.3}$$

where $\rho$ is the average density of rocks above depth l, $\alpha$ is a parameter dependent on the frictional properties of the material (e.g. C and $\mu_f$) and on the orientation of the stress field, and $\lambda$ is the Hubbert-Rubey coefficient, describing the fluid pressure, if present..

21

From equation 3.1, we obtain the scaling ratio σ* for stress in materials with brittle behaviour (Hubbert, 1937; Ramberg, 1981):

$$\sigma^* = \rho^* l^* g^* \tag{3.4}$$

where the ρ* is the ratio between material density $\rho_m$ and nature density $\rho_n$, g* is the ration between the gravitational forces (g*=1 in normal gravity experiments, but need to be scaled in enhanced gravity experiments, see section 3.1.3.2.) and l* the length ratio.
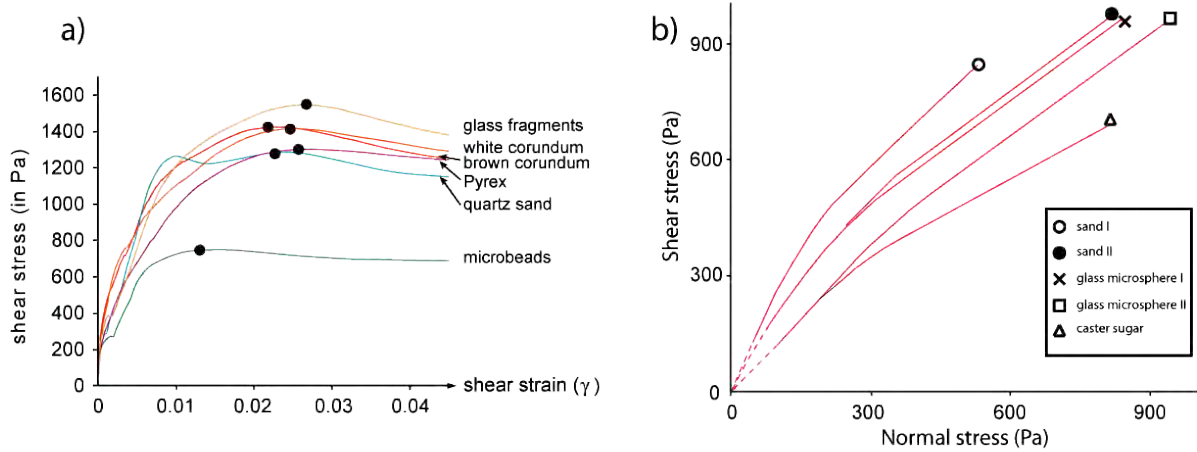


Figure 3.3: a) flow curves (stress-strain graph) for different granular material with brittle behaviour. Depending on the material properties, the brittle failure (black dots) occurs at different amount of strain. Modified after Panien et al. 2006. b) Shear stress plotted as a function of normal stress for different dry granular materials. Red lines are the approximate best-fit envelopes (dashed lines are extrapolated for very low normal stresses (<50–100 Pa)). Modified after Schellart, 2000.

As the density of the analogue material imposes the value of ρ*, it is sufficient to fix the length ratio (usually varying between $10^{-6}$ and $10^{-4}$) to obtain the stress scaling ratio σ*.The cohesion C (see eq. 3.1) has the same dimension of stress and consequently it requires a similar scaling factor (even if generally it is considered negligible both in models and in nature). Similarly, the adimentional coefficient of internal friction μ must share similar values both in model and in nature.

### 3.1.2.2. Ductile behaviour analogue materials

In laboratory experiments, rock ductile behaviour is commonly reproduced using silicone putties with different characteristics (e.g. Davy and Cobbold, 1991; Weijermars, 1993; Koyi, 1997, Corti et al., 2003). One of the more common silicone variety used in analogue modelling is the polydimethylsiloxane (PDMS). To obtain different rheological characteristic in term of density, viscosity, ecc., silicone putties are usually mixed with other materials as plasticine and sand and also with acids that reduce the viscosity and the strength (e.g. oleic acid, Corti, 2008).

These materials are expected to model the rock behaviour at high temperature and low strain rates conditions. In the ductile conditions, mechanical properties of rocks mainly deform according to three flow laws that are very different one another: Power Law, Newtonian, and, even if unusual in solid rocks and analogue materials, Bingham.

Analogue materials should thus simulate one of these behaviours: experimental materials should present flow curves (stress-strain graph, Fig. 3.4) comparable to the rocks flow curves that have to simulate (Weijermars and Schmeling, 1986).
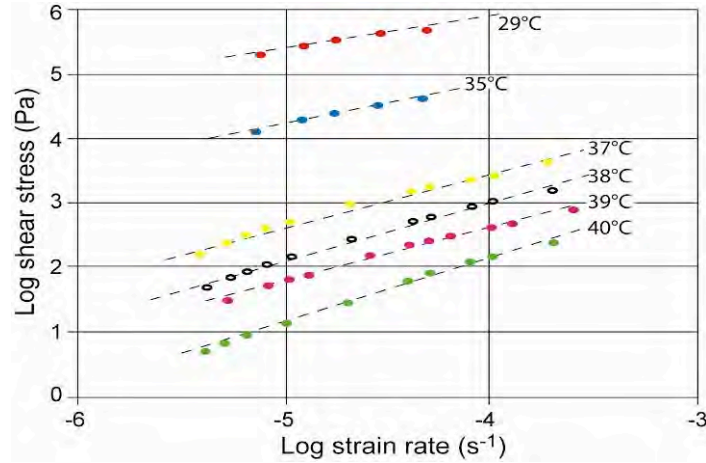


Figure 3.4: Paraffin wax log-log plot of strain rate versus stress at different temperatures. Best-fit lines are also shown (after Rossetti et al., 1999).

Ductile behaviour is expressed by a ductile power-law equation (e.g. Geotze and Evans, 1979):

$$\dot{\varepsilon}_1 = a_0 \exp\left(-Q/RT\right)\left(\sigma_1 - \sigma_3\right)^n \tag{3.5}$$

where $\dot{\varepsilon}_1$ is the normal principal strain rate, T is the absolute temperature (in °K) and R the universal gas constant (8.13 kJ mol$^{-1}$ °K$^{-1}$). Q (activation energy, kJ mol$^{-1}$), n and $a_0$ (frequency factor Pa$^{-n}$ s$^{-1}$) are material parameter that can be either dependent or independent on temperature and pressure. Equation 2.5 can be simplified in:

$$\dot{\gamma} = A\tau^n \tag{3.6}$$

In a Newtonian flow n=1. Thus equation 2.6 becomes:

$$\dot{\gamma} = \eta\tau \tag{3.7}$$

where η is the dynamic viscosity. The equation 2.7 allows to obtain a simple way to scale down model velocity and viscosity. Weijermars and Schmeling (1986) observed that, in a Newtonian flow, the geometrical similarities and similar boundary conditions are sufficient to attain dynamic similarity, provided that inertia is insignificant in solid rock flow. In these conditions, following the equation 3.7, the scaling laws for a material with a Newtonian flow behaviour are:

$$\gamma^* = \tau^*/\eta^* = \sigma^*/\eta^* = \dot{\varepsilon}^* \qquad (2.8a) \qquad\qquad \gamma^* = V^*/L^* \qquad (2.8b)$$

where, $\gamma^*$ is strain rate ratio between the model and natural values, $\tau^*=\sigma^*$ is the stress ratio, $\eta^*$ the viscosity ratio and $V^*$ the velocity ratio.

The following equation provides the scaling ratio of time:

$$t^* = \frac{t_{mod}}{t_{nat}} = \frac{1}{\dot{\varepsilon}^*} = \frac{H_d \varepsilon_{nat}}{v_{mod}} \qquad (2.9)$$

where $H_d$ is the ductile layer thickness in simple shear and the layer length in pure shear and $v_{mod}$ is the velocity of deformation of the model.

The flow law for a material with a non-Newtonian behaviour is expressed by the power law creep equation for non-Newtonian fluid (e.g. Ranalli, 1995). This equation provides the scaling rules for materials with this behaviour:

$$\dot{\varepsilon}^* = A^* \frac{(\sigma_m)^{n_m}}{(\sigma_n)^{n_n}} \qquad (2.10)$$

Where $A^*$ is the scaling ratio of the constant A.

The parameter A and n of different ductile analogue materials can be easily determined from the log-log plot from a stress-strain laboratory tests (Fig. 3.5): n is the slope of the curve and the value of A is yield by the intercept with the stress axes (Fig. 3.4).
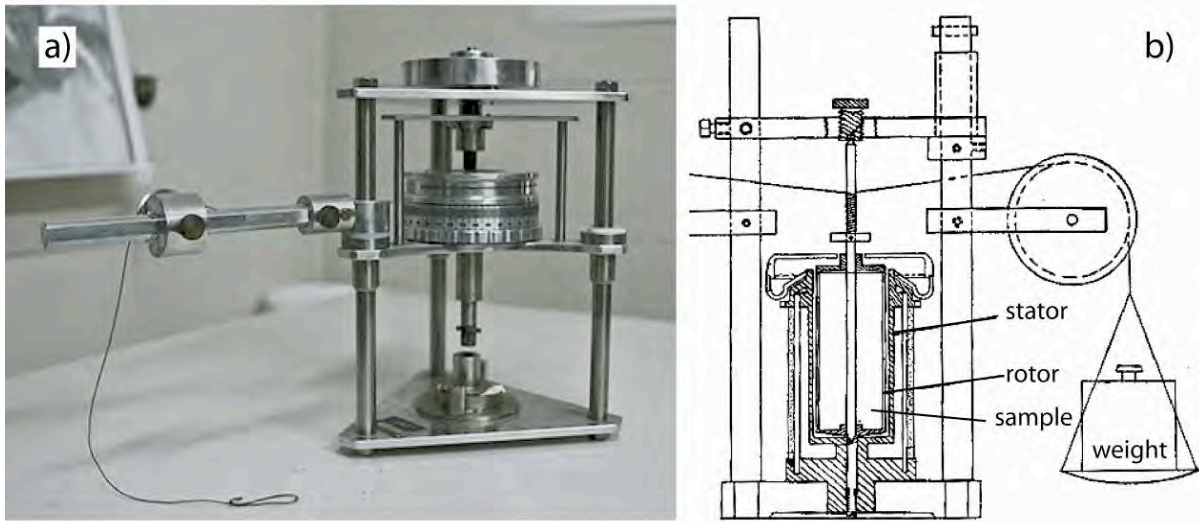


Figure 3.5: a) coni-cylindrical (Coutte) viscometer of the IGG-CNR Tectonic Modelling Laboratory at the Earth Science Department of Florence University (Italy). b) schematic representation of the first coni-cylindrical viscometer by Mooney and Ewart (1934).

3.1.3. Modelling technique

Models are deformed using apparatus that allow to reproduce the different tectonic settings that are found in nature. The apparatus can be subdivided in two main categories: apparatus that allow to reproduce deformation in the normal (terrestrial) gravitational field, and apparatus for deformation in an enhanced gravitational field.

*3.1.3.1. Normal-gravity apparatus*

Normal gravity apparatus can deform an experimental model applying deformation that can vary from simple shear (Fig. 3.6a) to pure shear (Fig. 3.6a,b). In these experiments, models are deformed by the displacement of a movable wall, activated by stepping motors controlled by a computer. Models are built directly on the work surface of the apparatus (Fig. 3.6a) or inside a plastic box (Fig. 3.6b).

These apparatus allow reproducing both compressive kinematics (pushing one side of the model) and extensional tectonics (pulling one side of the model, in this case usually built on two independent rigid plates forming a velocity discontinuity at their interface).
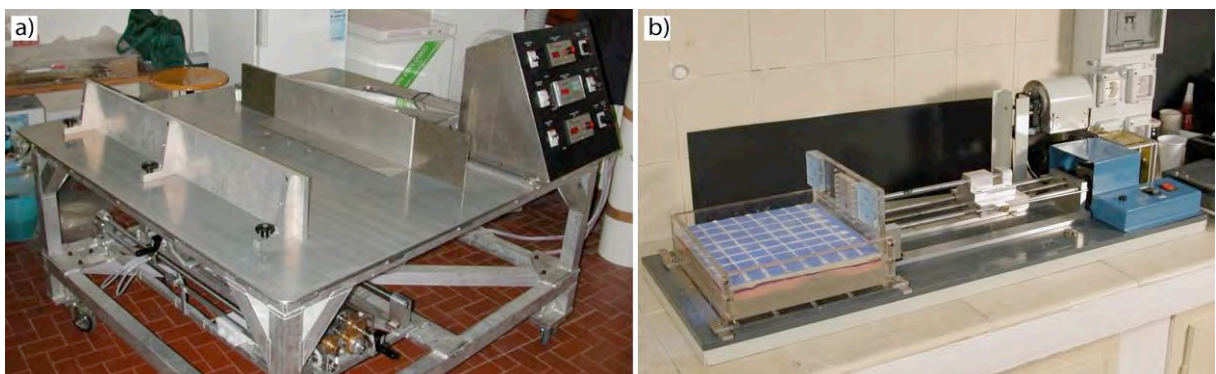


Figure 3.6: a) pure and simple shear apparatus. Two orthogonal motors allow to impose different movement directions at the mobile wall. This apparatus is also equipped with a piston that allow to inject analogue material simulating magma inside the model during the deformation. b) pure shear apparatus (squeeze-box). Both apparatus are at the IGG-CNR Tectonic Laboratory at the Earth Science Department of Florence University (Italy).

Experiments taken in normal-gravity field can have relatively big dimensions, that allow detailed observation of the structures; moreover, the entire evolution can constantly be monitored. Limitations in these experiments mostly arise from the long time they require (from many hours to some days).

*3.1.3.2. Gravity enhanced apparatus*

Gravity enhanced analogue models are performed using a centrifuge (Fig. 3.7). This technique was mainly developed by Ramberg (1967, 1981), who suggested that the centrifugal forces developed by the rotational movement act as gravity in nature. Centrifuge analogue models are thus indicated in the analysis of many tectonic settings, like diapirism, gravity sliding and magma emplacement where the gravity play a big role (e.g. Talbot, 1977; Dixon and Summer, 1987; Liu and Dixon, 1991; Koyi and Skelton, 2001) and in modelling extensional setting (e.g. Mulugeta and Ghebreab, 2001; Corti et al., 2003; Corti, 2008; Agostini et al., 2009 and this thesis work).

One of the principal benefits of the centrifuge technique is the extremely reduced time of deformation. Moreover the enhanced gravity highlights the rheological differences between the used materials, and allows using also stronger materials than in normal-gravity experiments, where these materials would not deform under 1g and the properly scaled applied stress field.

The centrifuge imposes that model dimensions must be smaller (compared to normal-gravity techniques), often limiting a detailed analysis of the structures. Moreover, the model evolution can not constantly be controlled, as models can be observed only between centrifuge runs.
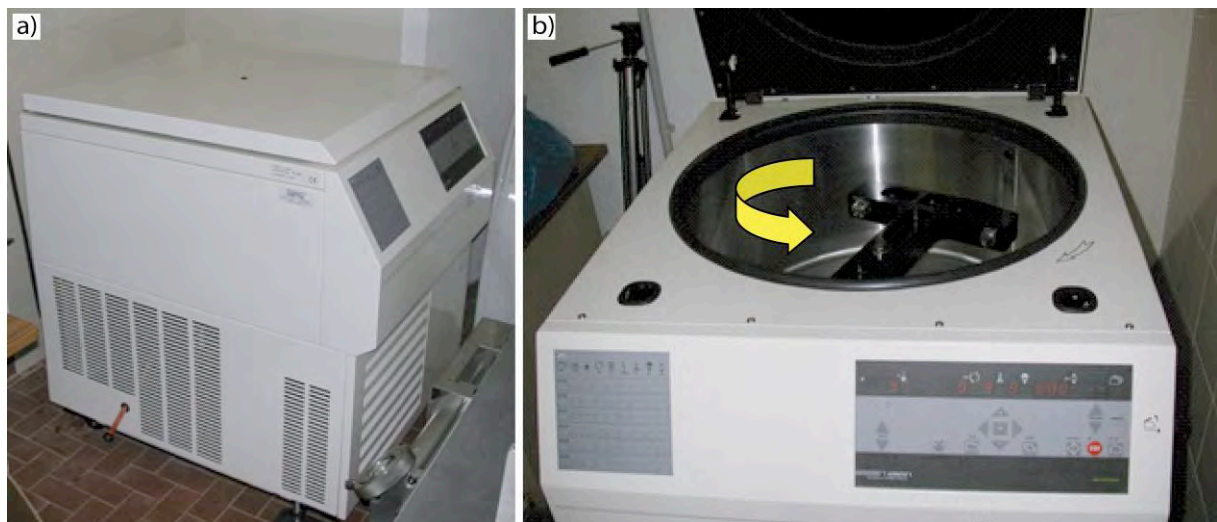


Figure 3.7: a) lateral view of the high capacity centrifuge at the IGG-CNR Tectonic Laboratory at the Earth Science Department of Florence University (Italy). b) view of the centrifuge rotor. The yellow arrow indicate the direction of rotation direction.

## 3.2. Oblique continental rifting lithospheric-scale models

Hereafter we present the results of the centrifuge analogue models performed for this thesis work. The models are characterized by the presence of a central lithospheric weakness that localizes deformation during progressive extension (see section 3.2.1. for details). The angle between the weak zone and the orthogonal to the direction of extension was varied between 0° (orthogonal extension) and 75°, at increments of 15°. On average, five different models were performed for each obliquity angle α (i.e., angle between the orthogonal to the rift trend and the direction of extension). We performed 70 models in all: many of them were necessary to define to right set-up. Although the models may have differed in small details, the first order deformation pattern and evolution were always comparable.

The following sections are largely based on:

Agostini, A., G. Corti, A. Zeoli, and G. Mulegeta (2009). Evolution, pattern and partitioning of deformation during oblique continental rifting: Inferences from lithospheric-scale centrifuge models. Geochem. Geophys. Geosyst., 10, Q11015, doi:10.1029/2009GC002676.

### 3.2.1. Model set-up

The experiments were performed in an artificial gravity field of ~18g by using the large capacity centrifuge at the Tectonic Modelling Laboratory of the Institute of Geosciences and Earth Resources (National Research Council of Italy) at the Earth-Sciences Department of the University of Florence (Fig. 3.7). Following the set-up adopted in Corti (2008), the models reproduced the upper part of the continental lithosphere (crust + upper lithospheric mantle) floating above a low viscosity material simulating the asthenosphere (Fig. 3.8). They were built inside a transparent rectangular Plexiglas box and confined by two moveable side walls; removal of rectangular blocks (spacers) at the sides of these moving walls allowed vertical thinning and lateral expansion of the models in response to the centrifugal forces to fill the empty space (Fig. 3.8). Sequential removal of spacers during successive runs in the centrifuge allowed controlling the amount and rate of extension (see Corti et al., 2003). Top-view photos and laser scans of the models were taken after the end of each centrifuge run. After a successful experiment, the models were frozen before taking a number of cross-sections to study their 3D internal geometry.

In order to model oblique rifting conditions, the experimental lithosphere contained a central weakness zone that localizes deformation during progressive extension (see Van Wijk, 2005; Corti, 2008); the trend of this weakness (with respect to the extension direction) was varied in different experiment, to reproduce different obliquity angles α from 0° to 75°, at increments

of 15° (Fig. 3.9). With this set-up, the centrifuge forces impose a uniform stress field on the models and the distribution of deformation is imposed by the lateral variation in rheology and strength due to the presence of the weakness zone (e.g., Mulugeta and Ghebreab, 2001; Corti, 2008). This represents a reasonable approximation of the natural process of continental rifting at a regional scale, where extensional stresses are applied to a pre-deformed, anisotropic lithosphere and deformation is not randomly distributed but tend to follow the trend of pre-existing weaknesses inherited from previous deformation phases avoiding stronger regions (e.g., Dunbar and Sawyer, 1989; Versfelt and Rosendahl, 1989; Morley, 1999a; Tommasi and Vauchez, 2001; Ziegler and Cloetingh, 2004; Van Wijk, 2005; see also below section 3.3.2.1. and chapter 5 for the discussion on the role of inherited lithospheric-scale weaknesses evidenced by recent geophysical findings in the Main Ethiopian Rift).
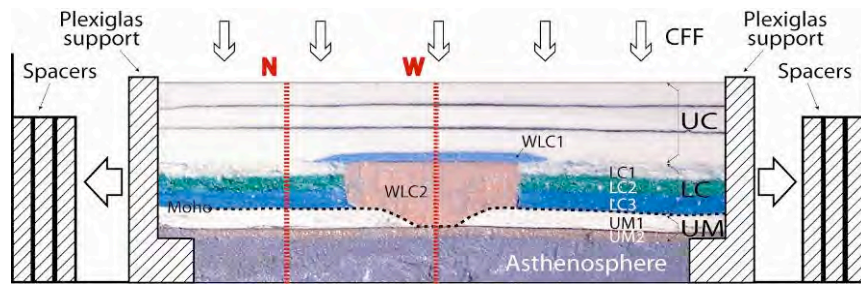


Fig. 3.8: Set-up of the lithospheric-scale of oblique rifting. Model cross-section illustrating the vertical rheological layering and schematic representation of the extension conditions in the experimental apparatus. The models were built inside a transparent rectangular Plexiglas box (with internal dimensions of 25x16x7 cm) and confined by two moveable Plexiglas supports; removal of rectangular blocks (spacers) at the sides of these moving walls allowed vertical thinning and lateral expansion of the models in response to the centrifugal forces (CFF) to fill the empty space (Fig. 3.8). LC1-3: lower crustal layers 1-3; UM1-2: upper mantle layers 1-2; WLC1-2: weak lower crustal layers 1-2. N (normal lithosphere) and W (weak lithosphere) are the traces of the strength profiles in Fig. 3.11.
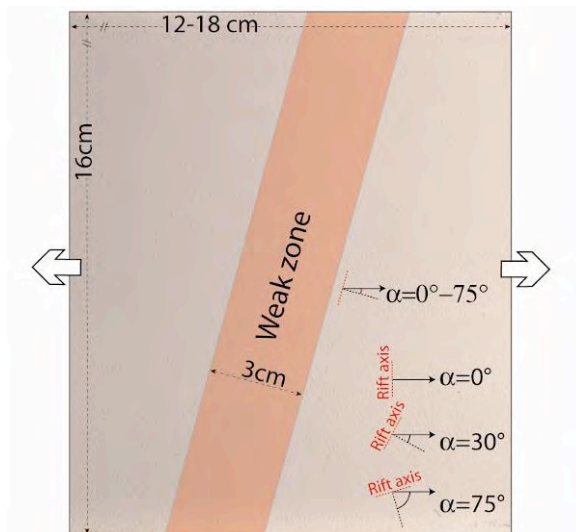


Fig. 3.9: Top view photo of the models, showing the obliquity of the weak zone with respect to the orthogonal to the stretching vector (white arrows) and the resulting angle α.

*3.2.1.1. Rheological layering and experimental materials*

Building on previous numerical modeling (Van Wijk, 2005), the models reproduced the complex brittle-ductile rheological multilayering characteristics of the extending continental lithosphere (Fig. 3.8). The brittle upper crust UC was simulated by a K-feldspar powder, showing a linear increasing in the strength with depth. The ductile lower portion of the crust was made by three different levels (LC1, LC2, LC3), with the same density but decreasing viscosity (strength) with depth (see stress/strain rate relationships in Fig. 3.10). This set-up allows approximating the temperature-related decrease in strength with depth in natural ductile layers, thus improving previous models of continental extension where a depth-independent behavior of ductile layers was modeled (see Brun, 1999 or Corti et al., 2003 reviews). These layers were made of a mixture of plasticine (Pongo modelling dough, distributed by FILA) and Polydimethylsiloxane (silicone SGM36 distributed by Dow Corning, hereafter referred to as PDMS) (100:45 % in weight). Plasticines with different colors were used to model the ductile layers with decrease in strength with depth: the different color corresponds indeed to a different viscosity that decreases passing from white to blue to green plasticine (Fig. 3.10).

The upper lithospheric mantle was made by two different layers with decreasing strength (and constant density) with depth (Fig. 3.10). The strong uppermost mantle layer (UM1) was made of a mixture of white plasticine and PDMS (100:20 % in weight), whereas the underlying layer (UM2) was made of a mixture of silicone (Wacker Silicone Bouncing Putty 29 distributed by CRC France, hereafter referred to as Wacker BP29), corundum sand and oleic acid (100:100:5 % in weight, respectively). As in previous modeling (e.g., Van Wijk, 2005; Corti, 2008), this layering assumes that resistance in the mantle decreases rapidly with depth, and most of the strength is retained in a strong uppermost layer.

Following previous analogue (e.g., Corti and Manetti, 2006; Corti, 2008) and numerical (Van Wijk, 2005) models, the weak zone in the centre of the models was modeled by considering a local increase in crustal thickness (analogous to the presence of a pre-existing crustal root), which is expected to greatly reduce the integrated resistance of the lithosphere by 1) replacing the strong lithospheric mantle material with weak crustal material and 2) increasing initial Moho temperatures and thus softening the crustal materials with respect to the surroundings (e.g., Afonso and Ranalli, 2006). Consequently, the weak crust was made of two layer: an upper thin layer (WLC1) with the same composition as the lowermost crustal layer LC3, and a underlying layer (WLC2) made of a mixture of silicone Wacker BP29, corundum sand and oleic acid (100:75:5 % in weight) (Fig. 3.10).

These crustal-mantle layers rested on a low viscosity mixture made of silicone Wacker BP29, corundum sand and oleic acid (100:100:20% in weight) simulating the asthenosphere and providing the isostatic support for the deforming continental lithosphere (Fig. 3.8).

The characteristics of the analogue materials used in these models are reassumed in Table 3.1.
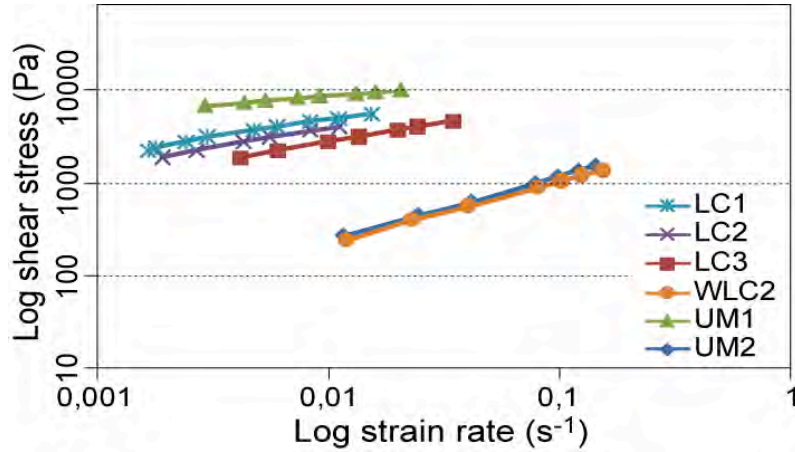


Fig. 3.10: log-log plot of strain rate versus stress for materials simulating different rheological layers of the lithosphere. LC1, LC2, LC3: lower crust. WLC2: weak lower crust. UM1 and UM2: upper mantle. Note the increase in the resistance of the ductile materials passing from UM2 and WLC2 to UM1 (see also strength profiles in fig. 3.9b).

| Behaviour | Layer | Materials | Density | μ | C |
|---|---|---|---|---|---|
| britlle | Upper Crust | K-Feldspar powder | 1220 kg m$^{-3}$ | 0.06 | 60 Pa |
|  |  |  |  | **n** | **A** |
| ductile power-law | Lower Crust 1 | White Plasticine-PDMS (100:45 %) | 1500 kg m$^{-3}$ | 2.04 | 2 10$^{-11}$ |
|  | Lower Crust 2 | Green Plasticine-PDMS (100:45 %) | 1500 kg m$^{-3}$ | 2.03 | 5 10$^{-11}$ |
|  | Lower Crust 3 Weak Lower Crust 1 | Blue Plasticine-PDMS (100:45 %) | 1500 kg m$^{-3}$ | 2.04 | 7 10$^{-11}$ |
|  | Weak Lower Crust 2 | Silicone-corundum sand-oleic acid (100:70:5 %) | 1500 kg m$^{-3}$ | 1.05 | 3 10$^{-6}$ |
|  | Upper Mantle 1 | White Plasticine-PDMS (100:20 %) | 1750 kg m$^{-3}$ | 5 | 2 10$^{-22}$ |
|  | Upper Mantle 2 | Silicone-corundum sand-oleic acid (100:100:5 %) | 1750 kg m$^{-3}$ | 1.04 | 3 10$^{-6}$ |

Table 3.1: Characteristics of experimental materials. Brittle parameters (from equation 3.3, see also Corti et al., 2004): μ, coefficient of internal friction; C, cohesion. Ductile parameters (see equation A11 in Corti 2004): n, stress exponent; A, constant.

### 3.2.1.2. Scaling

The models were built with a geometric scale ratio of $6.7 \times 10^{-7}$ (1cm in the experiments corresponds to 15km in nature), so that we modelled ~42km of total extension of the uppermost ~50km of the continental lithosphere. Dynamic-kinematic similarity (Ramberg, 1981) was tested through dimensionless ratios relating gravitational, viscous and frictional

stresses acting in the system (e.g., Corti et al., 2004, see section 3.1.1); this similarity condition ensured that the velocity of extension in the models (~$10^{-4}$ ms$^{-1}$, ~3mm of displacement in 9 second, duration of a single centrifuge run) scaled to natural values of 4-6 mm yr$^{-1}$, a reasonable value for continental rift systems (e.g., Corti, 2008).

Rheological or strength profiles, in which the differential stress is plotted against depth, have been widely used to represent the rheological characteristics of the lithospheric multilayer (e.g., Ranalli, 1995), and were used in this thesis to define the scaling of strebgth of the experimental lithosphere. Integration of the local differential stress with depth gives the strength of the different brittle and ductile layers; in turn, the sum of the single layer strengths give the total strength of the lithosphere (for a detailed description of the procedure for calculations of brittle and ductile differential stresses see Corti et al. (2004).

For brittle layers (upper crust, UC), the differential stress is calculated with the governing equation for tensional faulting in Coulombian brittle layers (equation 3.1), with the following parameters (Table S1): cohesion=50 Pa, internal friction=0.6, density=1220 Kg m(-3), depth=0.015 m, gravity=176 m s(-2), and Hubbert-Rubey coefficient of fluid pressure=0, resulting in a critical stress difference at the base of the model upper crust of 2.2 10(3) Pa (see strength profile in Fig. 3.11).

For ductile layers (lower crustal layers, LC, and upper mantle layers, UM), the differential stress was calculated with the power-law equation for non-Newtonian fluids, with parameters indicated in Table 3.1.
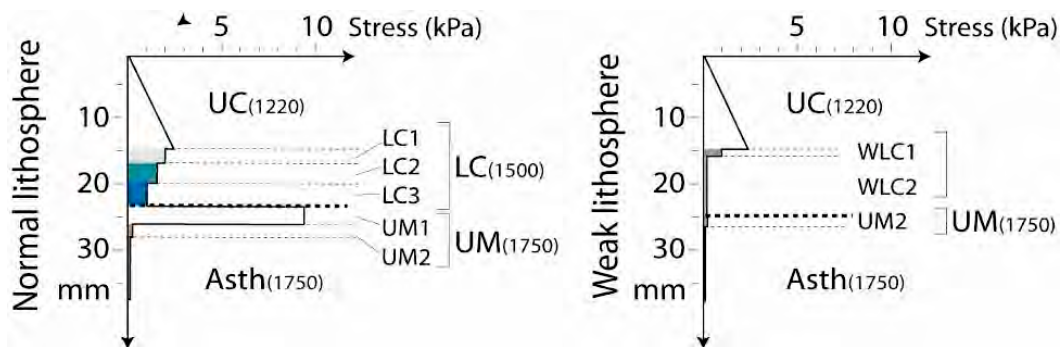


Fig. 3.11: Strength profiles of the model lithosphere. UC: upper crust; Asth: asthenosphere; other symbols as above. Numbers in brackets indicate the density of the different materials in kg m$^{-3}$. Traces of the profiles are indicated in Fig. 3.8.

The strength of the single layers is calculated by integrating the differential stress with depth; the total strength of the lithosphere is a measure of the average stress required to extend the lithosphere at a given rate and it is given by the sum of the strength of the single layers.

The resistance of the analogue layers and lithosphere can be scaled to nature by considering that the integrated resistance has the dimensions of a pressure by a length, such that the scaling factor can be obtained by assuming that $R*=S* L*$, where S and L are the scaling rations of stress and length and the asterisk denotes the ratio between model and nature.

For the current models, the length scaling factor $L*=6.7 \times 10^{-7}$, together with the model-to-nature ratios of density ($d*\sim0.45$) and gravity ($g*=18$), dictate a ratio of normal stress of $S*=L*g*d*=5.5 \times 10^{-6}$, such that $R*=3.7 \times 10^{-12}$ (Table 3.2).

From the above equations, the total resistance of the lithosphere, scaled from models to nature, can be estimated to vary between $\sim5 \times 10^{12}$ Pa m (for the weakest region corresponding to the pre-existing weakness) and $\sim4 \times 10^{13}$ Pa m (for the rift strong surrounding regions; see Table 3.2). These values are well in the range of estimates for natural lithospheres (see for instance Ranalli, 1995; Afonso and Ranalli, 2004; Corti et al., 2004) thus indicating that the adopted rheology represents a good approximation for the rheological characteristics of an extending continental lithosphere in nature.

| Analogue layer | Resistance (Pa m) | Scaled resistance (Pa m) |
|---|---|---|
| Upper crust | 17 | $4.6 \times 10^{12}$ |
| Lower crust 1 | 4 | $1.1 \times 10^{12}$ |
| Lower crust 2 | 5.05 | $1.5 \times 10^{12}$ |
| Lower crust 3 | 3.06 | $1.0 \times 10^{12}$ |
| Weak lower crust 1 | 1.08 | $5.1 \times 10^{11}$ |
| Weak lower crust 2 | 0.05 | $1.4 \times 10^{11}$ |
| Lithospheric mantle 1 | 119 | $3.3 \times 10^{13}$ |
| Lithospheric mantle 2 | 0.01 | $2.8 \times 10^{10}$ |
| Lithosphere (strong) | ~150 | $\sim4 \times 10^{13}$ |
| Lithosphere (weak) | ~17 | $\sim5 \times 10^{12}$ |

Table 3.2: Resistance of the analogue layers and scaled values for natural lithospheres

### 3.2.2. Model results

Model results are illustrated in the following sections, subdivided in four different groups on the basis of the angle of obliquity α, from orthogonal extension (α=0°) to low (α=15°, 30°), moderate (α=45°) and high (α=60°, 75°) obliquity.

#### 3.2.2.1. Orthogonal extension (α =0°)

During orthogonal rifting, extensional deformation nucleates at the strong-weak lithosphere boundaries in the early stages of the experiment giving rise to major boundary fault systems

bordering a subsiding rift depression (Figs. 3.12, 3.13, 3.18). The development of minor normal faults, antithetic to the major systems, gives rise to a pair of marginal grabens, delimiting a central horst. In these initial stages, all the extensional deformation is accommodated by slip on boundary and antithetic faults, whereas the floor of the rift depression (central horst) is undeformed (Fig. 3.13).

At ~18 mm of stretching (corresponding to ~25 km in nature), a change in deformation style occurs: extensional deformation starts to affect the rift floor with development of normal faults which form a graben structure within the central horst (Figs. 3.12, 3.13). Increasing extension leads to deepening of this graben, with an increasing amount of deformation accommodated by internal faults concomitant with a decrease of the amount of slip along boundary faults (Fig. 3.13), such that internal faults accommodate more than ~70% of the total extensional deformation at the end of the experiment (~27 mm of bulk extension, corresponding to ~42 km in nature; Fig. 3.13). We term the initial rifting phase (in which boundary fault activity dominate deformation and the rift floor is undeformed) Boundary Faults Stage (BFS), and the later deformation stage (in which internal faults accommodate the majority of deformation and border fault activity is strongly reduced), Internal Faults Stage (IFS; Figs. 3.12, 3.13).

The final structural pattern of the model displays boundary escarpments and remnants of marginal grabens flanking a rift depression characterized by a graben-in-graben structure caused by activity of internal faults (Figs. 3.12b,d,e and Fig. 3.14). The majority of normal faults are long and linear; statistical analysis suggests that these structures are parallel to the weak zone and perpendicular to the extension vector (Fig. 3.12f).

*3.2.2.2. Low obliquity (15°≤α≤30°)*

In low obliquity rift models (Fig. 3.15), the initial stages of extension are characterized by the nucleation of 3-4 major boundary faults for each rift margin in correspondence to the strong-weak lithosphere boundaries. These are en-echelon, almost linear extensional faults delimiting a subsiding rift depression; their length tend to decrease passing from α=15° to α=30°. As a group, these faults follow the orientation of the weak zone (i.e. the rift trend), but individually they are oblique to both the strong-weak lithosphere boundaries and the orthogonal to the extension direction (see below). Antithetic faults develop in the rift depression defining a couple of marginal grabens which delimit an undeformed rift floor. With increasing extension, the border and antithetic faults become longer and increase their vertical throw, resulting in a widening and deepening of the rift depression. Many minor faults develop

inside the marginal grabens, but the floor of the central horst remains undeformed; these initial stages of extension correspond to the Boundary Faults Stage (BFS) observed during orthogonal rifting.

## Orthogonal rifting α=0°
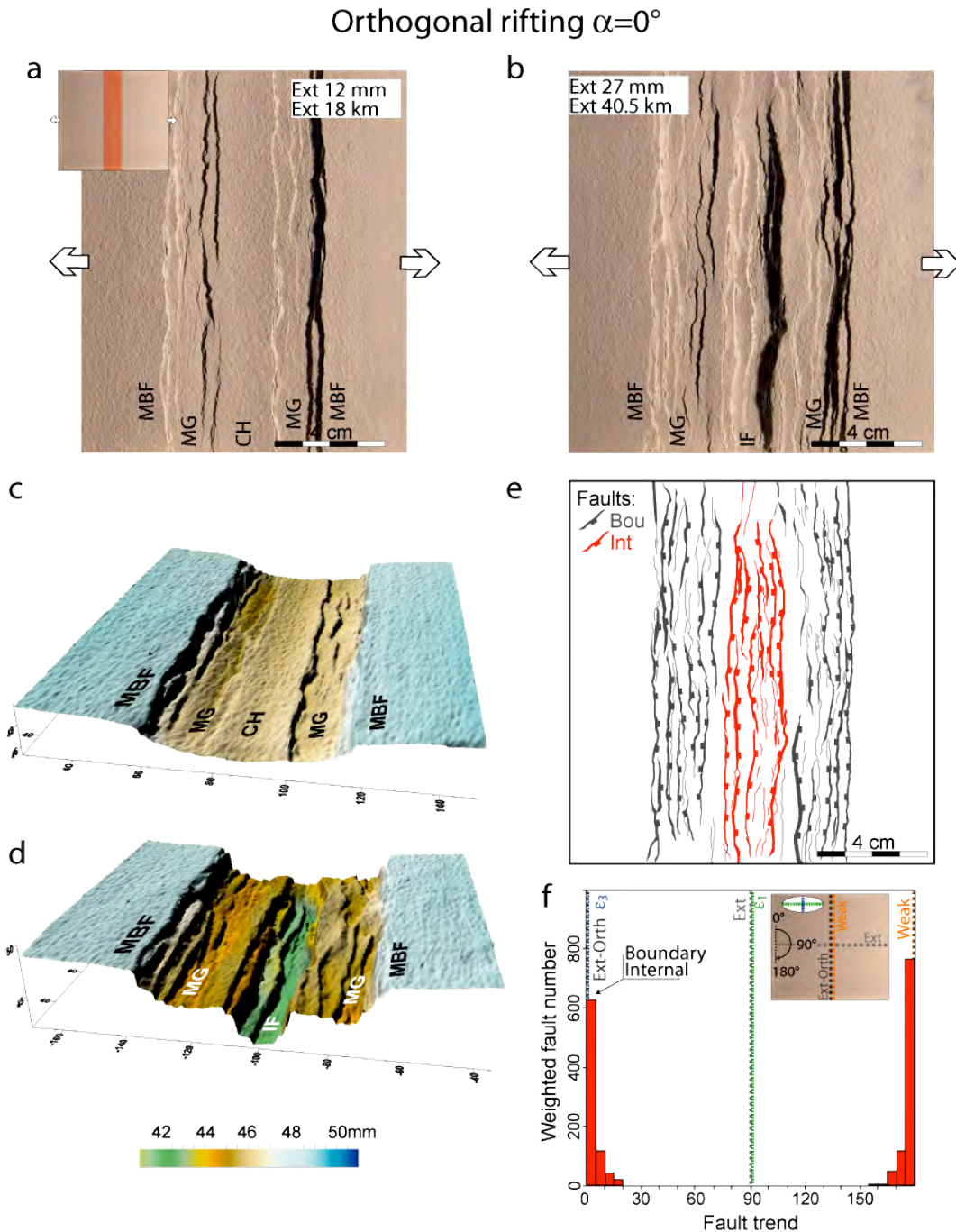


Fig. 3.12: Evolution and pattern of deformation during orthogonal rifting (α=0°). a) The initial stages of rifting (amount of extension <18 mm) show the development of major boundary fault systems (MBF) that accommodate subsidence of the rift depression; together with minor antithetic faults, the boundary faults delimit two marginal grabens (MG) that bound an undeformed central portion of the rift floor (central horst, CH). b) Increasing extension leads to a change in deformation style: extensional deformation starts to affect the central horst with development of conjugate internal normal faults (IF) delimiting a central graben. At the end of the experiment (amount of extension ~27 mm) the majority of deformation is accommodated by slip along the internal faults and subsidence of the central graben; although still active, the boundary faults accommodate a minor part of deformation. c-d) 3D visualization of digital elevation models of the model surface for the deformation stages illustrated in panels a and b (i.e., at 12 mm and 27 mm of extension). Note the marginal grabens and the undeformed central horst in c, and the graben-in-graben structure resulting from activation of the

internal faults in d. e) Line drawing of structures at the end of the experiment (Bou: boundary faults; Int: internal faults). f) Fault distribution illustrated as histogram of the fault azimuths, weighted for the (tip-to-tip) fault length. The weighting factor for each fault is the ratio between the length and the minimum length of the whole data set, such that long faults have higher ratio (weight) than short ones. The frequency of the azimuth of a fault directly relates to this ratio, the longer the fault the higher its frequency. Also reported in the graph are the direction of extension (Ext), the orthogonal to this direction (Ext-Orth), the trend of the weakness zone (Weak) and the principal strain axis ($\epsilon_1$ and $\epsilon_3$) of the strain ellipse, calculated after Fournier and Petit (2007) for a rift-orthogonal stretching factor of $\beta \sim 2$. The small inset schematically shows these different trends, together with the strain ellipse. Fault distribution shows a main peak at ~0°, indicating that the faults form orthogonal to the direction of extension (and to the greatest principal strain axis $\epsilon_1$) and parallel to the weak trend (and to the smallest principal strain axis $\epsilon_3$).
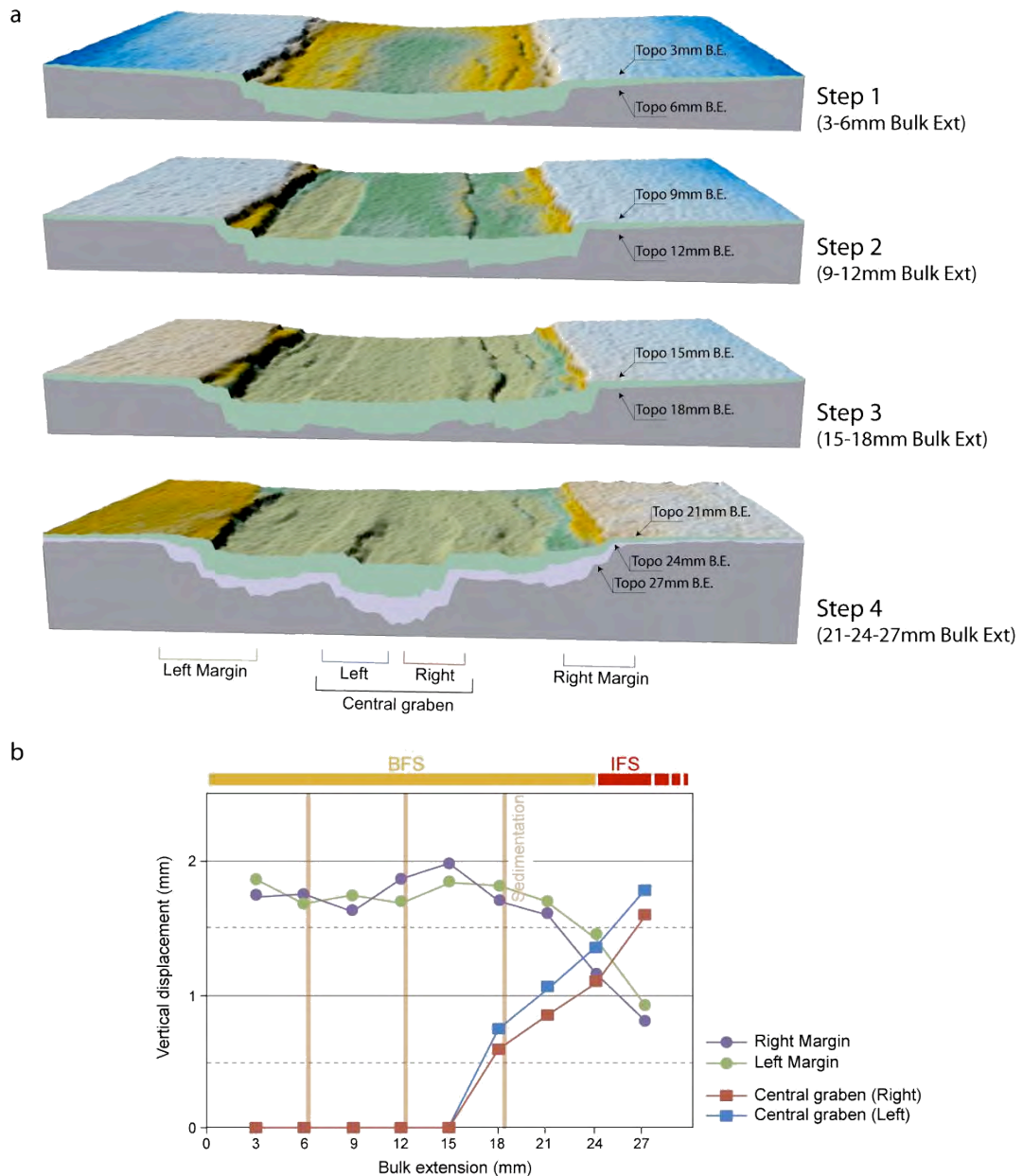


Fig. 3.13: Evolution of surface topography during orthogonal rifting (α=0°). a) Variation in surface topography is analyzed through comparison of digital elevation models acquired through laser scanning of the model surface at the end of four different deformation intervals. Note that at the beginning of each of these intervals the model surface is horizontal, due to model building at the beginning of the experiments and to filling of the rift depression simulating syn-rift sedimentation after 6 mm, 12 mm and 18 mm of bulk extension. Analysis of the evolution of the surface topography clearly highlights the two-phase evolution of model deformation, with activation of boundary faults and marginal graben in a first deformation stage and the subsequent inward

migration of deformation with development of internal faults delimiting a central graben in the second evolutionary stage. b) Variation in surface topography is used to analyze quantitatively the vertical displacement on four different model domains, namely: left and right margins of the rift depression (labeled Left Margin and Right Margin, respectively) and left and right margins of the central graben (labeled Central graben (Right) and Central graben (Left), respectively). This quantitative analysis is reported in the graph of the lower panel, plotting the vertical displacement accommodated by the different model domains versus the bulk extension. Up to ~15 mm of extension, all the extension-related deformation is taken up by the rift margins, which accommodate ~1.7-2.0 mm of vertical displacement for each deformative step; internal faults are not yet developed (0 mm of vertical displacement). The central graben starts to form between ~15 mm and ~18 mm of bulk extension, as testified by the beginning of slip on internal faults. The vertical displacement on these faults increase with increasing extension, in parallel with a decrease of slip on boundary faults such that at ~24 mm of bulk extension the two fault systems (boundary and internal) have the same vertical displacement whereas in the last step of deformation (24-27 mm) the vertical displacement on internal faults overcome that of boundary faults. This marks the transition from the Boundary Faults Stage (BFS), when boundary faults accommodated most of deformation, to the Internal Faults Stage (IFS), when internal faults accommodated most of deformation.
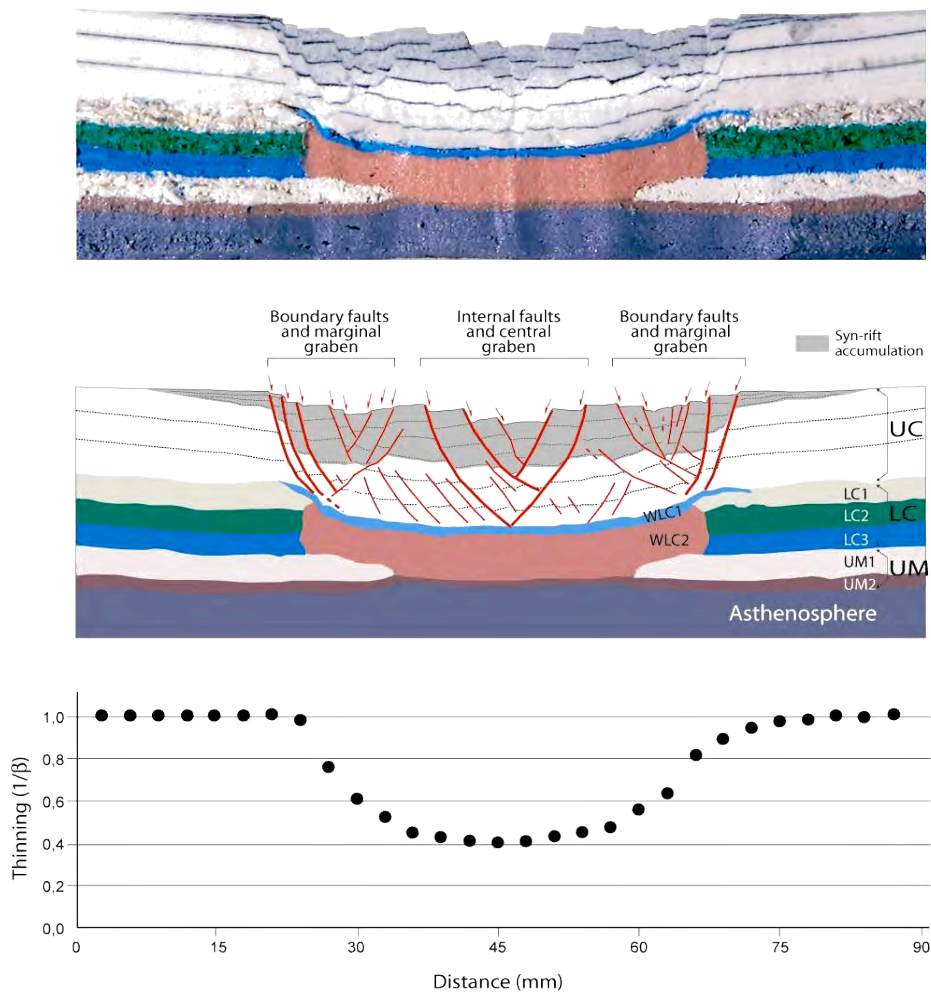


Fig. 3.14: Cross-section of the orthogonal rifting model, displayed as photo (upper panel), line drawing of structures (central panel) and thinning factor of ductile layers (lower panel). The cross-section is taken from the central part of the model. The lower crust and upper mantle deform and thin by distributed ductile flow in the weak zone, which is accommodated by development of normal faults in the brittle upper crust. These normal faults are inclined of >70° at surface and the dip tend to slightly decrease with depth; all the major normal faults cut through the whole brittle layer and terminate at the brittle-ductile transition. Note that the distribution of the syn-rift sediments (grey pattern) and the pre-rift topography (white pattern) indicates the symmetry of deformation with respect to the rift centre. The detailed analysis of the vertical displacement of pre-rift horizontal markers (dotted lines), syn-rift deposits and the model surface testifies the decrease in slip on boundary faults and the later activation and increase in slip on internal faults. In lower panel, the thinning factor of the ductile layers is reported as 1/beta ratio, i.e. ratio between the final and initial total thickness of the layers; note that maximum thinning is observed in the centre of the rift below the central graben.

As for orthogonal rifting, increasing extension leads to the activation of internal faults within the previously undeformed rift depression: this change in deformation style occurs at ~18mm of stretching for α=15° and at ~21mm of stretching for α=30° (corresponding to ~27 and ~32 km in nature, respectively; Fig. 3.18). Internal faults are normal faults striking almost perpendicular to the stretching direction; differently from the orthogonal rifting case, these faults do not define a single central graben but are arranged into two main en-echelon basins (rift segments) connected by a complex transfer zone characterized by a significant strike-slip component of motion (Figs. 3.15, 3.19). The increase in extension leads to the deepening of the en-echelon basins and increase in vertical displacement on internal faults, with consequent decrease of slip on boundary faults and transition to the Internal Faults Stage (IFS) at ~21 mm (~31 km) and ~24 mm (~36 km) of bulk extension for obliquity of 15° and 30° respectively (Fig. 3.18). In parallel, the complexity of the transfer zone connecting the two fault segments increases and a main oblique-slip fault develop sub-parallel to the trend of the weakness zone (Figs. 3.15, 3.19).

As observed for orthogonal rifting, at the end of the experiment internal faults accommodate the largest part of deformation (~70-80%; Fig. 3.18). Statistical analysis of the fault pattern (Fig. 3.15f, n) clearly highlights the two distinct fault systems: boundary and internal. The internal faults are for both experiments almost perpendicular to the extension direction (Fig. 3.15f, n). The orientation of the en-echelon boundary faults is slightly oblique to both the orthogonal to the extension direction and the weak zone (that they follow as a group), but is orthogonal to the greatest principal strain axis $\varepsilon_1$ (i.e., parallel to the smallest principal strain axis $\varepsilon_3$). The angle between boundary faults and the weak zone (i.e., rift trend) increases as α shift from 15° to 30° (Fig. 3.15f, n).

# Low obliquity α=15°
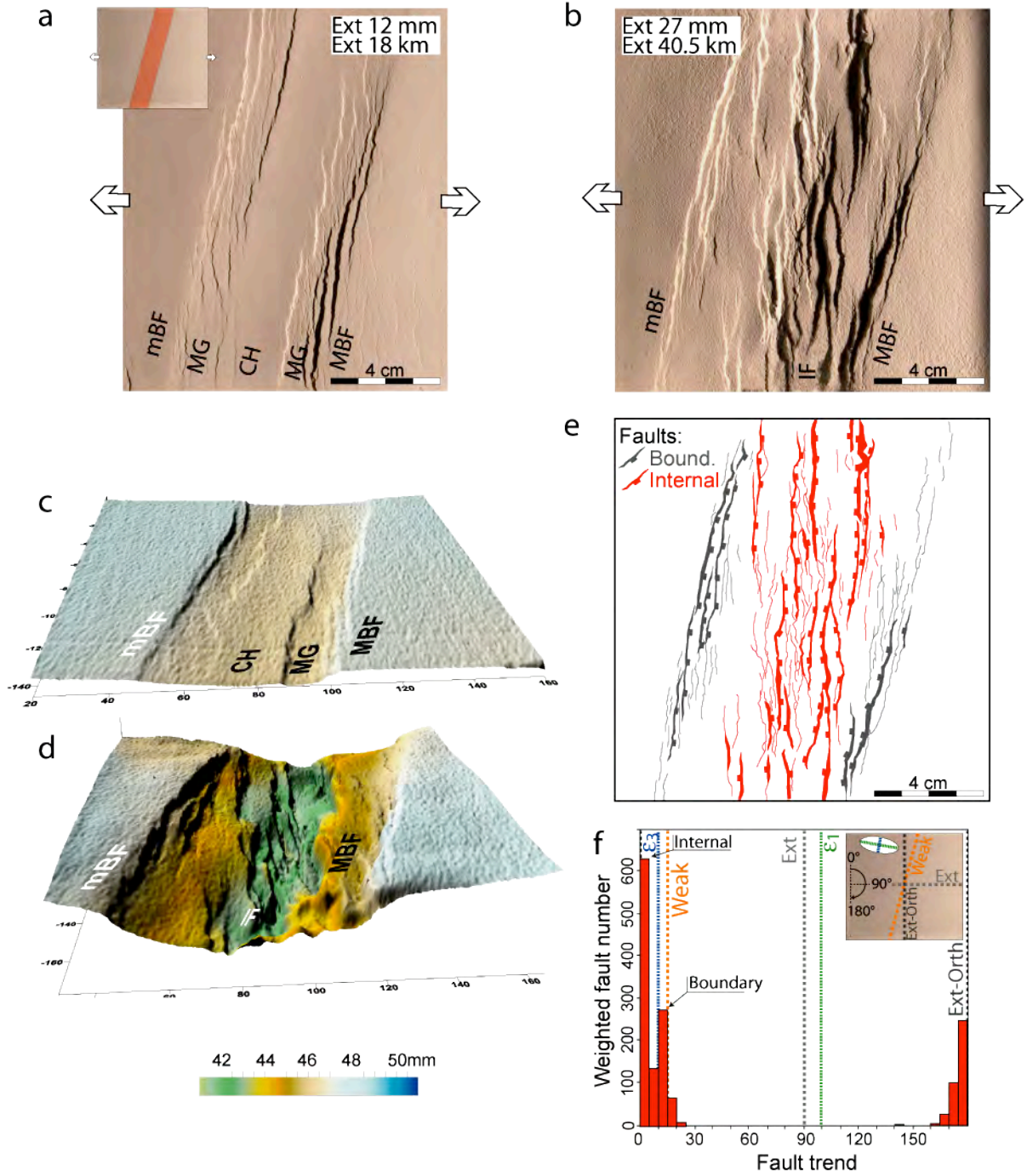


Fig. 3.15 (continues)
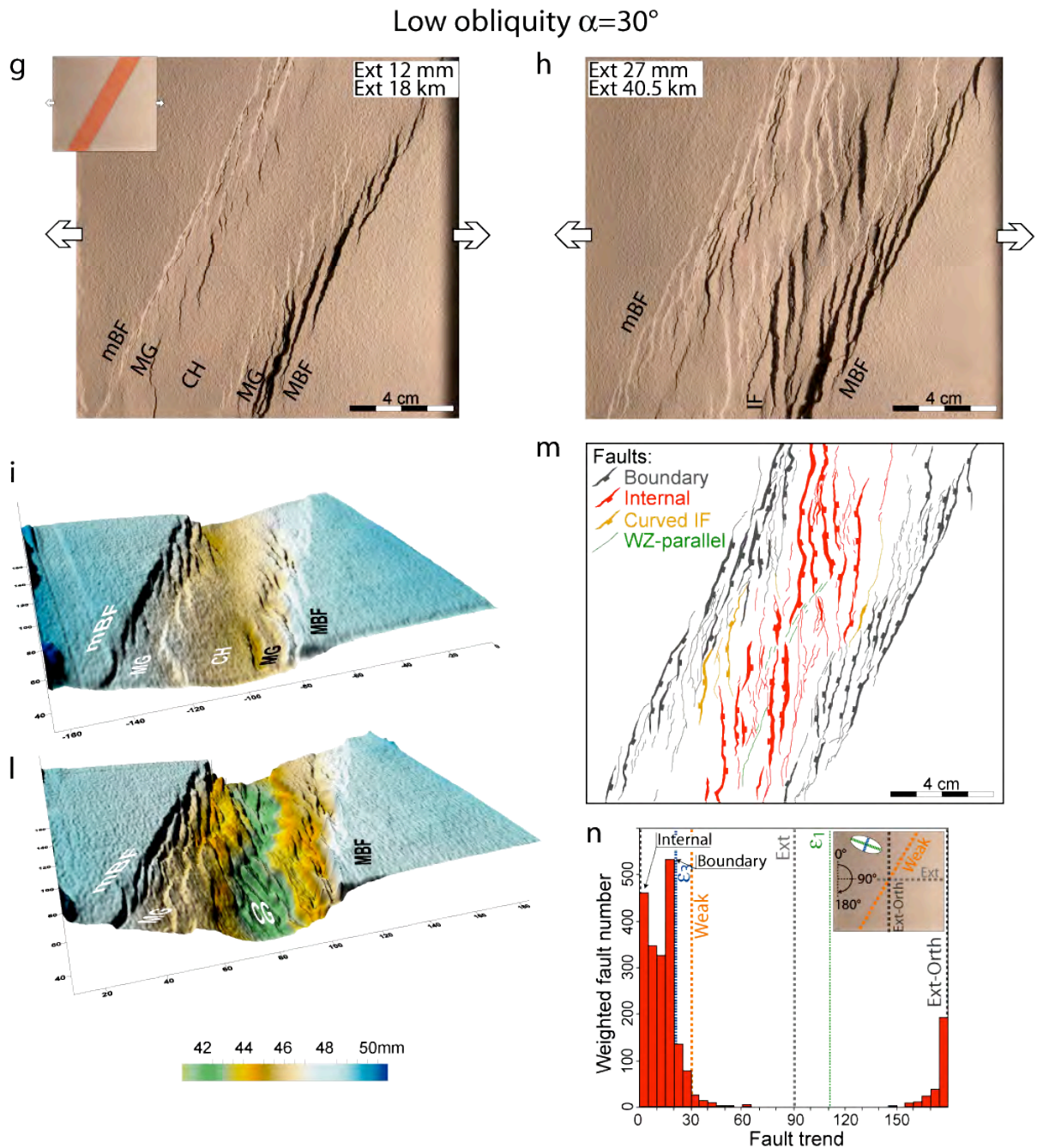
Fig. 3.15: Evolution and pattern of deformation during low obliquity rifting, illustrated as in Fig. 3.12. a-f: model with α=15°, g-n: model with α=30°. Note the two-phase evolution, with transition from Boundary Faults Stage (panels a, c, g, i) to the Internal Faults Stage (panels b, d, h, l). Also note the en-echelon arrangement of boundary faults, and the clustering of internal faults into two en-echelon fault segments affecting the rift depression connected by a transfer zone (see text for details). In panels f and n, internal faults are characterized in both experiments by a main peak between 0° and 5°, indicating that they are almost perpendicular to the extension direction. Boundary faults are instead slightly oblique to both the orthogonal to the extension direction and the weak zone; the angle between these faults and the weak zone (i.e., rift trend) increases with α, as displayed by the azimuths of boundary faults that peak around 10-15° for α=15° and around 15-20° for α=30°. Note that in both cases, the en-echelon boundary faults are orthogonal to the greatest principal strain axis ε₁ and parallel to the smallest principal strain axis ε₃, calculated after Fournier and Petit (2007) for a rift-orthogonal stretching factor of β~1.9 and β~1.7 for obliquity of 15° and 30° respectively.

*3.2.2.3. Moderate obliquity (α=45°)*

As in previous experiments, few en-echelon boundary faults nucleate at the boundaries between strong and weak lithosphere; again these faults follow the orientation of the weak zone as a group and individually they are oblique to both the strong-weak lithosphere boundaries and the orthogonal to the extension (Fig. 3.16). This initial deformation phase, dominated by these boundary faulting and subsidence of the rift floor, still corresponds to the Boundary Faults Stage outlined above. However, if compared to the previous models, the deformation migrates inside the rift depression earlier during moderate obliquity: the first internal faults can be detected at ~9 mm of stretching (corresponding to ~13.5 km in nature) and the transition to the Internal Faults Stage occurs at ~15 mm (~22.5 km) of bulk extension (Fig. 3.18). As in the previous models, in this latter deformation stage the largest part of extensional deformation is accommodated by the nucleation and lengthening of internal faults; in contrast to low obliquity models, these faults are not orthogonal to the stretching vector but strike at small angle to this direction (Fig. 3.16). Although the surface deformation pattern is more complex than in previous models, still two main en-echelon rift segments, connected by a complex transfer zone can be identified (Figs. 3.16, 3.19). An increase of extension leads to further deepening of the basins and further propagation of the internal faults that close to the rift margins gently curve and acquire an S-shaped geometry to adjust with the border fault systems (Fig. 3.16).

At the end of the experiment, the internal faults accommodate ~85% of vertical displacement (Fig. 3.18); rift segments are characterized by a sigmoidal shape and are connected by oblique-slip faults sub-parallel to the weakness zone trend within the transfer zone (Figs. 3.16, 3.19). Differently to the previous experiments, statistical analysis of fault azimuths in the moderate obliquity models display three different main peaks (Fig. 3.16f). The main peak corresponds to the internal faults that, as stated above, are oblique to the orthogonal to the extension direction; a secondary peak is related to the en-echelon boundary faults, individually oblique to both the weak trend and the orthogonal to the extension but orthogonal to the greatest principal strain axis $\varepsilon_1$ (i.e., parallel to the smallest principal strain axis $\varepsilon_3$).; the third, minor peak corresponds to the oblique-slip faults developing sub-parallel to the trend of the pre-existing weakness (i.e., rift axis) within the transfer zone.
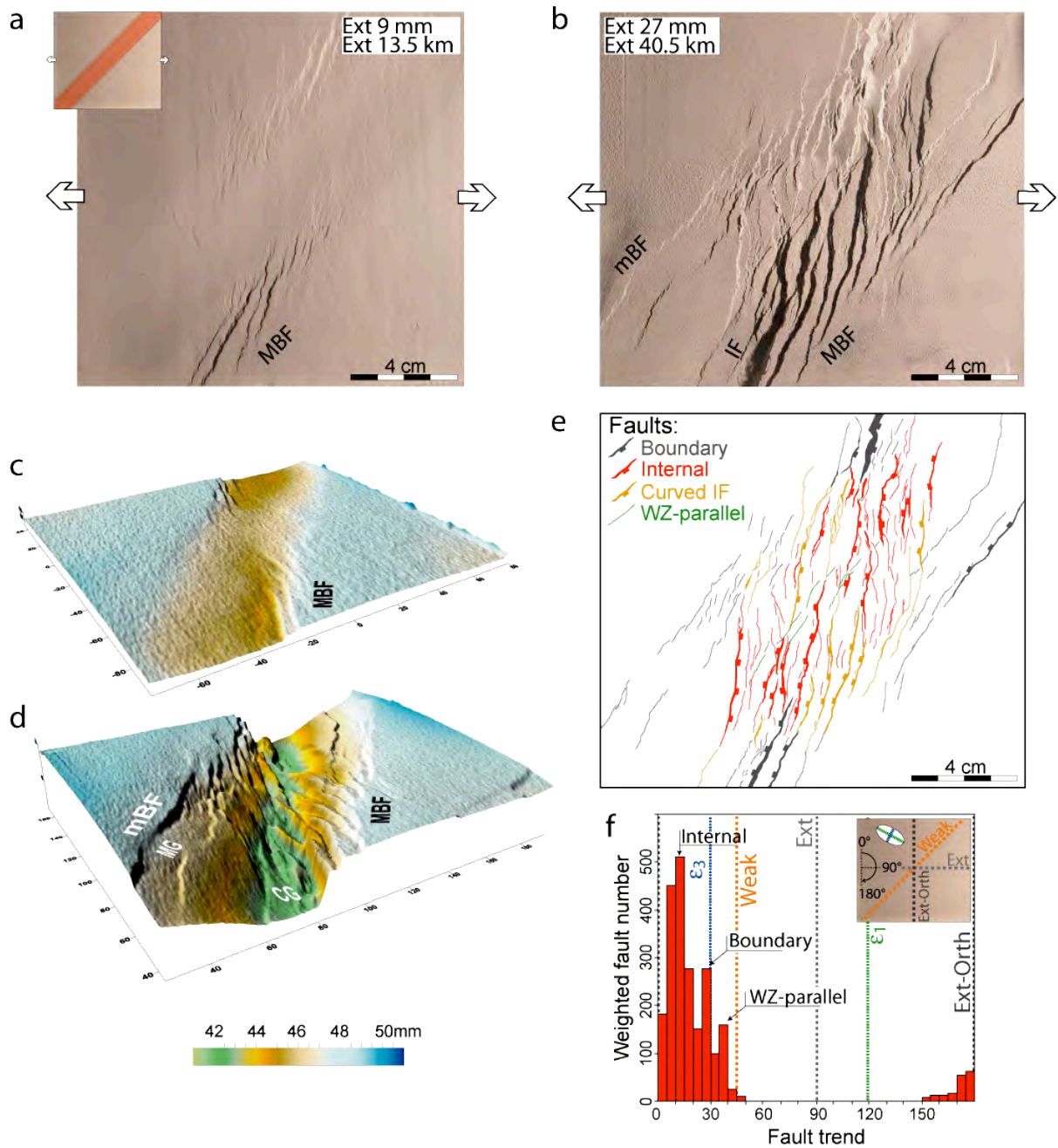
Fig. 3.16: Evolution and pattern of deformation during moderate obliquity rifting, illustrated as in Fig. 3.12. In panels b and e note that some internal faults (indicated as curved IF) gently curve close to the rift margins and acquire an S-shaped geometry to adjust with and reactivate parts of the border faults. In the histogram of fault distribution note the three main peaks corresponding to the internal faults (main peak at around 10°-15°), boundary faults (peak at 25°-30°) and faults subparallel to the trend of the pre-existing weakness (WZ-parallel; minor peak at 35°-40°). Note that as in the previous cases, the en-echelon boundary faults are orthogonal to the greatest principal strain axis $\varepsilon_1$ and parallel to the smallest principal strain axis $\varepsilon_3$, calculated after Fournier and Petit (2007) for a rift-orthogonal stretching factor of $\beta\sim1.6$.

*3.2.2.4. High obliquity (60°≤α≤75°)*

Conversely to previous kinematical boundary conditions, deformation does not nucleate at the strong-weak lithosphere boundaries with development of boundary faults; rather, oblique internal faults accommodate extension since the early stages of stretching (Fig. 3.17). These faults are characterized by a predominantly oblique-slip kinematics, which accommodates the strong strike-slip component of motion imposed by the high obliquity rifting (Figs. 3.17, 3.19).

As extension increases, the internal faults growth in length and different fault systems interact in the rift centre, increasing the structural complexity of this area where rift-parallel faults with dominant strike-slip kinematics develop at ~18 mm of stretching (~25 km in nature). Boundary faults do not develop at all for α=75° or develop as very minor structures in the late stages of extension for α=60° experiment; as a consequence, subsidence of the rift floor is limited in these models. Overall, in contrast to the behavior shown by low to moderate obliquity rifting, a single Internal Faults Stage characterizes the evolution of high obliquity models (Fig. 3.18).

At the end of the experiment, oblique-slip and strike-slip faults within the rift characterize the structural pattern; their interaction close to the rift axis gives rise to complex rhomboidal structures (Fig. 3.17). These two distinct fault systems are indicated by two distinct peaks in the histograms of fault distribution: the main peak corresponds to the oblique-slip faults that are oblique to both the weakness zone (i.e., rift trend) and the orthogonal to the extension direction; the minor peak is instead related to the strike-slip faults, sub-parallel to the rift axis trend (Fig. 3.17f, m).

# High obliquity α=60°
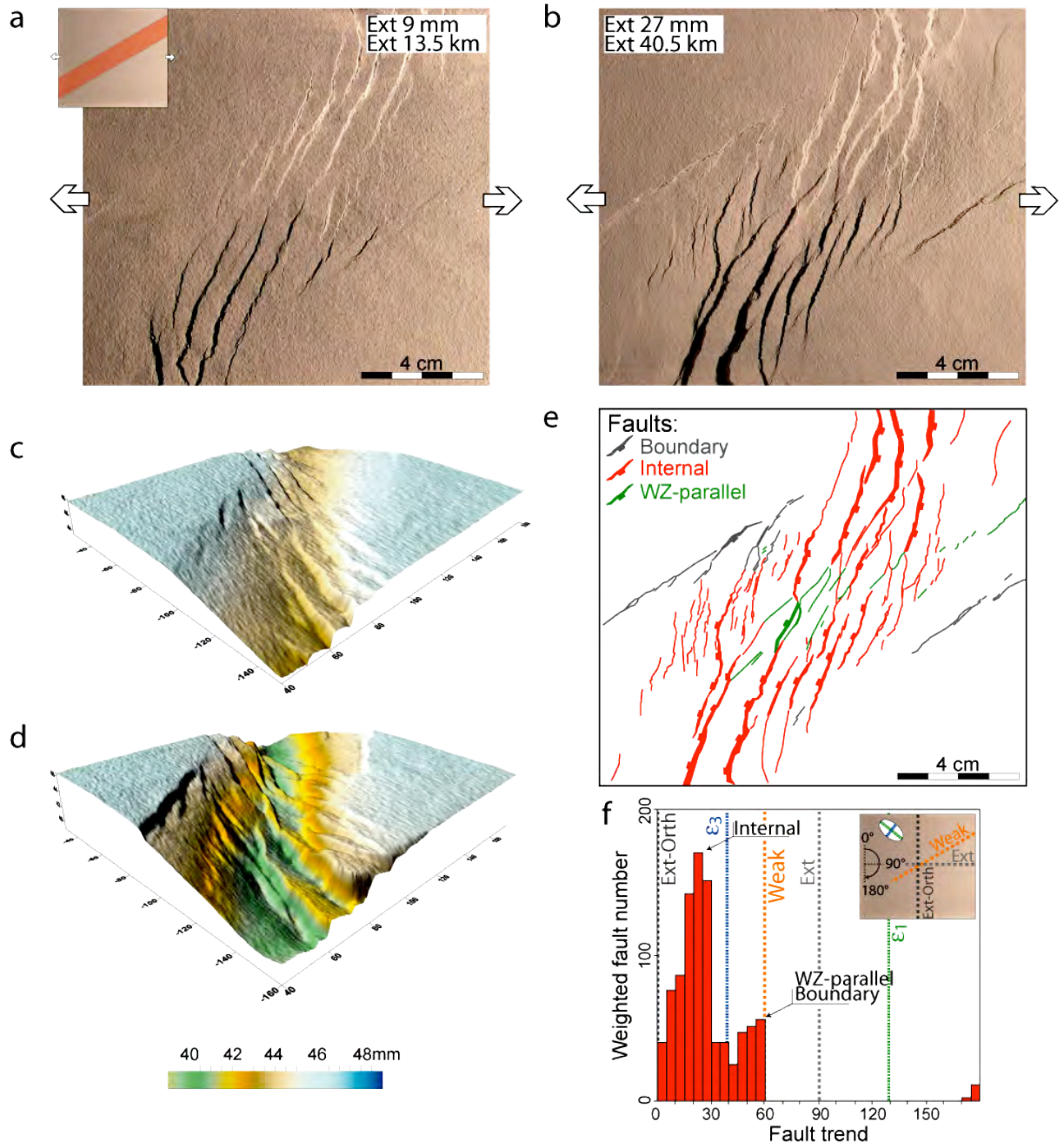


Fig. 3.17: (continues)
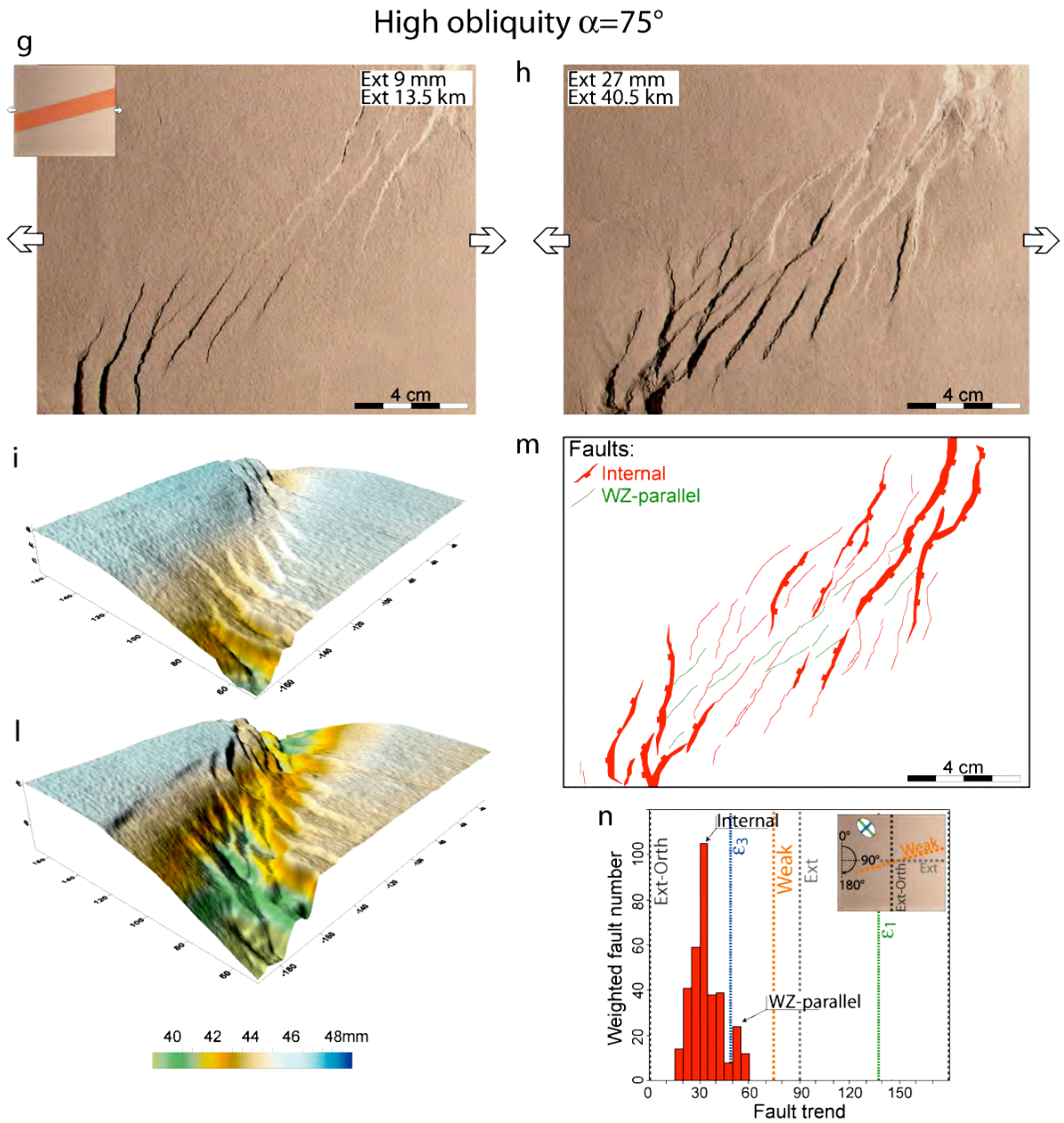
Fig. 3.17: . Evolution and pattern of deformation during high obliquity rifting, illustrated as in Fig. 3.12. a-f: model with α=60°, g-n: model with α=75°. In the histogram of fault distribution note two main peak corresponding to the internal fault oblique to the extension direction (main peak at around 20-25° for α=60° and around 30°-35° for α=75°) and faults subparallel to the trend of the pre-existing weakness (WZ-parallel; peak at around 55°-60° for α=60° and around 50°-55° for α=75°). Note that the minor peak corresponding to the boundary faults α=60° experiment is coincident with the WZ-parallel peak (panel f). Reported in graphs are the directions of the principal strain axis ε1 and ε3, calculated after Fournier and Petit (2007) for a rift-orthogonal stretching factor of β~1.4 and β~1.2 for obliquity of 60° and 75° respectively.
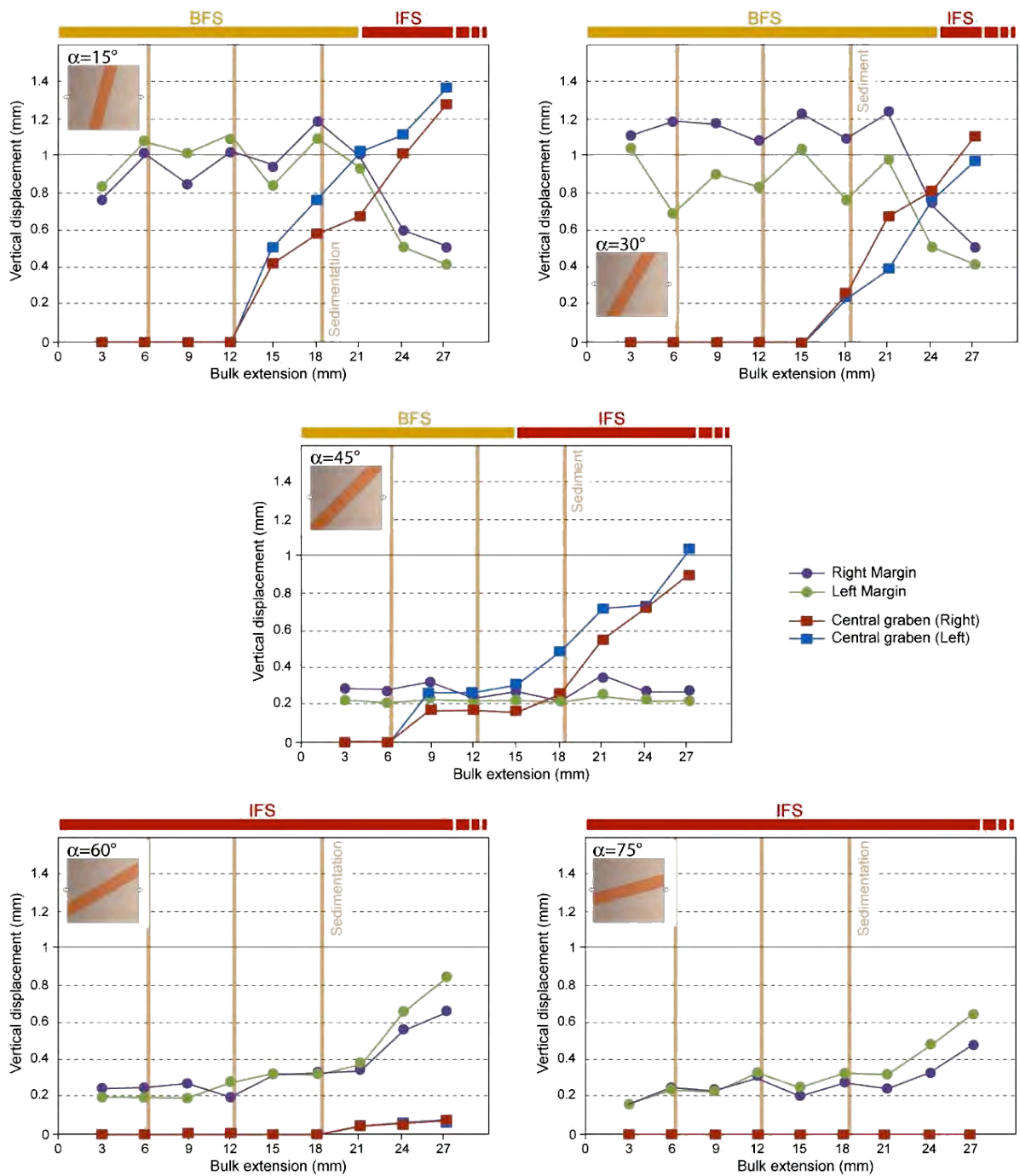
Fig. 3.18: Graphs plotting the vertical displacement accommodated by the different model domains (rift margins, central graben) versus the bulk extension (see Figure 3.13 for details of calculations). Note the two-phase evolution with transition from the Boundary Faults Stage (BFS) to the Internal Faults Stage (IFS) in low to moderate obliquity models, and the single-phase rifting with no BFS in high obliquity rifting experiments.
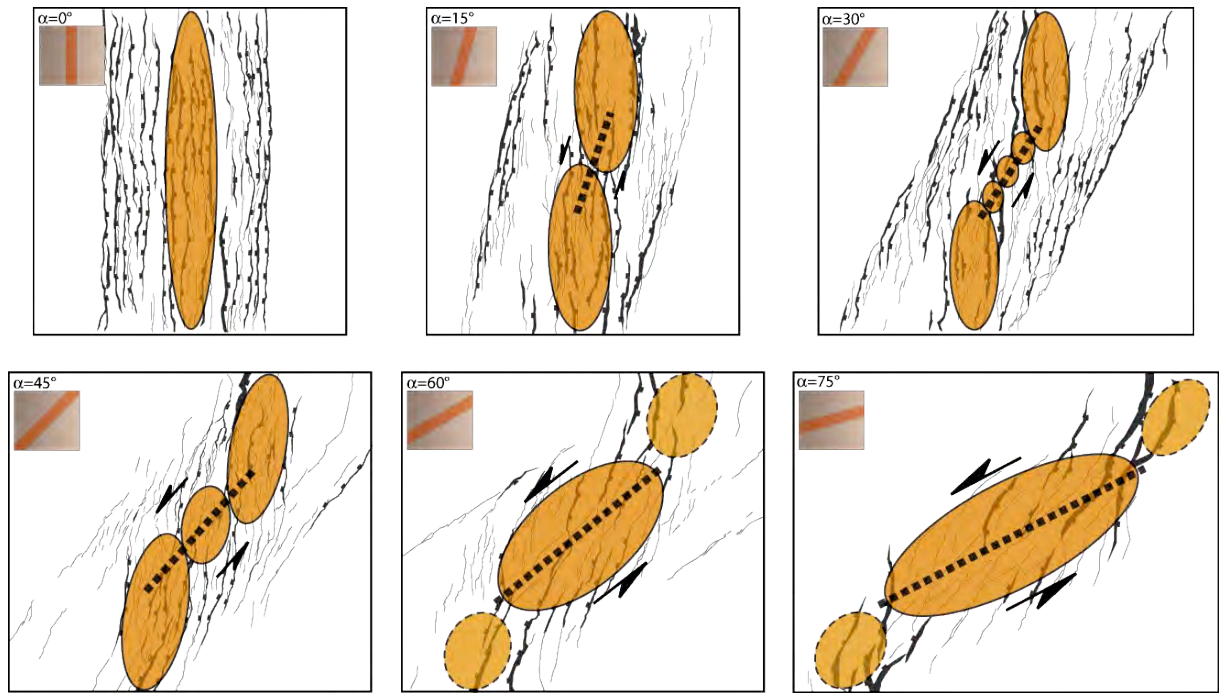
Fig. 3.19: Schematic structural pattern of the models illustrating the different fault segments that accommodate extension within the rift depression (interpretation based on the extension-related thinning of the model lithosphere from analysis of longitudinal cross-sections; see Corti, 2008). Note that for α≤45°, deformation is characterized by two en-echelon segments (sub-orthogonal to the extension direction) connected by a transfer zone; for α>45°, deformation is characterized by the (predominantly) strike-slip deformation in the model centre.

## 3.3. Discussion

### 3.3.1. Evolution, pattern and partitioning of deformation during oblique continental rifting

The above experiments support that the way the continental lithosphere respond to extension is influenced by the presence of weakness zones, inherited from previous deformation phases. Model results suggest that the evolution, pattern and partition of deformation are highly influenced by the orientation of the weakness with respect to the stretching vector, resulting in two end-member evolutions and characteristics of deformation, observed in orthogonal (and low- to moderate-obliquity) rifting and high-obliquity rifting (Fig. 3.20).

### 3.3.1.1. Evolution of deformation

During orthogonal and low to moderate obliquity rifting (α≤45°), deformation is characterized by a two-phase evolution, with activation of large boundary faults during the initial stages of rifting followed by rift-ward migration of faulting for increasing deformation (Figs. 3.12-3.17, 3.20). The initial rift phase gives rise to subsidence of the rift depression in response to strong thinning of the ductile layers in the weak zone; slip along main marginal faults, combined with the thinning of the ductile layers and downwarping of the brittle layer in the central rift zone, contribute to the total subsidence of the rift depression.

46
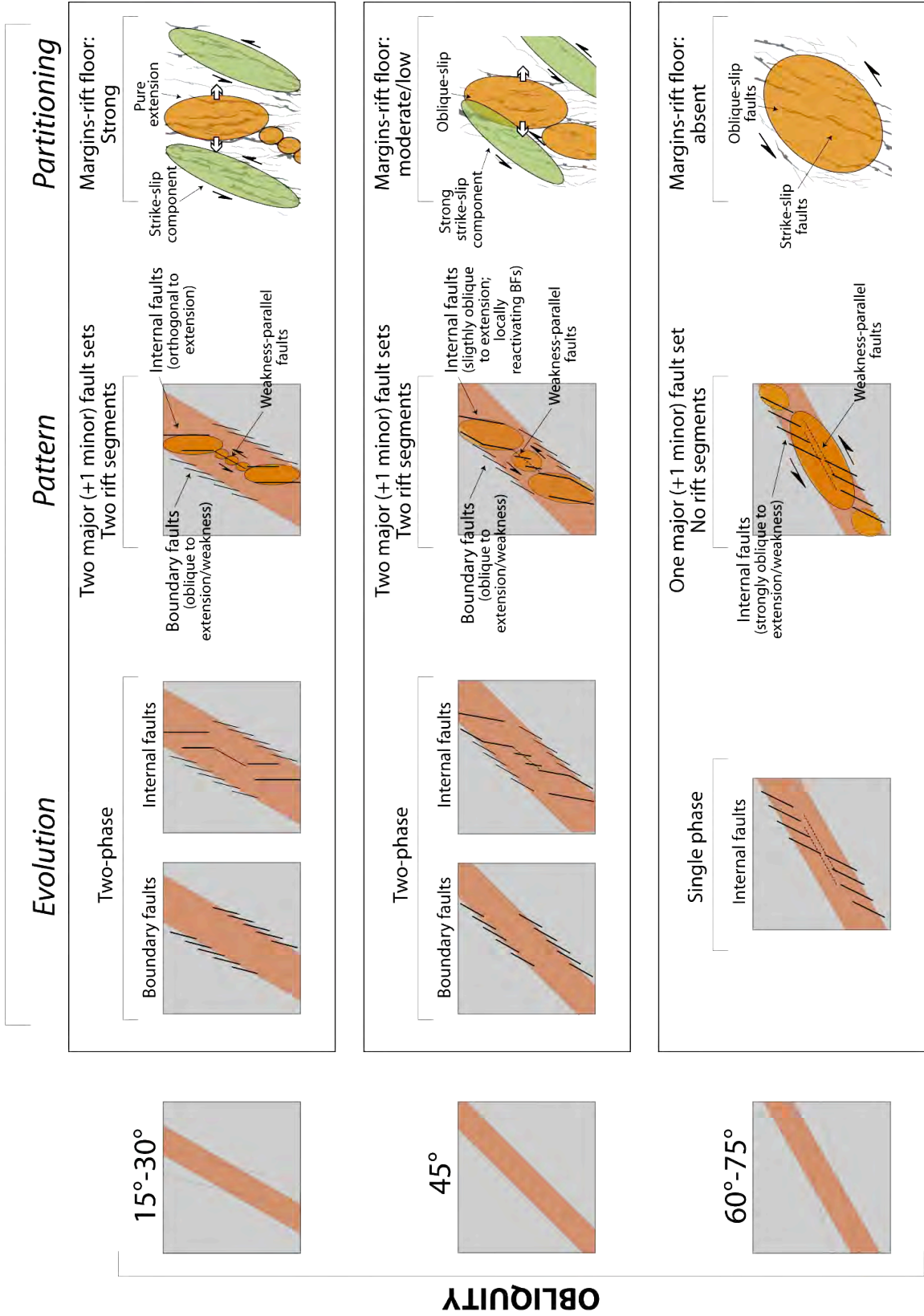
Fig. 3.20: Summary of experimental results in terms of evolution, pattern and partitioning of deformation as a function of rift obliquity.

From mechanical considerations, this is analogous to a necking instability of the lithosphere (e.g., Mulugeta and Ghebreab, 2004). Increasing extension leads to the development of new high-angle normal faults (internal faults) in the thinnest parts of the model lithosphere (i.e., in the centre of the rift depression; see Corti, 2008); this rift-ward migration of deformation mimics the typical evolution of natural narrow rifts (e.g., Ziegler and Cloetingh, 2004). For low to moderate obliquity rifting, this evolution corresponds to the successive activation of differently oriented fault systems under constant rift kinematics, a conclusion that greatly improves previous modeling works that resulted in a roughly contemporaneous activation of the different fault sets (e.g., Tron and Brun, 1991; Clifton and Schlische, 2001; McClay et al., 2002; see below section 3.3.1.4).

The current models also suggest that the timing of both development of internal faults and the transition from the initial boundary faults stage to the later internal faults stage is a function of the rift obliquity and decreases increasing the angle $\alpha$ (Fig. 3.21a). For obliquity of 45° boundary fault activity is strongly reduced and deformation is soon transferred to the internal faults affecting the rift depression. This effect is emphasized for high obliquity rifting ($\alpha \geq 60°$), where deformation is accommodated within the rift floor (i.e., above the initial weakness) since the early stages of extension and the role of the border faults on accommodation of deformation becomes negligible. In this case, no significant changes in the spatial distribution of deformation are observed during progressive extension: in contrast to the above-discussed models, a single phase of rifting thus characterizes high obliquity models (Fig. 3.21a).

### 3.3.1.2. Pattern of faulting

As discussed above, the current experiment show that the pattern of deformation is strongly controlled by orientation of the weak zone with respect to the stretching vector. For low obliquity rifting, the final fault pattern is characterized by en-echelon, oblique boundary faults that -as a group- follow the trend of the weak zone but individually are oblique to both the weak zone trend and the orthogonal to the direction of extension, and orient orthogonal to the local maximum horizontal extensional strain. Internal faults are orthogonal to extension (Fig. 3.15). Fault geometries show similarities with some of the previous models (Clifton et al., 2000; Clifton and Schilsche, 2001; McClay et al., 2002), although in all the previous works the mean fault trends are never perpendicular to the stretching vector (see also Tron and Brun, 1991). In the current models internal faults clustered in two en-echelon segments linked by a complex transfer zone, whereas in previous models faults are more evenly distributed over the

deformed zone with no development of distinct rift segments (Withjack and Jamison, 1986; Tron and Brun, 1991; Smith and Durney, 1992; Dauteuil and Brun, 1993; Clifton et al., 2000; Clifton and Schilsche, 2001; McClay et al., 2002).

Due to the increase in strike-slip component of deformation, in moderate obliquity models ($\alpha$=45°) the final fault pattern is still composed of boundary and internal faults, but geometrically more complex than in the previous low obliquity models (Fig. 3.16). Indeed, distinction between boundary and internal faults is less clear as internal faults, now trending oblique to the orthogonal to the stretching vector, curve to reactivate the border faults approaching the margins of the depression and acquire an overall sigmoidal shape. As above, this geometry is substantially comparable to that obtained in previous models (Clifton et al., 2000; Clifton and Schilsche, 2001; McClay et al., 2002), but again clustering of internal faults in distinct rift segments (connected each other by oblique-slip rift-parallel faults) differentiate the current experiments from the existing works (see below section 4.1.4).

In high obliquity rifting, faults are distributed over the whole deformation region and not clustered in any clear rift segment; they accommodate the predominant strike-slip component of motion, whereas boundary faults are absent or negligible. The final pattern is characterized by internal faults oblique to the orthogonal to the extension direction and rift-parallel faults in the axial zone (Fig. 3.17). The fault orientation is comparable to existing works (e.g., Tron and Brun, 1991; Clifton et al., 2000; Clifton and Schlische, 2001), although a more complex fault pattern (with presence of sigmoidal fault systems nearly orthogonal to extension) is observed in some of the previous models (Clifton et al., 2000; Clifton and Schlische, 2001).

Comparison of different deformation characteristics as a function of $\alpha$ is summarized by the graphs of Fig. 3.21a-e. These graphs show that:

1) the angle between the orientation of the different fault systems and the direction of extension ($\theta$) shows a general decrease increasing $\alpha$, indicating that the main fault systems tend to parallelize the direction of extension increasing obliquity (see Tron and Brun, 1991). This conclusion is in line with previous results (e.g., Tron and Brun, 1991; Clifton et al., 2000);

2) the number of faults shows a general increase up to $\alpha$ between 30° and 45° and then a general decrease increasing obliquity, in a similar fashion to previous results (e.g., Tron and Brun, 1991; Clifton et al., 2000);

3) the mean fault length decreases up to $\alpha$~45°, then increases with obliquity; this trend fits the results by Tron and Brun (1991) but is substantially different from the

experiments by Clifton et al. (2000) where a general decrease in fault length as $\alpha$ increases is observed.

4) the fault dip increases with $\alpha$, fitting the experimental results and the theoretical predictions for a Coulomb material subjected to extension with an increasing component of strike-slip deformation reported in Tron and Brun (1991);

5) the rift floor subsidence decreases increasing $\alpha$, in accord with the decrease in the extensional component of deformation (and the parallel increase in strike-slip motion) increasing obliquity.

Notably, dispersion of azimuths increases increasing obliquity up to $\alpha\sim30°$-$45°$ (Fig. 3.21b), concomitant with a parallel increase in fault number and a decrease in mean fault length; for $\alpha>45°$, both the dispersion of azimuths and fault number decrease, whereas the fault length increases. Again, this behavior may be explained by considering the orientation of weak zone with respect to the stretching direction, and the transition from extension- to strike-slip dominated deformation occurring for $\alpha=45°$ (Fig. 3.22).

For $\alpha\leq45°$, extension dominates and the growth of major fault systems (boundary, internal) is influenced by the orientation of the weak-strong boundary with respect to the extension direction and the relative width of the rift depression (Fig. 3.22). Boundary faults nucleate in correspondence to the weak-strong transition zone and are oblique to its trend, with obliquity increasing with $\alpha$. The growth of these structures is influenced by their orientation with respect to the weak-strong boundary: in fact, boundary faults cannot propagate neither outside the rift (where the lithosphere is too strong) nor inside the rift depression (where either basal ductile shear stresses have not grew enough to rupture the brittle crust in the early stages of extension, or deformation is accommodated by extension-orthogonal internal faults in the latest stages of stretching). As a result, for low obliquity ($\alpha=15°$) boundary faults are sub-parallel to the weakness and can grow long distances in this direction, whereas for $\alpha=45°$ they are more oblique to the weakness such that their growth is limited (Fig. 3.22). Similarly, internal faults form and grow orthogonal or sub-orthogonal to the direction of extension; their lateral growth is limited by the relative narrowing of the rift depression in the extension-orthogonal direction as $\alpha$ increases (Fig. 3.22).

For $\alpha>45°$, strike-slip deformation dominates, the major fault systems form inside the rift but are strongly oblique to the orthogonal to the extension and consequently no more limited in their lateral growth by the width of the rift depression. In this case, few, long faults with predominant strike-slip motion accommodate deformation (Fig. 3.22).
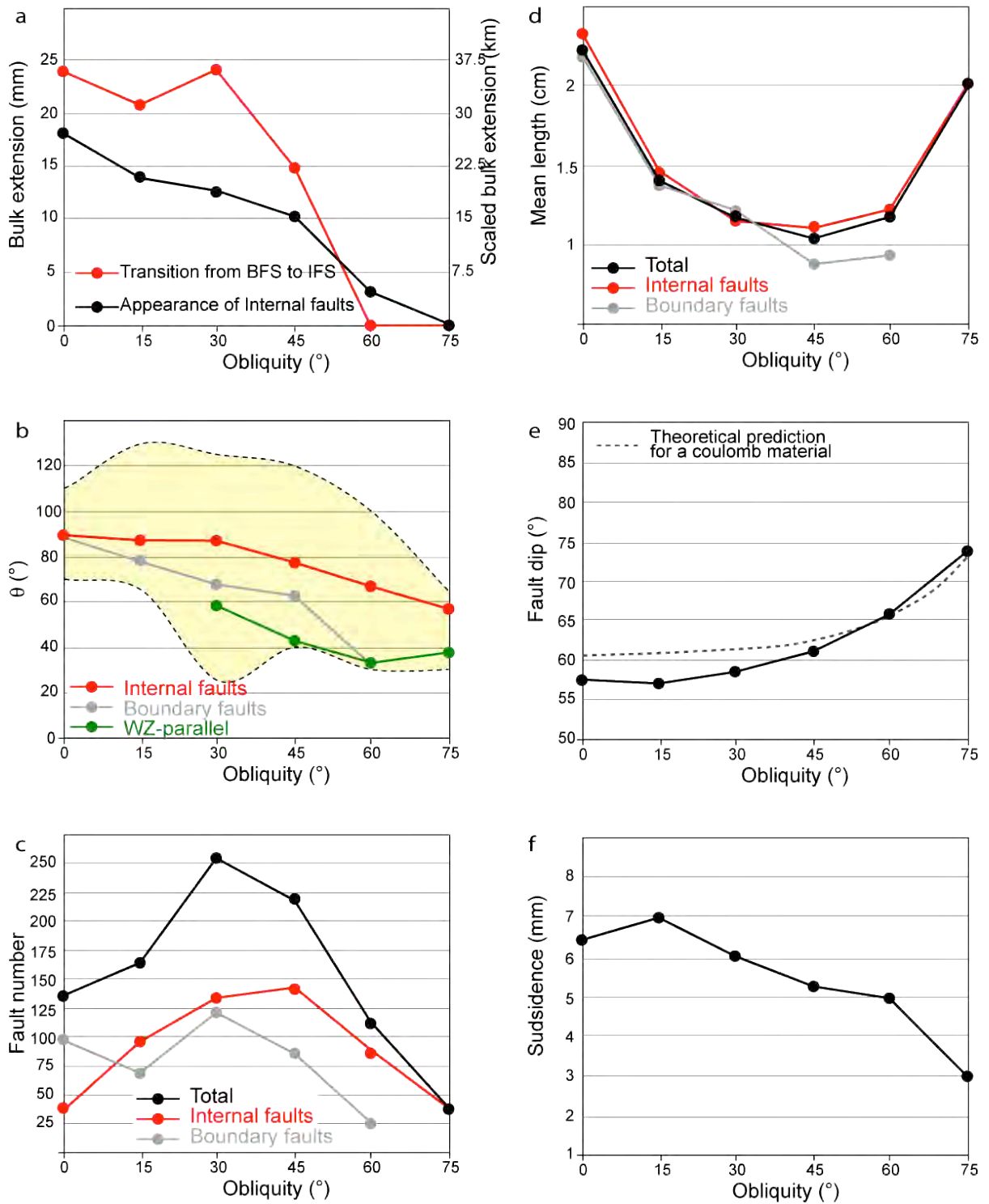
Fig. 3.21: Graphs summarizing the variations as a function of rift obliquity α of different characteristics of faulting, specifically: (a) amount of bulk extension needed for internal faults development and the transition from the Boundary Faults Stage (BFS) to the Internal Faults Stage (IFS). Bulk extension is calculated as mean value of 3 to 6 experiments for each obliquity angle; (b) θ, , i.e. the angle between the orientation of each fault system (defined on the basis of the peaks in the histograms of fault orientation) and the direction of extension (see Tron and Brun, 1991). The yellowish area enclosed between dotted lines represents the total span of fault orientations displayed on histograms; (c) fault number; (d) mean tip-to-tip fault length; (e) fault dip calculated from model cross-sections; (f) maximum subsidence of the rift depression calculated in the central portion of the models.
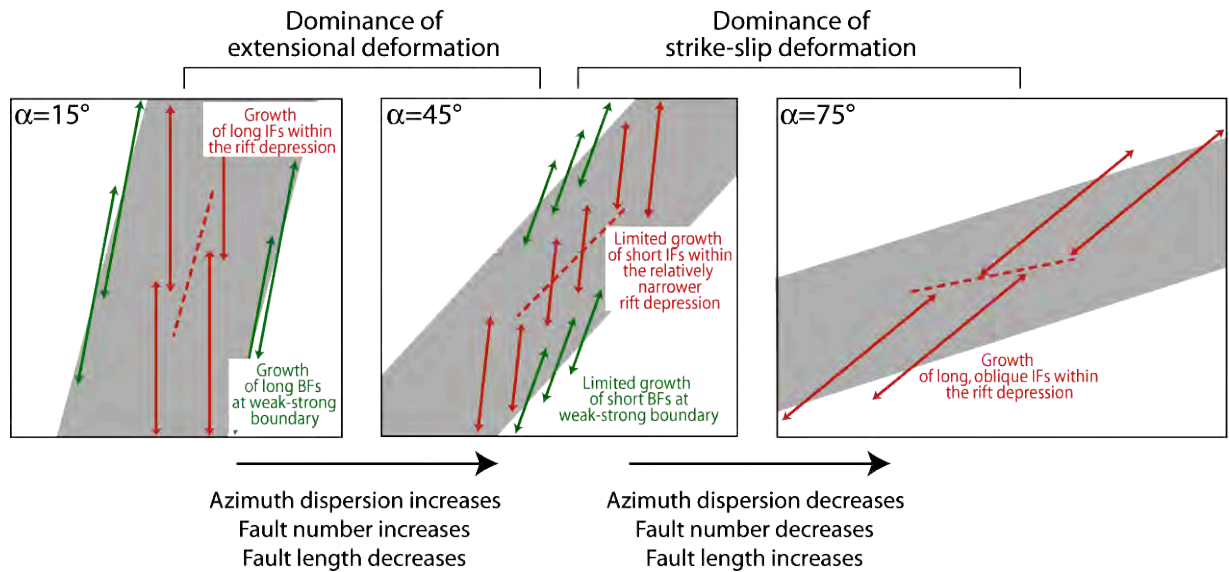
Fig. 3.22: Schematic explanation for the variations of dispersion of azimuths, fault number and mean fault length as a function of the obliquity angle.

### 3.3.1.3. Partition of deformation

In low-obliquity models deformation is spatially and kinematically partitioned between the rift margins and the valley floor (Figs. 3.20, 3.23). At rift margins, the en-echelon arrangement of boundary faults testify a strike-slip component of motion, resulting in an overall oblique-slip kinematics of fault systems; conversely, the fault swarms affecting the valley floor are characterized by a nearly dip-slip kinematics (pure extension), although a local complex kinematics is observed at the transfer zones connecting the fault segments. Similar patterns of strong rift margins/rift floor partitioning of deformation have not been described in previous modeling, but have been described in natural continental (e.g., Main Ethiopian Rift, see Corti, 2009) and oceanic (e.g., Mohns Ridge, see Dauteuil and Brun, 1996; Gulf of Aden, see Dauteuil et al., 2001) rifts.

Deformation partitioning between the rift margins and the valley floor is still observed during moderate obliquity ($\alpha$=45°), but is less developed than in low-obliquity models. In this case, a distinction between internal and boundary faults is -at places- less clear (see above) and internal faults are not orthogonal to the direction of extension and thus accommodate a (minor) component of strike-slip deformation (Fig. 3.20).

For high obliquity (>45°) rifting, strain partitioning between the rift floor and the margins is not observed; deformation affects the rift floor and is kinematically accommodated by oblique-slip and strike-slip faults (Figs. 3.20, 3.23; e.g., Tron and Brun, 1991).
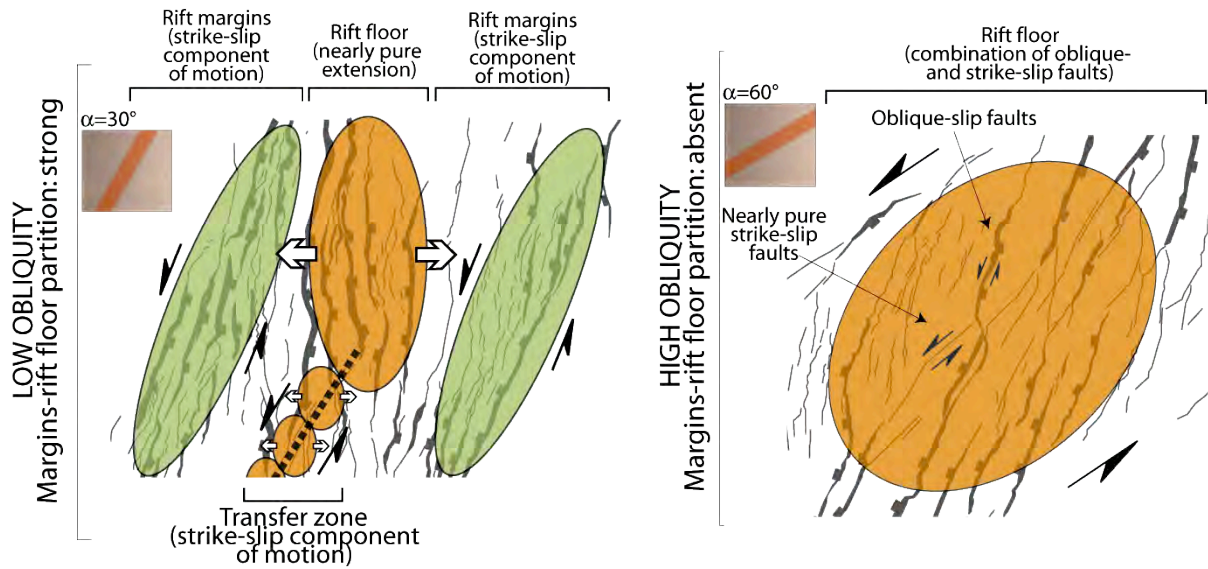
Fig. 3.23: Characteristics of distribution and partition of deformation in low and high obliquity models. See text for details.

### 3.3.1.4. Differences/similarities with previous models

As outlined above, existing analogue modeling works on oblique extension mostly focused on the analysis of the influence of obliquity on the pattern of faulting of the brittle upper crust. The only previous lithospheric-scale experiments (Mart and Dauteuil, 2000) mostly focused on the large-scale patterns of growth/interaction of different rift segments; these models only investigated orthogonal and low obliquity rifting ($\alpha=0°$, 15°, 30°) and adopted a simplified brittle/ductile two-layer rheology as analogue of the continental lithosphere, which was pulled by using lateral metal plates generating a velocity discontinuity. Deformation was accommodated in these experiments by an en-echelon pattern of propagating and interacting rift segments; the results were analyzed in terms of rift architecture resulting from (along-axis) segment growth, linkage and transfer zones development, such that the patterns of evolution, faulting and strain partitioning at the scale of a single rift segments were not investigated in these models.

As discussed in sections 3.3.1.1.and 3.3.1.3., the current experiments support previous findings in that the evolution, pattern and partition of deformation during oblique rifting are strongly controlled by the angle of obliquity $\alpha$, in turn controlling the relative proportion between extension and shear (e.g., Withjack and Jamison, 1986; Tron and Brun, 1991; Clifton et al., 2000; Corti et al., 2001). Similarities with previous models are observed in the variations of fault parameters such as orientation, length and dip as a function of $\alpha$, with main changes in the deformation styles occurring for $\alpha\sim30°/45°$, which marks the transition from extension- to strike-slip-dominated deformation (e.g., Withjack and Jamison, 1986; Tron and

53

Brun, 1991; Smith and Durney, 1992; Clifton et al., 2000; Corti et al., 2001). However, the main differences concern some of significant aspects of rifting, particularly (Fig. 3.20):

1)    the patterns of evolution of deformation (diachronous activation of different fault systems in some of the current experiments versus. absence of evolution in previous works, which required a successive change in the direction of extension to obtain the above-documented two-phase rift evolution, e.g., Bonini et al., 1997),

2)    rift architecture (development of distinct rift segments, with major extension-orthogonal fault systems versus. diffuse deformation within the rift, and predominance of oblique-extension fault trends in previous works),

3)    strain partitioning (strong margins/floor partitioning in current work versus absence of significant margins/floor partition in previous experiments).

We attribute these differences to the improvements in rheological layering and boundary conditions of deformation adopted in the current experiments, which make the modeling more similar to natural process of extension of the continental lithosphere. Crustal-scale models were indeed limited by the simplified boundary conditions in terms of application of extensional stresses and rheology. Stresses were in these models applied at the base of the brittle crust through either extension of a viscous layer above a basal velocity discontinuity or a rubber sheet pulled by metal plates; the model rheological layering was simplified by using a single brittle layer (either clay or sand), lying above either a thin viscous layer used to distribute extension or directly above a rubber sheet. Basal application of stresses through a velocity discontinuity may affect the local stress orientation in a dominant way (e.g., Morley, 1999b); the use of a basal rubber sheet may help to avoid this problem, but in both cases the absence of ductile layers and isostatic support provided by the asthenosphere prevent the model to properly respond to the progressive, heterogeneous thinning. The current models tried to overcome these problems by adopting a complex brittle/ductile rheology and an experimental set-up in which the centrifuge forces impose a uniform stress field on the models and the distribution of deformation is controlled by lateral variations in strength and rheology due to the presence of a pervasive weakness zone, a reasonable approximation of the natural process of continental oblique extension (see section 3.3.2.). As in nature, stresses evolve in the models in response to the progressive heterogeneous thinning of the lithosphere. For low to moderate obliquity rifting this results in complex patterns of evolution, architecture and partitioning of deformation illustrated above (two-phase evolution with activation of differently oriented fault systems, development of discrete rift segments with strong partition of deformation between the margins and the rift floor; Fig. 3.20) that, although being different

from previous (crustal-scale) models, are strikingly similar to both numerical models with similar boundary conditions (Van Wijk, 2005; see also van Wijk and Blackman, 2007) and natural examples from continental and oceanic settings (see above; see also Ziegler and Cloetingh, 2004). These results also exactly fits those obtained in oblique rifting models with $\alpha=30°$ and $45°$ and comparable boundary conditions by Corti (2008). For high obliquity rifting, dominance of horizontal over vertical displacement due to the predominant strike-slip deformation limits lithospheric thinning. In this case, the models do not have to respond to substantial changes in layer thicknesses, such that stresses are mainly controlled by the strike-slip displacement of the rift borders and the differences with previous crustal-scale models (in terms of strain evolution and partitioning) are less significant.

### 3.3.2. Oblique reactivation of lithospheric-scale pre-existing weaknesses and implications for natural oblique rifts

The thermo-mechanical process of continental rifting results from the application of extensional stresses to a pre-deformed, and thus already structured, anisotropic lithosphere; as a consequence, rift segments preferentially localise along pre-existing weaknesses (such as ancient orogenic belts or suture zones) avoiding stronger regions (such as cratons; e.g., Dunbar and Sawyer, 1989; Versfelt and Rosendahl, 1989; Morley, 1999a; Tommasi and Vauchez, 2001; Corti et al., 2003; Ziegler and Cloetingh, 2004). Many structural, geophysical and experimental studies have suggested that reactivation of pre-existing structures may strongly influence the way the continental lithosphere respond to extension and play an important role in controlling the evolution and the architecture of rift systems (e.g., Ziegler and Cloetingh, 2004). The current experimental findings support these observations and evidence two end-members behaviors in terms of evolution, pattern and partition of extensional deformation that result from the different orientation of the weakness with respect to the stretching vector, and from the potential of the strength contrast between the weak-strong lithosphere at its boundaries to be reactivated during extension.

In particular, during orthogonal and low to moderate obliquity rifting ($a \leq 45°$), deformation is strongly influenced by the strong rheological contrast at the margins of the weak zone where the velocity discontinuity between the strong and weak lithosphere produces differential thinning between the strong and weak ductile lithosphere and hence induces high shear stresses at the base of the brittle crust (Fig. 3.24). As a consequence, boundary faults develop above the rheological interface once the frictional resistance of the brittle layer is overcome. In orthogonal rifting models, these normal faults are perpendicular to extension, whereas in

low-obliquity models deformation in the upper crust responds both to the far-field extension vector and the local stress reorientation imposed by the obliquity of the weak zone, resulting in en-echelon arranged boundary faults characterized by an oblique slip displacement. The brittle crust within the subsiding rift depression is undeformed during these initial stages of rifting. The thinning of the ductile layers above the uprising asthenosphere occurs by strong outward flow that accumulates shear stresses at the base of the brittle crust below the rift depression (Fig. 3.24). During progressive extension, strain rates locally increase in the centre of the depression as a consequence of concentration of deformation in the ductile layer, a process aided by the pre-defined central increase in thickness of the weak crust; this leads to an increase in shear stresses acting at the base of the brittle crust. Although sedimentation acts to (locally) increase the thickness and strength of the brittle crust, the increasing basal shear stresses eventually overcome the frictional resistance, leading to the rupture of the model brittle crust (Fig. 3.24) (see also Corti, 2008). At this stage, faulting migrates inward with the development of new high-angle normal faults in the rift depression and activity on boundary faults decreases. Since the rift depression is homogenous (no rheological contrasts exist), the internal faults can form orthogonal (or sub-orthogonal) to the regional extension vector, resulting in the successive activation of differently oriented fault systems under constant rift kinematics. The accommodation of deformation by boundary and internal faults testifies a strain partitioning between the rift margins and rift floor, as illustrated in above section 3.3.1.3. Model results predict that, for the adopted boundary conditions, a bulk extension of ~35 km (i.e., ~7 Myr of extension for a velocity of ~5 mm/yr) is needed to activate internal faults in orthogonal and low-obliquity rifting (Fig.3.21a). For obliquity of 45°, boundary fault activity is strongly reduced and a bulk extension of ~20 km (i.e., ~4 Myr of extension) is needed to activate internal faults (Fig.3.21a).

This two-phase evolution is not observed in high-obliquity rifting, where the weak-strong rheological boundary tends to parallelize the extension direction and the extensional component and vertical displacements across it are strongly reduced as the strike-slip component dominate. In these conditions, the weak-strong boundary is no more able to localize extensional deformation and the boundary faults do not form, reducing rift evolution to a single phase in which extensional deformation is accommodated by a complex fault arrangement within the rift floor (Fig. 3.20). The weak zone becomes indeed a distributed zone of wrenching that controls the formation of more continuous oblique to strike-slip faults in the upper crust, with no partitioning between the rift floor and margins (see above sections).
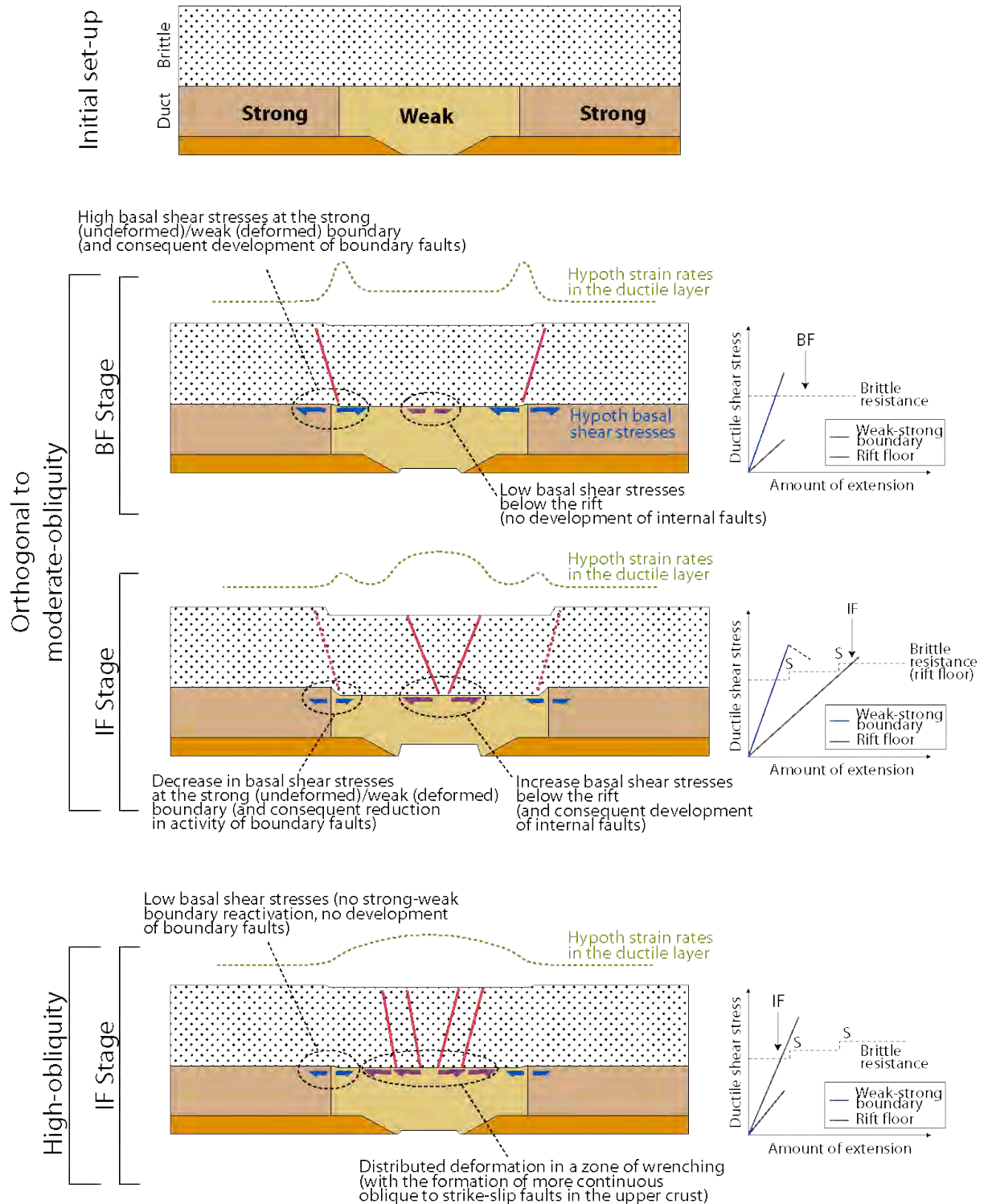
Fig. 3.24: (left) Dynamical explanation for the end-member behaviors of the evolution of extensional deformation based on detailed analysis of model results. Reported in the drawing are the hypothesized strain rates in the ductile layer and the shear stresses acting at the base of the brittle crust in different portions of the model. Variations in local strain rates can be measured by mapping local variations in the thinning factor (see Fig. 3.14): increase in thinning corresponds to increase in local strain rate, and vice-versa; in turn, strain rates are proportional to the shear stresses acting at the base of the brittle crust (e.g., Corti et al., 2004). (right) The hypothesized variations in ductile shear stresses at the strong-weak boundary and below the rift depression responsible for the observed evolution of faulting are reported as a function of bulk extension. BF, development of boundary faults; IF, development of internal faults; S, increase in brittle resistance due to accumulation of synrift sediments. See section 3.3.2. for further details.

57

*3.3.2.1. Assumptions and limitations of the modelling approach*

The setup of the current centrifuge models necessarily imply a simplification of the complexities of the natural process; thus, when applying the model findings to natural oblique rifts some important assumptions related to the experimental approach have to be borne in mind.

The above results are indeed dependent on the model set-up and different starting boundary conditions (e.g., geometry of the weak zone, strength contrast, amount of syn-rift sedimentation, etc.) may influence the evolution of the system. We have tested simpler geometrical boundary conditions (such as a flat Moho in weak area) and the cases of absent or increased syn-rift sediment accumulation and found no major differences in the fault pattern and rift architecture resulting from oblique rifting (see Figure 3.25). We did not test more complex initial geometries of the weak zone (e.g., gradual gradual lateral change in rheology and strength instead of a sharp, vertical rheological boundary) and future experimental work is needed to explore the influence of these parameters on oblique rifting. However, the adopted initial boundary conditions follow a well established approach tested in several previous analogue (e.g., Sokoutis et al., 2007, and references therein)] and numerical (e.g., van Wijk, 2005) models that has been proven to represent a reasonable approximation of the natural continental rifting process and thus able to provide valuable insights into the process of extension in relation to pre-existing weaknesses. The similarity in evolution and rift architecture with different natural examples (see below and Chapter 6) supports that the first-order results in terms of evolution, pattern and partitioning of deformation have general relevance and applicability. Thus, oblique reactivation of pre-existing lithospheric weaknesses may be a major parameter in controlling the characteristics of natural oblique rifts, not only in terms of fault pattern as outlined by previous experiments but also in evolution and strain partitioning. Complex patterns and timings of deformation may result from simple rift (and plate) kinematics, thus complicating the interpretation of geological data from natural oblique rifts as in case of low to moderate obliquity, where the diachronous activation of differently oriented fault systems may result from a constant plate motion, as exemplified below and in Chapter 6.
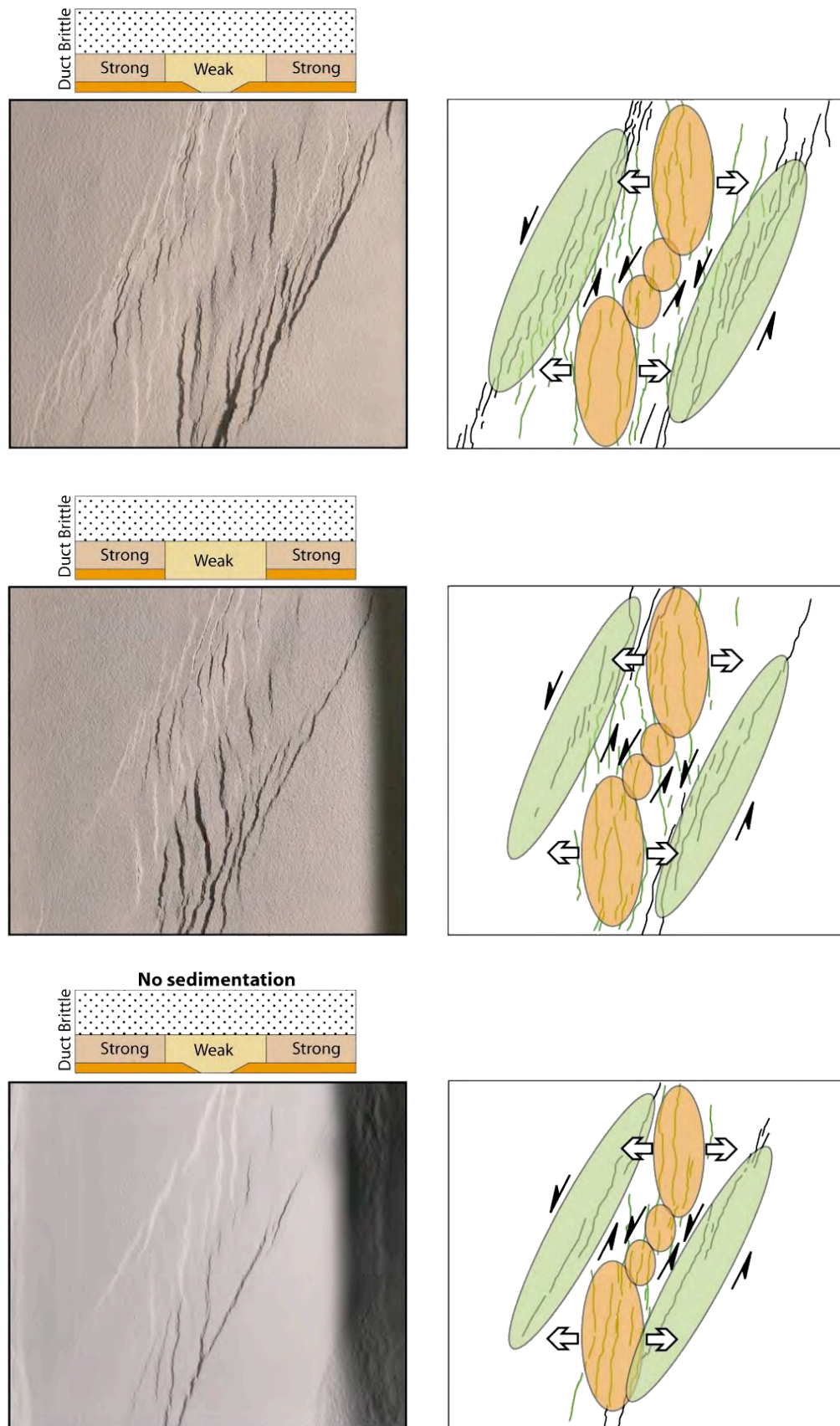
Fig. 3.25: Comparison of low-obliquity models (α=30°) characterized by "standard" boundary conditions (upper panel), flat Moho in the weak area (central panel) and absence of syn-rift sedimentation (lower panel). Experiments show similar rift evolution, fault pattern and general architecture; differences in fault number and width of the deformed zone depend on the slightly different bulk extension adopted in the models.

59

*3.3.2.2. Selected natural examples*

As it will be shown in Chapter 6, many aspects of model evolution are comparable to and provide insights into the architecture and evolution of the Main Ethiopian Rift. Model results are in addiction compared to other rift settings. For instance, the Gulf of Aden has been interpreted as a typical example of oblique rift with moderate obliquity where extension has progressed to continental break-up and creation of an oblique spreading centre within an oceanic basin separating the Arabian and Somalian plates (Fig. 3.26; e.g., Dauteuil et al., 2001). Consistent with the modeling results, thinning during the continental stage of extension has created an en-echelon system of basins within an oblique rift valley (Fig. 3.26); extensional deformation has been accommodated by three distinct fault systems, with orientations 1) sub-perpendicular to the plate divergence, 2) intermediate between the rift axis and normal to the divergence, and 3) parallel to the rift axis (Bellahsen et al., 2006). Similar fault patterns have been observed in the current low to moderate obliquity models (see Figs. 3.15, 3.16), with obliquity values ($30°<\alpha<45°$) matching those resulting from the Arabia-Somalia separation (Bellahsen et al., 2006). Thus, although other additional parameters (e.g., reactivation of discrete fabrics, stress rotation in the latest stages of rifting) may complicate the deformation pattern of the Gulf of Aden region (e.g., Bellahsen et al., 2006), the overall deformation evolution and architecture of lithospheric thinning are strikingly comparable to the current modeling results. Notably, the current modeling results also fit the deformation pattern and partitioning of the resulting oblique spreading centers, where faults inside the axial valley have a sigmoidal shape (with a central part perpendicular to the spreading direction and tips parallel to the walls of the axial valley) and accommodate a pure extension, whereas faults on the valley walls display a right-lateral en-échelon pattern and accommodate a strike-slip component of motion (Dauteuil et al., 2001).

Overall, the model results may have a general relevance for other oblique rifts worldwide (e.g., Gulf of California, Viking Graben in the North Sea), where fault patterns similar to those observed in oblique models have been described (Withjack and Jamison, 1986; Brun and Tron, 1993), and may have experienced similar evolutions of deformation driven by oblique rifting kinematics. Model findings may also be applicable to other oceanic spreading ridges undergoing oblique extension (e.g., Reykjanes and Mohns ridges in the North Atlantic), where patterns of faulting, lithospheric thinning and strain partitioning similar to the current experiments have been described (see Dauteuil and Brun, 1993, 1996; Corti et al., 2001; Clifton and Schlische, 2003; van Wijk and Blackman, 2007).
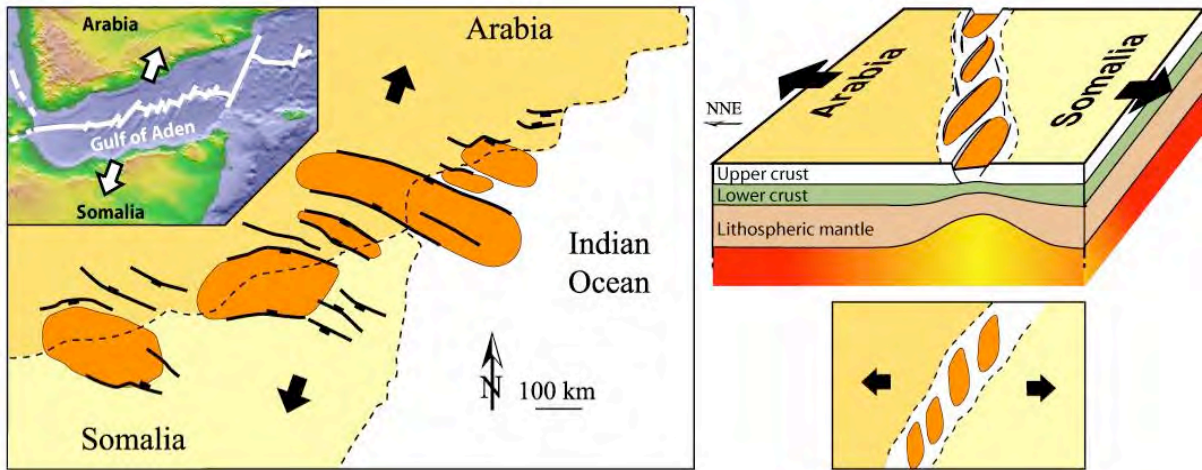
**Fig. 3.26:** Exemplificative natural example of oblique rifting. En-echelon arrangement of Oligocene sedimentary basins in the Gulf of Aden region resulting from a hypothesized oblique continental rifting between Arabia and Somalia plates (modified from Bellahsen et al., 2006). Inset shows the system of oblique spreading centers in the Gulf of Aden. Also shown is the model for the lithospheric evolution resulting from oblique rifting (upper right panel) and a schematic top-view representation of en-echelon basins, rift valley trend and direction of extension, rotated and reflected to fit the set-up of the analogue models presented in this chapter.

# Chapter 4

# Fault analysis from satellite images

In this Chapter, we present a new database of faults affecting the whole MER. Faults were mapped through satellite images analysis (section 4.1). The new database analysis allowed to better define the characteristics and the distribution of the structures affecting the Main Ethiopian Rift (section 4.2).

The results of these analysis are presented and discussed from North to South, referring to the traditional subdivision of the MER in three main rift segments (NMER, CMER and SMER; see Chapter 2 and Fig. 4.1), that differ in terms of rift trend, fault patterns and lithospheric characteristics. Since the southern segment exhibits a more variable orientation, it has been further subdivided into two sub-segments: (1) a northern (SMERn) trending ~N20°E segment and stretching from Lake Awasa up to latitude 06° 04', and (2) a southern sub-segment (SMERs) showing a roughly N05°E trend and reaching southward northernmost sectors of the Kenya Rift (Fig. 4.1). This subdivision results particularly useful in the fault trend analysis (see section 4.2.2.).

## 4.1. Data acquisition and methods

The faults were identified and mapped on a mosaic of 25 ASTER images (displayed as RGB false colour composites with band 3 in the red channel, band 2 in the green channel and band 1 in the blue channel; 15m x 15m lateral resolution, Fig. 4.1) covering the entire area of interest, and on the associated digital elevation models (15m x 15m lateral resolution, extracted from the orthogonal stereoscopic pair of ASTER channels 3N and 3B) (Fig. 4.1).

Fault data acquisition was based on the fault trace detection. Fault traces were identified by the change in pixel opacity and by the characteristic nearly linear shape compared to the other geomorphologic elements (e.g. Soliva and Schultz, 2008). Digital elevation models and slope maps (Fig. 4.2) implemented the interpretation of fault traces, which were drawn at the base of their scarp. Fault traces were approximated with polyline features and digitized in a GIS environment to the UTM projection (zone 37N, datum WGS1984) (Figs. 4.3, 4.4).

The minimum fault length that could be resolved with reliable confidence is ~100m. The mapped fault traces could underestimate the real length of the structures: at the faults tips the vertical throw decreases until it becomes not detectable at the resolution of the images employed in the database realization (e.g. Campbell et al., 2007).

The mapped data were integrated and verified with existing geological data (e.g Kazmin, 1978; Abebe et al., 1999; Le Turdu et al., 1999; Abebe et al., 2005). The reliability of our database was also tested during the three different field surveys in 2007-2009 (see also chapter 5).
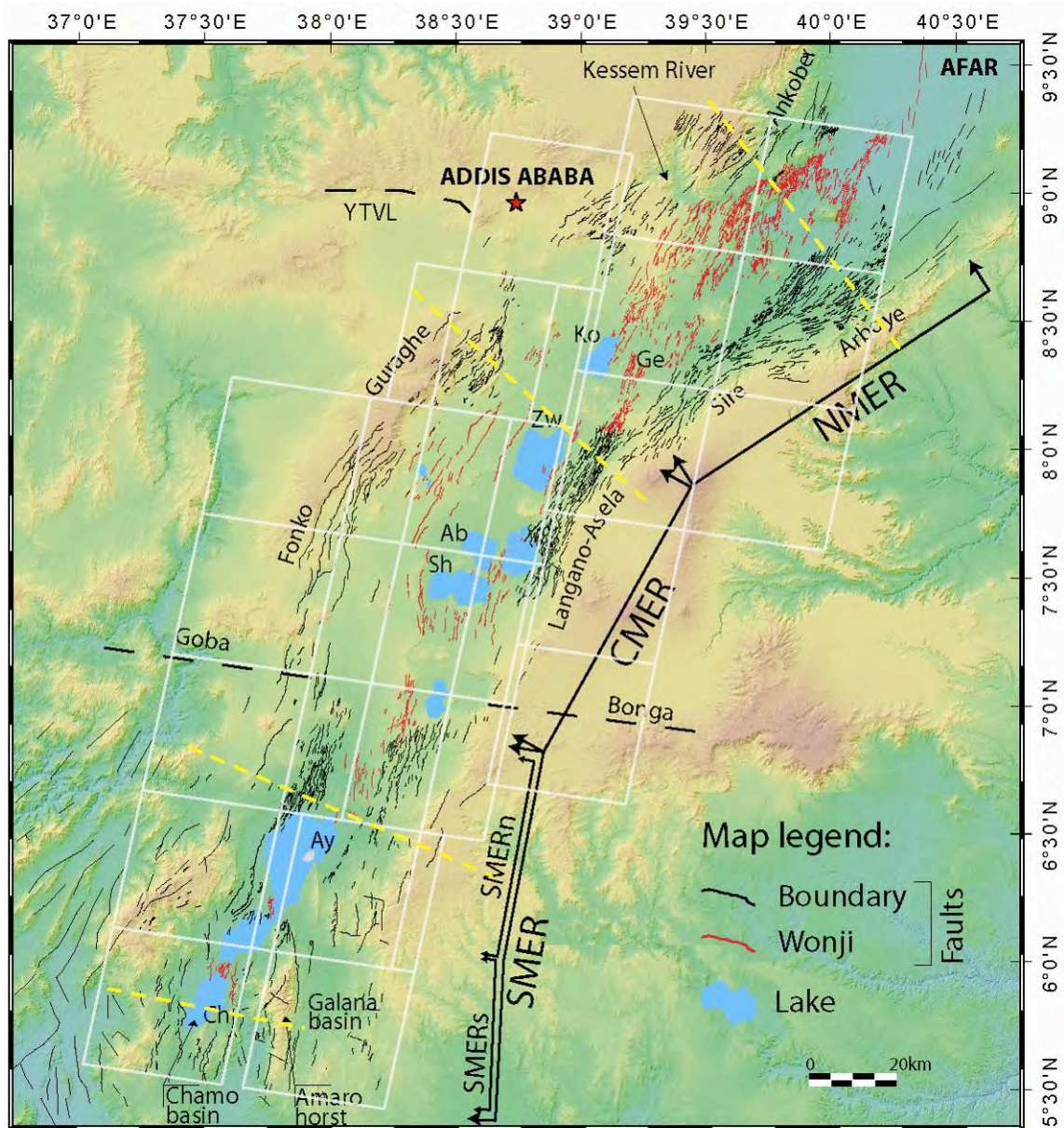


Fig. 4.1: Tectonic sketch map of the Main Ethiopian Rift superimposed to a digital elevation model from SRTM data. Note the classical division in the three segments and the proposed further subdivision of the southern segment in SMERn and SMERs. The pale grey rectangles indicate the ASTER images used in the analysis of MER faulting (see text). Ko: Lake Koka; Ge: Gedemsa Caldera; Zw: Lake Ziway; Ln: Lake Langano; Ab: Lake Abyata; Sh: Lake Shala; Aw: Lake Awasa; Ay: Lake Abaya; Ch: Lake Chamo. YTVL: Yerer-Tullu Wellel volcano-tectonic lineament.
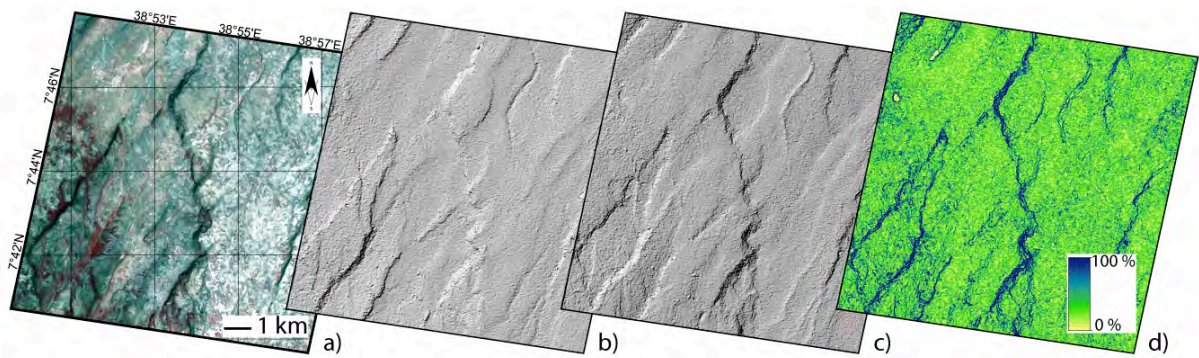
Fig. 4.2: Example of ASTER satellite image and elaborations employed for the creation of the new fault dataset. a) RGB false colour composites with band 3 in the red channel, band 2 in the green channel and band 1 in the blue channel. b) Hillshade image with sun elevation 45° and sun azimuth 315°. c) Hillshade image with sun elevation 45° and sun azimuth 135°. d) Slope map, the legend in the small inset shows the slope percentage. Slope maps were calculated for each cell as the maximum rate of change in elevation over each cell and its eight neighbours in a raster digital elevation model.
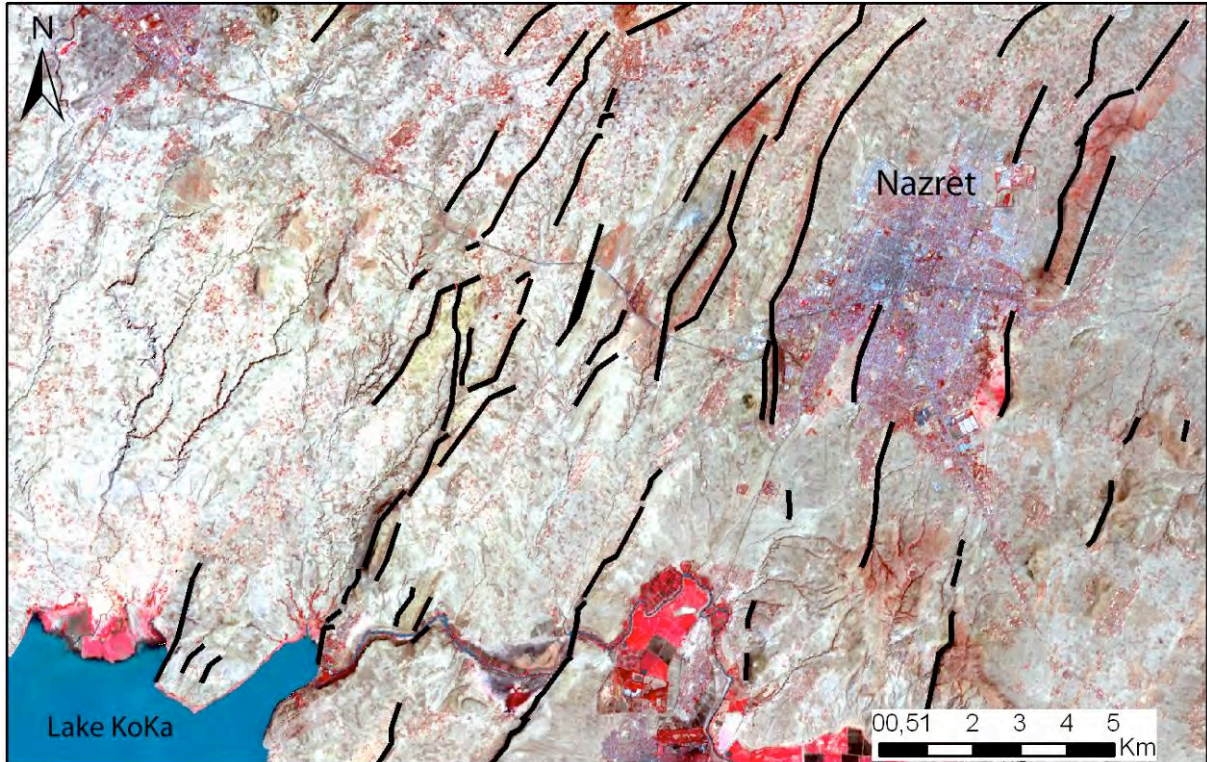


Fig. 4.3: Example of mapped faults superimposed on an ASTER composit 321 (area between Lake Koka and the Nazret town).
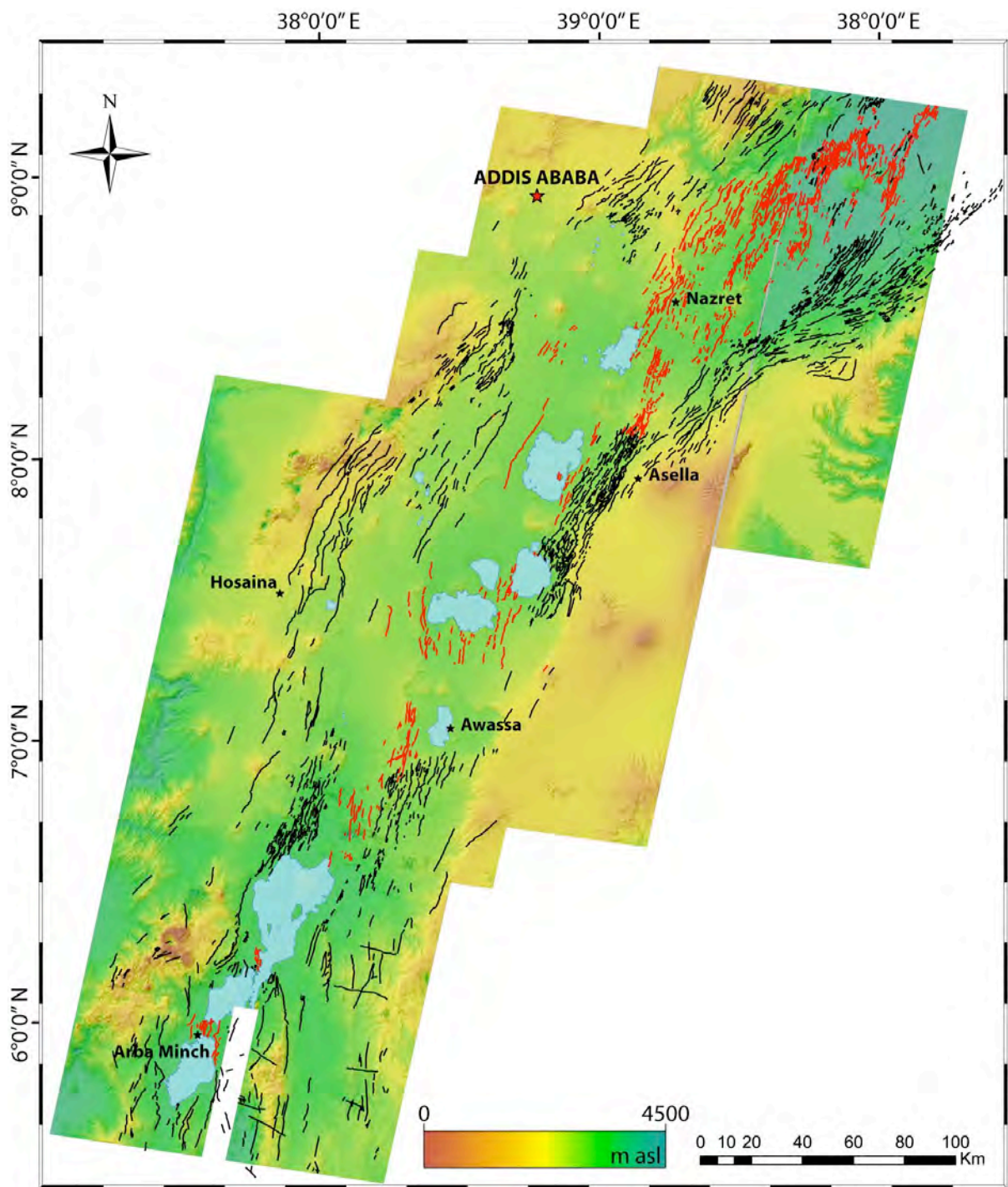
Fig. 4.4: New structural database presented in this thesis work, superimposed onto a digital elevation model, built as a mosaic of the 25 ASTER images used in this analysis. Black lines are the border faults, red lines are the internal WFB faults. As the quality of the ASTER images was not always good (i.e. some areas were covered by clouds) and they do not cover the NE corner of study area (i.e. the), we integrated the ASTER images with images obtained from Google Earth and Landast7 satellite images (http://glcfapp.umiacs.umd.edu:8080/esdi/index.jsp).

Curved faults were carefully processed: when the length ratio between the two arms of a curved feature was ~1 and the angle between them yielded a significant change in strike (>25°), the tip-to-tip line was considered not representative of the azimuth direction of the whole structure. In this case the curved features were segmented into two different lines, in correspondence of the interception of the two arms, where the fault trace present the minimum radius of curvature (see for instance Campbell et al. 2007) (Fig. 4.5b). Fault traces shorter than 2 km were not segmented but the tip-to-tip line was considered (Fig. 4.5a).
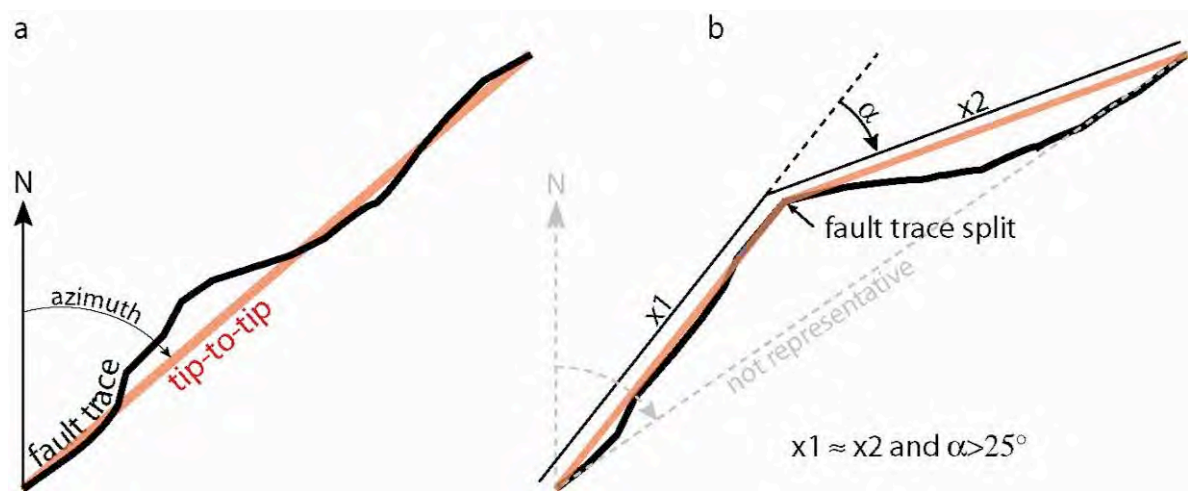


Fig. 4.5: a) Definition of a tip-to-tip line from a fault trace. b) Segmentation of a curved fault trace by splitting it at the minimum radius point.

The tip-to-tip azimuths data were weighted for the length of the corresponding fault: the weighting factor for each fault was the ratio between its length and the minimum fault length in the whole data set (i.e. ~100m), such that long faults have higher ratios than short ones. The frequency of the azimuth of a tip-to-tip fault directly relates to this ratio, the longer the fault the higher its frequency (e,g., Mazzarini and D'Orazio, 2003). The azimuth data were plotted on 0°-180° histograms at 5° intervals (Fig. 4.7). All the graphs were constructed using the same weighting factor (i.e. fault length), so that the statistical weight of each orientation interval (i.e. the height of each histogram column) is easily comparable with those of the other graphs.

## 4.2. Results of the statistical fault analysis

The remote sensing analysis allowed recording 3312 structures (Table 4.1), spanning almost three orders of magnitude in length, from ~100m to the 75km of the Fonko fault, on the western border of the Central MER (Fig. 4.1).

Faults were distinguished in internal and border faults according to their position with respect to the rift depression.

The analysis of the entire fault dataset shows that border faults are, on the whole, higher in number and longer in average than internal faults (border 2.25 km, internal 1.38 km), whereas average spacing is similar in both cases (about 1000 m, Table 4.1).

These statistical analyses of faults were carried out in each segment composing the Main Ethiopian Rift. The results are summarized in Table 4.1 and discussed from North to South. It will be first considered the number and length of faults, and then their azimuth.

Faults lengths and fault spacing always follow a log-normal distribution, both for the complete database (all the MER faults) and the faults of the different MER segments, as usual for spacing and length of faults and fractures (e.g Priest et Hudson, 1981; Gillespie et al., 1993, 2001; Bonnet et al., 2001). The internal and border fault subsets are also described by a log-normal distribution. To statistically represent our data we thus used the geometric mean, which is the central tendency to be used for a population described by a log-normal distribution.

### 4.2.1. Fault number and length

In the NMER, the internal WFB faults, well organized in en-echelon segments, result higher in number than the border faults (the border faults/internal faults ratio is 0.57). The border faults consist of long and spaced en-echelon structures (length 1.80 km on average, maximum length ~25 km, average spacing 1035 m), whereas the internal faults are shorter (length 1.26 km on average, and a maximum length ~15km) and more closely spaced (955 m on average). We have to note that the NMER border faults, particularly those on the western border in the Kessem River basin and those on the eastern border (Arboye border fault; Fig. 4.1), do not show a clear morphological expression.

In the CMER and SMER, the border faults/internal faults ratio shows high values (4.35 and 5.26, respectively) thus manifesting the clear predominance of the border faults over the internal ones. These latter are en-echelon arranged as in the NMER, but they are longer (2.56

km and 2.64 km in the CMER and in the SMER, respectively) and more spaced (1200 m and 1260 m in the CMER and SMER, respectively) compared with the northern segment (Table 5.1). Average length and spacing values for the internal faults in the CMER and SMER cannot be provided, because their number is too limited for a meaningful statistical analysis.

Qualitatively, the internal faults in the SMER segments appear as short structures (only a few faults are longer than 10 km) with small vertical separation (e.g. Boccaletti et al., 1998), resulting individually similar to those in the NMER. Nevertheless, the en-echelon arrangement of the NMER internal faults is not clearly detectable in the CMER and SMER, where internal faults are concentrated mainly near the margins of the rift depression, and only a few faults affect the centre of the rift valley.

Overall, a decreasing trend of the borders faults length from the NMER southward, and a strong along axis variation of the relative importance (in number) of internal and border faults can be highlighted. This in turn reflects a different distribution of brittle deformation, respect to the orthogonal to the rift axis, across the rift: in the NMER faulting affects primarily the rift depression with the well developed WFB, while in the CMER and SMER the deformation is concentrated on the rift margins (Fig. 4.6).

| | TOTAL | | | | Border Faults | | | | | Internal Faults | | | | | Bord/Int |
|---|---|---|---|---|---|---|---|---|---|---|---|---|---|---|---|
| Data Set | N | L km | Sp m | Orient. | N | L km | MaxL km | Sp m | Orient. (m. peak) | N | L km | MaxL km | Sp m | Orient. (m. peak) | |
| MER | 3312 | 1.80 | 920 | - | 1784 | 2.25 | ~75 | 1025 | - | 1545 | 1.38 | ~15 | 1000 | | 1.15 |
| N MER | 1980 | 1.43 | 925 | ~N45° | 716 | 1.80 | ~25 | 1035 | 35°-40° | 1254 | 1.26 | ~15 | 955 | 20°-25° | 0.57 |
| C MER | 700 | 2.44 | 1230 | ~N30° | 570 | 2.56 | ~75 | 1200 | 25°-30° | 130 | - | ~15 | - | 10°-15° | 4.38 |
| S MER | 632 | 2.62 | 1250 | N0°-15° | 530 | 2.64 | ~30 | 1260 | 25°-20° | 102 | - | ~13 | - | 15°-5° | 5.26 |

Table 4.1: Statistic of the Main Ethiopian Rift faults. N: number; L: length; Sp: spacing. Orient: orientation (referred to the main peak orientation of the histograms in Figure 4.7); Bord/Int: border versus internal faults number ratio. Faults spacing was analyzed calculating the minimum distance between each faults and the remaining ones; the average value is considered as a good proxy for the fault spacing (Mazzarini and D'Orazio, 2003). Given the limited number of data (i.e. <200, see Bonnet et al., 2001 for a complete treatment of this argument), in this analysis the SMER data were considered on the whole and not split in the two sub segments (SMERn and SMERs).
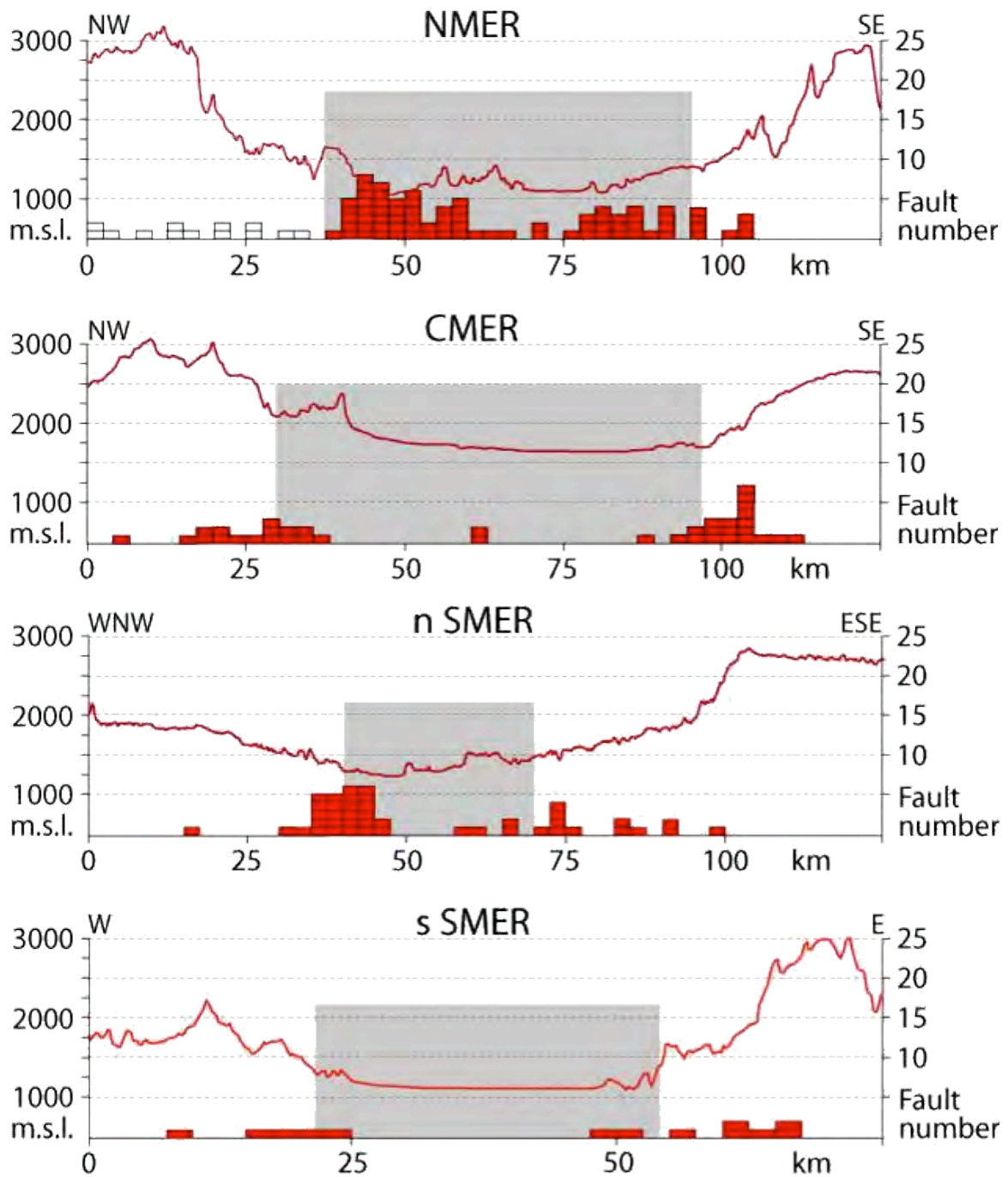
Fig. 4.6: Distribution of deformation in the different MER segments with respect to the orthogonal to the rift axis, illustrated along four topographic profiles (profile traces are the yellow dotted lines in Fig. 4.1). Each fault that lies over a 2.5 km wide belt over the profile trace is projected onto the profiles and indicated with a red rectangle. White rectangles in the NMER profile indicate the eroded border faults in the Kessem River area (Fig. 4.1, see text for details). The pale grey area indicates the width of the rift depression. The faults affecting the valley floor in the CMER, SMERn and SMERs are mainly related to the marginal grabens and can not be considered as WFB faults.

4.2.2. Fault azimuth

Fault trace orientations were analyzed in term of azimuthal distribution in the different rift segments (Fig. 4.7); the results are presented on 0°-180° histograms at 5° intervals for each MER segments individually, and further subdivided by reference to internal and border faults (Fig. 4.7).

In the roughly NE-SW trending NMER, the total fault azimuth histogram shows a main orientation peak (i.e. higher statistical weight) trending between N20° and N25° (Fig. 4.7). This peak corresponds to the orientation of the WFB internal faults. Border faults are instead characterized by a main orientation peak at ~N40°, slightly oblique to the rift trend (Fig. 4.7).

The ~N30° trending CMER segments shows a main orientation peak varying between N25° and 30°, which essentially corresponds to the border faults orientation. As in the NMER, the border faults are slightly oblique to the rift trend. The WFB faults in the CMER, although less expressed than in the NMER (see above), exhibit an orientation histogram characterized by a main peak between N10° and N15°.

The analysis of the fault distribution in the SMER was performed considering the further subdivision into the ~N20°E trending SMERn and the ~N05°E trending SMERs. In the SMERn, border faults orientation shows a main peak varying between N20° and N25°, whereas in the southernmost zone (SMERs) the border faults peak trends ~N10°-15° (Fig. 4.7). In both sub-segments, the internal faults peak is oriented ~N10°-15°, although their importance results marginal (see above section 3.2.1) A minor secondary orientation peak trending between N100° and N105° can be detected in the SMERs histogram (Fig. 4.7).
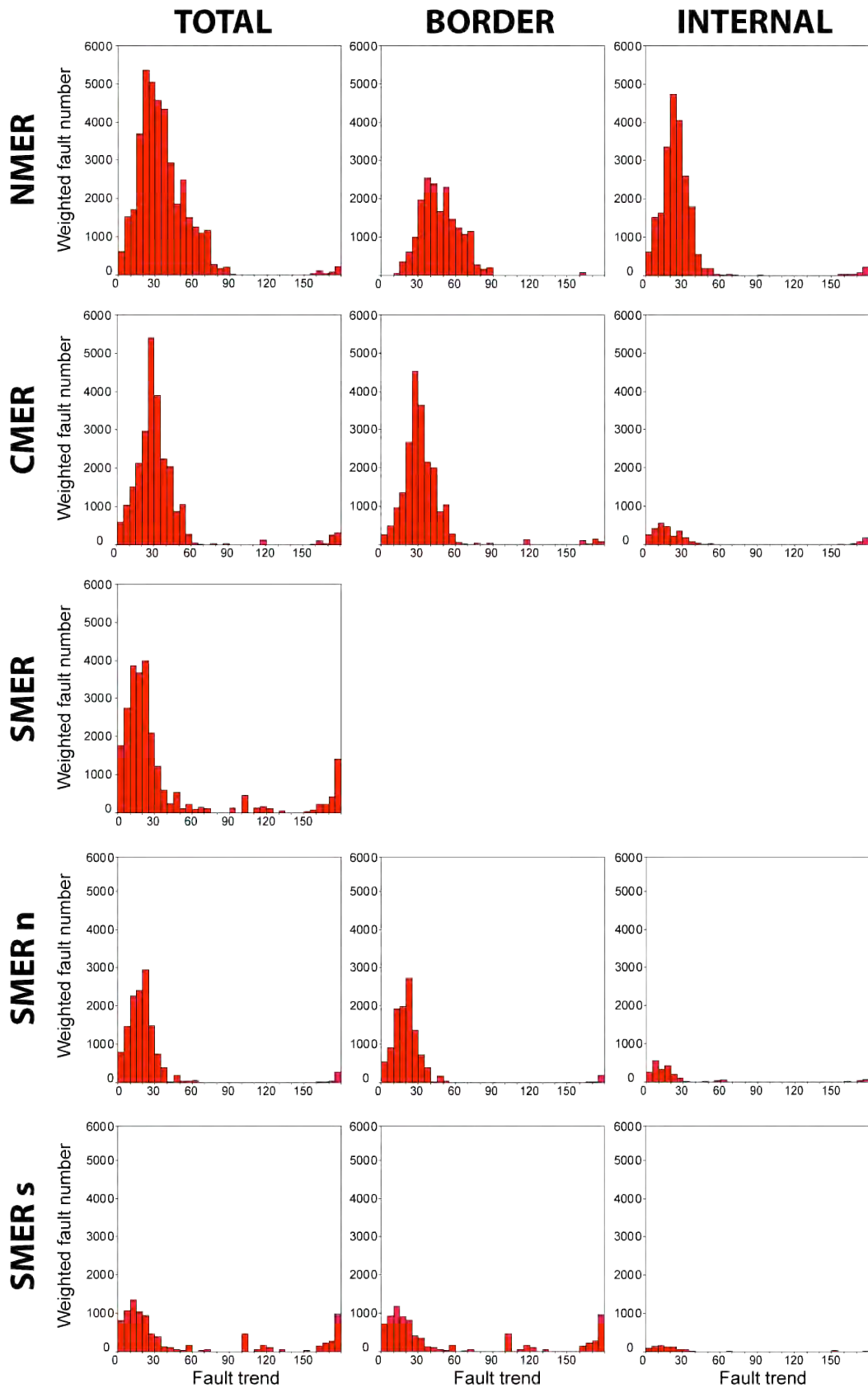
Fig. 4.7: Weighted fault distribution of the MER faults illustrated as histograms of faults trend. The histograms in the left column show the distribution trend of all the faults affecting each MER segment; panels in the central and right columns display the distribution trend of border and internal faults respectively. As all the graphs were constructed using the same weighting factor (see text), the height of each histogram column is directly comparable with those of the other graphs. Note that the subdivision of the Southern MER into two distinct sectors (SMERn and SMERs) help to better localize to main fault peaks.

The analysis of the fault azimuth distribution in the different MER segments histograms (Fig. 4.7) reveals that the angle between internal and border faults decreases from the NMER (~20°) southward (~15° in CMER and SMERn), reaching a semi-parallelism between the two fault systems in the southernmost MER segment (Figs. 4.7, 4.8). Similarly, the total span of fault orientations (i.e the azimuth dispersion) is again maximum in the NMER and decreases southward (Figs. 4.7, 4.8), as testified by the decreasing trend of the standard deviation value of the weighted fault azimuth distributions (Table 4.2).
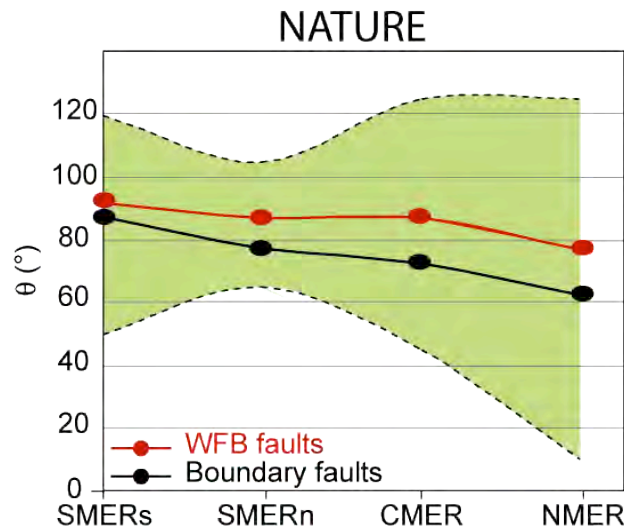


Fig. 4.8: Fault orientation displayed by the angle θ, , i.e. the angle between the orientation of each fault system (defined on the basis of the peaks in the histograms of fault orientation, Fig. 4.7) and the average N100°E-trending direction of extension (see section 2.2) (see Tron and Brun, 1991). The yellowish area enclosed between dotted lines represents the total span of fault orientations displayed on histograms. Note that the faults related to the secondary orientation peak (N100°-N105°) in the SMERs were not considered in this elaboration.

| | azimuth dev. stand. |
|---|---|
| **NMER** | 18.20 |
| **CMER** | 15.39 |
| **SMERn** | 10.57 |
| **SMERs** | 16.02 |

Table 4.2: Standard deviation of the weighted fault azimuth distribution (whole dataset) in the different MER segments.

Nevertheless, it must be noted that the SMERs total span of fault orientation does not follow the north to south decreasing trend, but it shows a wider azimuth range than the SMERn segment (see Table 4.2 and Fig. 4.8). This is probably related to the exposure of extremely folded and foliated pre-Cambrian basement rocks in these southernmost sectors of the MER.

Structures related to these rocks may have been mapped during the satellite images analyses and may have locally controlled the fault geometry, giving rise to the observed dispersion of the fault azimuth in the SMERs. Moreover it must be considered that the SMER the actual extensional deformation is superimposed onto previous extensional structures, possibly related to a northward propagation of the Kenya Rift, which developed at about 20-21 Ma and lasted up to ~11Ma (Bonini et al., 2005). The presence of these pre-existing structures may concur in the dispersion of azimuths.

Finally, a secondary peak, trending between 100° and 105°, is recognizable in the orientation histogram of the SMREs (Fig. 4.7). Again, this peak can be probably referred to pre-rift structures with orientation comparables to the roughly E-W inherited structural trends to the North. These has been related to an early deformation phase characterized by a NNE-SSW trending extension, derived from a south propagation of the extensional regime affecting the Afro-Arabian boundary during Oligocene times (Abbate and Sagri, 1980; Abebe et al., 1998; Bonini et al., 2005), such as the Yerer-Tulu Wellel (Abebe et al, 1998) and the Goba-Bonga volcanotectonic lineaments (Bonini et al., 2005.)(Fig. 4.1).

# Chapter 5
# Field structural data

Three field surveys in the Main Ethiopian Rift (2007-2009) were planned in order to verify the results of the remote sensing analysis (see Chapter 4), better characterize the kinematics of the rift-related fault systems (i.e. border and WFB faults) and find evidences of Quaternary activity along the MER structures. Data from a 1997 field survey (Bonini et al., 2005) were also included in the dataset of measures collected during the 2007 and 2009 field survey.

All the main MER segments were investigated. Nevertheless the field work concentrated on the CMER, where the previously collected data were sparse (e.g. Woldegabriel et al., 1990; Acocella and Korme, 2002; Bonini et al., 2005; Pizzi et al., 2006; Corti, 2009). Similarly, also for the SMER we have only a few data at disposal in literature (e.g. Ebinger et al., 1993; Boccaletti et al., 1998; Acocella and Korme, 2002; Bonini et a., 2005). In this area, the faults do not show an excellent morphological expression that thus makes finding suitable sites and collecting data difficult. On the contrary, the data collection in the NMER, especially on the western margin (e.g. Wolfenden et al., 2004, 2005), are abundant and of excellent quality. We thus concentrated our work on the eastern margin of the NMER, at the transition with the CMER.

## 5.1. Data collection and analysis method

The fieldwork focused on both the main border fault systems of both margins and the faults composing the Wonji Fault Belt, which mostly affects the rift floor. The morphological expression of the two faults systems is very different, especially in term of length (see Chapter 4) and vertical throw: the border faults are long and usually display a large vertical offset, whereas the WFB faults are normally shorter and display a relative small throw (Fig. 5.1). To evaluate the kinematics of the different faults systems, the local paleostress field orientations have been determined in suitable sites of measurement on both fault systems. Kinematic indicators on faults surface (i.e. fault slip data) were measured in order to establish the orientation of the stress axis for each observation site. Data were colleted in more than 60 structural sites; data collected on the same structure during the different field surveys were grouped and the measures elaborated firstly separated and then together, such the number decreases to 53 single structural stations (Fig. 5.2). Kinematic indicator quality was normally good, at place excellent. Nevertheless in some cases the structures are not completely reliable (red lines in Table 5.1). On the whole, the quality resulted dependent on the lithology of the

outcropping fault plane. Strongly welded ignimbrites and basalts are often (but not always) not favourable lithologies for recording and preserve striations on fault plane. Moreover, these lithologies are often affected by well organized columnar joint sets that confer a polygonal appearance to the rock volume and a saw-toothed shape to the fault plane: data are thus collected on secondary planes forming rocks columns, and these latter may result tilted, further decreasing the reliability of the  kinematics indicators. The best data are collected on softer rocks (e.g. poorly welded ignimbrites and tuffs), sediments and fault breccia shear planes (see below) which develop continuous fault planes and clear kinematic indicators. Obviously, ashes and loose sediments do not represent favourable lithologies for recording slip data.
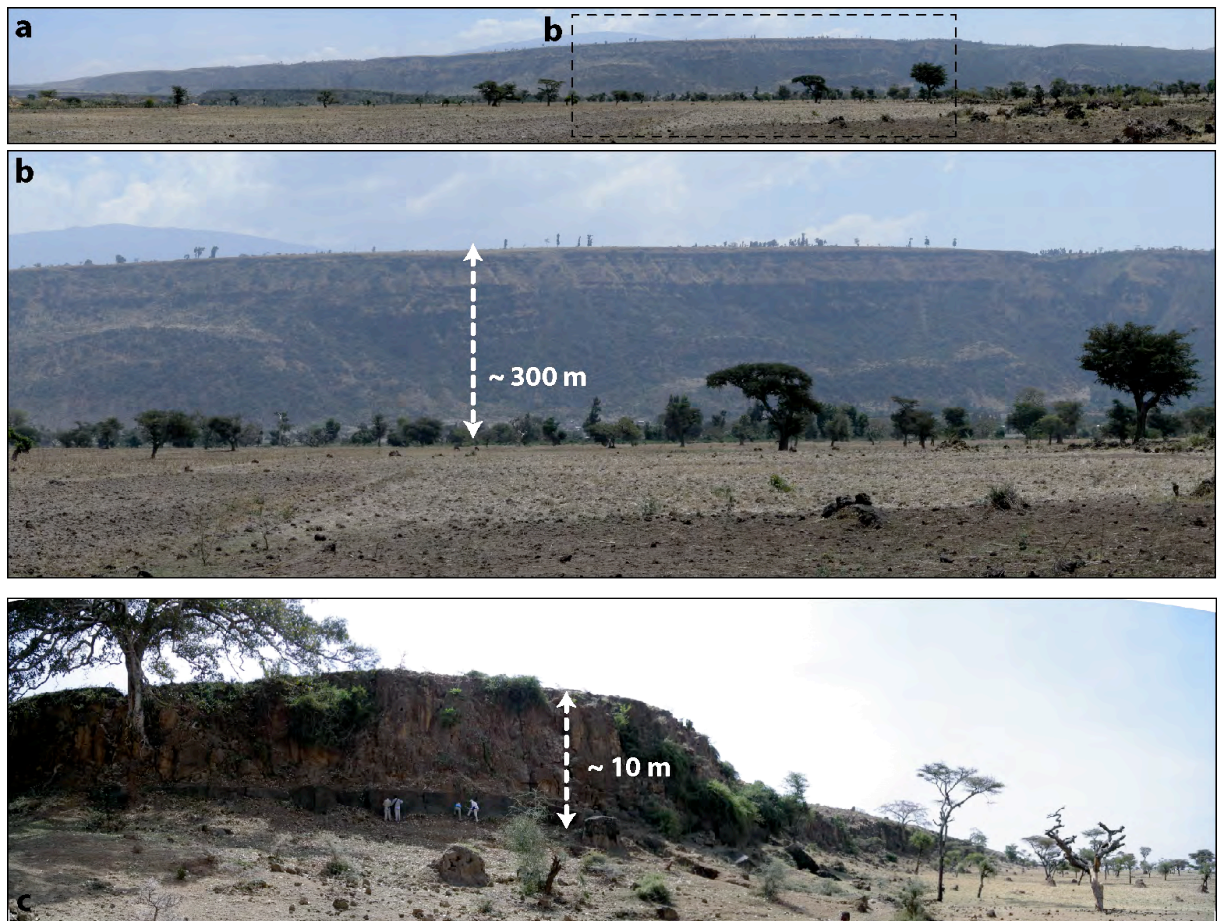


Fig. 5.1: a) Photo of the Asela border fault. Note the persistence and the large vertical throw (indicated in the close-up of panel b). c) Photo of a WFB fault near Lake Ziway showing the limited vertical offset (modified after Corti, 2009).

Kinematics indicators on fault surfaces were measured in order to establish the local orientation of stress axes for each structural site by using three different inversion methods: the dihedron area (Angelier and Mercheler, 1977; Angelier, 1979), the P&T axes method (Caputo and Caputo, 1988) and the Carey (1979) methods (this latter method was not

employed with less than 4 fault slip data). The obtained stress axis orientations are shown in Table 5.1. For the minimum stress axes $\sigma_3$ (i.e. the extension direction), we computed the average trend value of the different orientations obtained with the above methods. The trends of the computed $\sigma_3$ axes are reported (black arrows) on the stereonets showing the fault slip data (Figs. 5.4, 5.6 and 5.8).

A large part of the fieldwork focused on the characterization of geological and morphological evidence of Late Quaternary activity of the MER structures. We thus focused our attention on situations where faults affected Quaternary rocks, debris and deposits, especially on the rift borders, as well as the morphological indications of recent tectonic activity, such the freshness of the fault scarps and alluvial cones cut or deformed.

The results of our fieldworks are illustrated in the following sections. Firstly, the local paleostress field orientations determined by the fault slip data inversion are described (the complete database is displayed in Table 5.1). Then, we focus on the description of the different MER fault systems, stressing out the differences and the evidences of Quaternary activity. Situations of particular interest have been illustrated in detail, also with the help of local geological sections. Finally, the fault slip data were plotted onto two transects across the whole MER to better illustrate the variations throughout the rift margins and the valley floor.

The results are presented from North to South to highlight differences and analogies found among the main MER segments. Emphasis will be given to the evidence of Quaternary activity. Dating of magmatic and unconsolidated rocks (i.e. colluvium) affected by the faults, is still mostly in progress.
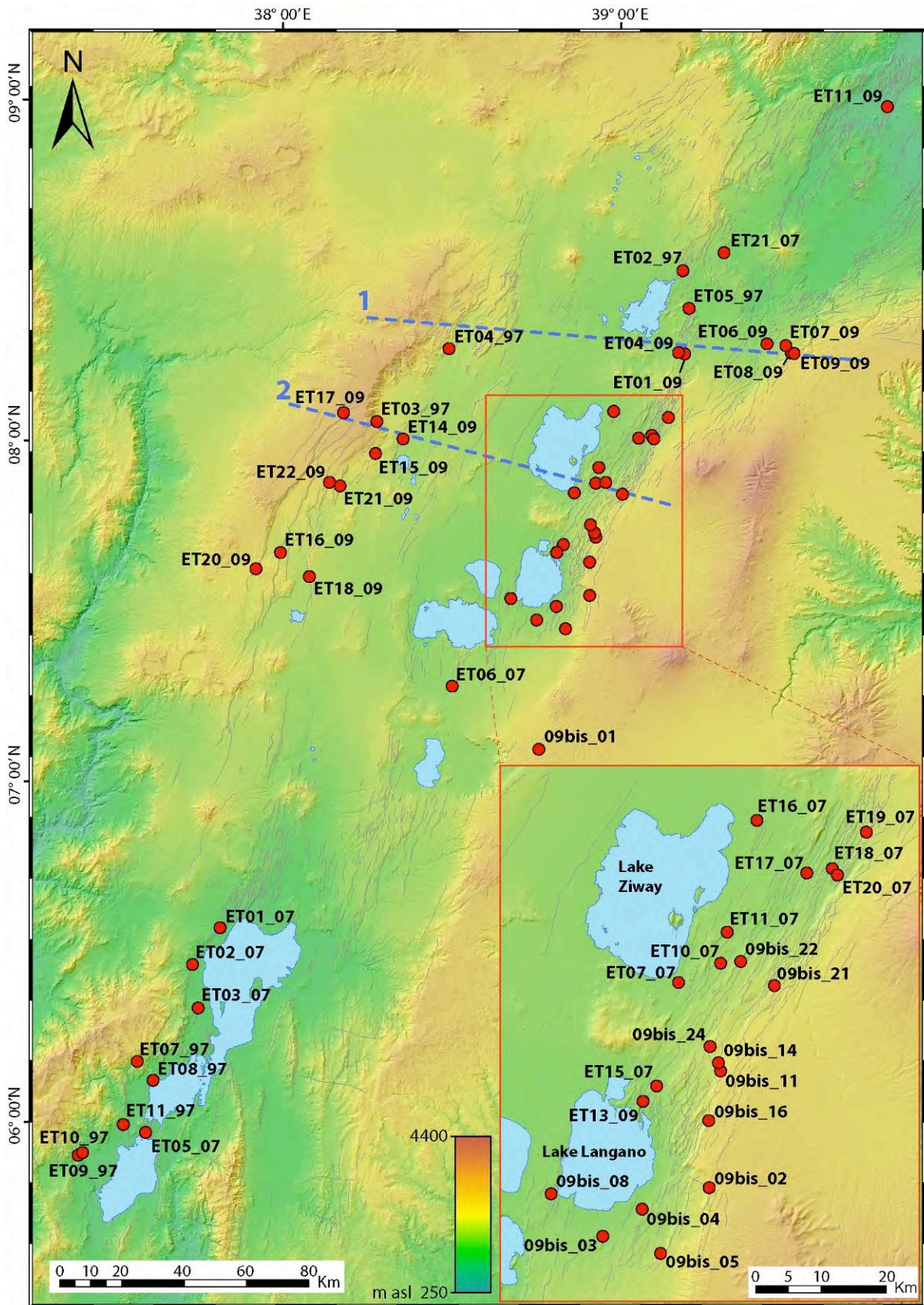
Fig. 5.2: Digital Elevation Model of the study area. Red circles indicate the sites of structural measurement. Each point corresponds to a stereo plot (see following sections) with the fault planes collected at the site. Labels indicate the name of the structural station (see Table 5.1): ETXX_97 indicates data collected during the 1997 field survey (Bonini et al., 2005); ETXX_07 during the 2007 field survey, ETXX_09 and 09bis_XX data collected during two field surveys in 2009. Blue dotted lines are the traces of the two transects (Figs. 5.9, 5.12).

| station | n° data | Angelier & Mecheler method | | | | | | P&T axes method | | | | | | Carey method | | | | | | average σ3 | |
|---|---|---|---|---|---|---|---|---|---|---|---|---|---|---|---|---|---|---|---|---|---|
| | | σ1 | | σ2 | | σ3 | | σ1 | | σ2 | | σ3 | | σ1 | | σ2 | | σ3 | | | |
| | | dip dir. | dip | dip dir. | dip | dip dir. | dip | dip dir. | dip | dip dir. | dip | dip dir. | dip | dip dir. | dip | dip dir. | dip | dip dir. | dip | dip dir. | dip |
| ET02_97 | 10 | 318 | 85 | 181 | 6 | 90 | 5 | - | - | - | - | - | - | 359 | 82 | 166 | 7 | 256 | 2 | 85 | 3 |
| ET03_97 | 7 | 65 | 80 | 196 | 6 | 287 | 7 | 116 | 78 | 18 | 1 | 287 | 12 | 116 | 74 | 216 | 3 | 307 | 15 | 113 | 11 |
| ET04_97 | 10 | 1 | 86 | 230 | 2 | 140 | 3 | 290 | 78 | 196 | 1 | 106 | 12 | 82 | 78 | 236 | 10 | 327 | 5 | 131 | 3 |
| ET05_97 | 7 | 278 | 56 | 187 | 1 | 96 | 34 | - | - | - | - | - | - | 247 | 45 | 344 | 7 | 81 | 43 | 89 | 38 |
| ET07_97 | 7 | 298 | 56 | 84 | 29 | 183 | 16 | 291 | 57 | 67 | 25 | 167 | 20 | 95 | 76 | 287 | 13 | 196 | 3 | 182 | 13 |
| ET08_97 | 13 | 159 | 86 | 46 | 1 | 315 | 3 | 240 | 80 | 28 | 8 | 118 | 5 | 177 | 83 | 61 | 3 | 330 | 7 | 138 | 7 |
| ET09_97 | 11 | 353 | 83 | 128 | 5 | 219 | 5 | 30 | 78 | 182 | 12 | 273 | 6 | 353 | 78 | 136 | 9 | 227 | 7 | 209 | 8 |
| ET10_97 | 8 | 245 | 62 | 29 | 23 | 126 | 15 | 268 | 68 | 43 | 16 | 138 | 15 | 242 | 57 | 34 | 30 | 131 | 13 | 132 | 14 |
| ET11_97 | 7 | 190 | 66 | 353 | 23 | 86 | 6 | 197 | 83 | 7 | 7 | 98 | 1 | 218 | 86 | 8 | 4 | 98 | 2 | 94 | 3 |
| ET01_07 | 3 | 246 | 7 | 100 | 81 | 337 | 5 | 115 | 47 | 226 | 18 | 330 | 37 | - | - | - | - | - | - | 154 | 21 |
| ET02_07 | 4 | 91 | 22 | 230 | 61 | 354 | 17 | 129 | 46 | 248 | 25 | 356 | 33 | 223 | 72 | 102 | 10 | 9 | 15 | 0 | 22 |
| ET03_07 | 11 | 277 | 68 | 115 | 22 | 22 | 6 | 276 | 67 | 163 | 10 | 69 | 21 | 262 | 34 | 164 | 11 | 59 | 53 | 48 | 28 |
| ET05_07 | 4 | 87 | 30 | 262 | 60 | 356 | 2 | 90 | 30 | 276 | 60 | 180 | 1 | 108 | 44 | 238 | 33 | 348 | 27 | 164 | 30 |
| ET06_07 | 8 | 118 | 60 | 11 | 10 | 276 | 28 | 123 | 54 | 14 | 10 | 346 | 9 | 85 | 44 | 276 | 32 | 247 | 44 | 88 | 35 |
| ET07_07 | 6 | 340 | 51 | 208 | 29 | 104 | 24 | 336 | 51 | 219 | 20 | 116 | 32 | 2 | 25 | 253 | 35 | 119 | 44 | 112 | 33 |
| ET09_07 | 8 | 274 | 67 | 21 | 7 | 114 | 22 | 272 | 66 | 22 | 9 | 116 | 22 | 253 | 44 | 360 | 17 | 105 | 41 | 112 | 28 |
| ET10_07 | 8 | 323 | 56 | 220 | 8 | 124 | 32 | 338 | 55 | 230 | 12 | 132 | 32 | 350 | 43 | 241 | 19 | 133 | 41 | 129 | 35 |
| ET11_07 | 4 | 331 | 51 | 225 | 13 | 124 | 36 | 325 | 52 | 228 | 5 | 134 | 38 | 334 | 74 | 216 | 8 | 124 | 14 | 127 | 30 |
| ET15_07 | 6 | 48 | 82 | 243 | 7 | 152 | 2 | 305 | 48 | 48 | 11 | 147 | 40 | 244 | 76 | 54 | 14 | 145 | 2 | 148 | 14 |
| ET16_07 | 3 | 180 | 17 | 62 | 56 | 280 | 28 | 128 | 58 | 20 | 11 | 283 | 29 | - | - | - | - | - | - | 101 | 28 |
| ET17_07 | 3 | 88 | 54 | 237 | 32 | 337 | 15 | 88 | 56 | 210 | 20 | 310 | 27 | - | - | - | - | - | - | 144 | 21 |
| ET18_07 | 5 | 53 | 3 | 308 | 78 | 144 | 11 | 267 | 60 | 18 | 12 | 114 | 27 | 199 | 75 | 28 | 15 | 297 | 2 | 125 | 13 |
| ET19_07 | 6 | 172 | 34 | 48 | 40 | 286 | 32 | 128 | 57 | 22 | 10 | 286 | 32 | 164 | 45 | 62 | 12 | 321 | 43 | 116 | 36 |
| ET20_07 | 8 | 102 | 74 | 244 | 13 | 336 | 10 | 109 | 68 | 214 | 6 | 306 | 21 | 103 | 58 | 194 | 1 | 285 | 32 | 130 | 22 |
| ET21_07 | 4 | 316 | 60 | 170 | 25 | 74 | 15 | 330 | 57 | 186 | 27 | 87 | 16 | 5 | 72 | 178 | 78 | 269 | 2 | 83 | 11 |

Table 5.1 - continues

| station | n° data | Angelier & Mecheler method | | | | | | P&T axes method | | | | | | Carey method | | | | | | average | |
|---|---|---|---|---|---|---|---|---|---|---|---|---|---|---|---|---|---|---|---|---|---|
| | | σ1 | | σ2 | | σ3 | | σ1 | | σ2 | | σ3 | | σ1 | | σ2 | | σ3 | | σ3 | |
| | | dip dir. | dip | dip dir. | dip | dip dir. | dip | dip dir. | dip | dip dir. | dip | dip dir. | dip | dip dir. | dip | dip dir. | dip | dip dir. | dip | dip dir. | dip |
| ET01_09 | 3 | 183 | 11 | 67 | 66 | 277 | 21 | 118 | 68 | 12 | 62 | 280 | 21 | - | - | - | - | - | - | 98 | 21 |
| ET04_09 | 5 | 119 | 62 | 10 | 10 | 275 | 26 | 116 | 64 | 9 | 8 | 275 | 25 | 145 | 53 | 34 | 15 | 293 | 33 | 100 | 28 |
| ET06_09 | 10 | 186 | 80 | 9 | 10 | 279 | 10 | 123 | 54 | 23 | 7 | 288 | 35 | 232 | 82 | 24 | 7 | 114 | 4 | 107 | 13 |
| ET07_09 | 10 | 178 | 65 | 56 | 14 | 320 | 20 | 156 | 71 | 42 | 8 | 309 | 17 | 212 | 39 | 89 | 34 | 334 | 33 | 140 | 25 |
| ET08_09 | 2 | 83 | 55 | 249 | 35 | 344 | 6 | 81 | 54 | 200 | 19 | 301 | 29 | - | - | - | - | - | - | 144 | 19 |
| ET09_09 | 7 | 83 | 69 | 236 | 19 | 329 | 9 | 106 | 74 | 208 | 3 | 299 | 15 | 109 | 57 | 211 | 8 | 306 | 32 | 131 | 19 |
| ET11_09 | 8 | 117 | 58 | 26 | 0 | 296 | 32 | 134 | 57 | 30 | 9 | 294 | 31 | 150 | 63 | 42 | 9 | 307 | 25 | 119 | 29 |
| ET13_09 | 12 | 243 | 73 | 357 | 7 | 89 | 16 | 241 | 70 | 0 | 10 | 93 | 17 | 229 | 53 | 346 | 18 | 87 | 30 | 91 | 21 |
| ET14_09 | 6 | 295 | 59 | 204 | 1 | 114 | 31 | 306 | 57 | 207 | 6 | 113 | 32 | 296 | 43 | 197 | 10 | 97 | 45 | 107 | 36 |
| ET15_09 | 4 | 316 | 66 | 200 | 11 | 105 | 21 | 303 | 68 | 202 | 4 | 110 | 21 | 17 | 86 | 278 | 1 | 188 | 4 | 108 | 21 |
| ET16_09 | 16 | 350 | 62 | 167 | 28 | 258 | 1 | 48 | 73 | 150 | 4 | 242 | 17 | 84 | 85 | 343 | 1 | 253 | 5 | 71 | 8 |
| ET17_09 | 8 | 273 | 55 | 20 | 12 | 118 | 33 | 291 | 58 | 29 | 5 | 123 | 31 | 250 | 43 | 2 | 22 | 111 | 39 | 117 | 34 |
| ET18_09 | 7 | 88 | 62 | 340 | 9 | 245 | 26 | 85 | 63 | 330 | 12 | 235 | 24 | 195 | 71 | 329 | 14 | 63 | 13 | 61 | 21 |
| ET20_09 | 12 | 288 | 69 | 48 | 10 | 141 | 17 | 271 | 68 | 30 | 11 | 124 | 19 | 18 | 84 | 258 | 3 | 168 | 15 | 144 | 18 |
| ET21_09 | 4 | 19 | 78 | 246 | 8 | 154 | 8 | 4 | 85 | 217 | 4 | 127 | 3 | 218 | 84 | 67 | 6 | 336 | 3 | 145 | 5 |
| ET22_09 | 3 | 293 | 60 | 198 | 3 | 106 | 30 | 274 | 62 | 14 | 5 | 106 | 28 | 261 | 48 | 11 | 17 | 114 | 37 | 106 | 29 |
| 09bis_01 | 12 | 214 | 64 | 120 | 2 | 29 | 30 | 226 | 61 | 131 | 3 | 39 | 29 | 235 | 66 | 137 | 3 | 45 | 24 | 38 | 28 |
| 09bis_02 | 5 | 10 | 80 | 192 | 10 | 102 | 0 | 298 | 52 | 207 | 1 | 117 | 38 | 272 | 87 | 17 | 1 | 106 | 3 | 108 | 14 |
| 09bis_03 | 8 | 233 | 74 | 37 | 15 | 129 | 4 | 287 | 55 | 21 | 3 | 114 | 35 | 277 | 77 | 41 | 8 | 132 | 10 | 125 | 16 |
| 09bis_04 | 6 | 28 | 52 | 191 | 36 | 287 | 8 | 104 | 57 | 200 | 4 | 293 | 33 | 333 | 89 | 211 | 1 | 121 | 1 | 114 | 14 |
| 09bis_05 | 3 | 109 | 58 | 248 | 25 | 346 | 18 | 111 | 58 | 216 | 10 | 312 | 30 | - | - | - | - | - | - | 50 | 25 |
| 09bis_08 | 6 | 13 | 73 | 204 | 16 | 113 | 3 | 3 | 83 | 202 | 7 | 112 | 2 | 283 | 82 | 14 | 0 | 103 | 8 | 109 | 4 |
| 09bis_11 | 3 | 101 | 59 | 239 | 24 | 337 | 18 | 103 | 59 | 212 | 11 | 308 | 30 | - | - | - | - | - | - | 143 | 25 |
| 09bis_14 | 4 | 132 | 58 | 26 | 10 | 291 | 30 | 146 | 57 | 41 | 9 | 305 | 32 | 189 | 47 | 8 | 43 | 276 | 2 | 118 | 31 |
| 09bis_16 | 6 | 194 | 70 | 359 | 19 | 90 | 5 | 134 | 49 | 29 | 12 | 289 | 38 | 210 | 80 | 27 | 10 | 117 | 0 | 105 | 14 |
| 09bis_21 | 22 | 58 | 63 | 195 | 20 | 291 | 17 | 132 | 57 | 38 | 3 | 306 | 33 | 63 | 69 | 159 | 2 | 250 | 20 | 109 | 25 |
| 09bis_22 | 20 | 303 | 60 | 213 | 0 | 123 | 30 | 300 | 59 | 209 | 1 | 119 | 31 | 328 | 67 | 232 | 2 | 141 | 22 | 127 | 28 |
| 09bis_24 | 4 | 55 | 68 | 179 | 13 | 273 | 17 | 72 | 64 | 170 | 4 | 261 | 26 | 100 | 48 | 6 | 4 | 273 | 41 | 87 | 21 |

Table 5.1: Orientation of the stress axes for each structural site, calculated by using three different inversion methods. In the last column to the right are indicated the average orientation values of the computed $\sigma_3$ axes (i.e. the direction of extension). In red, data that were considered not fully reliable (see text for details).

## 5.2. Fault slip data analysis

The structural analysis indicates a complex fault kinematics, with oblique-slip displacements prevailing at places over purely dip-slip faulting. Fault slip data collected in the MER revealed the occurrence of two prevalent mean direction of extension: (1) a ~N110°-130°E and (2) ~N90°-100°E directed extensions.

The ~N110°-130°E trending extension has been determined primarily on the border faults of each MER segment (Figs. 5.3-5.8). Such faults exhibit an essential pure dip-slip kinematics, even though a left lateral oblique slip component of motion can be often observed (Figs. 5.4, 5.6, 5.8). Notably, the ~N110°-130°E extension direction suggest an overall left-lateral component of motion along some suitably oriented MER segments, such as the N35°-40° trending NMER border faults and partly the N25°-30° trending CMER border faults. The oblique component of motion of these border faults is reflected by their right-stepping en-echelon arrangement and local complex geometries (Corti, 2009 and references therein). Fault slip data on the SMER border faults reveals a more complex kinematics, with the superimposition of different tectonics phases. In particular, we observe some structural sites characterized by a roughly NNE-SSW extension direction (Figs. 5.7, 5.8), related to transverse elements (joints, faults) to the SMER trend (Bonini et al., 2005), activated during older phases (~20 Ma).
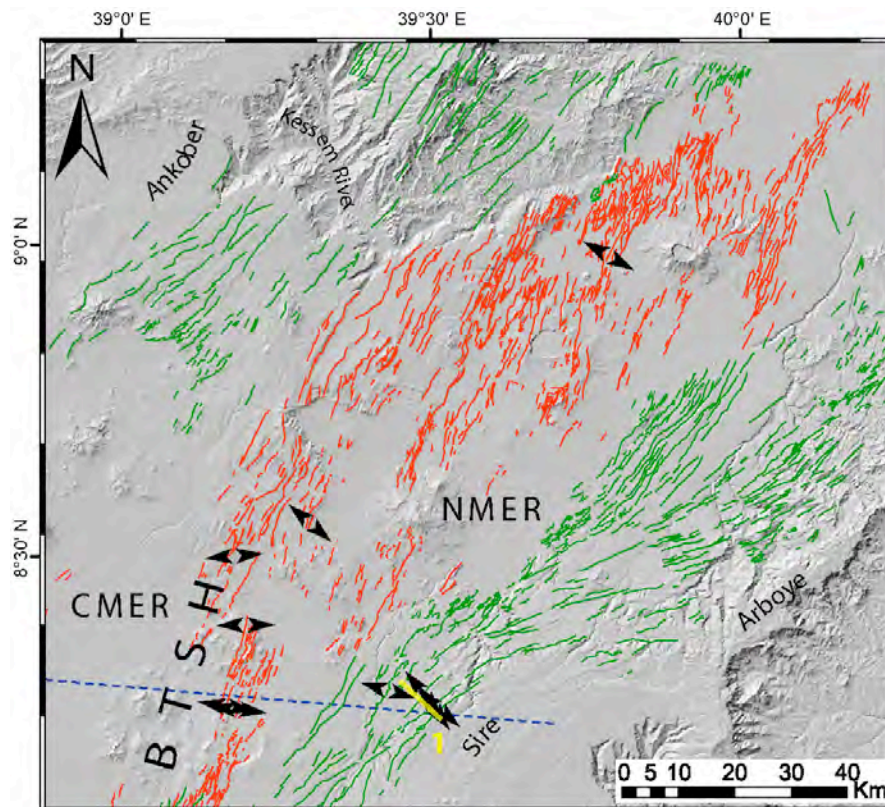


Fig. 5.3: Representative fault kinematics data for the NMER (locations and names of each sites of measurement are shown in Fig. 5.2). Doublehead black arrows indicate the calculated direction of extension. The WFB faults are in red; border faults in green. Yellow line is the trace of the geological section in Fig. 5.9., blue dotted line is the trace of the transect 1. BTSH: Boru Toru structural high.
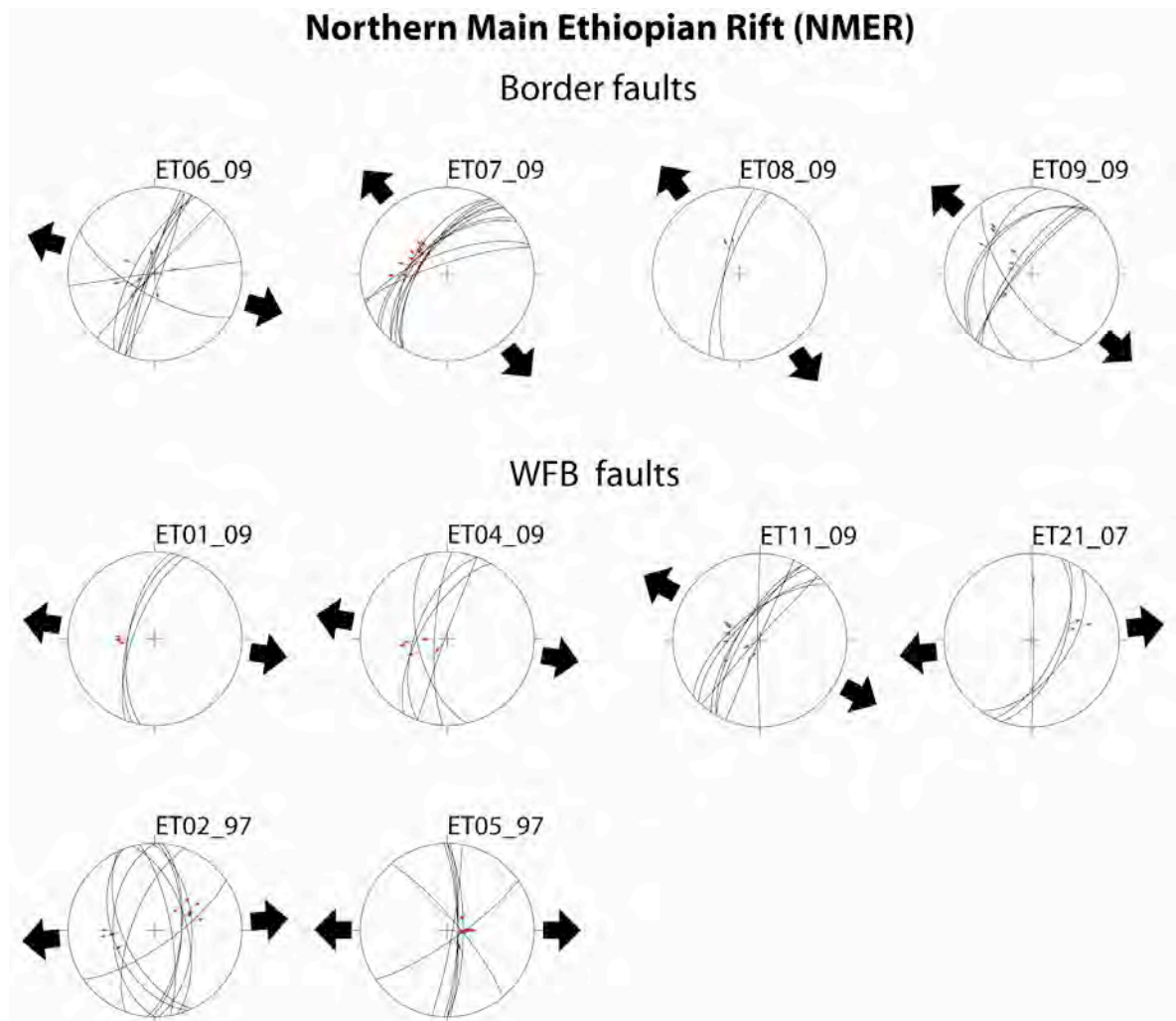
Fig .5.4: Stereonets of the fault slip data collected in the NMER. The locations of the site of measurements are shown in Fig. 5.2; black arrows represent the direction of the computed $\sigma_3$ (see text for details).
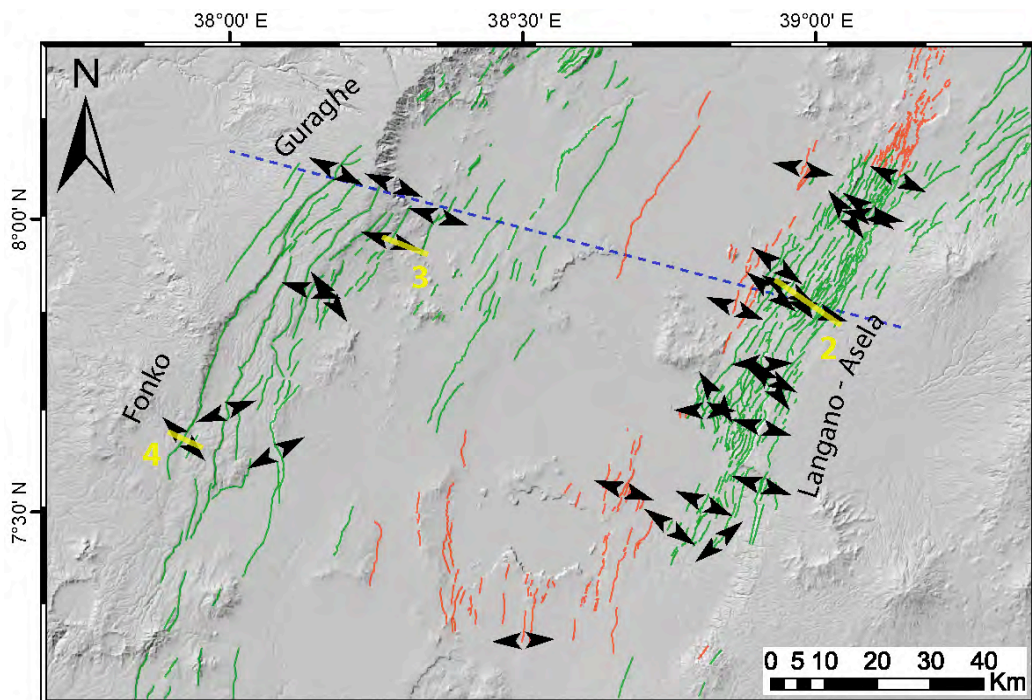


Fig. 5.5: Representative fault kinematic data for the CMER (locations and names of each sites of measurement are shown in Fig. 5.2). Doublehead black arrows indicate the calculated direction of extension. In red, the WFB faults; in green the border faults. Yellow lines are the traces of the geological sections in Figs. 5.12, 5.16 and 5.18; blue dotted line is the trace of the transect 2.

# Central Main Ethiopian Rift (CMER)

## Border faults

ET03_97  ET04_97  ET10_07  ET11_07

ET15_07  ET17_07  ET18_07  ET19_07

ET20_07  ET20_07b  ET13_09  ET14_09

ET15_09  ET16_09  ET17_09  ET18_09

ET20_09  ET21_09  ET22_09  09bis_02
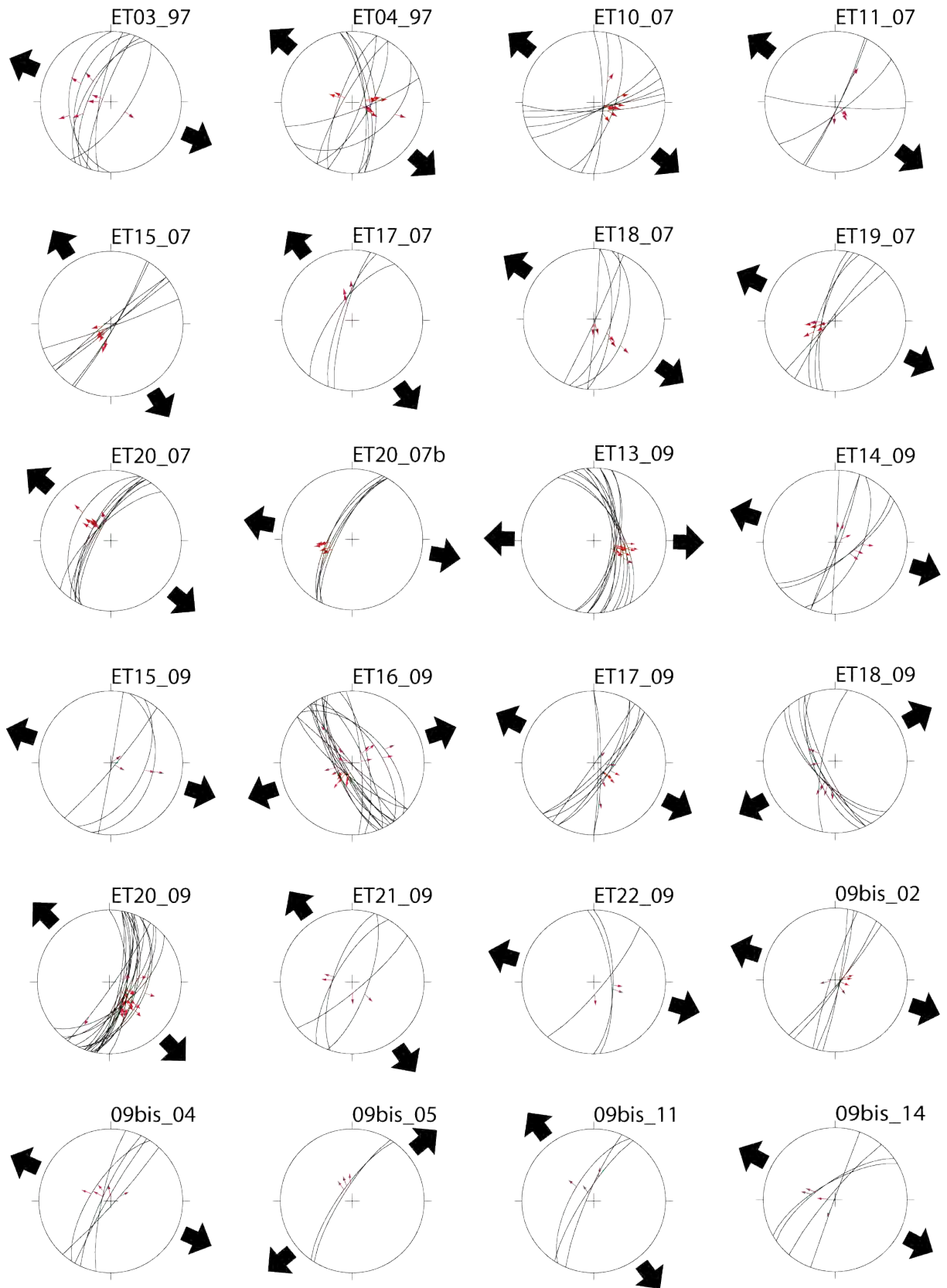
09bis_04  09bis_05  09bis_11  09bis_14
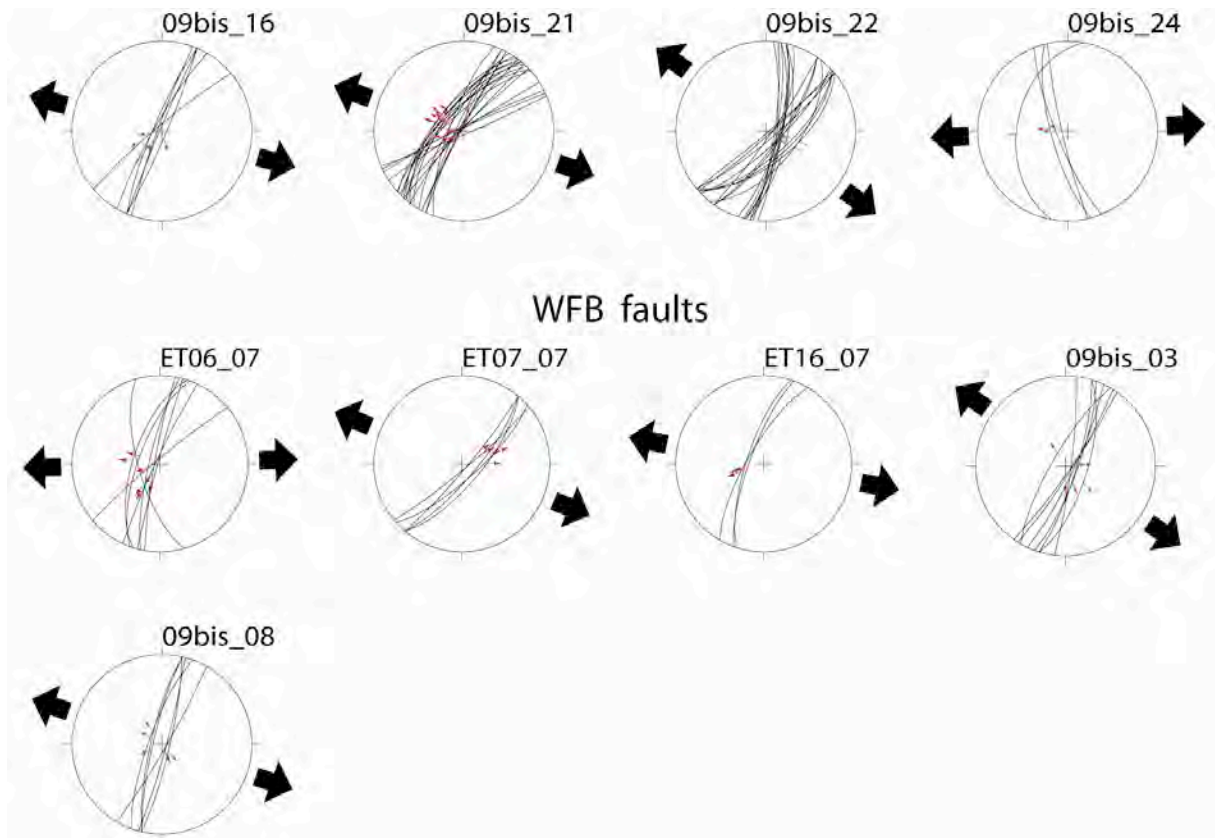
Fig. 5.6: continues

Fig. 5.6: Stereonets of the fault slip data collected in the CMER. The locations of the sites of measurements are shown in Fig. 5.2; black arrows represent the direction of the computed $\sigma_3$ (see text for details).

The ~N90°-100°E directed extension has been instead determined primarily on the WFB faults of the rift floor (Figs. 5.3-5.8). This direction is nearly perpendicular to the average trend of the WFB structures in each MER segments, resulting in an almost pure dip-slip kinematics.

Only in few cases on the fault planes have been recorded two different generations of kinematic indicators. In these cases have been performed two different elaborations. However, we found two well represented kinematic indicators only in the ET20_07 measurement site (Fig. 5.5), where an early ~E-W direction of extension is superimposed onto a previous ~NW-SE extensional episodes. Other sites with well documented different extensional episodes are reported in Bonini et al. (2005), specifically in the SMER and the Boru Toru structural high (Fig. 5.3), this latter characterized by a really complex fault kinematics with three distinct fault episodes that were interpreted as the results of a local stress field change (see Bonini et al., 2005 for details).
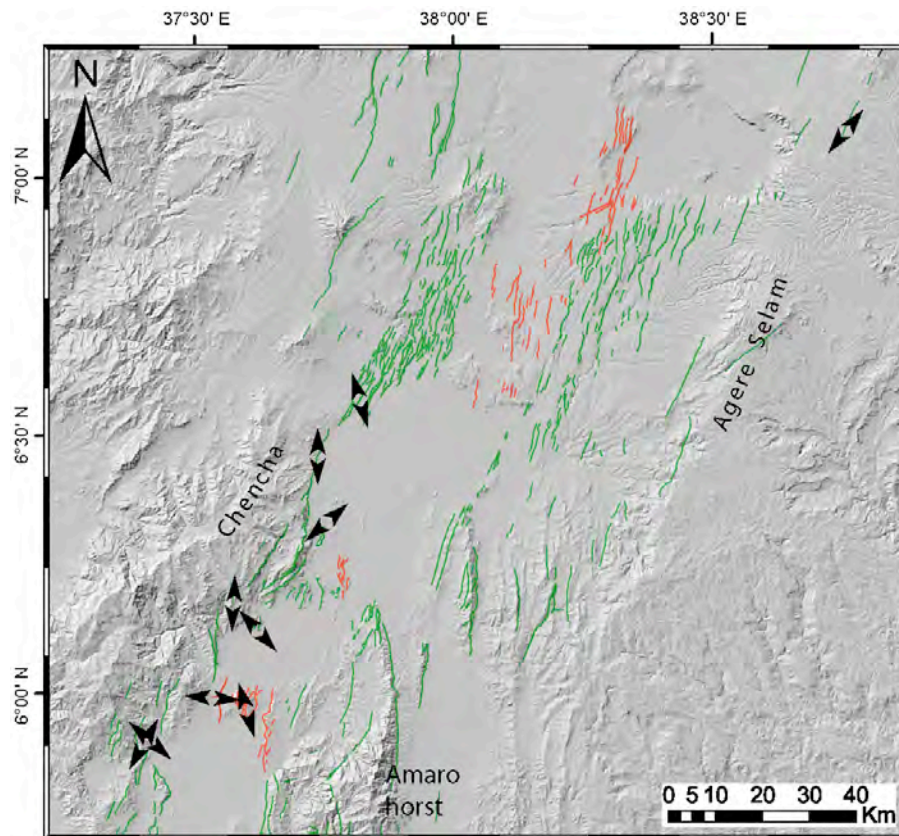
Fig. 5.7: Representative fault kinematic data for the SMER (locations and names of each site of measurement are shown in Fig. 5.2). Doublehead black arrows indicate the calculated direction of extension. In red, the WFB faults; in green the border faults.

## Southern Main Ethiopian Rift (SMER)

### Border faults
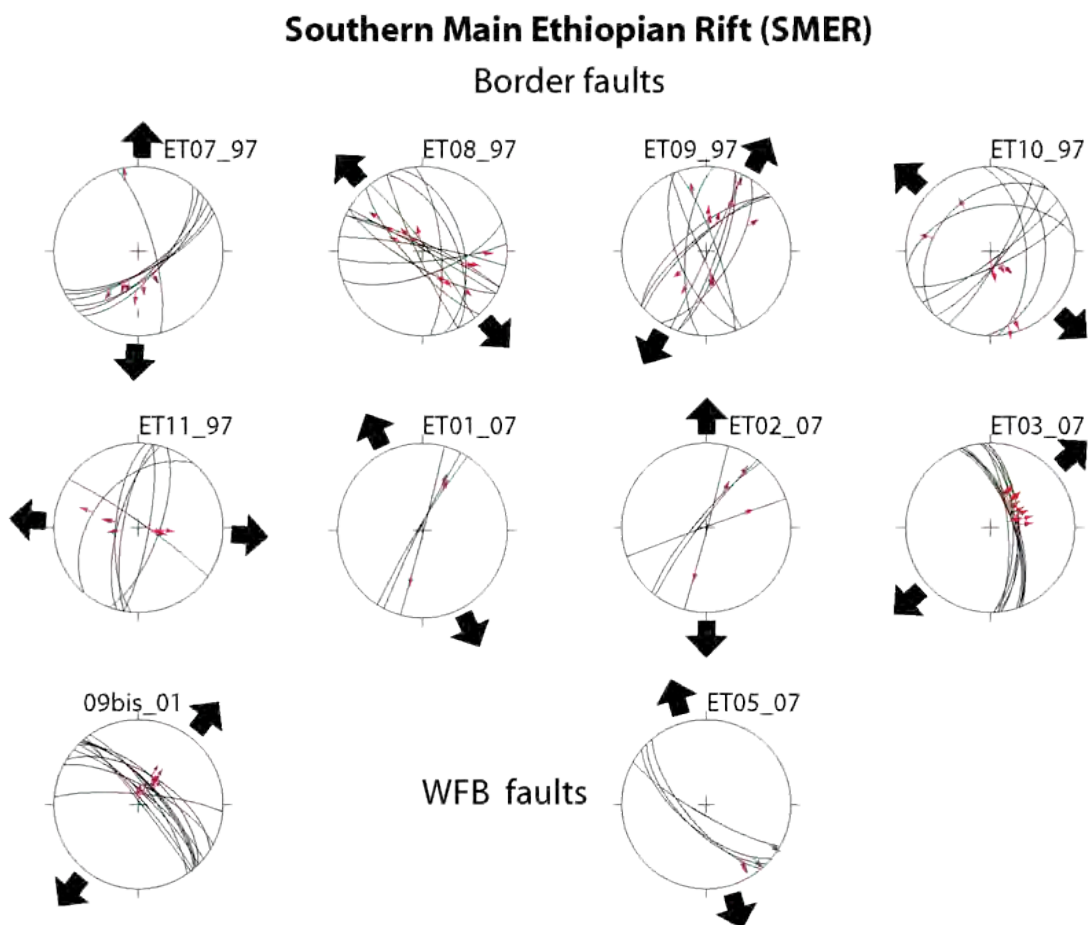


Fig. 5.8: Stereonets of fault slip data collected in the SMER. The locations of the sites of measurements are shown in Fig. 5.2; black arrows represent the direction of the computed $\sigma_3$ (see text for details).

84

## 5.3. Fieldwork analysis

The different kinematics observed between the borders and the rift floor are illustrated in two E-W transects across the NMER and the CMER. Owing to the low number of data and to their scattering (Fig. 5.2 and 5.7), a transect has not been constructed for the SMER.

### 5.3.1. Transect 1

Transect 1 (trace in Figs. 5.2, 5.3) cuts both the NMER, on the eastern side, the CMER, on the western, and the transition zone between these two rift segments, that is marked by the N-S trending Boru Toru structural high (Bonini et al., 2005) (Fig. 5.9a). The stereonets of the structures, plotted over the transect (Fig. 5.9a), show that on both the eastern (NMER) and the western (CMER) sides the extension directions inferred from the fault slip data analysis indicate a ~N110°-130°E trend. Conversely, the WFB faults crossed by the transect point to a ~N100°E direction of extension. Moreover, the topographic profile, although exaggerated, highlights the strong difference in the vertical separation between border and internal faults (Fig. 5.9a).

A particularly interesting situation on the eastern margin, at the NMER-CMER transition (Sire master faults, section trace in Fig. 5.3) is shown in detail trough a geological section (section 1, Fig. 5.9b). The rock units were defined using the existing geological data (e.g Kazmin, 1978; WoldeGabriel et al., 1990; Abebe et al., 1999; Le Turdu et al., 1999; Abebe et al., 2005) and were correlated with the units defined in Abebe et al. (2005) (Fig. 5.10). The stereonets show the ~N110°-130°E trending extension direction, typical for the NMER and CMER rift border faults. The faults section displaces the exposed ignimbrites of the Nazaret (Np) and Chefe-Donsa (CDp) units, likely the underlining pre-rift Guraghe-Anchar basalts, that are not exposed (Fig. 5.9b). Particularly, at station ET07_09 a normal fault displaces a Quaternary colluvial debris that clearly abuts against the fault plane (Fig. 5.9b and Fig. 5.11). This structure represents thus a clear evidence of recent tectonic activity of the borders faults at this latitude, and might contrast with previous geological and geophysical works suggesting NMER border faults to be totally deactivated (e.g. Keir et al., 2006).
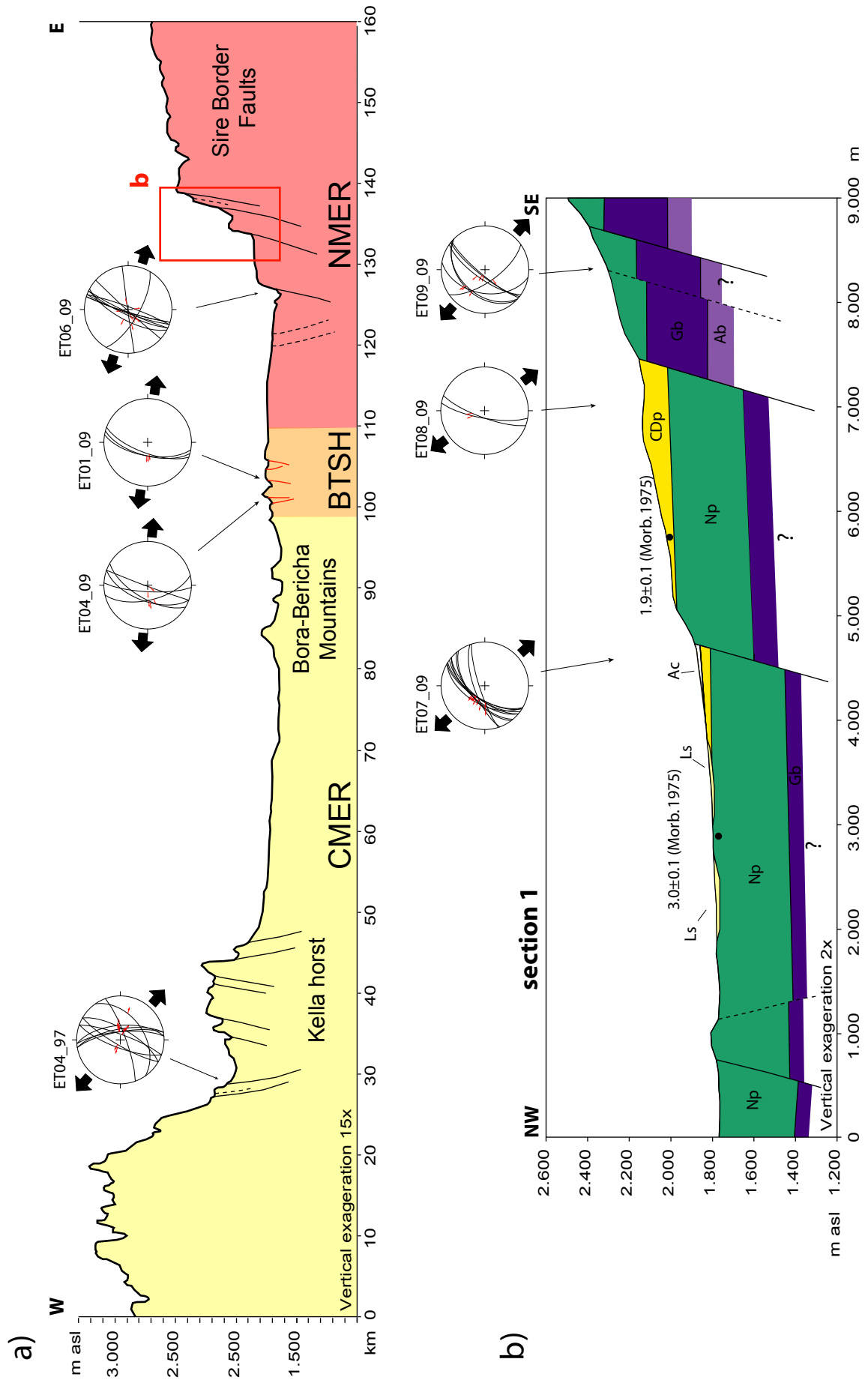
Fig. 5.9: a): Transect 1. The black lines indicate the border faults, the WFB faults in red. b): Section 1(the box indicates the location in the upper panel, section trace in Fig. 5.3). Legend in Fig. 5.10. Radiometric ages (K/Ar) are from Morbidelli et al., (1975). BTSH: Boru Toru structural high.

### 5.3.2. Transect 2

Transect 2 (trace in Figs. 5.2, 5.5) cuts exclusively across the CMER, from the western Guraghe rift border to the eastern Asela-Langano rift border (Fig. 5.12). Unfortunately, given the low number of WFB faults affecting the CMER (see section 4.1.2.1.), the transect does not interest any of these structures. Nevertheless, stereonets of fault slip data collected on the CMER margins indicate a ~N110°-130°E extension direction. Likewise in the NMER, the comparison with the stereonets from WFB fault slips data (Fig. 5.6) indicates that the extension direction in the rift floor varies between ~N90°E and ~N120°E, and thus evidences a slightly difference passing from the rift margins to the rift floor. It is worth mentioning that the elaboration of all the kinematic indicators collected on the WFB faults in the CMER indicates an average ~N100°E extension direction (Fig. 5.12b).

Very interesting settings have been identified along the transect 2, which are shown in geological sections. Geological section 2 (trace in Figs. 5.5, 5.12c) illustrates the eastern rift margin in the Asela area. This zone is characterized by the excellent morphological expression of the faults (see Fig. 5.1), with huge lateral persistence, large vertical offset and fresh fault scarps, suggesting a limited reworking by erosional processes, and therefore recent tectonic activity.

## Legend

**Alluvial cover (Ac)**
*Age: Holocene - present*
Alluvial, soil, slope scree and debris deposits.
Caldera, crater and graben fillings deposits.
Thickness: >0.5 m

### Main-Rift

*Inner Rift*

**Wonji basalts (Wb)**
*Age: Pleistocene - Holocene (<1.6 Ma)*
Alkaline to olivine basaltic lava flows with minor tholeiites, hawaiites and benmoreites
Maximum exposed thickness: 10m

Scoria cones and fall-out deposits

**Bora-Bericha Rhyolites (Br)**
*Age: Pleistocene - Holocene (<1.6 Ma)*
Peralkaline trachytes and rhyolites with comenditic and pantelleritic affinity of the central volcanoes

**Lacustine Sediments (Ls)**
*Age: <500 ka*
Sand and silt with abundant components of volcanic origin
Maximum estimated thickness: about 600 m

**Chefe Donsa Pyroclastic Deposits (CDp)**
*Age: 2.54 - 1.7 Ma*
Unwelded to poorly welded, ignimbrites and volcanoclastic deposits
Maximum exposed thickness: 40 m

### Syn-Rift

**Nazret Pyroclastic Rocks (Np)**
*Age: 5.2 - 2.6 Ma*
Welded peralkaline pantelleritic ignimbrites with minor intercaleted basaltic lava flows
Maximum estimated thickness: 700 m

### Pre-Rift

*Upper plateau*

**Guraghe-Anchar Basalts (Gb)**
*Age: 10.6 and 8.3 Ma*
Aphyric to phyric basalts and trachybasalts, intercalated with rhyolitic pyroclastic deposits
Maximum estimated thickness: more than 300 m

*Lower plateau*

**Aiba-Alaje Basalts (Ab)**
*Age: 32-29 Ma*
Fine grained basaltic lava flows, with minor pyroclastic deposits
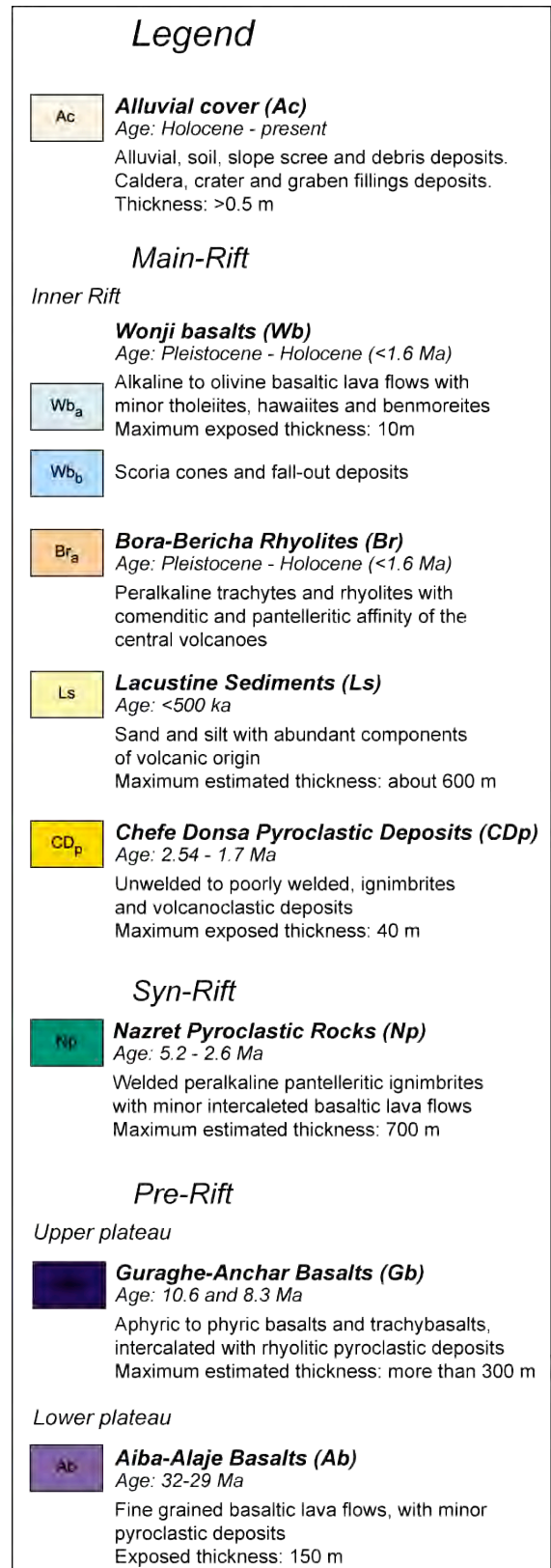Exposed thickness: 150 m

Fig 5.10: Legend of the geological sections in Fig. 5.9, 5.12, 5.16 and 5.18 (see text for details, modified after Abebe et al., 2005).
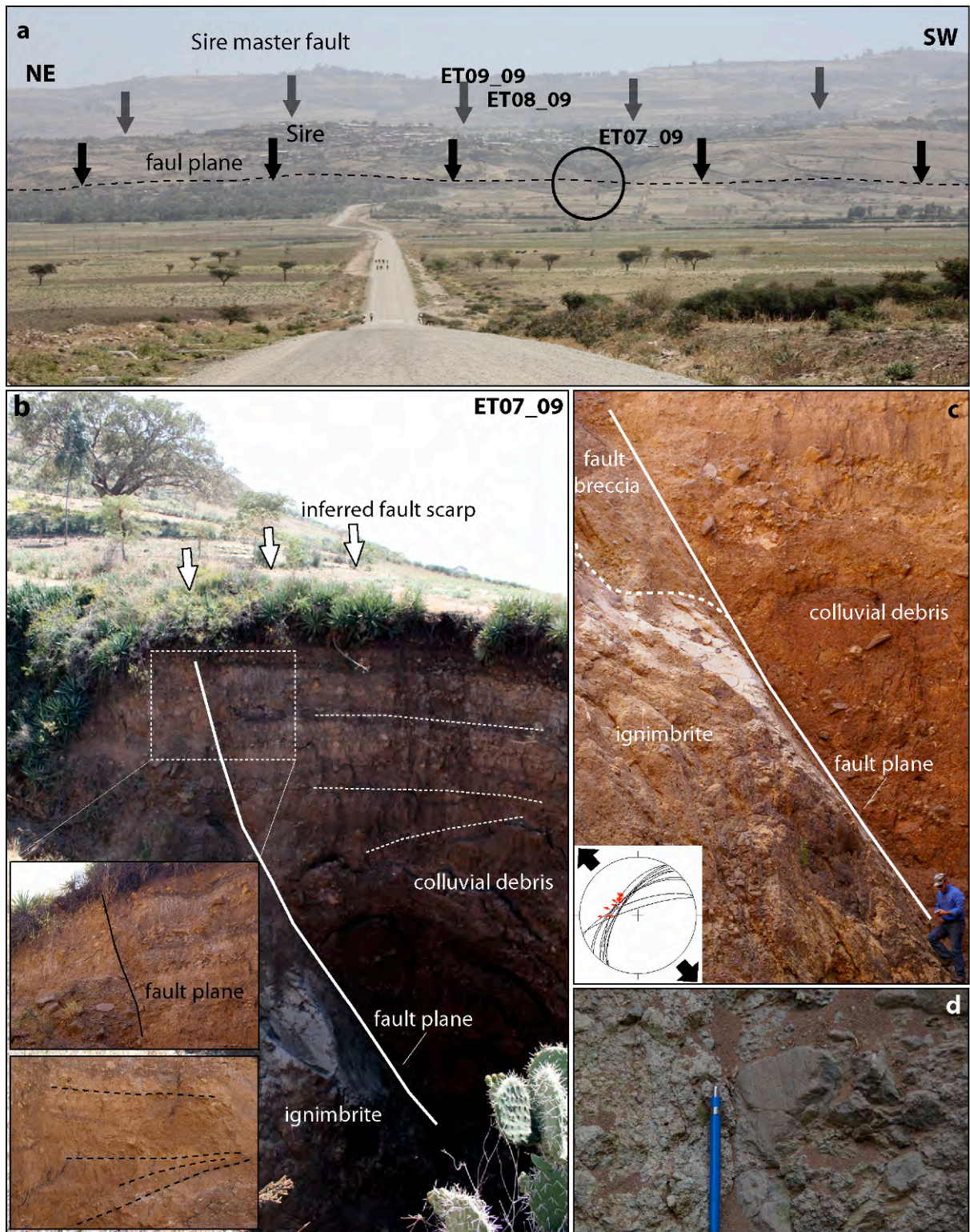
Fig. 5.11: a) Panoramic view of the NMER border in the Sire area. The circle indicates the faults of station ET09_07 in the foreground, and behind the structures of stations ET08_09 and ET09_09 in section 1 (Fig. 5.9). Note the tilting of the downthrown block. b): fault displaces the ignimbrite (Nazret and Chefe-Donsa units) and a colluvial deposit (see also the close-up). The deposits present also a clear wedging, further testifying the recent syn depositional activity of this structure. c) close-up of the fault plane and (d) of the associated fault breccia. Note well striated pebble to the right of the pen.
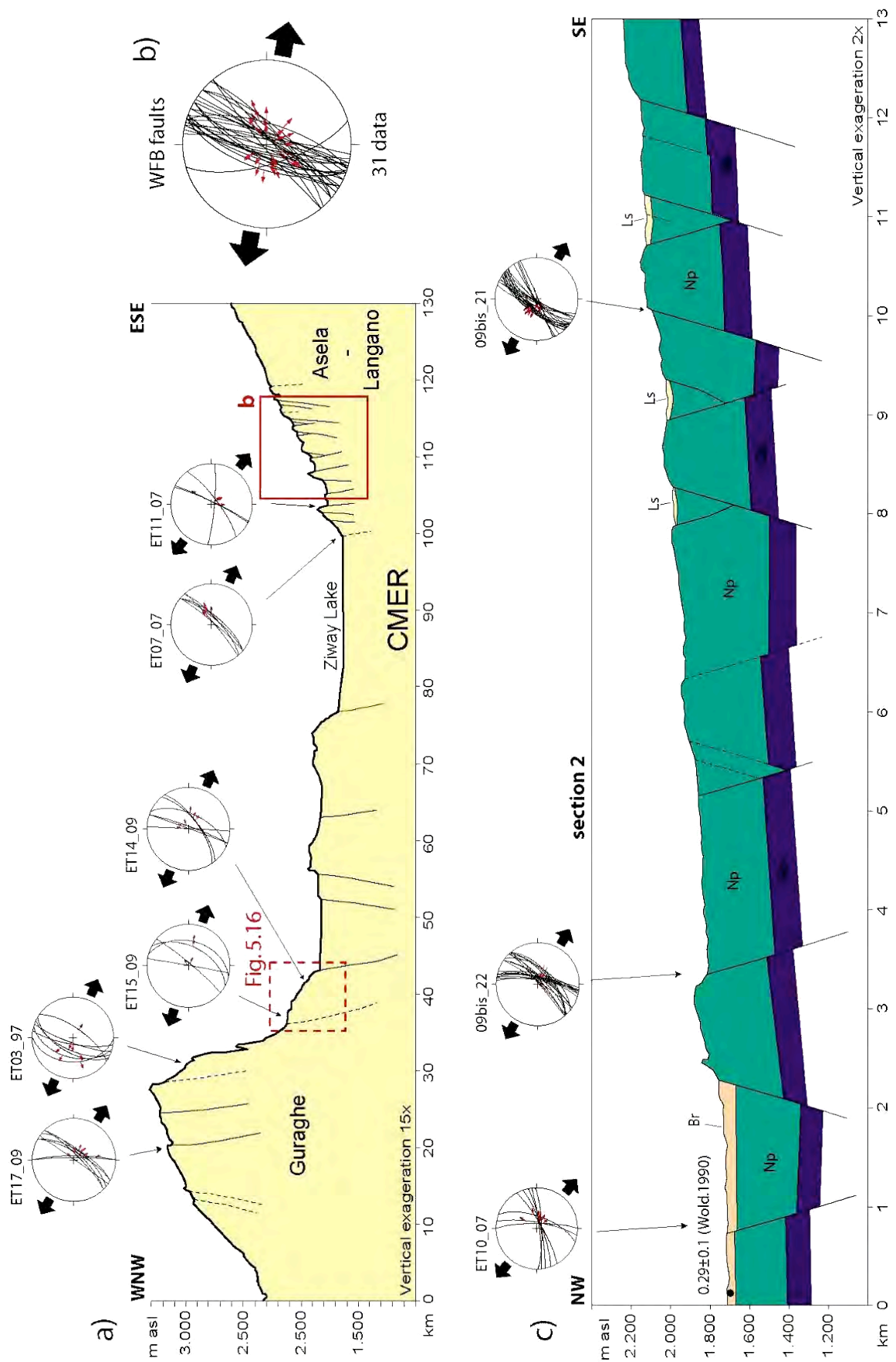
Fig. 5.12: : a): Transect 2. The black lines indicate the border faults.. b): Section 2 (location red square in lower panel, section trace in Fig. 5.5). Legend in Fig. 5.10. Radiometric ages (K/Ar) are from WoldeGabriel et al., (1990). The red dotted square indicates the location of the section 3 (Fig. 5.16) projected on the transect (see Fig. 5.5). c) The stereonet indicates the extension direction inferred from all the kinematics indicators collected on WFB fault planes in the CMER (see text).

The section 2 (Fig. 5.12c) shows a complex fault system with predominant west-dipping faults and only few secondary antithetic east-dipping faults, which give rise to a wider staircase fault profile that differ from the steeper western border (Guraghe margin), marked only by a few major faults with very high vertical offset (Fig. 5.12). Some small grabens are filled with lacustrine sediments (Fig. 5.12c).

Along section 2 faults affect mainly ignimbrite belonging to the Nazaret unit (Fig. 5.10). The fault slip data collected on the structures of Section 2 revealed an overall NW-SE extension direction (Fig. 5.12c).



Fig. 5.13: Characteristics of fault plane at site 09bis_21 (see text for details).

Particularly interesting is the structural site 09bis_21 (Fig. 5.13) which shows a clear evidence of Late Quaternary tectonic activity. A normal fault displaces recent coarse slope debris. Really good quality kinematic indicators can be identified both on the fault plane (strongly welded Nazret ignimbrite, Fig. 5.13 c) and on shear planes in the fault breccia (Fig. 5.13d). The slope deposits displaced by the faults of site 09bis_21 show, in a gully 30 m distant from the measurement site, a well developed wedging (Fig. 5.14), which further indicates the recent tectonic activity of this fault system.



Fig. 5.14: wedge shape slope deposits, close to the measurement site 09bis_21.

Relationships with Quaternary activity can be also recognised at measurement site 09bis_22. There, a normal fault displaces the strongly welded ignimbrite of the Nazret unit (Fig. 5.12). This very competent rock is affected by well organized columnar joint sets which confer a sawtooth shape to the fault plane. In the receding zones formed by two saw teeth we found an old debris (bearing clasts derived from the same lithology of the fault plane, Fig. 5.15b, d) displaced by the fault itself. Abutting against this old debris we observed a ~40 cm wide fault breccia (with very good quality kinematics indicators, Fig. 5.15c) and recent coarse slope debris, resting on the fault breccia.

Evidences of Quaternary activity were detected also along the western rift margin at the Guraghe escarpment and along the Fonko fault (Fig.4.1), where border faults displace recent deposits. A geological section helps to visualize these settings (Figs. 5.16, 5.17, 5.18, 5.19).
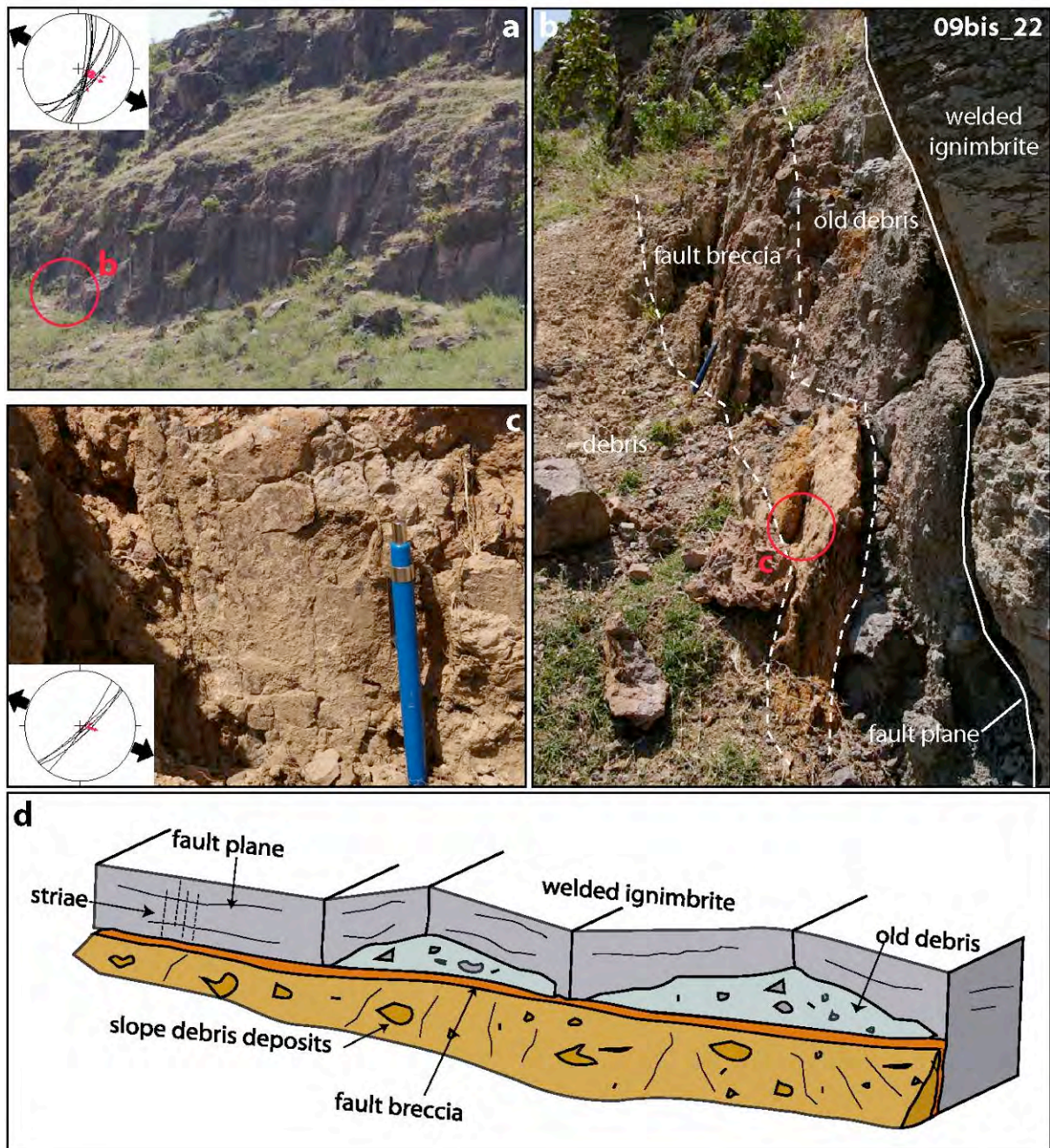
Fig. 5.15: Measurement site 09bis_22, see text for details. a) panoramic view of the faults and localization of the closeup of panel (b), which shows the fault plane and the associated fault breccia. c) striae on a plane in the fault breccia (location in panel b). d) 3D schematic interpretation.

The geological section 3 (trace in Fig. 5.5 and projected on the near transect 2 in Fig. 5.12; Fig. 5.16) is mainly characterized by the outcropping Nazret ignimbrite. The underlying Guraghe-Anchar basalts, outcropping further north (e.g. WoldeGabriel et al., 1990; Bonini et al., 2005), here are not exposed. On the central and eastern side of the section the Pliocene Chefe-Donsa unit crops out (Fig. 5.10); it is overlain by the Quaternary Wonji basalts associated with the Butajira volcanic chain (see section 2.4.2.2.). At the measurement site ET15_09, the Nazret ignimbrite is covered by slope debris, which in turn are cut by the same fault (Fig. 5.17).
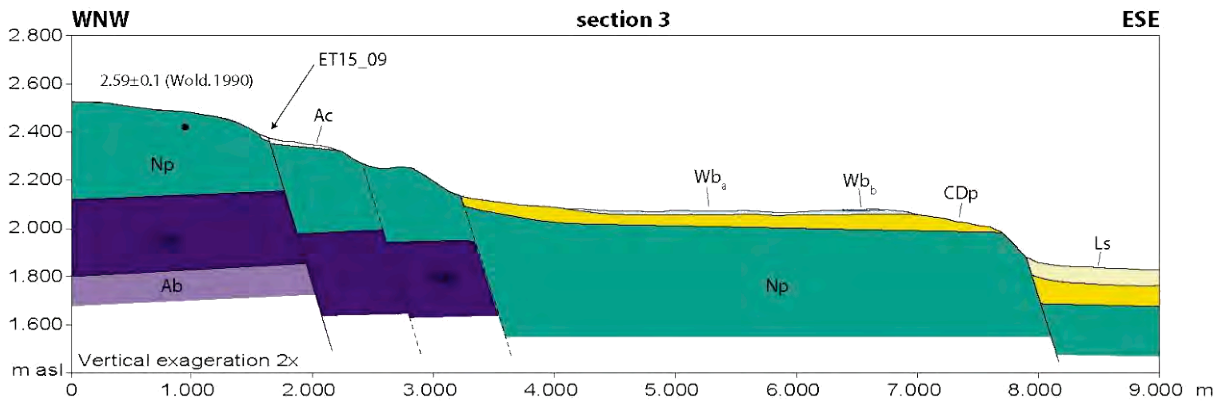
Fig 5.16: Geological section 3, Guraghe margin. Trace in Fig. 5.5, and red dotted square in Fig. 5.12). Legend in Fig. 5.10. Radiometric ages (K/Ar)are from WoldeGabriel et al., (1990)
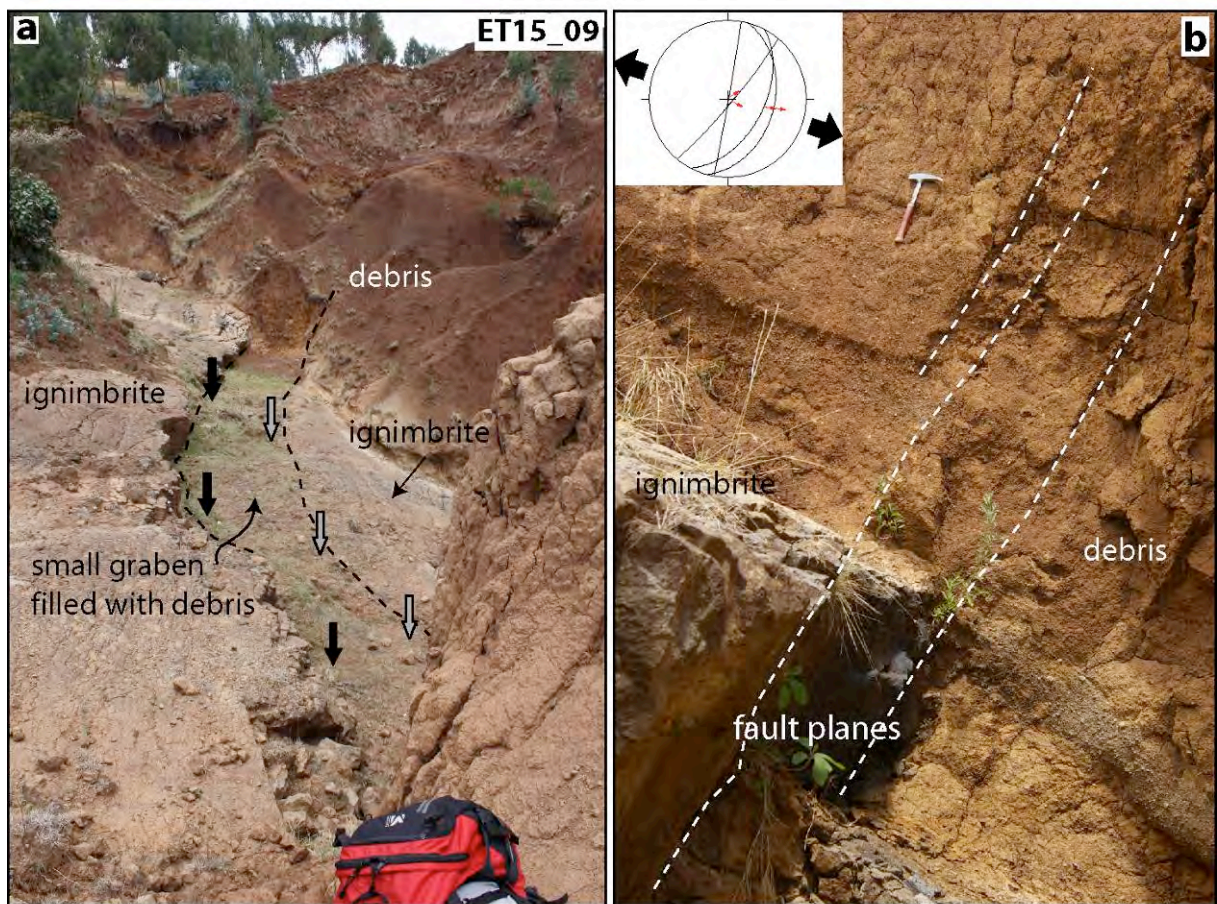


Fig. 5.17: Measurement site ET15_09 (see text). a) note the small graben formed by two small antithetic (west-dipping) normal faults, filled with debris. b) close-up of the faulted debris.

Similarly, the faults in the geological section 4 (Fig. 5.18), located on the western margin at Fonko (trace in Fig. 5.5), mainly affect the Nazaret ignimbrite and terrains of the Chefe-Donsa unit, here represent by pyroclastic deposits. Faults of the structural section ET20_09 show again evidence of recent tectonic activity as they displace recent colluvial deposits (Fig. 5.19b).
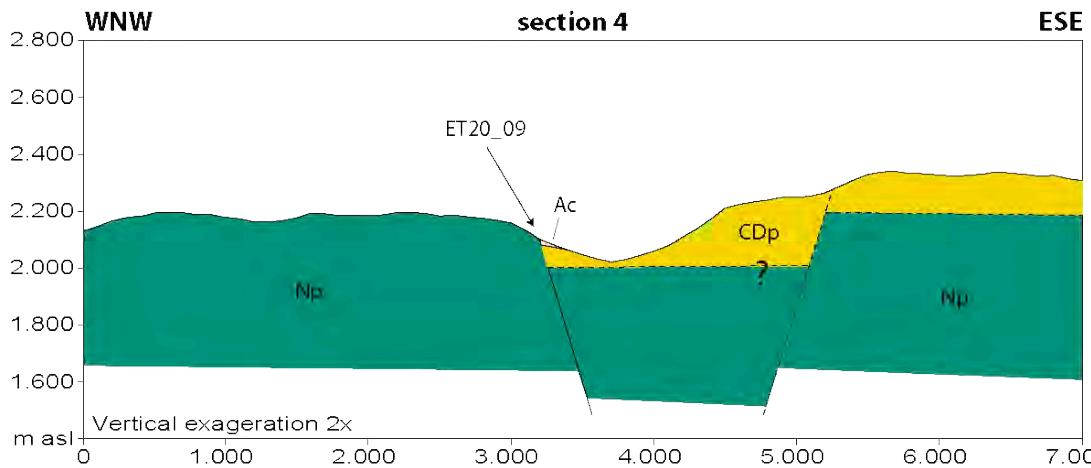
Fig: 5.18: Geological section 3, Fonko margin. Trace in Fig. 5.5. Legend in Fig. 5.10. The lack of existing detailed geological data in this MER sector did not allow a reliable reconstruction of this geological section.
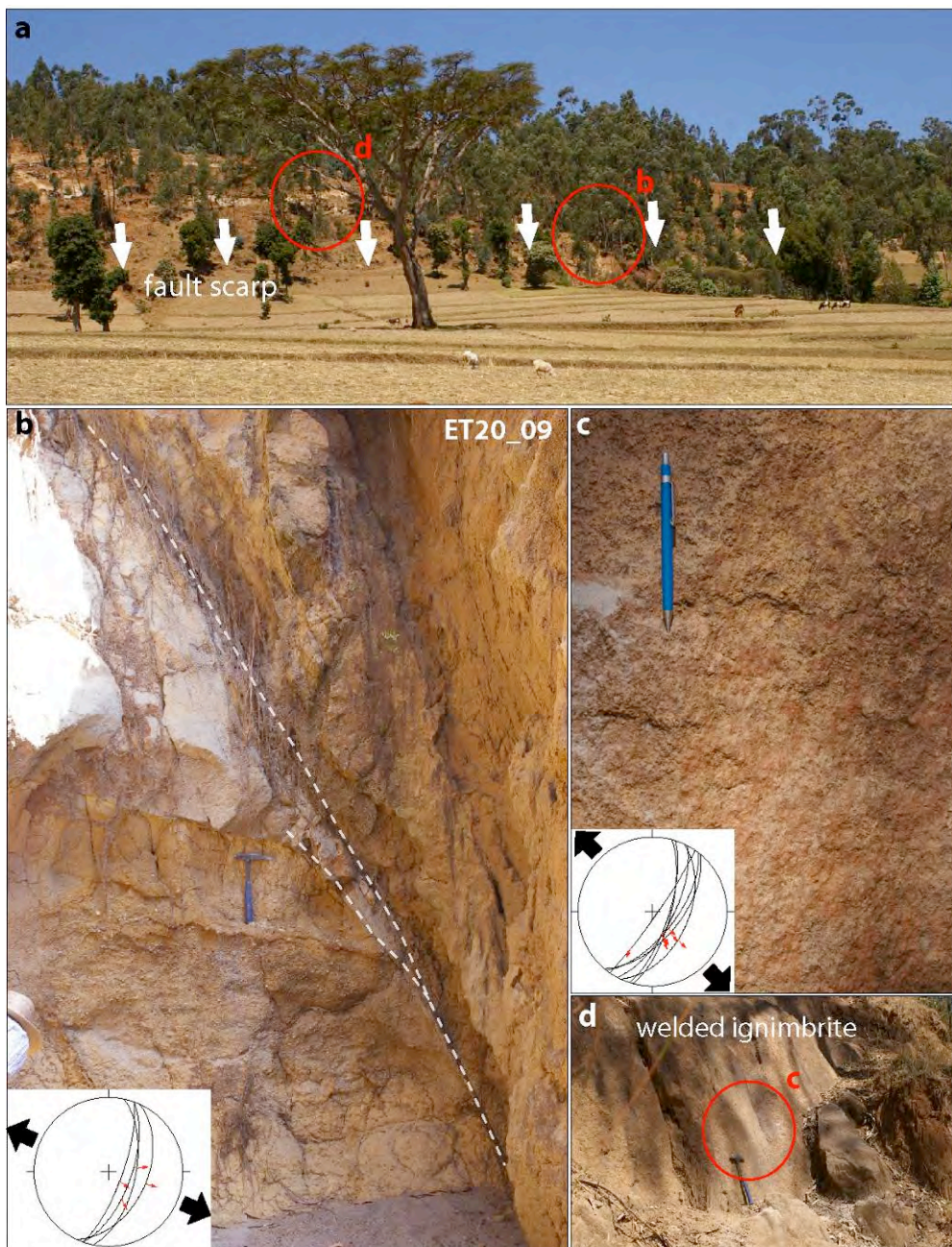
Fig. 5.19: Measurament site ET20_09. a) panoramic view of the fault scarp. b) fault planes in recent slope deposits, resting on the welded ignimbrite (not in the picture). c) close-up of the kinematics indicators on the principal fault plane displacing the welded ignimbrite (displayed in panel d).

In addition, many others structural station testifying a recent tectonic activity in the surveyed area were found during the fieldwork (Figs. 5.20- 5.23).

A roughly N-S trending fault (ET13_09) of the Langano Rhomboidal Fault System (see close-up in Fig. 5.2), result of the interaction between NE-SW border faults and pre-existing NW-SE structures (e.g. Boccaletti et al., 1998, Le Turdu et al., 1999; Corti, 2009), displaces a secondary fault plane cutting a coarse grained slope debris and lacustrine deposits bearing abundant *Melanoides tubercolata* shells (Fig. 5.20b,c,d). The fault plane displays very good quality kinematics indicators (close-up in Fig. 5.20b). Samples of the shells were analysed at the Beta Analytic Laboratories through AMS and standard techniques and the results summarized in Tab.5.2. The radiometric conventional ages vary between 9730±60 years BP and 6200±60 years BP (Table 5.2), testifying a Holocene activity of this fault.
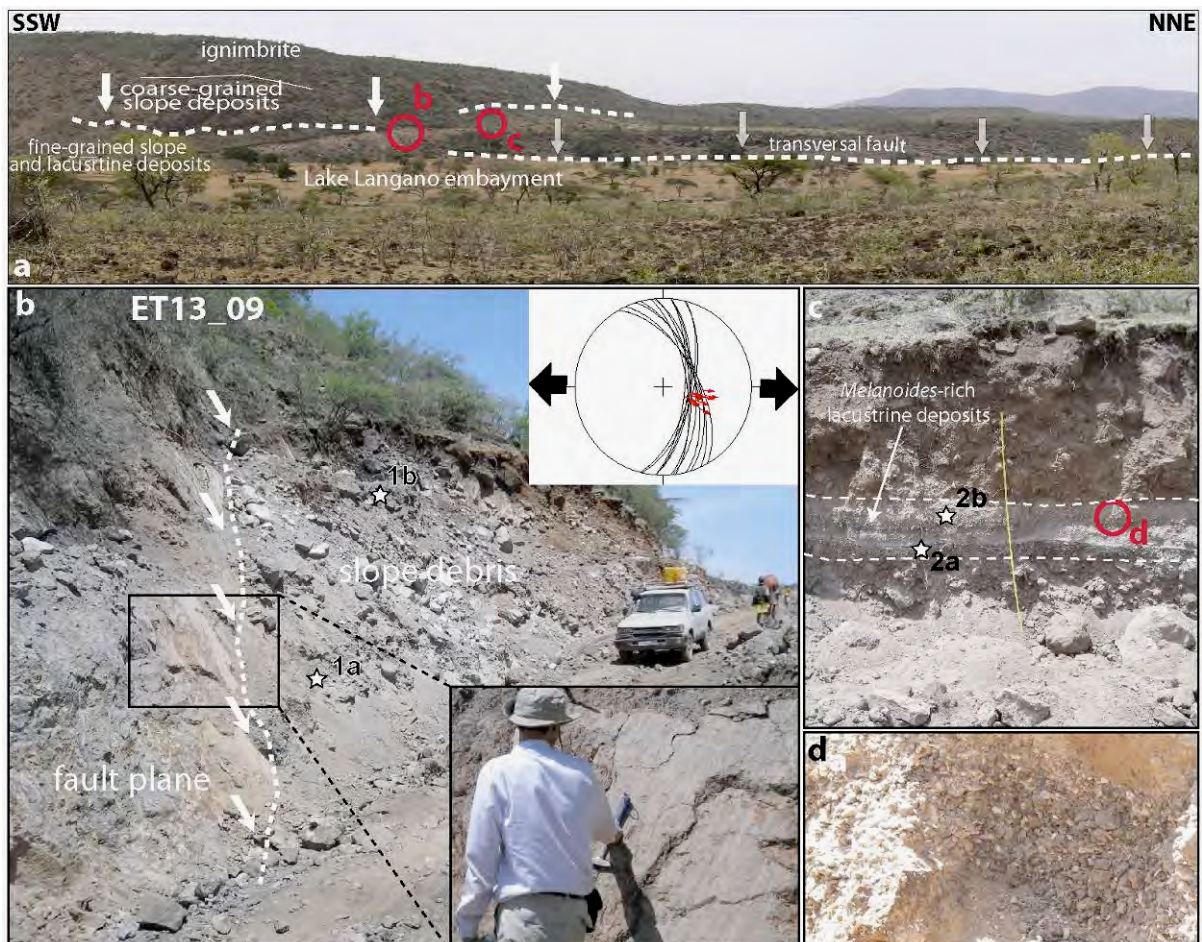


Fig. 5.20: Measurement site ET13_09. a) panoramic view of the structure. b) fault plane on slope debris. c) shelly levels. d) close-up of the shells.

| Sample | Laboratory code | Measured age | 13C/12C | Conventional age | Calibrated age 2σ |
|--------|-----------------|--------------|---------|------------------|-------------------|
| 2b | Beta 231102 | 5940 +/- 50 BP | +0.2 o/oo | 6350 +/- 50 BP | Cal BC 4990 to 4750 (Cal BP 6940 to 6700) |
| 2a | Beta 231101 | 9400 +/- 60 BP | -5.0 o/oo | 9730 +/- 60 BP | Cal BC 8790 to 8530 (Cal BP 10740 to 10480) |
| 1b | Beta 263657 | 6720 +/- 50 BP | +3.8 o/oo | 7190 +/- 60 BP | Cal BC 6210 to 5980 (Cal BP 8160 to 7930) |
| 1a | Beta 231103 | 5840 +/- 60 BP | -3.3 o/oo | 6200 +/- 60 BP | Cal BC 5310 to 4990 (Cal BP 7260 to 6940) |

Table 5.2: results of the radiocarbon dating of the shells collected in different levels (location in Figs. 5.2a, 5.2b).

A similar setting can be identified in the Lake Ziway area (measurement site ET11_07, Fig. 5.21; close-up in Fig. 5.2), where faults affect reworked pomiceous fluvio-lacustrine levels attributed to Late Pleistocene (Benvenuti et al., 2002).
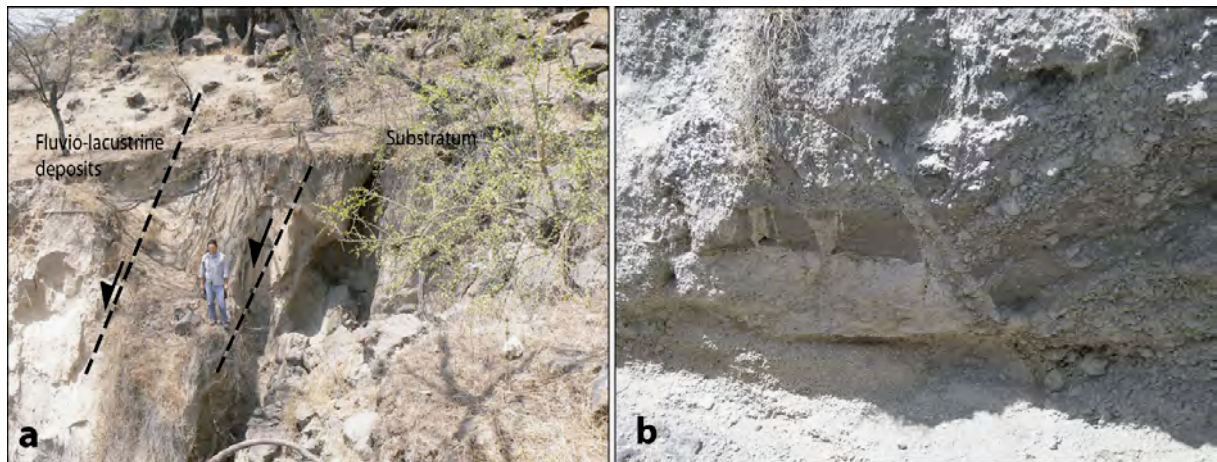


Fig. 5,21: Measurement site ET11_07. a)Fault surface near Lake Ziway affecting Late Pleistocene fluvio-lacustrine sediments. (b) Close-up of another near normal fault displacing the same deposits.

Again, in the measurement site 09bis_11 on border fault south of Asela, four different slope debris have been identified to be separated by fault planes containing very good quality kinematic indicators (Fig. 5.22).

Finally, in the Langano Rhomboidal Fault System, the successive activation of two normal fault tilted a recent alluvial cone in such a way that its apical portion attains a lower elevation (2160 m asl) than its base (2200 m asl) (Fig. 5.23).
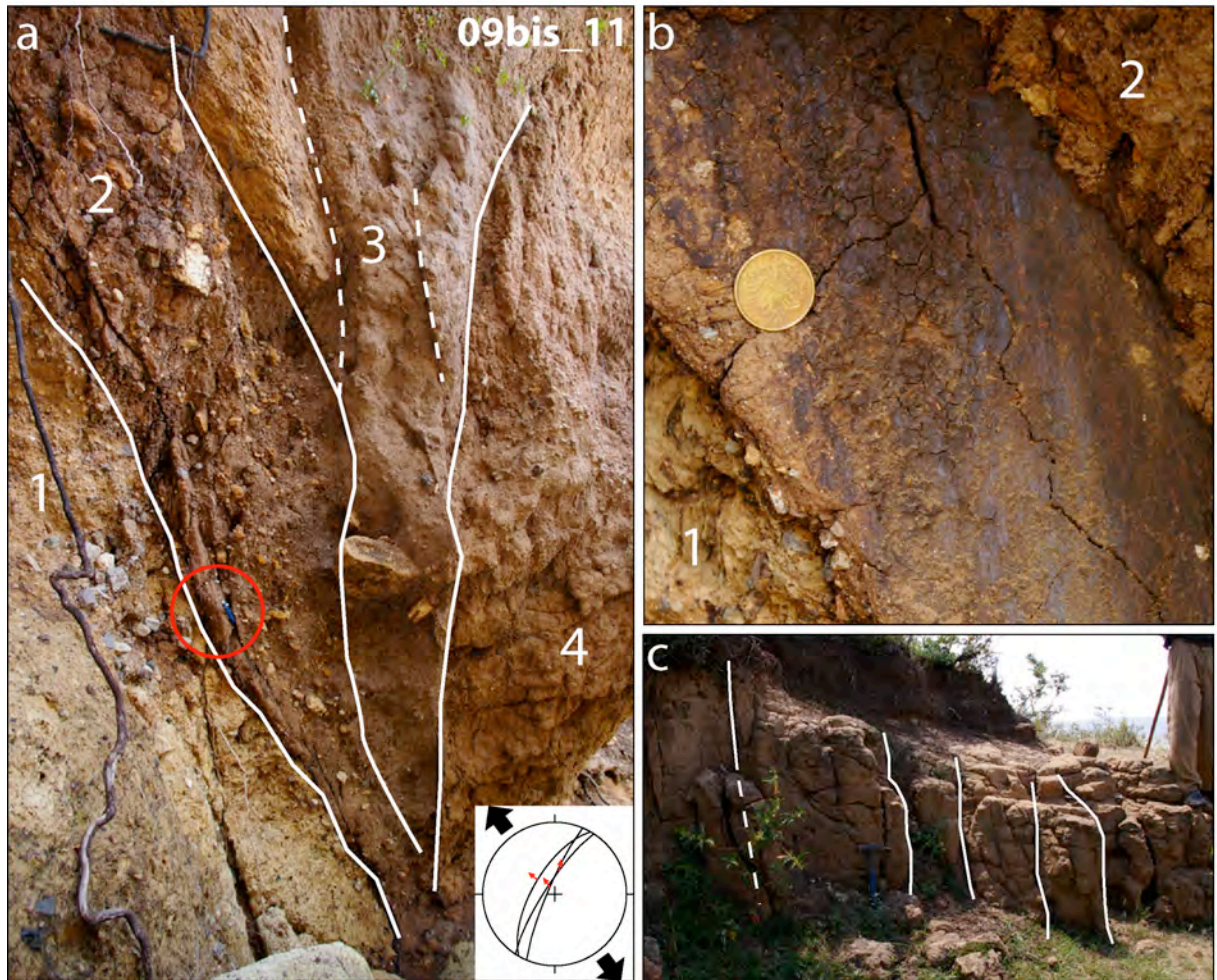
Fig. 5.22: Measurement site 09bis_11. a) Four different faulted deposits (white lines indicate different planes separating different deposits. Dotted lines indicate planes internal at the same deposit). b) kinematics indicators on a plane between deposit 1 and the earlier deposit 2. c) small faults displacing deposit 4.
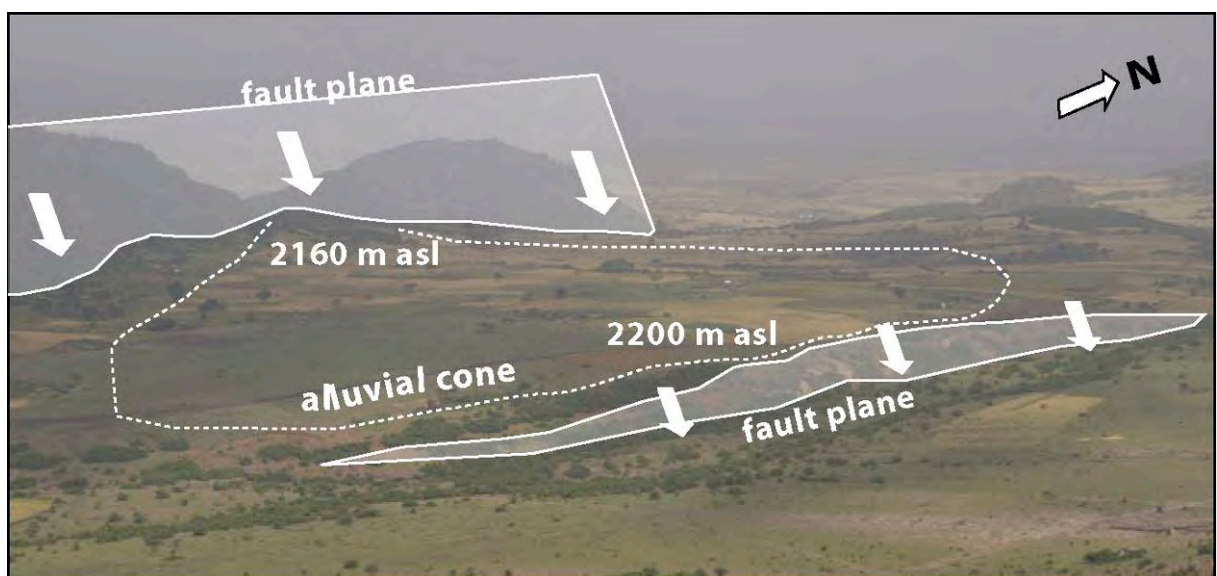


Fig. 5.23: Line drawing of tilted alluvial cone in the Langano Rhomboidal Fault System (photo taken from the rift margin).

In summary, these results document the occurrence of Quaternary, and in some cases Holocene, tectonics for the faults of both the margins and the rift floor (WFB faults). The obtained extension directions vary from ca. N110°-130° on the MER margins (with an average value from the cumulative analysis indicating a ~N110°E extension; Fig. 5.24), up to N90°-120° along the WFB. The cumulative analysis of the WFB data reveals a consistent N100°E±5° (Fig. 5.24) extension that, on the basis of the analogue modelling results (see Chapter 3), is expected to represent the regional extension direction acting in the system (see section 6.3).
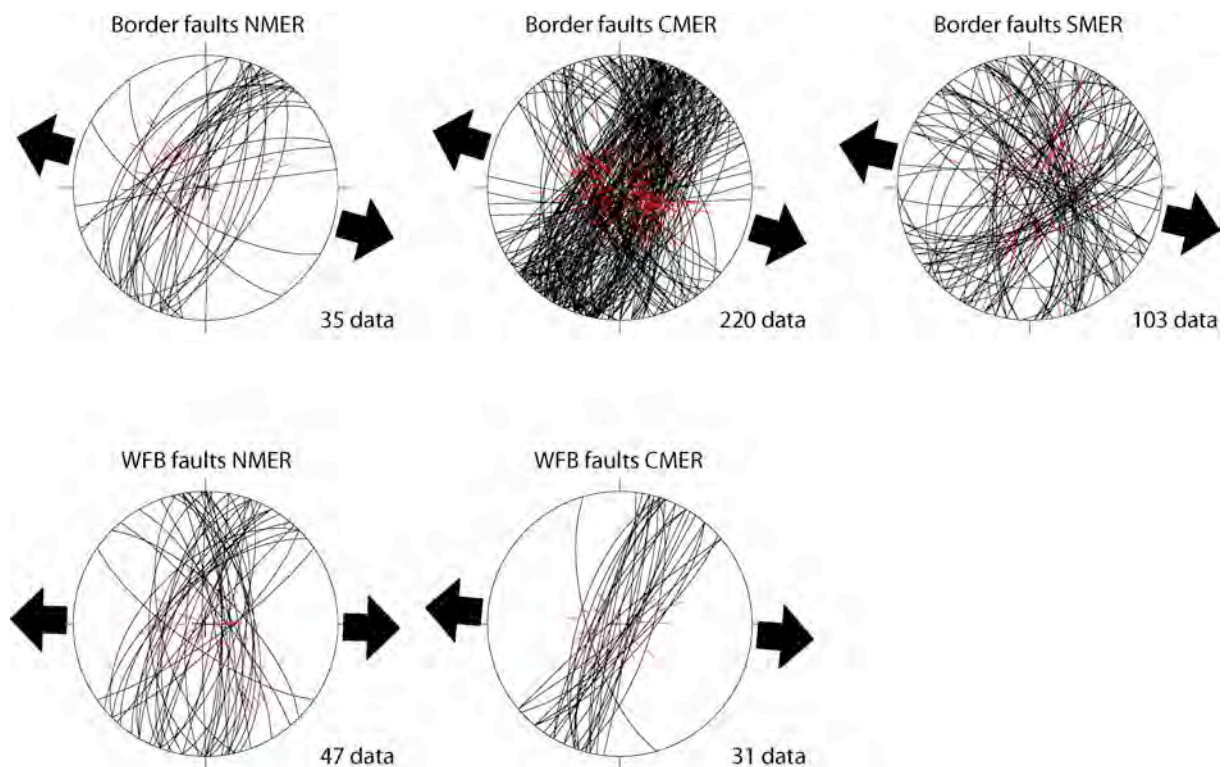


Fig. 5.24: cumulative analyses of the border and WFB faults in the three main MER segments. The data number on WFB faults in the SMER do not allowed a significant and reliable result.

# Chapter 6

## Discussion and conclusion

In this chapter, the results of oblique rifting analogue modelling (Chapter 3) are compared with satellite image analysis (Chapter 4) and field structural data (Chapter 5). Previous works have compared the results of analogue models either with the whole MER fault pattern (Bonini et al., 1997) or considering two main segments only (Corti, 2008). This thesis refines such previous analyses by presenting a complete and more detailed investigation of the whole fault pattern of the four distinct MER segments (NMER, CMER, SMERn and SMERs). This allowed to shed new light on the MER kinematics boundary conditions, to discriminate an along axis variation of the rift evolution, to investigate the role of pre-existing lithospheric weakness and the partition of deformation between the rift margins and the valley floor, and, finally, to propose a new general evolutionary model for the continental rifting process.

### 6.1. Comparison between analogue models and nature

The peculiar organization, trend, pattern, distribution and architecture of faulting of the different MER segments (see Chapters 2,4) can be associated and compared with different obliquity models (see Chapter 3).

Specifically, in term of fault pattern and rift architecture, the NMER can be compared to the 45°-obliquity models, the CMER to the 30°-obliquity models, and the SMERn and SMERs to the 15°-obliquity and orthogonal extension models, respectively (Fig. 6.1).

Some points highlighting the similarity between the rift architecture in models and in the different MER segments were discussed below:

1)     The two-stage model evolution (Fig. 6.2; see section 3.3. for details) mimics the diachronous activation of border faults during the Early Pliocene-Late Miocene, and internal Wonji faults, active since the Late Pliocene-Early Pleistocene (Fig. 6.3). This aspect of the MER evolution is well evident in the NMER (e.g. Wolfenden et al., 2004).

2)     The analogue models and natural prototype display similar fault patterns, characterized by the two distinct fault families affecting the border and the rift depression respectively (Fig. 6.1; Corti, 2008). The best fit of main fault orientation peaks (i.e. border and internal faults) between models and nature is obtained for a 10° clockwise rotation for all the different obliquity-rift models (Figs. 6.3, 6.4). After such a rotation the main fault orientation peaks of the analogue models almost perfectly coincide with the main fault orientation peaks of the corresponding MER segments (Fig. 6.4). Note that the nature-model

comparison has been performed using completely extended models that simulate bulk extension with β factor varying between ~2 for orthogonal extension model and ~1.6 for moderate obliquity model (being β the ratio between the actual and the pre-rift width). These values are higher than that estimated for the MER, in which β≈1.12 in the SMER (Ebinger et al., 1993); β≈1.2 in the CMER (Tiberi et al., 2005) and β≈1.5 in the NMER (Wolfenden et al., 2004). Nevertheless, during model evolution the orientation of the main fault peak (Fig. 6.4) is constant, and thus, independently of the different maturity, the comparison between model and nature is reliable. The discrepancy in rift maturity between model and nature leads only to a difference in the relative importance of internal faults peaks and border faults peaks. In particular the internal faults peak, which develop mainly during the second
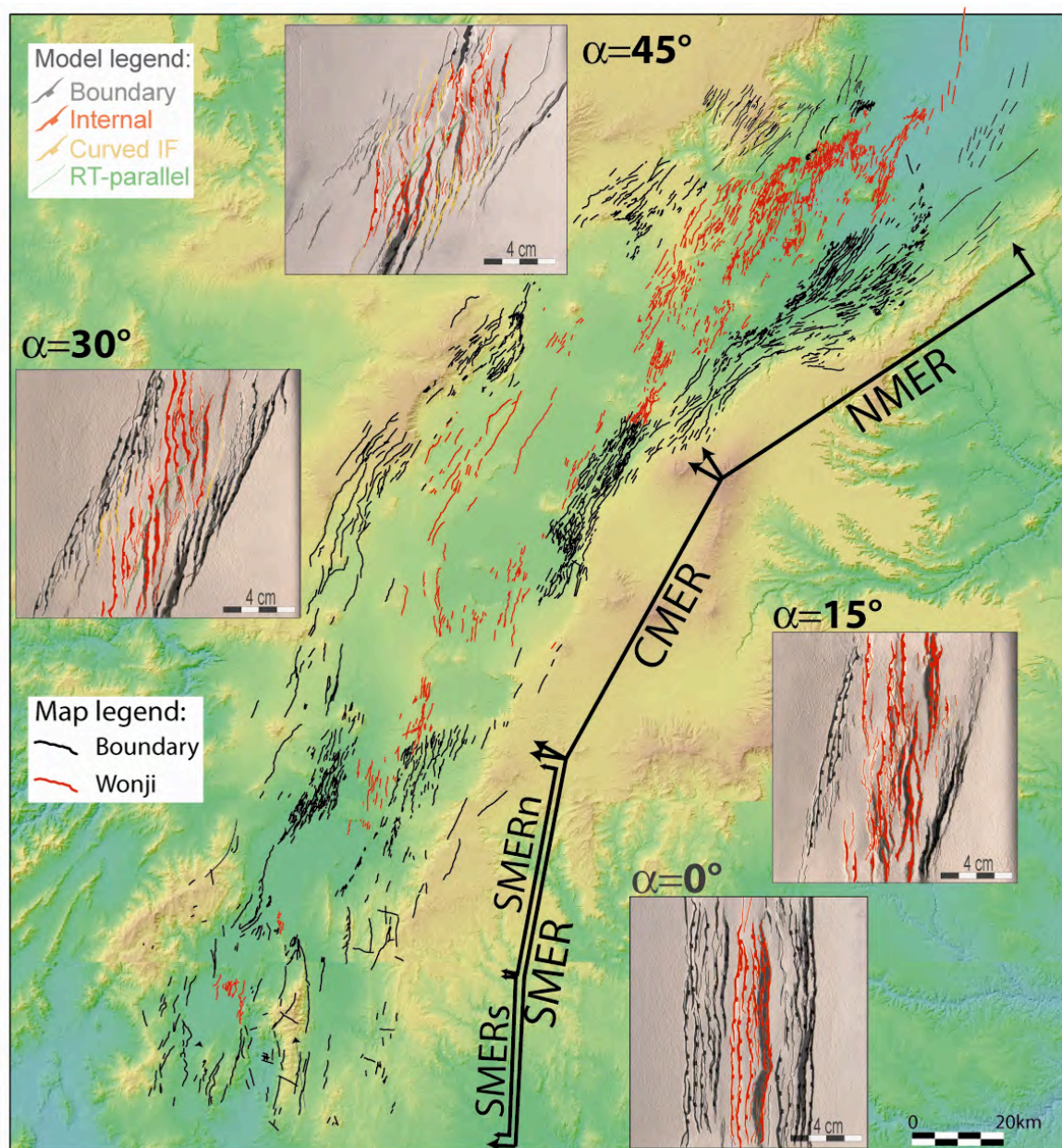


Fig. 6.1: The different MER segments are associated with different obliquity models on the basis of its similarities in term of fault pattern and rift architecture (see text for details).

evolutionary stage (cfr. Fig. 6.2), results comparatively higher in models than in the MER (Fig. 6.4).

3) The internal faults in orthogonal and low obliquity models (α=0°-30°) are perpendicular to the direction of extension (see section 3.2.2. and Figs. 3.20, 6.4), whereas the internal faults are slightly oblique in the 45° obliquity models , forming a ~10°-15° angle (see section 3.2.2. and Figs. 3.20, 6.4). In the MER an analogous behaviour can be observed:  the Wonji faults, which trend between N10° and N15°E in the Southern and Central segments, are essentially perpendicular to the average ~N100°E direction of extension (section 2.2), whereas in the NMER the WFB faults trend ~N20°E and form an average 10° angle with the orthogonal to ~N100°E extension direction.
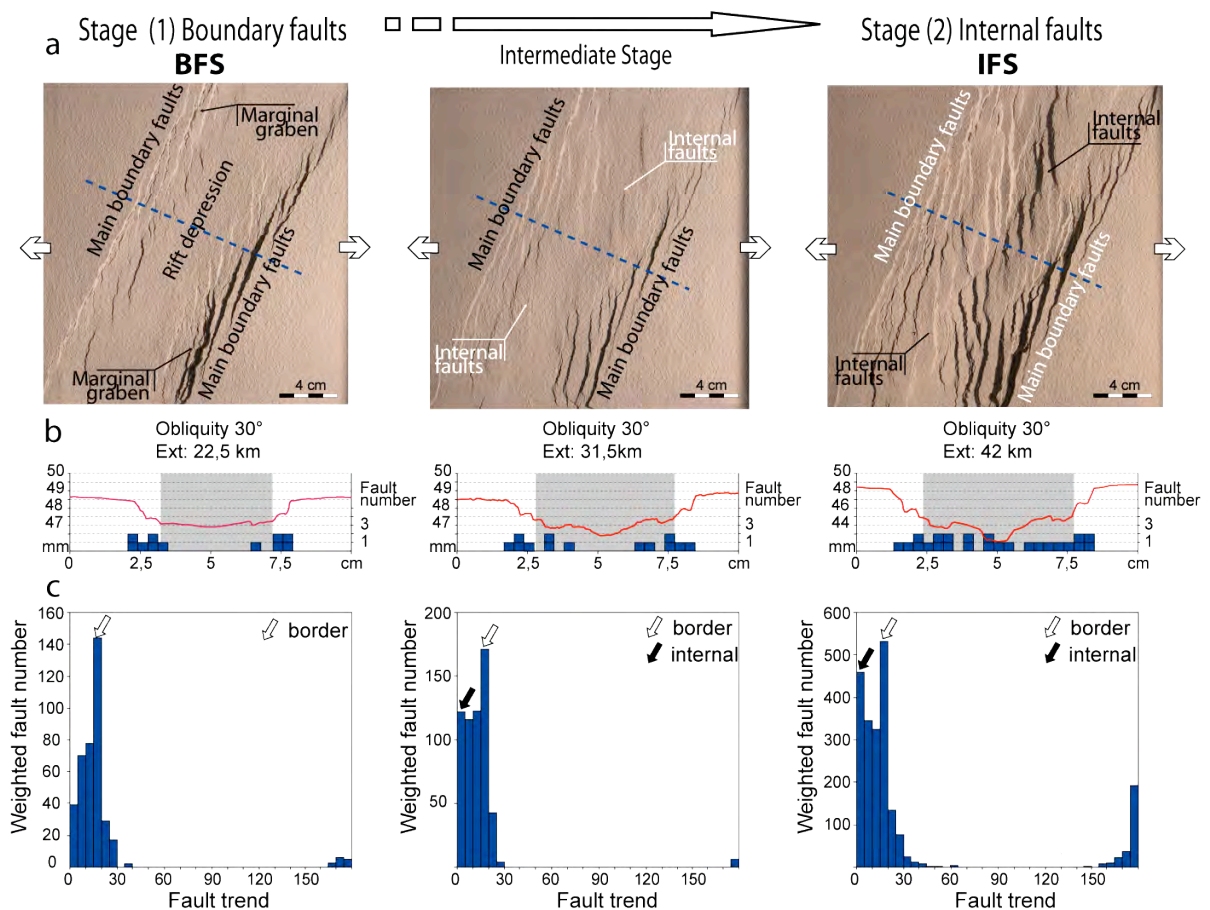


Fig. 6.2: Two stage model evolution (see section 3.3 for details), summarized through three representative stages of the low obliquity model (α=30). Upper panels (a): top-view photos of the model in three different evolutionary stages. Left panel: initial stage of rifting, first evolutionary phase with development of the boundary faults (~15mm of extension that scales down ~22.5 km in nature). Central panel: intermediate stage, comparison of the first internal faults (~21 mm of extension that scales down ~31.5 km in nature). Right panel: final stage, second evolutionary phase with most of the deformation accommodated by internal faults (~27 mm of extension that scales down ~ 42 km in nature). Central panels (b): Model topographic profiles (data from laser scanning) perpendicular to the rift (profile traces are the dotted blue lines in the upper panels). Each profile is 10 cm long; the blue rectangles are faults projected onto the profiles; they lie over a 0,33 cm wide belt over the profile trace. The pale grey area indicates the rift depression width. Lower panels (c): Weighted fault distribution illustrated as 0°-180° histogram at 5° intervals: note the increase in importance of the internal fault peak as the system evolves.
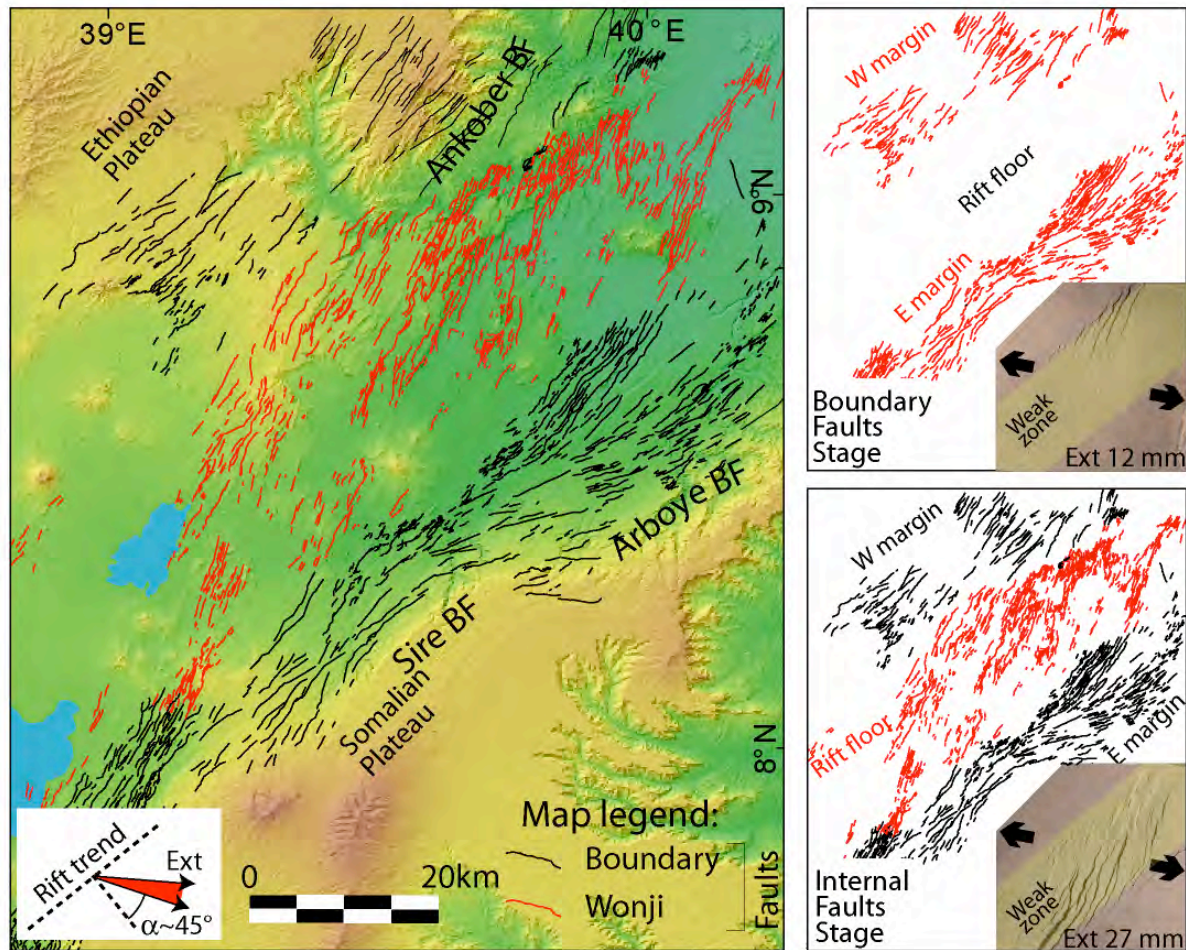
Fig 6.3: Simplified structural map of the NMER. The right panels schematically show the similarity between model (obliquity 45° for the comparison with the NMER, see also Fig. 3.16) and nature in term of evolution of deformation (cfr. Fig. 6.3): in both cases, a first phase of boundary faults development, basin subsidence and no deformation of the rift floor (boundary faults stage) is followed by activation of en-echelon faults obliquely cutting the rift depression, strongly reducing the slip on boundary fault systems (internal faults stage). BF: boundary fault. Red lines are the WFB (internal in the models) faults. In black, boundary faults. Black arrows in NMER and CMER panels indicate the local extension direction obeteined from fault-slip data analysis

4)      Border faults in moderate obliquity models (α=45°) reduce their activity sooner than in models with α<30° (as the transition to the second evolutionary phase requires a minor amount of bulk extension, see section 3.3.1. and Fig. 3.18), resulting in a less clear morphological expression and consequently in a minor statistical weight of these structures respect with the border faults characterizing orthogonal extension and low obliquity models. This is in collusion with the nature where the NMER seems to be more evolved and its border faults are largely inactive and on the whole eroded, as indicated by geological data and historic and local seismicity (Gouin, 1979; Wolfenden et al., 2004; Keir et al., 2006). The CMER and SMER border faults are instead tectonically active (e.g. Keir et al., 2006). Consequently, that the number and length of the NMER border faults may result underestimated, leading the corresponding orientation peak to show a minor statistical weight (Fig. 6.4).
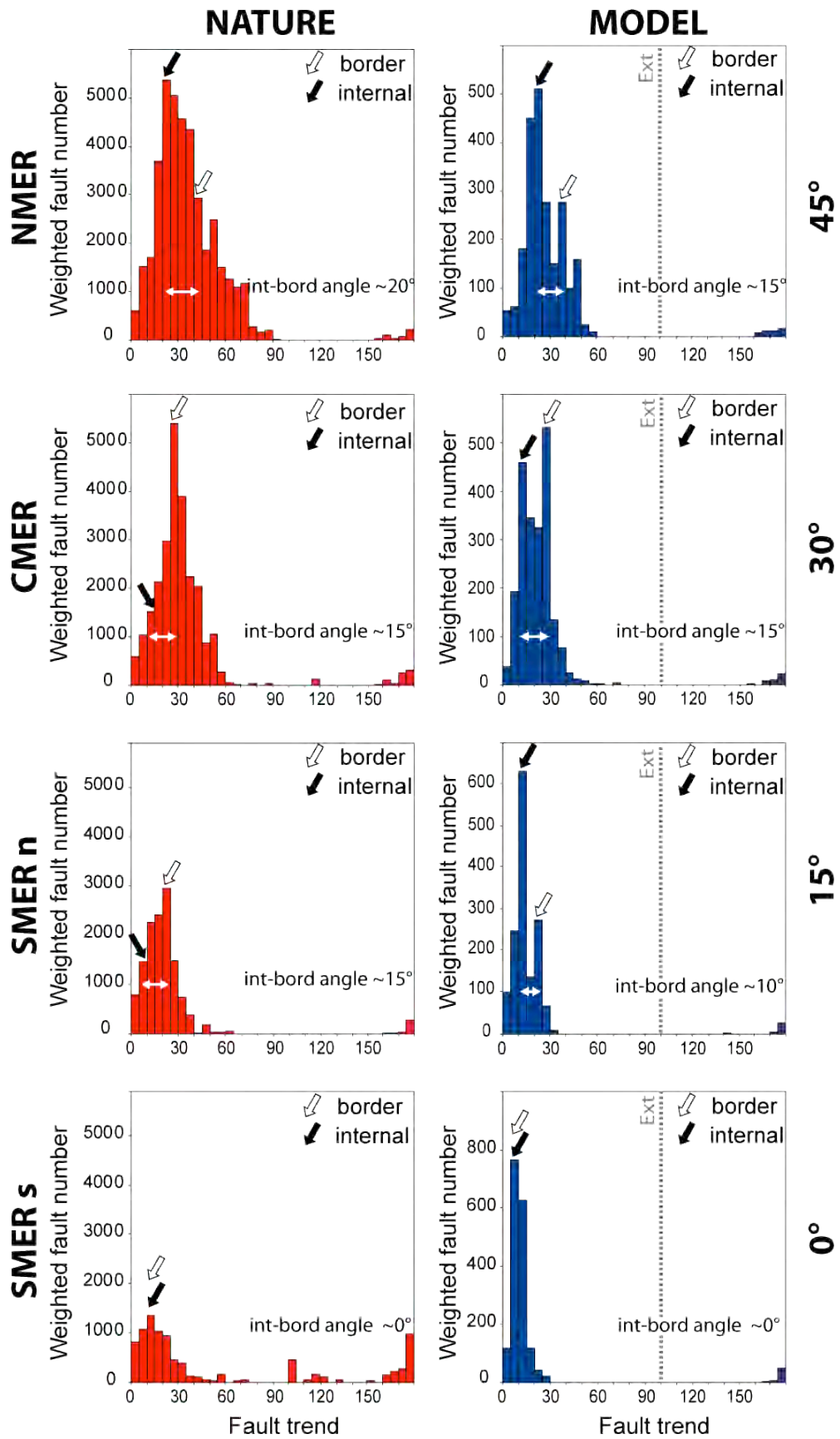
Fig. 6.4: Main Ethiopian Rift versus model fault azimuth distribution. Left panels: distribution histograms of the fault azimuths of the Main Ethiopian Rift segments. Right panels: fault azimuth distribution histograms of the corresponding obliquity models after a 10° clockwise rotation, that is necessary to achieve the best fit between models and nature (see text for details). The resulting N100°E direction of extension is reported in right graphs. White horizontal doublehead arrows indicate the angle between internal and border faults.

CMER and SMER border faults are instead still active (i.e. Keir et al., 2006) and present a more clear morphology. This is manifested by a major statistical weight of their main orientation peak (Fig. 6.4).

5)     The internal faults (WFB faults in nature), both in the models and in nature, are arranged in right-stepping en-echelon segments. This arrangement is more evident and organized in the NMER and in the correspondent 45° obliquity model (Fig. 6.5).
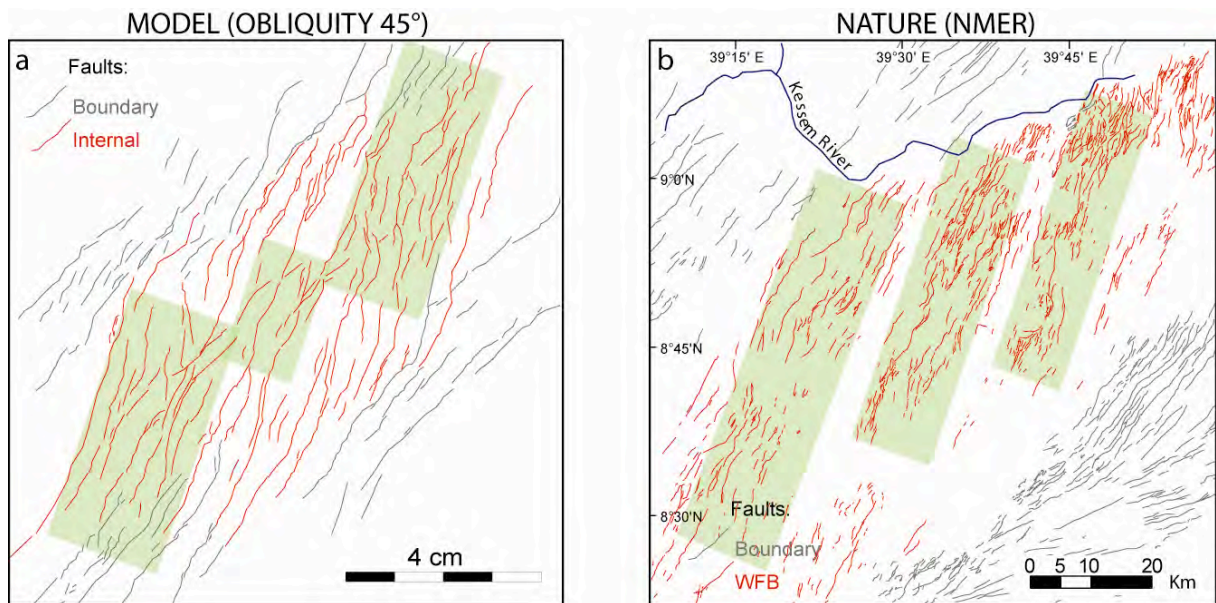


Fig. 6.5: Comparison of fault patterns and rift architecture in (a) models (obliquity 45°) and (b) nature (NMER segment). Note the similar right-stepping en-echelon arrangement of the internal fault segments (pale green area) (WFB in nature).

6)     The length of border faults increases from NMER to SMER (see section 4.1.2.), and, in a similar fashion, model fault length increases from α=45° to α=0° (see section 3.3.1.2. and cfr. Fig.3.21d).

7)     Both in the MER and in the models, the angle between internal and borders faults is a function of the rift trend orientation (i.e the rift obliquity), presenting higher values as the obliquity angle α increases (Figs. 6.4, 6.6). The values that internal/border faults angle shows in the different MER segments are comparable with the values measured in the correspondent obliquity model (Figs. 6.4, 6.6 and cfr. Fig. 3.21b).

Moreover, both MER segments and models show an overall similar trend of the total span of fault orientation (again function of the rift obliquity), which is larger for higher α values (Fig. 6.6). This is also testified by the standard deviation values of the weighted fault azimuth distributions (see caption of Fig. 3.12 and section 4.1.1.) (Table 6.1). Higher values presented in the azimuth dispersion by the SMERs data are attributable to the influence of pre-existing

basement structures that are largely exposed in this area, and to the superimposition of the present kinematics onto previous deformative stages (see section 4.1.2.3.).
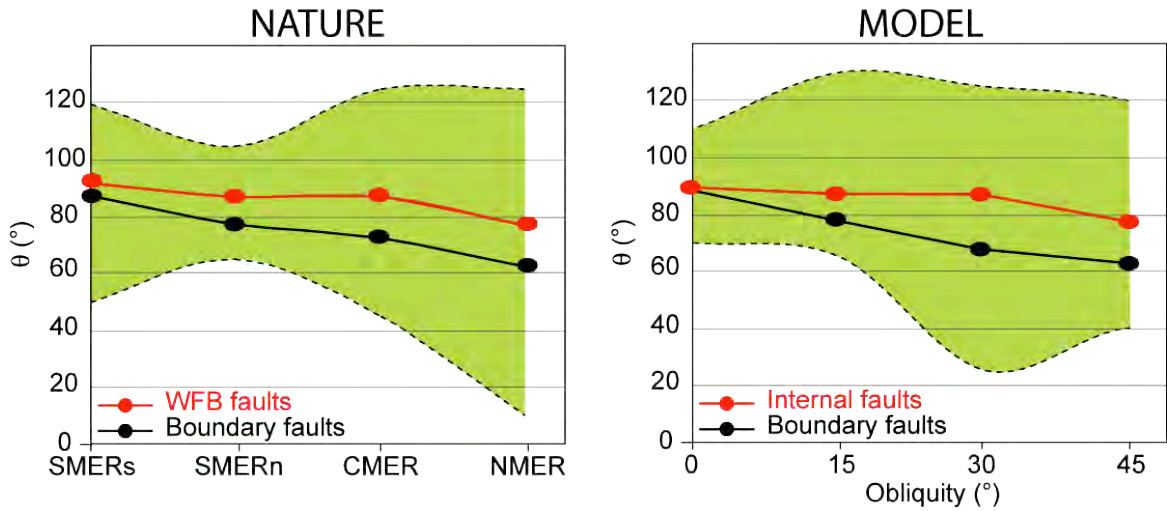


Fig. 6.6: Comparison between the fault systems orientation in the MER segments (left panel) and in the associated models (right panel), displayed as the value of the angle θ, i.e. the angle between the orientation of each fault system (defined on the basis of the peaks in the histograms of fault orientation, see Fig. 6.4) and the direction of extension (see Tron and Brun, 1991). For the MER segments, we considered the average direction of extension N100°, see section 2.2). The greenish area enclosed between dotted lines represents the total span of fault orientations displayed on histograms (Fig. 6.4).

| Nature | azimuth dev. stand. | Model | azimuth dev. stand. |
|--------|---------------------|-------|---------------------|
| NMER | 18.20 | $\alpha = 45°$ | 12.28 |
| CMER | 15.39 | $\alpha = 30°$ | 9.90 |
| SMERn | 10.57 | $\alpha = 15°$ | 6.96 |
| SMERs | 16.02 | $\alpha = 0°$ | 4.93 |

Table 6.1: comparison between the deviation standard values of the fault azimuth distribution of the different MER segments (left columns) and the corresponding analogue models (right columns).

Finally, we have to note that the minor secondary orientation peak, trending N100°-105°, observed in the SMERs faults orientation histogram (Fig. 6.4), was not reproduced in the corresponding orthogonal extension (α=0°) model (Fig. 6.4). As we have previously noted, these structures are referred to inherited pre-rift structures (see section 4.2.). Since models are not pre-deformed, they cannot develop similar structures.

## 6.2. Oblique reactivation of lithospheric-scale pre-existing weakness zones and partition of deformation: integration of model and paleostress data

Many authors have hypothesized a correlation between the MER localisation and a NE-SW-trending lithospheric-scale pre-existing weakness zone (Bastow et al., 2005, 2008; Corti, 2008; Keranen and Klemperer, 2008; Keranen et al., 2009) represented by a suture zone separating two distinct Proterozoic basement terranes underlying the Ethiopian and Somalian plateaus (Keranen and Klemperer, 2008). Channeling and ponding of hot plume material beneath this suture zone likely contributed to thermal weakening of the area of the future rift (Ebinger and Sleep, 2008). Overall, the presence of this pre-existing weakness created a strong, sharp lateral strength contrast with respect to the surrounding "normal" lithosphere. In agreement with previous findings (Corti, 2008), the comparison between models and nature suggests that the oblique reactivation of a lithospheric-scale inherited weakness may have controlled the two-phase rift evolution in the Main Ethiopian Rift (see section 3.3.2). In fact, extrapolation of model results suggests that the initial Mio-Pliocene MER deformation localized at strong rheological contrast between the pre-existing weak zone and the strong lithosphere underlying the surrounding plateaus, giving rise to large boundary fault systems bordering the subsiding, largely undeformed rift depression. Prolonged extension and thinning of the lithosphere below the rift led to the activation of the en-echelon WFB segments and the riftward migration of deformation observed during the Quaternary (see section 3.3.2.); successive magma upraising in these area of enhanced deformation contributed to the observed tectono-magmatic segmentation.

From this point of view, the differences in the lithosphere rheology affected by border faults (at the strong rheological contrast) and WFB faults (in a weakened but "homogenous" lithosphere) could explain the spatial and kinematical partition displayed by the two different faults systems in the Northern and Central MER segments (Fig. 6.7).

In fact, the strong differences between the two faults systems suggest a strain partition between border and rift floor: a nearly pure dip-slip kinematics marks the WFB faults of the rift floor, whereas a sinistral component of motion characterizes the fault systems at rift margins, as testified by the en-echelon arrangement of structures (Boccaletti et al., 1998; Corti, 2009 and references therein).

This is supported by paleostress data (see Chapter 5) in turn showing two different situations for borders and WFB faults: an overall ~N110°-130°E direction of extension on the borders faults and, conversely, an average N90°-N100° extension direction for the WFB faults (see Chapter 5). The partition of deformation between the rift margins of the MER and the valley

floor mimics that one observed in low and moderate obliquity models (see section 3.3.1.3.; Fig. 6.7). Consequently, on the basis of the analogue modelling results (see Chapter 3), the ~N90°-100°E direction of extension provided by WFB fault slip data is expected to represent the regional extension direction acting in the system. (Fig. 6.4). Conversely, the N100°-130° extension directions determined on the MER border faults likely represent a local stress perturbation at the rift borders. In fact, the internal WFB faults developed on a weak but "homogeneous" lithosphere that allows an almost pure extension, whereas the rheological discontinuity (i.e. the strong rheological contrast between the weakness zone and the surrounding "normal" lithosphere) over which the boundary faults have developed could represent a major source of stress perturbation, resulting in a local stress reorientation (e.g. Homberg et al., 1997).
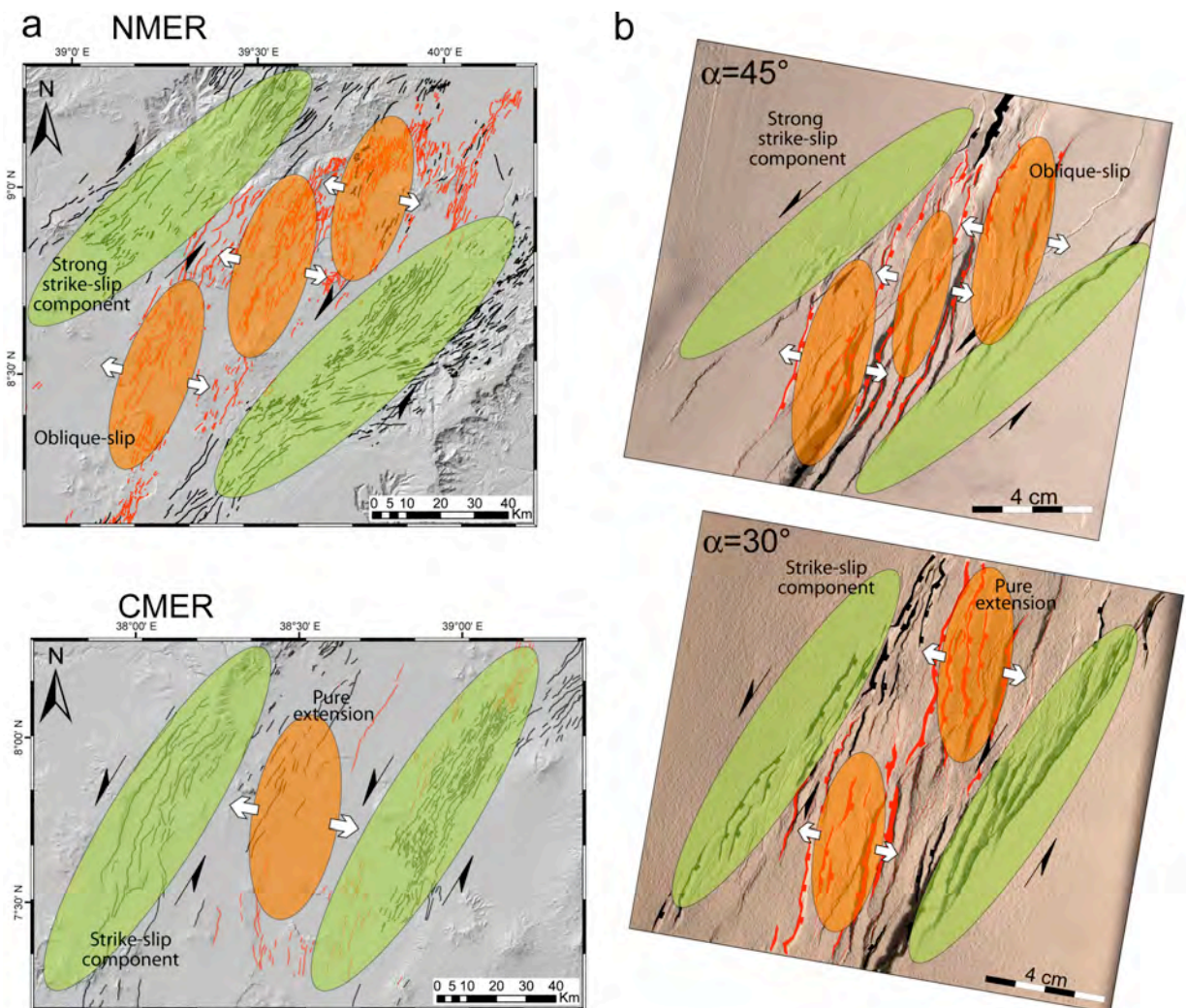


Figura 6.7: Partitioning of deformation: comparison between a) MER segments and b) model (α=45° and α=30°). Models were rotated 10° clockwise, to obtain the best fit between nature and model fault orientation (see section 6.1). Note that, as in moderate obliquity model (α=45°), the NMER shows a less developed partition of deformation, as the WFB faults results slightly oblique to the current ~N100° direction of extension (see Fig. 6.4), thus accommodating a (minor) component of strike-slip deformation.

Evidence of Quaternary activity both on internal and border faults (see Chapter 5) testifies different coeval extension vectors, over a short distance. For instance, WFB structural stations ET09_01 and ET09_04 in Quaternary Wonji Basalt show N98° and N100° extension directions respectively, while the border fault station ET09_07 shows a N140° extension direction and the fault cuts a Quaternary colluvium (see Fig. 5.11). These structural stations are only ~20 km distant. This observation may be represent an alternative model to the hypothesis that the different observed kinematics are the result of a change in the Nubia-Somalia motion (e.g. Boccaletti et al., 1998; Wolfenden et al., 2004, Bonini et al., 2005).

The scarcity of data and the almost perpendicular trend of the southern MER segments to the average ~N100°E extension direction (see section 2.2 and Fig. 6.8) does not allow the recognition of the same deformation partition observed on the northernmost MER segments, even if a sinistral component of motion along the border faults can be observed (Boccaletti et al., 1998; Corti, 2009 and references therein).

## 6.3. Implication for the Nubia-Somalia kinematics

The 10° clockwise rotation that the fault peaks of each model require to match those in the MER, results in an overall N100°E direction of extension between the opposite sides of each model (Fig. 6.4). This direction is in very good agreement with the results of geodetic measurements that indicates a current ~N100° ±5° extension vector between Nubia and Somalia plates (e.g. Fernadez et al., 2004; Bendick et al., 2006; Calais et al., 2006; Stamps et al., 2008), as well as it with paleostresses and geological data (Bonini et al., 2005; Casey et al., 2006; Pizzi et al., 2006) and plate motion analysis (Chu and Gordon, 1999; Royer et al., 2006; Horner-Johnson et al., 2007) (Fig. 6.8; see section 2.2 for details).

In the analogue models the applied kinematics was kept constant during the experiment and thus it controls the two-phase rift evolution (Fig. 6.2). On this basis, one can infer that between Nubia and Somalia plates a constant ~N100°E motion could have acted in the MER since the onset of the rifting process and could have controlled the diachronous activation of boundary and Wonji faults (e.g., Corti, 2008). On this basis, a simple ~N100°E extensional kinematics could be responsible for the whole rift evolution, highlighting the major role that the rift obliquity plays in the MER evolution (Corti, 2008).

From this point of view, the compatibility of the same direction of extension with all the different MER segments can help constraining also the less defined pre 3.2 Ma kinematical boundary condition. The pre 3.2 Ma MER evolution may thus result coherent with a constant

N100°E extension direction, that therefore would have been acting since 11 Ma, i.e. since the early phases of rifting (see section 2.2).
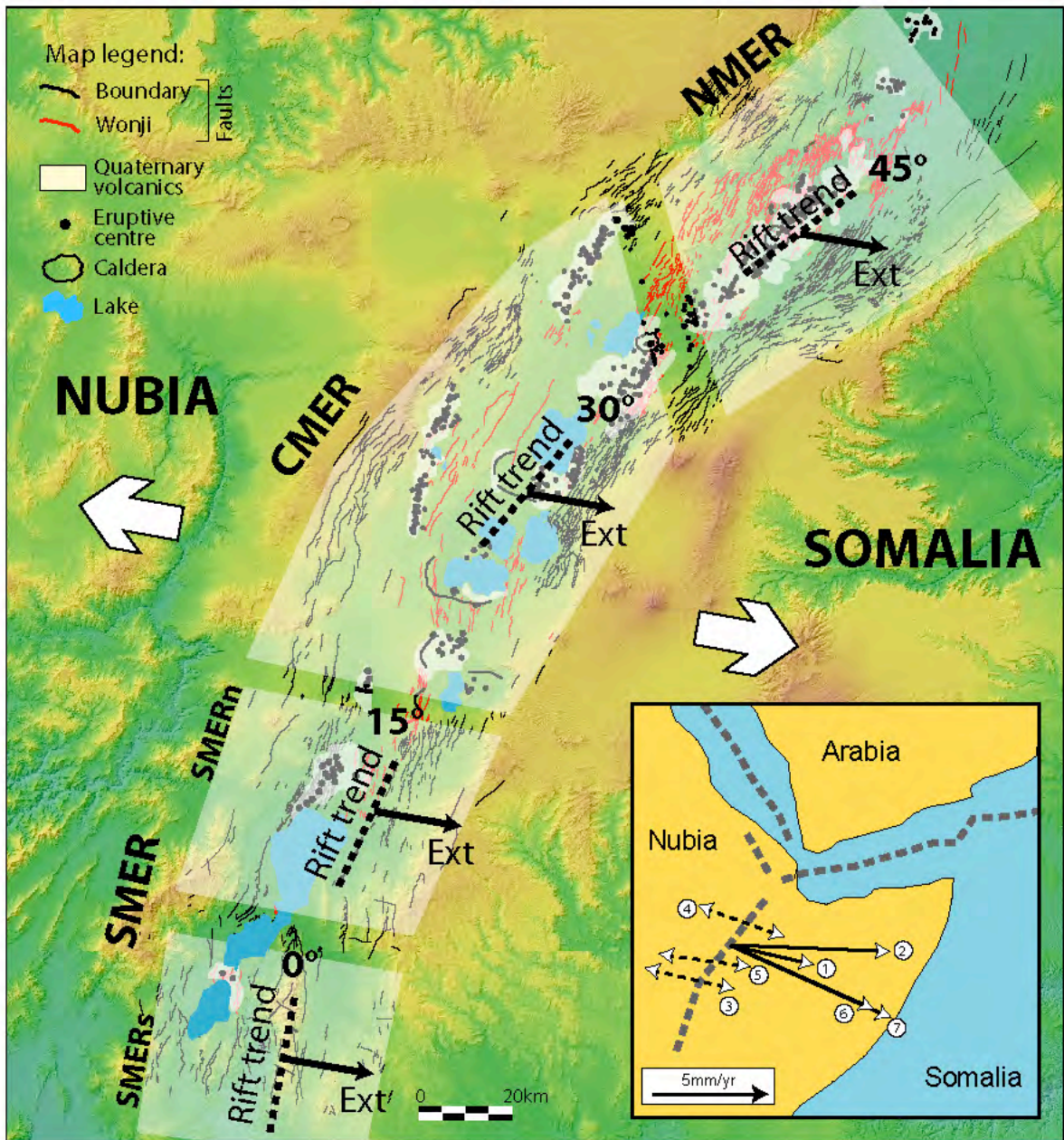


Fig. 6.8: Structural setting of the Main Ethiopian Rift (as in Fig. 6.1). The pale grey transparencies indicate the four MER segments: Northern, Central and the two Southern subsegments. The rift trend and the extension direction inferred from analogue modelling are indicated for each with black arrows. White arrows indicate the Nubia-Somalia motion deduced from model analysis. Inset (modify after Corti, 2009): Nubia-Somalia displacement vectors at Main Ethiopian Rift latitude calculated with different methodologies: 1-2) geodetic observations (Bendick et al., 2006; Stamps et al., 2008); 3) geophysical data (Keir et al., 2006); 4-5) geological data (Casey et al., 2006; Pizzi et al., 2006); 6-7) plate motion data (Royer et al., 2006; Horner-Johnson et al., 2007).

## 6.4. Evolution of different MER segments

The comparison between natural settings and the model evolution suggests that the differences observed in the fault pattern and in the distribution of deformation along the MER segments (see section 4.2) may result from different rift maturity. This is illustrated by the plotting of faults along topographic profiles on the MER segments and the models (Fig. 6.9), which helps to characterize the deformation distribution, and the along axis rift maturity.

The NMER fault pattern is characterized by well developed WFB fault segments that affect the rift floor and accommodate ~80% of the current extensional deformation (Billham et al., 1999), whereas the boundary faults are generally deactivated and eroded (Fig. 6.9). These characteristics accord with the fault pattern and the distribution of deformation that is typical of the stage 2 of model evolution (Figs. 6.2, 6.9). At this stage a model has already experienced the riftward migration of the deformation. On this basis, the NMER can be considered as a mature rift.
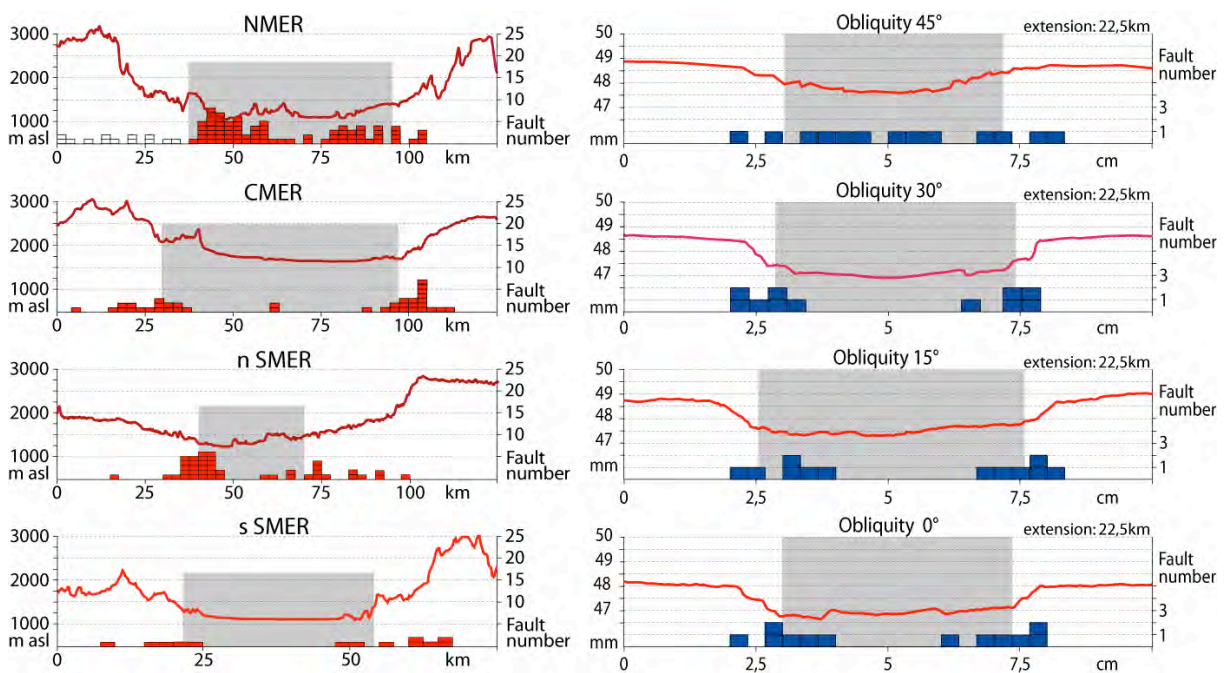


Fig. 6.9: Evolution of different MER segments illustrated as comparison between the faults observed along four topographic profiles (traces are the yellow dotted lines in Fig. 4.1) across the MER segments (left panels), and along profiles across the corresponding obliquity models (at ~15 mm of extension, corresponding to ~22.5km in nature; right panels). White rectangles in the NMER profile indicate the eroded border faults in the Kessem River area (Fig. 4.1, see text for details). Model topographic profiles (data from laser scanning) are perpendicular to the rift (cfr. Fig. 6.2). Each profile is 10 cm long; each fault that lies over a 0,33 cm wide belt over the profile trace is projected onto the profiles and indicated with a blue rectangle. The pale grey area indicates the rift depression width. Fault affecting the valley floor (pale grey area) in the CMER, SMERn and SMERs, and in the corresponding 30°, 15° and 0° obliquity models, are mainly related to the marginal grabens and thus to an early evolutionary stage (cfr. Fig. 6.2). Only in the Northern MER and 45° obliquity model, the faults in the rift depression can be related to a later evolutionary stage (cfr Fig. 6.2).

This finding is supported by geophysical data that point to a NMER lithosphere extensively modified by magmatic processes and that can be considered in a transitional stage between a completely continental and an oceanic lithosphere. The NMER lithosphere is in fact characterized by a relatively thin crust, thickening southward to the boundary with the CMER (e.g. Dugda et al., 2005; Maguire et al., 2006; Mickus et al., 2007) and, above all, an high concentration of Quaternary basaltic magmatism and a well developed magmatic plumbing system in correspondence of the tectono-magmatic WFB segments (e.g. Ebinger and Casey, 2001) that allows a fast magma rising (Rooney et al., 2007). Moreover, cooled mafic intrusions in the mid and lower crust (Keranen et al., 2004; Daly et al., 2008) and 3-5% of melt in the upper mantle (Cornwell et al., 2006) are found beneath the NMER.

In contrast with previous works suggestind NMER border faults to be completely deactivated (e.g. Wolfenden et al., 2004; Casey et al., 2006; Keir et al., 2006), the comparison with analogue model evolution suggests that the NMER border faults could still present a minor tectonic activity (see section 3.3.1. and Fig. 6.2); this is also supported by fieldwork results, which provided evidence of Quaternary activity along a structures at the NMER-CMER boundary (see Fig. 5.11).

The comparison between the CMER fault pattern (Figs. 6.4, 6.9) and low obliquity (α=30°) model evolution (Fig. 6.2), suggests that the internal faults, which are mostly concentrated near the rift margins, could represent incipient WFB faults propagating from the rift borders, or, in some cases, they are associated with marginal grabens, as in the Butajira area (Fonko-Guraghe western margin, Fig. 4.1). The predominance of the border faults and the incipient nature of the internal faults (Fig. 6.9) suggest that the CMER segment is in a transitional stage correlatable to the transitional evolutionary stage of analogue models (Fig. 6.2).

In the SMERn and the SMERs, the almost total absence of faults in the rift floor and the concentrated of the deformation at the rift borders (Fig. 6.9) indicate that such segments are in an early evolutionary stage, similar to the Stage 1 of model evolution (Fig. 6.2).

The lower maturity expressed by the CMER and the SMER segments is also reflected by the lithospheric characteristics, in particular by a minor amount of Quaternary volcanic products (see Fig. 6.8 and section 2.4.2.2.) with respect to the NMER. Cooled intrusions and crustal melts underneath the rift depression are rarely detected, as beneath the Debre Zeyt volcanic field (Keranen et al., 2004; Whaler and Hautot, 2006). Moreover, the crust is thicker, reaching a depth of ~38-40 km in the CMER (e.g. Dugda et al., 2005; Maguire et al., 2006; Mickus et al., 2007), and ~30 km in the SMER (Dugda et al., 2005). However, despite the lower rift

maturity, the SMER crust depth is lower than in the CMER, likely it was previously thinned be the northward Kenya Rift propagation at around 20 Ma (Bonini et al., 2005).

These features indicate that the CMER and SMER lithosphere is characterized by lower rates of magmatic modification (e.g. Keranen and Klemperer, 2008). In particular, the CMER lithosphere is considered as a continental lithosphere poorly modified by the incipient magmatic processes. Instead, in the less evolved SMERn and SMERs, occurring in an early continental rift stage, the lithosphere is considered as completely continental (Rooney et al., 2007).

Thus, a strong correspondence between the different rift maturity expressed along axis and the different lithospheric characteristics of each MER segment and its magmatic evolution can be highlighted (Corti, 2009 and references therein).

The evolution of different obliquity models shows that the timing of the riftward migration of the deformation is a function of the obliquity (i.e. the rift trend). This implies that the same amount of bulk extension may produce different rift maturity in different obliquity models (i.e. rift are more evolved as α increases). The comparison between the different MER segments and the corresponding models shows a clear similarity in the deformation distribution along the orthogonal to the rift axis (Fig. 6.9), suggesting a strong dependence of the MER evolution on the oblique kinematics.

Nevertheless, the effect of a southward rift propagation from Southern Afar to the SMER (Bonini et al., 2005), can represent a further factor promoting the inferred southward-decreasing rift maturity, in addiction to the rift obliquity dependence (on equal amount of extension) outlined above. This southward rift propagation could thus represent a concomitant cause in the definition of the observed pattern.

The above results highlight the major role of the kinematics in the MER evolution, showing the different maturity of the MER segments as a consequence of different obliquity angle, coupled with the southward rift propagation (Bonini et al., 2005). Moreover, the along axis variation of the WFB faults orientation (perpendicular to the inferred direction of extension in the CMER and SMER, and slightly oblique in the NMER) suggests that during the early stages the en-echelon arrangement of the WFB segments (Fig. 6.6) is primarily controlled by the tectonics and is essentially independent of magma rising. However, WFB segments guides and focus the magma uprising, as supported by the trend of the eruptive centres, which is variable along axis and follows the trend of the WFB faults themselves (Corti, 2008), such that as the process evolves, magma weakens the lithosphere and increasingly controls a largest part of the deformation (e.g. Buck, 2004; Keranen et al., 2004; Keir et al., 2006). This

results in the magmatic intrusions observed in the NMER, whose en-echelon arrangement traces, on the surface, the WFB segments distribution (Ebinger and Casey, 2001; Keranen et al., 2004; Keir et al., 2006, 2009).

## 6.5. Progression of continental rift

As discussed above (see section 6.4.), the different MER segments can be used to exemplify the typical evolution of continental narrow rifts that is outlined in Fig. 6.10.

The rift evolution begins with the definition of a main subsiding basin and the development of faults on the depression boundaries in response to the horizontal pull exerted by plate-driving forces. This early fault-dominated continental rifting stage is peculiar of the present Southern MER segments (Fig. 6.10a). As the system evolves, deformation migrates from the margins, where boundary faults are still active, to the centre of the rift depression where incipient internal faults start to form (Fig. 6.10b). This is characteristic of the transitional rifting stage, as can be identified in the CMER, where young faults affecting the rift floor may be observed and associated with incipient WFB propagating from the rift border. With increasing rift maturity, the system evolves toward an incipient continental rupture stage. Most of the volcano-tectonic deformation is focused on the magmatic segments located inside the rift depression (e.g. Ebinger, 2005): this stage is characterized by a strong feedback between magmatic and tectonic processes that involves a significant modification of the lithosphere rheology. Magma supply and diking (see above) prevents the increasing of the stress to a level able to activate the border faults, which consequently reduce or cease their activity (Buck, 2004). The NMER segment, and the associated en-echelon WFB tectono-magmatic segments, is a good exemplification of this magma-assisted evolutionary stage (Fig. 6.10c). In addition, the en-echelon arrangement of WFB tectono-magmatic segments typical of the NMER is also very similar to the en-echelon arrangement of the second-order segmentation of oceanic ridges (e.g. Hayward and Ebinger, 1996) and the crustal structures beneath the WFB (i.e. magmatic intrusions and diking) mimic those characterising the slow-spreading ridges, such as those in the Northern and Iceland neovolcanic seafloor spreading zones (Daly et al., 2008 and references therein). This may indicate a transitional stage between continental rifting to seafloor spreading (Daly et al., 2008). At this stage, crust and lithosphere are strongly modified by magmatism and new crust is formed in correspondence to the large crustal magmatic bodies of the tectono-magmatic segments. These crustal cooled magmatic bodies are expected to load the lithosphere and cause sills and basalt flows to dip toward the rift-or breakup axis to form seaward dipping lavas (see Appendix).
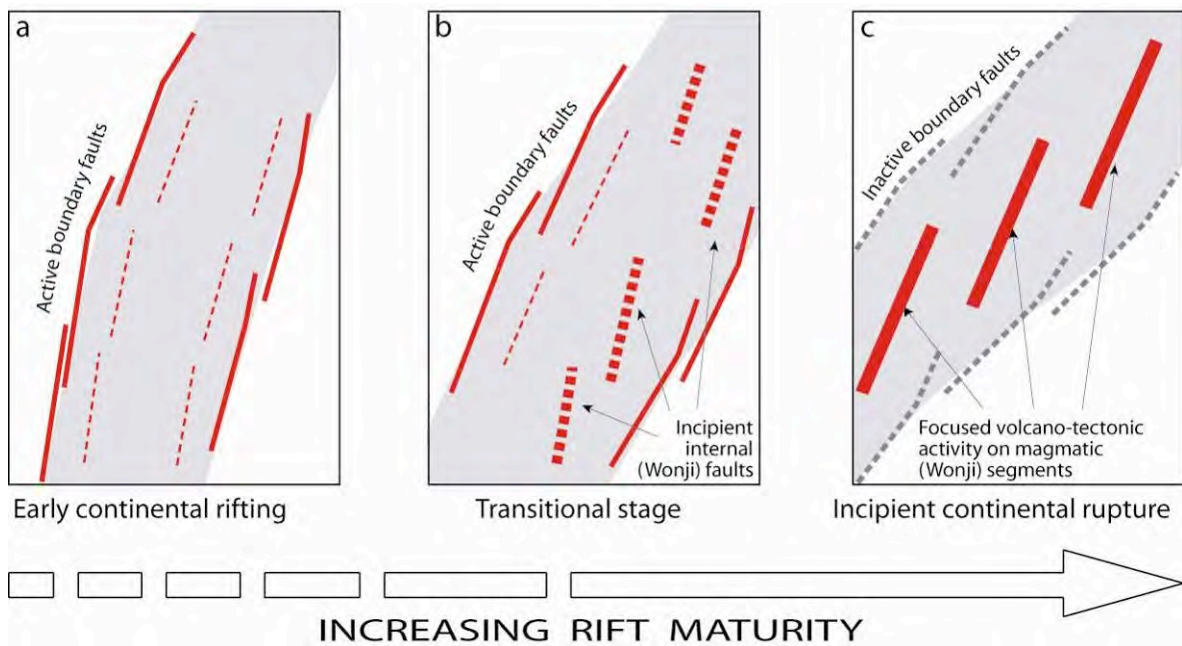
Fig. 6.10: Proposed schematic evolution of a continental rift based on the comparison between structural analysis of the MER and the analogue model results. Progression from (a) an early continental rifting stage with active boundary faults defining a subsiding undeformed basin, to a (b) transitional stage characterized by active boundary faults and incipient internal faults affecting the valley floor, to (c) incipient continental rupture stage, where deformation is mainly accommodated by volcano-tectonic segments inside the rift depression. Each MER segment is exemplificative of a specific evolutionary rifting stage.

The evolutionary model proposed in this work follows the evolutionary phases proposed in the magma-assisted rifting model (e.g. Ebinger, 2005; Kendall et al., 2005). Nevertheless, whereas the magma-assisted model emphasises the role of magma injection on the transition from boundary faults to magmatic segments (WFB in the Main Ethiopian Rift), our model suggests that rift evolution, and also the riftward migration of deformation, is primarily controlled by the oblique rifting kinematics during the early stages, interpreting the localization of the magmatic activity along the internal WFB faults as a passive feature (see above, e.g. Corti et al., 2003). Only later, magma-assisted model primarily controls the rift kinematics.

# Chapter 7

# Conclusive remarks

This thesis focused on the evolution of the Main Ethiopian Rift (MER), which is a continental rift separating the Nubia and Somalia plate. The MER offers a complete record of the time-space evolution of a continental rift, from its early stages to more evolved stages, and thus it may be taken as archetype for the continental break-up evolutionary process and for studying the continental rift evolution.

This work aimed at better constraining some aspects of MER evolution through a multidisciplinary approach, that integrates centrifuge experimental modelling applied to the MER, satellite images analysis and structural analyses in the field.

The centrifuge models have improved existing experimental studies of oblique rifting by considering a complex brittle-ductile lithospheric multilayering, and more realistic boundary conditions in terms of application of extensional stresses. These improvements have resulted in more complex scenarios of deformation, which suggest that rift obliquity may be a major parameter controlling the characteristics of natural oblique rifts not only in terms of fault patterns, as outlined by previous experiments, but also in terms evolution, architecture and strain partitioning. In particular, strong differences in these parameters have been observed between low to moderate and high obliquity rifting, with the main changes in the deformation styles occurring for obliquity ~30°/45° (angle between the orthogonal to the rift trend and the direction of extension), which marks the transition from extension- to strike-slip-dominated deformation. In details, for low to moderate obliquity we observe a clear two-phase evolution, characterized by the diachronous activation of two major fault systems, and a strong to moderate strain partitioning between margins and rift floor. High obliquity models are instead characterized by a single evolutionary phase (with the activation of only one major fault system) and absent strain partitioning.

Satellite images analysis allowed to better characterize the two MER main faults systems, in terms of length and orientation, in the three main MER segments. In particular, the results highlight the along-axis variation of the statistical weight of the two fault systems, showing a strong decreasing trend in the relative importance of the Wonji faults from the NMER southward.

The fieldwork documents the occurrence of Quaternary, and in some cases Holocene, tectonics for the faults of both the margins and the rift floor (WFB faults). In particular, evidence of recent tectonic activity was also found on a border fault at the transition between the Northern MER and the Central MER; this partly contrasts with previous geological and

geophysical works suggesting border faults to be totally deactivated at these latitudes. The obtained extension directions vary from ca. N110°-130°E on the MER margins up to N90°-100°E along the WFB.

The similarities showed between faulting in analogue models and in MER segments in terms of fault pattern, rift architecture, and diachronous activation of different fault sets allowed comparing the results of the different methodologies used in this thesis.

The best-fit of the main fault orientation peaks (internal and border faults) of analogue models to the results of the remote sensing structural analysis implies a ~N100°E extension direction that is in very good agreement with previous results of geodetic measurements, as well as with geophysical and plate motion data. Moreover, the cumulative analysis of the WFB fault slip data revealed a consistent N100°E extension that thus, on the basis of the analogue modelling results, is expected to represent the regional extension direction acting in the system. The N110°-130° extension directions determined on the MER border faults highlights a local stress redistribution around the rheological discontinuity marking the rift margins. Since the entire models evolution is determined by a constant kinematics, we speculated a constant Late Miocene-recent ~N100°E Nubia-Somalia motion.

The comparison between the characteristics of the different MER segments and analogue model evolution allows discriminating an along-axis variation in the rift evolution characterized by a southward decreasing rift maturity: from the Northern MER in a stage of incipient continental rupture, to a transitional stage in the Central MER, to the early continental rifting in the Southern MER. In this scenario, the different MER segments exemplify the typical evolution of continental narrow rifts.

# Appendix

## Influences of the magmatic intrusions: estimates of the flexure of the lithosphere

The lithosphere in the MER has been thinned and weakened by 11-18 Ma of extension (e.g. WoldeGabriel et al., 1990; Wolfenden et al., 2004; Bonini et al. 2005), and still it is under extension. This long period of extension has resulted in a relatively thin elastic plate thickness, which is generally considered a proxy for the strength of the lithosphere (e.g. Burov and Diament, 1995); Ebinger et al. (1999) and Keir et al. (2006) estimated an effective elastic thickness of less than 15 km in the NMER. The thickness of the elastic plate influences its flexural behaviour. In this boundary condition the weight of the cooled large magmatic bodies identified beneath the NMER (e.g. Keranen et al., 2004; Daly et al., 2008) could result in a bended and deflected lithosphere able to influence the following evolutionary phases. The flexure of the lithosphere as a result of the emplacement of the en echelon magma bodies has been thus estimated.

The flexural deformation was calculated using the method described in Li et al. (2004) for 3D modelling of flexural deformation. We performed models both with a single magma body (see Table A1) and, for a limited range of the parameter values, with two en-echelon bodies (Fig. A1 and Table A2).

The equation governing the elastic deformation is given by (Turcotte and Schubert, 2002):

$$D\frac{d^4w}{dx^4} + \left(\rho_m - \rho_{fill}\right)gw(x) = q(x) \qquad 5.1$$

where w is the deflection of the plate, $\rho_m$ and $\rho_{fill}$ are respectively the mantle and the sedimentary fill density, g is the acceleration of gravity, q the vertical load (given by the volume and the density of the magma body). The parameter D is the flexural rigidity and defines the resistance to bending of a lithospheric plate. It is given as:

$$D = \frac{ET_e^3}{12\left(1 - \upsilon^2\right)} \qquad 5.2$$

where E is the Young's modulus, $\upsilon$ is the Poisson's ratio, $T_e$ is the effective elastic thickness of the lithosphere.

The parameters that were thus used in the calculations are the: E=70 GPa, $\upsilon$=0.30, sedimentary fill =2300 kg/m$^3$, difference between the plate density and the loading density of the magma bodies =210 kg/m$^3$ (Cornwell et al., 2006), the dimensions of the magma body =20km x 40 km (see Fig. 5.10; Keranen et al., 2004). The plate thickness was varied between 4 and 14 km; shown in Fig. A1 are results with plate thickness 6 km, corresponding to a 1.38

$10^{21}$ Nm flexural rigidity. In all the calculations, volcanoes were also added as loads to the top of the plate. The setup shown in Fig. A1 represents a single en echelon pattern.

The comparison of the results of the single body calculations with the two en-echelon bodies results shows that the maximum subsidence (on equal $T_e$ value) is fully comparable (see Tables 5.2 and 5.3). The calculations show that the elastic plate bends around the igneous

| 3D MODELLING NO FILL | SUBSIDENCE (m) | SUBSIDENCE (m) | influence of the volcano |
|---|---|---|---|
| | Internal load only | Internal+ext. load | (% of the total) |
| Te=6km | 352 | 382 | 7,85 |
| Te=7km | 295 | 319 | 7,52 |
| Te=8km | 251 | 272 | 7,72 |
| Te=9km | 217 | 234 | 7,26 |
| Te=10km | 189 | 204 | 7,35 |
| | | | |
| 3D MODELLING SED. FILL | SUBSIDENCE (m) | SUBSIDENCE (m) | influence of the volcano |
| | Internal load only | Internal+ext. load | (% of the total) |
| Te=4km | 1169 | 1267 | 7,73 |
| Te=5km | 903 | 978 | 7,67 |
| Te=6km | 721 | 781 | 7,68 |
| Te=7km | 590 | 638 | 7,52 |
| Te=8km | 492 | 532 | 7,52 |
| Te=9km | 417 | 451 | 7,54 |
| Te=10km | 358 | 387 | 7,49 |
| Te=11km | 311 | 337 | 7,72 |
| Te=12km | 230 | 249 | 7,63 |
| Te=13km | 208 | 225 | 7,56 |
| Te=14km | 188 | 203,5 | 7,62 |

Table A1: Results of flexural modelling of a single magmatic body with different Te values. Models were performed both with sedimentary fill of the depression (upper panel) and without sedimentary fill (lower panel). The presence of a superficial volcanic edifice (external load) was also considered.

| DOUBLE LOAD 3D MODELLING SED. FILL | SUBSIDENCE (m) | SUBSIDENCE (m) | influence of the volcano |
|---|---|---|---|
| | Internal load only | Internal+ext. load | (% of the total) |
| Te=5km | 901 | 977 | 7,78 |
| Te=6km | 738 | 800 | 7,75 |

Table A2: Results of flexural modelling of two en-echelon magmatic body with different Te values. See Table 5.2 for details.

bodies in a ~100 km wide region, and in between the en echelon segments (Fig. A1). Amplitudes of plate bending are up to ~800 m at the location of the magmatic bodies, and up to ~550 m in between the segments in the transfer zones. In the topographic profiles orthogonal to the rift axis through the NMER segments (cfr. Figs. 4.6, 6.9) this deflection is

not detectable because the basin depressions are filled with sediments and lava flows. The magma body emplacement causes stresses in the lithosphere (see Beutel et al., submitted to Earth and Planetary Science Letters), but the resulting deflection is too small to be detected in the Moho topography profile. Nevertheless, the flexural depression of the plate caused by the magmatic intrusive bodies is expected to cause sills and basalt flows to dip toward the rift-or breakup axis, as observed in several passive margins worldwide (Ebinger, 2005).
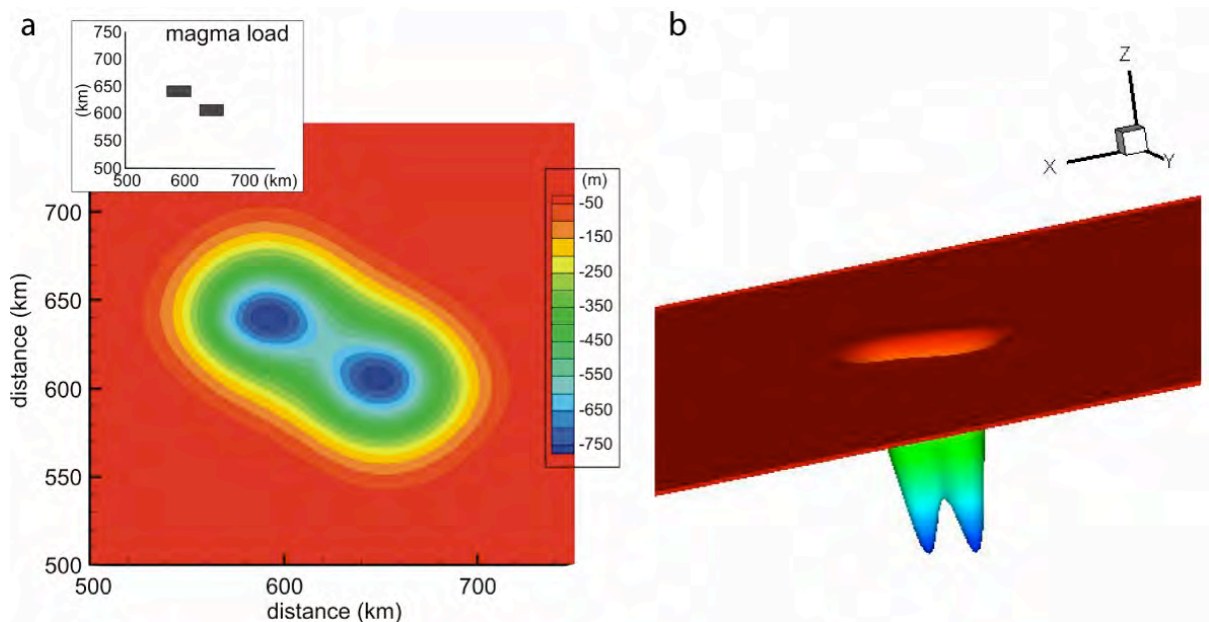


Fig. A1: Plate flexure resulting from the loading of intrusive igneous bodies. Inset: dimensions and distribution of magmatic load. a) top view of the predicted flexure and, b) 3D representation.

# References

Abebe, B., Boccaletti, M., Mazzuoli, R., Bonini, M., Tortrici, L., Trua, T. (1999). Geological Map of the Lake Ziway-Asela region (Main Ethiopian Rift). Scale 1:50,000. A.R.C.A., Firenze

Abbate, E., and M. Sagri (1980), Volcanites of Ethiopian and Somali Plateaus and major tectonic lines. Atti Convegni Lincei, 47, 219 – 227.

Abebe, T., F. Mazzarini, F. Innocenti, and P. Manetti (1998), The Yerer-Tullu Wellel volcanotectonic lineament: A transtentional structure in central Ethiopia and the associated magmatic activity. J. Afr. Earth Sci., 26, 135 – 150.

Abebe, T., Manetti, P:, Bonini, M., Corti, G., Innocenti, F., Mazzarini, F., and Pècksay, Z. (2005). Geological map (scale 1:200.000) of the northern Main Ethiopian Rift and its implications for the volcano-tectonic evolution of the rift: Geological Society of America Map and Chart MCH094, 20p., doi: 10.1130/2005MCH094TXT.

Acocella, V., Korme, T. (2002). Holocene extension direction along the Main Ethiopian Rift, East Africa. Terra Nova 14, 191–197.

Afonso J.C., and Ranalli G. (2004). Crustal and mantle strengths in continental lithosphere: is the jelly sandwich model obsolete? Tectonophysics 394, 221-232.

Agostini, A., G. Corti, A. Zeoli, and G. Mulegeta (2009). Evolution, pattern and partitioning of deformation during oblique continental rifting: Inferences from lithospheric-scale centrifuge models. Geochem. Geophys. Geosyst., 10, Q11015, doi:10.1029/2009GC002676.

Akermann, R. V., R. W. Schilsche, M. O. Withjack (2001). The geometric and statistical evolution of normal fault systems: an experimental study of the effects of mechanical layer thickness on scaling laws. Journ. Struct. Geol. 23, 1803-1819.

Anderson E. M. (1951). The Dynamics of Faulting and Dike Formation with Applications to Britain. Olivier & Boyd, Edinburg.

Angelier J. and Merchler P. (1977). Sur une méthode graphique de recherché des contraines pricipales également utilisable en tectonique et en sismologie: la méthode des dièdres droits. Bulletin de la Société Geologique de France. 19, 1309-1318.

Angelier J. (1979). Determination of the mean principal direction of stress for a given fault population. Tectonophysics, 56, T17-T26.

Asfaw, L.M. (1992). Constraining the African pole of rotation. Tectonophysics 209, 55–63.
Barton C. C. (1995). Fracyal analysis of scaling and spatial clustering of fractures, in Fractal in Earth Sciences, edited by C. C. Barton and P. R. La Pointe, pp141-178, Plenum, New York.

Bastow, I. D., A. A. Nyblade, G. W. Stuart, T. O. Rooney, and M. H. Benoit (2008). Upper mantle seismic structure beneath the Ethiopian hot spot: Rifting at the edge of the African low-velocity anomaly. Geochem. Geophys. Geosyst., 9, Q12022, doi:10.1029/2008GC002107.

Bastow, I.D., Stuart,G.W.,Kendall, J.M. and Ebinger, C.J. (2005). Upper mantle seismic structure in a region of incipient continental breakup: northern Ethiopian rift. Geophysical Journal International, 162(2), 479–493.

Bellahsen, N., Fournier, M., d'Acremont, E., Leroy, S. and J. M. Daniel, J.M. (2006) Fault reactivation and rift localization: Northeastern Gulf of Aden margin. Tectonics, 25, TC1007, doi:10.1029/2004TC001626.

Benes, V. and P. Davy (1996) Modes of continental lithospheric extension: experimental verification of strain localization processes. Tectonophysics, 254, 69-87.

Benoit, M.H., Nyblade, A.A., VanDecar, J.C. (2006)a. Upper mantle Pwave speed variations beneath Ethiopia and the origin of the Afar Hotspot. Geology 34, 329–332.

Benoit, M.H., Nyblade, A.A., Owens, T.J., Stuart, G. (2006)b. Mantle transition zone structure and upper mantle S velocity variations beneath Ethiopia: evidence for a broad, deep-seated thermal anomaly. Geochemistry, Geophysics, Geosystems 7, Q11013. doi:10.1029/2006GC001398.

Benvenuti, M., Carnicelli, S., Belluomini, G., Dainelli, N., Di Grazia, S., Ferrari, G.A., Iasio, C., Sagri, M., Ventra, D., Balemwald, Atnatu, Seifu, Ke, (2002). The Ziway–Shala lake basin (main Ethiopian rift, Ethiopia): a revision of basin evolution with special reference to the Late Quaternary. Journal of African Earth Sciences 35, 247–269.

Beutel, E., van Wijk, J., Ebinger, C., Keir, D., and A. Agostini (submitted to Earth and Planetary Science Letters). Formation and stability of magmatic segments in the Main Ethiopian and Afar rifts. Earth and Planetary Science Letters.

Billham, R., Bendick, R., Larson, K., Braun, J., Tesfaye, S., Mohr, P., Asfaw, L. (1999). Secular and tidal strain across the Ethiopian rift. Geophysical Research Letters 27, 2789–2984.

Boccaletti, M., Getaneh, A., Tortorici, L. (1992) The Main Ethiopian Rift: an example of oblique rifting. Annales Tectonicae, 6, 20-25.

Boccaletti, M., Bonini, M., Mazzuoli, R., Abebe, B., Piccardi, L., Tortorici, L. (1998). Quaternary oblique extensional tectonics in the Ethiopian Rift (Horn of Africa). Tectonophysics 287, 97–116.

Bonini, M., Souriot, T., Boccaletti, M., Brun, J.P. (1997) Successive orthogonal and oblique extension episodes in a rift zone: laboratory experiments with application to the Ethiopian Rift. Tectonics. 16, 347-362.

Boccaletti, M., M. Bonini, R. Mazzuoli, B. Abebe,L. Piccardi, and L. Tortorici (1998). Quaternary oblique extensional tectonics in the Ethiopian Rift (Horn of Africa). Tectonophysics, 287, 97–116.

Bonini, M., G. Corti, F. Innocenti, P. Manetti, F. Mazzarini, T. Abebe, and Z. Pecskay (2005). The evolution of the Main Ethiopian Rift in the frame of Afar and Kenya rifts propagation. Tectonics 24, TC1007, doi:10.1029/2004TC001680.

Bonnet E., O. Bour, N.E. Odling, P. Davy, I. Main, P. Cowie , and B. Berkowitz (2001). Scaling of fracture systems in geological media. Rev. of Geophysics. 39, 347-383.

Brun, J.-P. and Tron, V. (1993). Development of the North Viking Graben: inferences from laboratory modelling. Sedimentary Geology, 86, 31-51.
Brun, J.-P. (1999). Narrow rifts versus wide rifts: inferences for the mechanics of rifting from laboratory experiments. Philosophical Transactions Royal Society of London, Series A, 357, 695-712.

Buck, W. R. (2004). Consequences of asthenospheric variability on continental rifting, in Rheology and Deformation of the Lithosphere at continental Margins, edited by G. D. Karner et al., 1 – 30, Columbia Univ. Press, New York.

Bucky, B.P. (1931). The use of models for the study of mining problems. Technical Publication, American Institure of Mining Engineers, 425.

Burov, E. B. and M. Diament (1995). The effective elastic thickness ($T_e$) of continental lithosphere: what does it really means? J. Geophys. Res., 100, 3905-3927.

Campbell M. E., Rowland J. V., Wright I. C., and I. E. M. Smith (2007) Oblique rifting along the central and southern Kermadec Arc front (30°-36°S), SW Pacific. Geochem. Geophys. Geosyst., 8, Q01007, doi:10.1029/2006GC001504.

Calais, E., C. J. Ebinger, C. Hartnady, and J. M. Nocquet (2006) Kinematics of the East African rift from GPS and earthquake slip vector data, in The Afar Volcanic Province Within the East African Rift System, edited by G. Yirgu, C. J. Ebinger, and P. K. H. Maguire, Geol. Soc. Spec. Publ.,
259, 9 –22.

Caputo, M. and R. Caputo (1988). Structural analysis: new analytical approach and applications. Annales Tectonicae, 2, 84-89.

Carey E. (1979). Recherche des directions principales des contraintes associées au jeu d'une population de failles. Revue de Géologie et de Géographie Phisique. 21, 57-66.

Casey, M., Ebinger, C.J., Keir, D., Gloaguen, R., Mohamad, F. (2006). Strain accommodation in transitional rifts: extension by magma intrusion and faulting in Ethiopian rift magmatic segments. In: Yirgu, G., Ebinger, C.J., Maguire, P.K.H. (Eds.), The Afar Volcanic Province within the East African Rift System: Geological Society Special Publication 259, 143–163.

Chorowicz, J., Collet, B., Bonavia, F., Korme, T. (1994). Northwest to North–Northwest extension direction in the Ethiopian rift deduced from the orientation of extension structures and fault-slip analysis. Geological Society of America Bulletin 105, 1560–1570.

Chorowicz, J. (2005). The East African Rift system. Journal of African Earth Sciences 43, 379–410.

Chu, D., and R. G. Gordon (1999). Evidence for motion between Nubia and Somalia along the Southwest Indian Ridge. Nature 398, 64–67

Clifton, A.E., Schlische, R.W., Withjack, M.O., and Ackermann, R.V. (2000). Influence of rift obliquity on fault-population systematics: results of experimental clay models. Journal of Structural Geology, 22, 1491-1509.

Clifton A.E., and Schlische, R.W. (2001). Nucleation, growth, and linkage of faults in oblique rift zones: Results from experimental clay models and implications for maximum fault size. Geology, 29,455-458.

Clifton, A. E. and Schlische, R. W. (2003) Fracture populations on the Reykjanes Peninsula, Iceland: Comparison with experimental clay models of oblique rifting. Journal of Geophysical Research. 108, B2, 2074, doi:10.1029/2001JB000635.

Colletta, B., Letouzey, J., Pinedo, R., Ballare, J. F., and P. Balé (1991). Computer X-ray tomography analysis  of sandbox models: Examples of thin-skinned systems. Geology, 19,1063-1067.

Cornwell, D. G., Mackenzie, G. D., Maguire, P. K. H., England, R. W., Asfaw, L. M. and Oluma, B. (2006). Northern Main Ethiopian Rift crustal structure from new high-precision gravity data, in The Afar Volcanic Province within the East African Rift System, eds. Yirgu, G., Ebinger, C. J., and Maguire, P. K. H.: Geological Society of London Special Publications, 259, 309-323.

Cornwell, D. G., P. K. H. Maguire, R. W. England, and G. W. Stuart (2010), Imaging detailed crustal structure and magmatic intrusion across the Ethiopian Rift using a dense linear broadband array, Geochem. Geophys. Geosyst., 11, Q0AB03, doi:10.1029/2009GC002637.

Corti, G., Bonini, M., Innocenti, F., Manetti, P., and Mulugeta, G. (2001). Centrifuge models simulating magma emplacement during oblique rifting. Journal of Geodynamics, 31, 557-576.

Corti, G., Bonini, M., Conticelli, S., Innocenti, F., Manetti, P., and Sokoutis, D. (2003). Analogue modelling of continental extension: a review focused on the relations between the patterns of deformation and the presence of magma. Earth-Science Reviews, 63, 169-247.

Corti G., Bonini M., Sokoutis D., Innocenti F., Manetti P., Cloetingh S., and Mulugeta G. (2004). Continental rift architecture and patterns of magma migration: a dynamic analysis based on centrifuge models. Tectonics, 23, TC2012, doi:10.1029/2003TC001561.

Corti G., and Manetti P. (2006). Asymmetric rifts due to asymmetric Mohos: an experimental approach. Earth and Planetary Science Letters, 245, 315-329, doi:10.1016/j.epsl.2006.02.004.

Corti, G. (2008) Control of rift obliquity on the evolution and segmentation of the main Ethiopian rift. Nature Geoscience 1, 258-262.

Corti, G. (2009) Continental rift evolution: From rift initiation to incipient break-up in the Main Ethiopian Rift, East Africa. Earth Science Reviews 96, 1-53.

Coulié, E., Quidelleur, X., Gillot, P.Y., Coutillot, V., Lefevre, J.C., Chiessa, S. (2003). Comparative K–Ar and Ar/Ar dating of Ethiopian and Yemenite Oligocene volcanism: implication for timing and duration of the Ethiopian traps. Earth and Planetary Science Letters 206, 477–492. doi:10.1016/S0012-821X(02)01089-0.

Courtillot, V., Jaupart, C., Manighetti, I., Tapponnier, P., Besse, J. (1999). On causal links between flood basalts and continental breakup. Earth and Planetary Science Letters 166, 177–195.

Daly, E., Keir, D., Ebinger, C.J., Stuart, G.W., Bastow, I.D., Ayele, A., (2008). Crustal tomographic imaging of a transitional continental rift: the Ethiopian rift. Geophysical Journal nternational 172, 1033–1048.

Dauteuil, O. and Brun J.-P. (1993) Oblique rifting in a slow-spreading ridge. Letters to Nature. 361, 145-148.
Dauteuil, O. and Brun J.-P. (1996) Deformation partitioning in a slow spreading ridge undergoing oblique extension: Mohns Ridge, Norwegian Sea. Tectonics. 15, 870-884.
Dauteuil, O., Huchon, P., Quemeneur, F., and Souriot, T., (2001). Propagation of an oblique spreading centre: the western Gulf of Aden. Tectonophysics, 332, 423-442.

Davidson, A. and Rex, D. C. (1980). Age of volcanism and rifting in Southwestern Ethiopia. Nature 283, 657-658.

Davy, P., an Cobbold, P. R. (1991) Experiments on shortening of 4-layer model of the continental lithosphere. In P. R. Cobbold (Ed.), Experimental and Numerical Modelling of Continental Deformation, Tectonophysics, 188, 1-25.

Di Paola, G.M., 1972. The Ethiopian Rift Valley (between 7 and 8 40' lat. North). Bulletin of Volcanology 36, 517–560.

Dixon, J. M., and D. G. Summer (1987). Centrifuge modelling of laccolith intrusion. Journal of Structural Geology, 7, 87-103.

Dugda, M.T., Nyblade, A.A., Jordi, J., Langston, C.A., Ammon, C.J., Simiyu, S. (2005). Crustal structure in Ethiopia and Kenya from receiver function analysis: implications for rift development in Eastern Africa. Journal of Geophysical Research 110 (B1), B01303. doi:10.1029/2004JB003065.

Dugda, M., Nyblade, A.A., Julia, J. (2007). Thin lithosphere beneath the Ethiopian Plateau revealed by a joint inversion of Rayleigh Wave Group velocities and receiver functions. Journal of Geophysical Research 112. doi:10.1029/2006JB004918.

Dunbar, J.A., and Sawyer, D.S. (1989). Continental rifting at pre-existing lithospheric weaknesses. Nature, 242, 565-571.

Ebinger, C. J., Yemane, T., WoldeGabriel, G., Aronson, J. L. and Walter, R. C. (1993). Late Eocene-Recent volcanism and faulting in the southern main Ethiopian rift. Journal Geological Society London, 150, 99-108.

Ebinger, C., Sleep, N.H. (1998). Cenozoic magmatism in central and east Africa resulting from impact of one large plume. Nature, 395, 788-791.

Ebinger, C.J., Jackson, J. A., Foster, A. N., Hayward, N. J. (1999). Extensional basin geometry and the elastic lithosphere. Philosophical Transactions: Mathematical, Physical and Engineering Sciences, 357, 741-765.

Ebinger, C., T. Yamane, D.J. Harding, S. Tesfaye, S. Kelly, and D.C. Rex (2000). Rift deflection, migration, and propagation: Linkage of the Ethiopian and Eastern rifts, Africa. Geol. Soc. Am. Bull., 112, 163-176.

Ebinger, C. J. & Casey, M. (2001). Continental breakup in magmatic provinces: An Ethiopian example. Geology 29, 527–530.

Ebinger, C. (2005). Continental breakup: The East African perspective. Astron. Geophys. 46, 2.16-2.21.

Fernandes, R.M.S., Ambrosius, B.A.C., Noomen, R., Bastos, L., Combinck, L., Miranda, J.M., Spakman, W. (2004). Angular velocities of Nubia and Somalia from continuous GPS data: implications on present-day relative kinematics. Earth and Planetary Science Letters 222, 197–208.

Fournier M., and Petit C. (2007). Oblique rifting at oceanic ridges: Relationship between spreading and stretching directions from earthquake focal mechanisms. Journal of Structural Geology, 29, 201-208.

Garfunkel, Z., Beyth, M. (2006). Constraints on the structural development of Afar imposed by the kinematics of the major surrounding plates. In: Yirgu, G., Ebinger, C.J., Maguire, P.K.H. (Eds.), The Afar Volcanic Province within the East African Rift System: Geological Society Special Publication, 259, 23–42.

George, R.M., Rogers, N.W. (1999). The petrogenesis of Plio-Pleistocene alkaline volcanic rocks from the Tosa Sucha region, Arba Minch, southern Main Ethiopian Rift. Acta Volcanologica 11, 121–130.

Gibson, I.L. (1969). The structure and volcanic geology of an axial portion of the Main Ethiopian Rift. Tectonophysics 8, 561–565.

Gillespie P.A., C. B. Howard, J. J. Walsh, and J. Watterson (1993). Measurement and characterisation of spatial distributions of fractures. Tectonophysics 226, 113-141.

Gillespie P.A., J. J. Walsh, J. Watterson, C. G. Bonson, T. Manzocchi (2001). Scaling relationship of joint and vein arrays from The Burren, Co. Clare, Ireland. Journal of Structural Geology 23, 183-201.

Geotze, C., and B. Evans (1979). Stress and temperature in the bending lithosphere as constrained by experimental rock mechanics. Geophysical Journal of the Royal Astronomical Society, 59, 463-478.

Gouin, P. (1979). Earthquake History of Ethiopia and the Horn of Africa,258 pp., Int. Dev. Res. Centre, Ottawa, Ont

Hall Sir, J. (1815) On the vertical position and convolution of certain strata, and their relation with granite. Transaction of the Royal Society, Edimburgh 7,79-108.

Hayward, N.J. and Ebinger, C.J. (1996). Variations in the along-axis segmentation of the Afar Rift system. Tectonics 15, 244-257.

Hofstetter, R., Beyth, M. (2003). The Afar Depression interpretation of the 1960–2000 earthquakes. Geophysical Journal International 155, 715–732. doi:10.1046/j.1365-246X.2003.02080.x.

Homberg, C., Hu, J. C., Angelier, J., Bergerat, F., and O. Lacombe (1997). Characterization of stress perturbation  near major fault zones: insight from 2-D distinct-element numerical modelling and field studies (Jura mountains). Journal of Structural Geology, 19, 703-718.

Horner-Johnson, B.C., Gordon, R.G., Argus, D.F., 2007. Plate kinematic evidence for the existence of a distinct plate between the Nubian and Somalian plates along the Southwest Indian Ridge. Journal of Geophysical Research 112, B05418. doi:10.1029/2006JB004519.
Hubbert, M. K. (1937). Theory of scaled model as applied to the study of geological structures. Geological Society of American Bulletin, 48,1459-1520.

Kazmin, V. (1978). Geological Map of sheet NC37-15, Nazret, Ethiopia. Scale 1:250,000. Ethiopian Institute of Geological Surveys. Ministry of Mines, Energy and Water Resources. Printed by Ethiopian Mapping Agency, Addis Ababa, Ethiopia.

Kazmin, V. (1980). Transform faults in the East African Rift System. In: Geodynamic Evolution of the Afro-Arabian Rift System, Accademia Nazionale Dei Lincei, Atti dei Convegni Lincei  47, 65-73.

Keir, D., Kendall, J.-M., Ebinger, C., (2005). Variations in late syn-rift melt alignment inferred from shear-wave splitting in crustal earthquakes beneath the Ethiopian rift. Geophysical Research Letters, 32. doi:10.1029/2005GL024150.

Keir, D., Ebinger, C.J., Stuart, G.W., Daly, E., Ayele, A. (2006). Strain accommodation by magmatism and faulting as rifting proceeds to breakup: seismicity of the northern Ethiopian rift. Journal of Geophysical Research, 111 (B5), B05314. doi:10.1029/2005JB003748.

Keir, D., Bastow, I. D., Whaler, K. A., Daly, E., Cornewell, D. G., Hautot, S. (2009). Lower crustal earthquakes near the Ethiopian rift induced by magmatic processes. Geochem. Geophys. Geosyst., 10, doi:10.1029/2009GC002382

Kendall, J.M., Stuart, G.W., Ebinger, C.J., Bastow, I.D., Keir, D. (2005). Magma assisted rifting in Ethiopia. Nature, 433, 146–148.

Kendall, J.M., Pilidou, S., Keir, D., Bastow, I.D., Stuart, G.W., Ayele, A. (2006). Mantle upwellings, melt migration, and the rifting of Africa: insights from seismic anisotropy. In: Yirgu, G., Ebinger, C.J., Maguire, P.K.H. (Eds.), The Afar Volcanic Province within the East African Rift System: Geological Society Special Publication, vol. 259, pp. 55–72.

Kendall, J.M., Stuart, G.W., Ebinger, C.J., Bastow, I.D., Keir, D. (2005). Magma assisted rifting in Ethiopia. Nature, 433, 146–148.

Keranen, K., Klemperer, S.L., Gloaguen, R., Eagle working group (2004). Three-dimensional seismic imaging of a protoridge axis in the Main Ethiopian rift. Geology, 32, 949–952.

Keranen, K., Klemperer, S.L. (2008). Discontinuous and diachronous evolution of the Main Ethiopian Rift: implications for the development of continental rifts. Earth and Planetary Science Letters 265, 96–111. doi:10.1016/j.epsl.2007.09.038.

Keranen, K., Klemperer, S.L., Julia, J., Lawrence, J.L., Nyblade, A. (2009). Low lower-crustal velocity across Ethiopia: is the Main Ethiopian Rift a narrow rift in a hot craton? Geochemistry, Geophysics, Geosystems 10, Q0AB01. doi:10.1029/2008GC002293.

Kieffer, B., Arndt, N., LaPierre, H., Bastien, F., Bosch, D., Pecher, A., Yirgu, G., Ayalew, D., Weis, D., Jerram, D., Keller, F., Meugniot, C. (2004). Flood and shield basalts from Ethiopia: magmas from the African Superswell. Journal of Petrology 45, 793–834.

Koyi, H. (1997). Analogue modelling; from qualitative to a quantitative technique, a historical outline. Journal of Petroleum Geology, 20, 233-238.
Koyi, H. A. and A. Skelton (2001). Centrifuge modelling of the evolution of low-angle detachment faults from high-angle normal faults. Journal of Structural Geology, 23, 1179-1185.

Korme, T., Acocella, V., Abebe, B. (2004). The role of pre-existing structures in the origin, propagation and architecture of faults in the Main Ethiopian Rift. Gondwana Research 7, 467–479.

Kurz, T., Gloaguen, R., Ebinger, C., Casey, M., Abebe, B. (2007). Deformation distribution and type in the Main Ethiopian Rift (MER): a remote sensing study. Journal of African Earth Sciences 48, 100–114.

Lemaux, J., Gordon, R., Royer, J.-Y. (2002). Location of the Nubia–Somalia boundary along the Southwest Indian Ridge. Geology 30, 339–342.

Le Turdu C., J. Tiercelin, E. Gibert, Y. Travi, K. E. Lezzar, J. P. Richert, M. Massault, F. Gasse, R. Bonnefille, M. Decobert, B. Gensous, V. Jeudy, E. Tamrat, M. U. Mohammed, K. Martens, B. Atnafu, T. Chernet, D. Williamson, and M. Taieb (2005). The Ziway–Shala lake basin system, Main Ethiopian Rift: Influence of volcanism, tectonics, and climatic forcing on basin formation and sedimentation. Palaeogeography, Palaeoclimatology, Palaeoecology, 150, 135-177.

Li, F., Dyt, C., and C. Griffiths (2004). 3D modelling of flexural isostatic deformation. Computers and Geosciences, 30, 1105-1115.

Liu, S. and J. M. Dixon (1991). Centrifuge modelling of thrust faulting; structural variation along strike in fold-thrust belts. Tectonophysics, 188, 39-62.

Mackenzie, G.H., Thybo, G.H., Maguire, P. (2005). Crustal velocity structure across the Main Ethiopian Rift: results from 2-dimenional wide-angle seismic modeling. Geophysical Journal International 162, 994–1006.

Maguire, P.K.H., Ebinger, C.J., Stuart, G.W., Mackenzie, G.D., Whaler, K.A., Kendall, J.-M., Khan, M.A., Fowler, C.M.R., Klemperer, S.L., Keller, G.R., Harder, S., Furman, T., Mickus,

K., Asfaw, L., Ayele, A., Bekele, A. (2003). Geophysical project in Ethiopia studies continental breakup. Eos Transaction on American Geophysical Union 84, 337–340.

Maguire, P.K.H., Keller, G.R., Klemperer, S.L., Mackenzie, G.D., Keranen, K., Harder, S., O'Reilly, B., Thybo, H., Asfaw, L., Khan, M.A., Amha, M. (2006). Crustal structure of the Northern Main Ethiopian Rift from the EAGLE controlled source survey; a snapshot of incipient lithospheric break-up. In: Yirgu, G., Ebinger, C.J., Maguire, P.K.H. (Eds.), The Afar Volcanic Province within the East African Rift System: Geological Society Special Publication, vol. 259, 269–291.

Mart, Y., and Dauteuil, O. (2000). Analogue experiments of propagation of oblique rifts. Tectonophysics, 316, 121-132.

Mazzarini F. and M. D'Orazio (2003). Spatial distribution of cones and satellite-detected lineaments in the Pali Aike Volcanic Field (souhermost Patagonia): Insights into the tectonic setting of a Neogene rift system. J. Volcanol. Geotherm. Res. 125, 291-305. doi:10.1016/S0377-0273(03)00120-3.

Mazzarini, F., Corti, G., Manetti, P., Innocenti, F. (2004). Strain rate bimodal volcanism in the continental rift: Debre Zeyt volcanic field, northern MER, Ethiopia. Journal of African Earth Sciences 39, 415–420. doi:10.1016/j.jafrearsci.2004.07.025.
McClay, K.R., and White, M.J. (1995). Analogue modelling of orthogonal and oblique rifting. Marine and Petroleum Geology, 12, 137-151.

McClay, K.R., Dooley, T., Whitehouse, P. and Mills, M. (2002). 4-D evolution of rift systems: Insights from scaled physical models. American Association of Petroleum Geologists Bulletin, 86, 935-959.

Meyer, W., Pilger, A., Rosler, A. and Stets, J. (1975). Tectonic evolution of the northern part of the Main Ethiopian Rift in Southern Ethiopia. In: Afar Depression of Ethiopia (Edited by A. Pilger and A. Rosler), Schweizerbart, Stuttgart, 352-362.

Mickus, K., Tadesse, K., Keller, G.R., Oluma, B. (2007). Gravity analysis of the main Ethiopian rift. Journal of African Earth Sciences 48, 59–69.

Mohr, P. (1962). The Ethiopian Rift System. Bull. Geophys. Obs. Addis Ababa 5, 33-62.

Mohr, P. A. (1967). The Ethiopian Rift System. Bulletin of the Geophysical Observatory of Addis Ababa 11, 1-65.

Mohr, P. (1968). Transcurrent faulting in the Ethiopian Rift System. Nature 218, 938–941.

Mohr, P.A., Wood, C.A. (1976). Volcano spacing and lithospheric attenuation in the Eastern Rift of Africa. Earth and Planetary Science Letters 33, 126–144.

Mohr, P. (1983). Volcanotectonic aspects of the Ethiopian Rift evolution. Bulletin Centre Recherches Elf Aquitaine Exploration Production 7, 175–189.

Mooney, M. and R. H. Ewart (1934). The conicylindrical viscometer. Physics, 5, 350-354.

Moore, J.M., Davidson, A. (1978). Rift structure in Southern Ethiopia. Tectonophysics 46, 159–173.

Morbidelli, L., Nicoletti, M., Petrucciani, C., and E. M. Piccirillo (1975). K/Ar ages of the main volcanic events (Main Ethiopian Rift from 8°10'-9°00' lat. North). In Afar Depression of the Ethiopia, edited by A. Pilger and A. Rosler, 362-369, Scheweizerbart, Stuttgart, Germany.

Morley, C.K. (1999a). Influence of Preexisting Fabrics on Rift Structure. In: Morley, C.K. (Ed.), Geoscience of Rift Systems - Evolution of East Africa, American Association of Petroleum Geologists Studies in Geology, 44, 151-160.

Morley, C.K. (1999b). How successful are analogue models in addressing the influence of pre-existing fabrics on rift structures?. Journal of Structural Geology, 21, 1267-1274.

Mulugeta, G. and Ghebreab, W. (2001). Modeling heterogeneous stretching during episodic or steady rifting of the continental lithosphere. Geology, 29, 895-898.

Nyblade, A.A., Langston, C.A. (2002). Broadband seismic experiments probe the East African rift. EOS Transaction on American Geophysical Union 83, 405–408.

Panien, M, Schreurs, G., Pfiffner, A. (2006). Mechanical behaviour of granular materials used in analogue modelling: insights from grain characterisation, ring-shear tests and analogue experiments. Journal of Structural Geology, 28, 1710-1724.

Person, K. S. and Sokoutis, D. (2002) Analogue models of orogenic wedges controlled by erosion. Tectonophysics, 356, 323-336.

Pizzi, A., Coltorti, M., Abebe, B., Disperati, L., Sacchi, G., Salvini, R., 2006. The Wonji fault belt (main Ethiopian Rift): structural and geomorphological constraints and GPS monitoring. In: Yirgu, G., Ebinger, C.J., Maguire, P.K.H. (Eds.), The Afar Volcanic Province within the East African Rift System: Geological Society Special Publication 259, 191–207.

Priest S. D., and J. A. Hudson (1981). Estimation of discontinuity spacing and trace length using scanline surveys. Int. J. Rock Mech. Min. Sci. Geomech. Abstr. 18, 183-197.

Ramberg, H. (1963) Experimental study of gravity tectonics by means of centrifuged models. Bull. Geolo. Insts. Univ. Uppsala, 42,1-97.

Ramberg, H. (1967) Gravity, deformation and the Earth's crust (1st edition). Academic Press, London.

Ramberg, H. (1981). Gravity, deformation and the Earth's crust: London, Academic Press, 452pp.

Royer, J.-Y., Gordon, R.G., Horner-Johnson, B.C. (2006). Motion of Nubia relative to Antarctica since 11 Ma: implications for Nubia–Somalia, Pacific–North America, and India–Eurasia motion. Geology 34, 501–504. doi:10.1130/G22463.1.

Ranalli, G. (1995). Rheological of the Earth, 2nd edition, Chapman & Hall, London.

Ranalli, G. (2001). Experimental tectonics: from Sir James Hall to the present. Journal of Geodynamics, 32,65-76.

Rooney, T., Furman, T., Bastow, I., Ayalew, D., Yirgu, G. (2007). Lithospheric modification during crustal extension in the Main Ethiopian Rift. Journal of Geophysical Research 112, B10201. doi:10.1029/2006JB004916.

Rossetti, F., Faccenna, C., and G. Ranalli (2002) The influence of backstop dip and convergence velocity in the growth of viscous doubly-vergent orogenic wedges: insight from thermomecanical laboratory experiments. Journal of Structural Geology, 24, 953-962.

Schellart, W. P. (2000). Shear test results for cohesion and friction coefficients for different granular materials: scaling implications for their usage in analogue modelling. Tectonophysics, 324, 1-16.

Schreurs, G., Haenni, R., and Vock, P. (2001) Four dimensional analysis of analogue models; experiments on transfer zones in fold and thrust belts. In: Koyi, H. A., and Mancktelow, N. S. (Eds.), Tectonic modelling; a volume in honor of Hans Ramberg, Memoir – Geological Society of America, 193, 179-190.

Soliva, R. and R. Schultz (2008). Distributed and localized faulting in extensional settings: Insight from the North Ethiopian Rift-Afar transition area. Tectonics 27, TC2003, doi:10.1029/2007TC002148.

Stamps, D.S., Calais, E., Saria, E., Hartnady, C.,Nocquet, J.-M., Ebinger, C.J., Fernandes, R.M., (2008). A kinematic model for the East African Rift. Geophysical Research Letters 35, L05304. doi:10.1029/2007GL032781.

Stuart, G.W., Bastow, I.D., Ebinger, C.J. (2006). Crustal structure of the northern Main Ethiopian Rift from receiver function studies. In: Yirgu, G., Ebinger, C.J., Maguire, P.K.H. (Eds.), The Afar Volcanic Province within the East African Rift System: Geological Society Special Publication, 259, 253–267.

Talbot, C. J. (1977). Inclined and upward-moving gravity structures. Tectonophysics, 42, 159-181.

Tiberi, C., Ebinger, C., Ballu, V., Stuart, G., Oluma, B. (2005). Inverse models of gravity data from the Red Sea–Aden–East African rifts triple junction zone. Geophysical Journal International 163, 775–787. doi:10.1111/j.1365-246X.2005.02736.x.

Tommasi, A., and Vauchez, A. (2001). Continental rifting parallel to ancient collisional belts: an effect of the mechanical anisotropy of the lithospheric mantle. Earth and Planetary Science Letters, 185, 199-210.

Tron, V., and Brun, J.P. (1991). Experiments on oblique rifting in brittle-ductile systems. Tectonophysics, 188, 71-84.

Turcotte, D. L., and G. Schubert (2002). *Geodynamics*, 2nd edn. Cambridge University Press.

van Wijk, J.W. (2005). Role of weak zone orientation in continental lithosphere extension. Geophysical Research Letters, 32, doi:10.1029/2004GL022192.

van Wijk, J.W. and Blackman, D. (2007). Development of en echelon magmatic segments along oblique spreading ridges. Geology, 35, 599-602.

Versfelt, J., and B. R. Rosendahl (1989). Relationships between pre-rift structure and rift architecture in Lakes Tanganyika and Malawi: East Africa. Nature, 337, 354-357.

Weijermars, R. and H. Schmeling (1986). Scaling of Newtonian and non-Newtonian fluid dynamics without inertia for quantitative modelling of rock flow due to gravity (including the concept of rheological similarity). Physics of the Earth and Planetary Interiors, 43, 316-330.

Weijermars, R., Jackson, M. P. A., Vandeville, B. (1993). Rheological and tectonic modelling of salt province. Tectonophysics, 217, 143-174.

Whaler, K.A., Hautot, S. (2006). The electrical resistivity structure of the crust beneath the northern Main Ethiopian Rift. In: Yirgu, G., Ebinger, C.J., Maguire, P.K.H. (Eds.), The Afar Volcanic Province within the East African Rift System: Geological Society Special Publication, 259, 293–305.

Wilson, T. H. (2001). Scale transition in fracture and active fault networks. Mathematical Geol. 33, 591-613.
Withjack, M.O., and Jamison, W.R. (1986). Deformation produced by oblique rifting. Tectonophysics, 126, 99-124.

WoldeGabriel, G., Aronson, J.L.,Walter, R.C. (1990). Geology, geochronology, and rift basin development in the central sector of the Main Ethiopia Rift. Geological Society of America Bulletin 102, 439–458.

Wolfenden, E., Ebinger, C., Yirgu, G., Deino, A. & Ayale, D. (2004). Evolution of the northern Main Ethiopian rift: birth of a triple junction. Earth Planet. Sci. Lett. 224, 213– 228.

Wolfenden, E., Ebinger, C., Yirgu, G., Renne, P., Kelley, S.P. (2005). Evolution of the southern Red Sea rift: birth of a magmatic margin. Geological Society of America Bulletin 117, 846–864.

Ziegler, P.A., and Cloetingh, S.A.P.L. (2004). Dynamic processes controlling evolution of rifted basins. Earth-Science Reviews. 64, 1-50.